8.0 ASSESSMENT RESULTS

8.1 *Assessment Methodology Overview*

8.1.1 Introduction

This section describes the verification and validation performed for the S-RELAP5 code. The material included originates from the verification and validation report (Reference 8.1-1), which is intended to be a generic compilation of assessments supporting all S-RELAP5 based methodologies. The code assessments from Reference 8.1-1 applicable to the RLBLOCA methodology are those discussed in Section 6.0 and listed in the assessment matrix, Table 6-2. These assessments were chosen to address the important PIRT phenomena identified in Table 5-1. The cross correlation between assessments and PIRT phenomena is provided in Table 6-2. Additionally, some assessments were chosen to address issues of code scalability; these assessments, and the discussion with respect to scalability, are provided in Section 8.6.

Appendix A discusses the appropriate nodalization to represent PWR system components. The nodalization used in the assessments must be consistent with the large-scale plant nodalization in the regions where the phenomena are being assessed in order for the assessment results to apply to large scale PWRs. AREVA NP used the plant nodalization and the RLBLOCA S-RELAP5 input guidelines as described in Appendix A to the extent possible to derive assessment nodalizations, which are consistent with the PWR application nodalization. Unique features of small-scale facilities can require deviations from the guidelines. The assessment nodalizations are generally consistent with the plant application, and where deviations were made, the reasons for the deviations and the effects on results are discussed.

The assessments provided in this section demonstrate the code capabilities for simulation of important phenomena primarily associated with large-scale PWR systems LBLOCA. The report describes the experimental test facility and the tests benchmarked in this report to support S-RELAP5, for each assessment. Additionally, it also presents the S-RELAP5 nodalization and system representations, and the calculated results, along with comparable measured results. This section also defines acceptance criteria that describe how well the measured results are predicted and, using these criteria, draws conclusions regarding S-RELAP5 code capabilities

AREVA NP has verified the S-RELAP5 code. This process consisted of reviewing and comparing the code capabilities as documented in the theory manual with the as-programmed coding. All identified discrepancies were corrected as appropriate, by changing either the coding or the associated documentation. This process ensures that the code capabilities applicable to Large Break LOCA are as described in Section 7.0.

AREVA NP then assessed and validated the S-RELAP5 code. This process as documented in this section, consists of performing assessment calculations that allow comparison of calculated results with measured experimental data. The present report describes those specific assessments applicable to the RLBLOCA methodology due to the validation requirements varying among the methodologies supported.

8.1.2 Code Verification

The basic capabilities of the S-RELAP5 code are described in Section 7.0, which provides details of the theory behind the code, and the models and correlations used to implement that theory. Code verification is the process of ensuring that the models and correlations documented in the theory manual are implemented in the coding. A programmer's manual (Reference 8.1-2) is also a part of the code documentation, and documents the code structure and subroutines. Additionally, it provides flow diagrams of how the code functions.

Code verification is an essential part of code development and is documented in software development records required by quality assurance procedures. Since S-RELAP5 was originally developed from an existing code not under AREVA NP control, supplemental code verification (special review of codes developed outside AREVA) was performed and documented for the original submittal (Revision 0) of the RLBLOCA methodology. All code modifications made, since the completion of Revision 0 of this document (the version that supports EMF-2103(P)(A), Revision 0), have been made within the AREVA NP Software Quality Assurance Program (SQAP) in compliance with 10 CFR 50 Appendix B, as implemented by the requirements defined in Reference 8.1-3. The SQAP ensures all code development satisfies software quality expectations of CSAU and Regulatory Guide 1.203, including source code control and maintenance of User/Functional/Theoretical descriptions of all related codes.

8.1.3 Code Validation

To validate the code, calculations are performed for experimental test assessment cases. Parameter results from these calculations are then compared to the measured parameter values from the test data. The code version used in the validation is intended for application to full-scale analysis of nuclear power plant (NPP) systems. The experiment modeling is intended to demonstrate in a similar way, within the constraints of the test, that the modeling used for full scale studies simulates the appropriate phenomena effectively. The capability of the code to predict the important phenomena is demonstrated and quantified by comparing predicted versus measured results from these tests. Any code biases are identified and the uncertainty in predicting the important phenomena including both code and experimental uncertainties is quantified, estimated, or bounded. Generally, separate effects tests (SET) are used to quantify phenomena uncertainties, while integral effects tests (IET) confirm phenomena interactions and provide data to evaluate the effects of scaling.

The assessment validations are reported in the following sections according to the following general format:

- An introduction to describe the particular test and the purpose of the assessment
- A summary that includes the meaningful results and conclusions
- A facility description that describes the details of the specific test facility
- S-RELAP5 nodalization for the facility
- Calculation input for the test that describes how the test hardware, initial conditions, and boundary conditions were modeled in the calculation
- Comparisons of calculated and measured test results for the important phenomena and parameters
- A technical evaluation of the results comparisons
- Sensitivity analyses (if appropriate)
- Quantification of phenomena or parameter uncertainties (if appropriate)
- References related to the test

Section 8.2 includes the assessment calculations for the separate effects tests (SETs) and Section 8.3 contains the integral effects tests (IETs) assessments. Section 8.4 provides a summary of the determined biases and uncertainties for the code versus various sets of the test data.

8.1.4 Assessment Criteria

The assessments documented in this section demonstrate the S-RELAP5 code capabilities to predict the phenomena required in the performance of nuclear power plant analyses of LBLOCA transients.

The reported assessment results support the more detailed requirements of this procedure because the AREVA NP Realistic LBLOCA methodology follows the Code Scaling, Applicability, and Uncertainty (CSAU) methodology. The assessments were chosen to address the important PIRT phenomena identified in Table 5-1. The cross correlation between assessments and PIRT phenomena is provided in Table 6-2.

Consequently, the documented assessment results should provide quantitative statements about the code's capability to predict key parameters. NUREG 1737 Appendix C (Reference 8.1-4) suggests how this could be done by defining acceptance criteria associated with levels of code-data agreement. In this document, five levels of agreement are defined: (1) excellent agreement, (2) good agreement, (3) reasonable agreement, (4) acceptable agreement, and (5) insufficient agreement. These criteria move from the most desirable correlation of data to the code, to the unacceptable prediction of the data by the code, and are defined as follows:

- Excellent Agreement: The calculation of major phenomena, with rare exception, will lie within the scatter of the data including data uncertainty and any known data biases. The trends in the major phenomena also will therefore be predicted within the uncertainty of the data. For this criterion, the code-to-data comparison could be represented with an uncertainty and perhaps a small bias.
- Good Agreement: While the correct trends are predicted, the calculation of major phenomena will frequently lie outside the scatter of the data including data uncertainty and any known data biases. However, the correct conclusions about trends and phenomena would be reached if the code were used in similar applications. For the code to demonstrate good agreement, the calculation of major phenomena should, on average, not differ from the data by more than plus or minus 10%. For this criterion, the code-to-data comparison may be representable with a bias and uncertainty. For application wherein the code is conservative for a specific phenomenon, the code results could be used directly without determining a bias or uncertainty for that phenomenon.

- Reasonable Agreement: While the correct trends are predicted, the calculation of major phenomena will consistently lie outside the scatter of the data including data uncertainty and any known data biases. However, the correct conclusions about trends and phenomena would still be reached if the code were used in similar applications. For the code to demonstrate reasonable agreement, the calculation of major phenomena should, on average, not differ from the data by more than plus or minus 20%. For this criterion, the code-to-data comparison may be representable with a bias and uncertainty. For application wherein the code is conservative for a specific phenomenon, the code results could be used directly without determining a bias or uncertainty for that phenomenon.

- Acceptable Agreement: While the correct trends are predicted, the calculation of major phenomena lies considerably outside the scatter of the data including data uncertainty and any known data biases. ("Considerably outside" indicates a deviation from the data greater than 20% on average.) However, the correct conclusions about trends and phenomena would still be reached if the code were used in similar applications. For this criterion, the code-to-data comparison may be representable with a bias and uncertainty. For application wherein the code is conservative for a specific phenomenon, the code results could be used directly without determining a bias or uncertainty for that phenomenon.

- Insufficient Agreement: The calculated phenomena are outside the scatter of the data including data uncertainty and any known data biases. Additionally, the trends in the calculated phenomena provide an unacceptable prediction of the test data because the major trends are not predicted correctly. Incorrect conclusions for both phenomena and trends are likely to occur as a result. The determination of insufficient agreement indicates that both the code models and the model nodalization must be re-evaluated and modified, as necessary, before the code can be used in similar applications.

For the evaluation of cladding temperatures, it is best to use all of the appropriate measured data points, rather than using an average value at a given elevation. These comparisons are provided by showing the calculation as a continuous solid curve and the data as individual data points. A different symbol for each measurement is generally used. For example, thermocouples at each elevation, therefore, the origin of the data is clear. Additionally, the data presentation includes any known biases and uncertainty bars to demonstrate the actual data range. An example of a data bias is the bias for the external thermocouples used in the Loss-Of-Fluid-Test (LOFT) experiments.

Statements regarding the code predictive capability are intended to be quantitatively stated based on these defined criteria.

8.1.5 Evaluation Model Changes

During the development of EMF-2103-003, several code errors were identified and corrected. In addition, incremental changes to the Evaluation Model for the Realistic Large Break LOCA Methodology for Pressurized Water Reactors were introduced. As a part of the AREVA NP Software Quality Assurance program, the benchmarks were repeated prior to the release of each code version. This process, identified as the Continuity of Assessment, executes each benchmark, and the results are compared to the prior version to verify that any differences are appropriate to the change being made, and that no code change has a detrimental effect. Because the impact of the changes was minimal the benchmark figures and tables documented in Section 8 were not updated.

Each change to the EM with the expected impact on the benchmarks is characterized below:

1. The core nodalization has been slightly changed to align the node boundaries with the bottom of the grid spacers, instead of the grid centerline.

The change in the core nodalization effectively changes the hydrodynamic volume boundaries so they are aligned with the bottom of the grid spacers, in support of the implementation of the grid droplet shattering model (item #3 below). As the length of the hydrodynamic volumes will not be significantly changed, this change will have a negligible effect on the benchmarks.

2. The plant model has been modified to specify separate radiation enclosures for each rod.

   The implementation of separate radiation enclosures for each rod, instead of one enclosure for fresh rods, and one enclosure for burned rods, will have no impact on the benchmarks. This change to the system analyses was done so that an enclosure that was being heated by a very hot rod would not radiate back to a cooler rod and cause it to be hotter than it than it otherwise would be.

[ ]

4. The temperature correction on the Sleicher-Rouse correlation was corrected and extended to apply to the Wong-Hochreiter heat transfer correlation.

[

]

5. There was a correction to the vapor absorptivity that caused more radiation absorption by steam.

   Radiation heat transfer to steam in S-RELAP5 is reduced at high pressures as compared to previous versions. The steam absorptivity has been revised to use a conservative, limiting value based on a pressure of [ ] psi. Although this truncation of the simplified pressure relation is conservative, it will not impact reflood because the pressure during reflood is typically less than [ ] psi. The overall conclusion from the Continuity of Assessment is that this change has minimal impact.

6. The Fuel Swelling Rupture and Relocation (FSRR) model has been modified in its entirety and now includes a sub-channel cooling model to more realistically model the heat transfer mechanisms that occur at the rupture location.

   The implementation of a Swell, Rupture and Relocation model is not expected to have any impact on the benchmarks since none of the benchmarks experienced swelling or rupture. The overall conclusion from the Continuity of Assessment is that this change has minimal impact. This alteration is described in Section 7.9.3.3.

7. An error correction to the Level Tracking model required modification to the input interfacial drag specified at the inlet of the steam generator tubes.

As a part of the modifications to S-RELAP5, there were corrections to the level model that changed the effective criteria for the onset of vertical stratified flow at the inlet of the steam generator tubes. The FIJ multiplier is changed to a value of 30. The primary impact of this change is evaluated using the UPTF Test 29. Since the S-RELAP5 changes were accompanied by a compensating input change, only minimal impact will occur. The overall conclusion from the Continuity of Assessment is that this change has minimal impact.

8. The fuels sub-code COPERNIC will be used exclusively. Other fuels sub-codes are considered obsolete.

   The exclusive use of the fuels sub-code, COPERNIC, will have no impact on the benchmarks. All of the benchmarks, except for the LOFT benchmarks, have user-specified thermal properties to represent the simulator rods, and will therefore not be impacted by this change. The only benchmarks to use nuclear fuel, (the LOFT benchmarks), were already performed with COPERNIC, and will therefore not change. This was confirmed by repetition of the benchmarks in support of the Continuity of Assessment.

The only EM change expected to have a significant impact on the benchmarks is the implementation of a model to increase the heat transfer downstream of a grid spacer. This change is expected to have the greatest impact during a low pressure reflood. The FLECHT-SEASET and FLECHT Skewed benchmarks were repeated to assess the impact of the change (Section 8.4.1.4). Because the impact of the changes was minimal, the benchmarks documented in Section 8 were not updated and are considered valid.

8.1.6 References

8.1-1 AREVA NP, EMF-2102(P), Revision 1, S-RELAP5: Code Verification and Validation, November 2010.

8.1-2 AREVA NP, EMF-2101(P) Revision 3, S-RELAP5 Programmers Guide, May 2004.

8.1-3 AREVA NP FMM Revision 1, AREVA NP Fuel Sector Management Manual, April 2010.

8.1-4 NUREG-1737, System Quality Assurance Procedures for NRC Thermal-Hydraulic Codes, US NRC, December 2000.

8.2 *Validation Using Separate Effects Tests*

This section details the separate effects tests (SET). The tests were included from the following facilities:

- Oak Ridge National Laboratory (ORNL) Thermal Hydraulic Test Facility (THTF)
- GE Level Swell Test 1004-3
- FRIGG-2 Tests
- Bennett Tube Tests
- Full-Length Emergency Cooling Heat Transfer System Effects and Separate Effects Tests (FLECHT SEASET)
  - Reflood Tests - FLECHT SEASET Tests and FLECHT Skewed Tests
  - Steam Cooling
- Product Development Test Facility (PDTF) Small Array Reflood (SMART) Tests
- Marviken Tests
- Westinghouse/Electric Power Research Institute (W/EPRI) One-Third Scale Tests
- AREVA CCFL Tests
- Upper Plenum Test Facility (UPTF) Tests
  - Tests 6 and 7
  - Test 8
  - Tests 10 Run 080 and 12 Run 014
  - Tests 10B and 29B
  - Test 11 (used to determine CCFL coefficients only)
- Cylindrical Core Test Facility (CCTF) Tests
- Slab Core Test Facility (SCTF) Tests

- Achilles International Standard Problem (ISP) #25
- Multi-dimensional Flow Tests
- Moby Dick
- Ferrell-McGee

These facilities and the tests performed are detailed in the sections following this introduction. Note that these assessments, where applicable, will use the RLBLOCA plant model best-estimate multipliers developed by appropriate NRC approved methods.

8.2.1 ORNL THTF Tests

8.2.1.1 Introduction

The ORNL THTF is a high-pressure bundle thermal-hydraulic loop with a 64 rod electrically heated bundle simulating a fuel bundle. Three sets of THTF experiments were benchmarked: (1) mixture-level swell tests; (2) transient boil-off tests; and (3) reflood tests.

The ORNL level swell tests provide steam water slip data at steady-state conditions for rod bundles at high pressure low heat flux conditions (Reference 8.2-1). The drag model is validated by comparing the axial void profile for these tests

The transient boil-off tests consist of high pressure transient bundle boil-off tests conducted at ORNL (Reference 8.2-2). These tests are designed to assess high void fraction film boiling heat transfer in a fuel bundle. Heater rod temperatures at different axial locations are compared for this study.

The reflood tests are two sets of ORNL tests designed to simulate high pressure reflooding in a fuel bundle (References 8.2-3 and 8.2-4). This is achieved by establishing a water level within the bundle with a significant portion of the bundle uncovered at transient initiation. Flooding is introduced during the transient to simulate the reflooding event. Rod quench is investigated by comparing the heater rod temperatures at the top of the bundle.

The S-RELAP5 RLBLOCA Revision 3 Methodology nodalization guidelines have been followed where applicable for these separate effects test benchmarks. The recommended RLBLOCA plant model multipliers from Section 8.2 have also been applied. Deviations to the guidelines and multipliers are described in the following sections.

8.2.1.2 Summary and Conclusions

8.2.1.2.1 Level Swell Tests

The level swell benchmark generally shows good agreement with the test data for the three analyzed THTF level swell cases. The void fraction profiles show good agreement with the data with insignificant differences for the three cases, as shown in Section 8.2.1.6.1. The mixture level is well predicted for all three tests. These results show good agreement with the experimental data for this series of steady-state mixture level swell tests. For Tests 3.09.10j and 3.09.10m, vapor temperature and rod surface temperatures were well predicted. Vapor and cladding temperatures for Test 3.09.10dd was not compared because in this test, the mixture level was almost near the top of the bundle.

8.2.1.2.2 Transient Boiloff Tests

This analysis investigates the transient bundle dryout response. These investigations compare the S-RELAP5 film boiling heat transfer performance at near dryout conditions with THTF test data. A range of results is shown by modeling an upper and lower bound of the film boiling heat transfer in the S-RELAP5 model and comparing the resultant cladding temperature to the measured values.

At the peak temperatures, S-RELAP5 generally conservatively overpredicts the temperature at the lower elevations. At the higher elevations, the model results trend closer to the test data yet still show a general overprediction of the temperature.

Using the criteria established in Section 8.1.4, the S-RELAP5 results also show a good prediction of the time of the temperature peak with respect to the test data for the range of elevations. From this analysis, the film boiling and dispersed flow film boiling heat transfer correlation multipliers developed in support of the RLBLOCA Revision 3 Methodology are shown to be appropriate, with transient film boiling well predicted for the RLBLOCA Revision 3 model.

8.2.1.2.3 Reflood Tests

THTF reflood tests have been analyzed with S-RELAP5 RLBLOCA Revision 3 Methodology to show the performance of S-RELAP5 during high pressure reflood conditions. These investigations compare the S-RELAP5 cladding temperature during reflood with THTF test data, showing the performance of film boiling and dispersed flow film boiling heat transfer multipliers developed in support of the RLBLOCA Revision 3 Methodology. Two sets of THTF tests were analyzed as described in section 8.2.1.4.3 to cover a range of pressures and reflooding rates. The S-RELAP5 model in general shows later quench times than the data.

The quenching of a fuel bundle provides the end of the core heatup during a LOCA. S-RELAP5 predicts the cladding temperature cooldown profile for these tests with conservatism.

The first test set shows quenching to occur primarily in the range of 0 to 20 seconds after the test data. The second test set shows a longer overprediction, extending past 20 seconds, for the bundle to quench. These results show that, for the range of uncertainty in the film boiling heat transfer coefficients, S-RELAP5 overpredicts the quench time.

Additional discussion on the assessment of uncertainties and biases in the THTF tests is provided in Section 8.4.4.

8.2.1.3 Facility Description

The THTF facility, operated by ORNL, is a large high pressure thermal-hydraulic loop with non-nuclear (electrically heated) rods simulating a nuclear fuel bundle. The facility was designed to simulate the thermal-hydraulic environments expected during LOCA events. References 8.2-1 through 8.2-4 describe the facility and its configuration for the different tests. Figure 8.2-1 shows the layout of the facility. The bundle test section is shown in Figure 8.2-2. The hydraulic systems are shown in Figure 8.2-3 and Figure 8.2-4, each diagramming a slightly different configuration for the tests of interest. Figure 8.2-3 is the configuration for the level swell and transient boiloff tests, while Figure 8.2-4 represents the reflood test. A cross section of the simulated bundle and fuel rod are shown in Figure 8.2-5 and Figure 8.2-7, respectively. The axial locations of thermocouples and bundle grid spacers are shown in Figure 8.2-6. Areas of investigation for the facility, which are performed in these analyses, are described below.

8.2.1.4 Test Description

8.2.1.4.1 Level Swell

The THTF level swell tests are steady-state boiling experiments performed under high pressure with heat fluxes representative of conditions just following shutdown. For these tests, the power distribution is uniform in the axial direction. The void distribution along the bundle during these steady-state tests will be compared with the S-RELAP5 predicted void response. This will show the ability of the code to predict the void fraction under these conditions. Reference 8.2-1 details the three level swell tests analyzed here. The THTF test conditions are shown in Table 8.2-1.

8.2.1.4.2 Transient Boiloff

The transient boiloff test suite consists of high pressure transient bundle boiloff tests conducted at ORNL (Reference 8.2-2). These tests are designed to assess heat transfer (film boiling and dispersed flow film boiling heat transfer) in a fuel bundle near dryout conditions. From the initial conditions shown below in Table 8.2-2, the facility was depressurized and bundle power ramped up causing dryout conditions.

8.2.1.4.3 Reflood

The reflood tests performed at ORNL were designed to simulate high pressure reflooding in a fuel bundle (References 8.2-3 and 8.2-4). This is simulated by establishing a water level with 25-30 percent of the test bundle uncovered at steady-state. The transient is initiated by increasing the inlet makeup flow to simulate reflood. Table 8.2-3 shows the key conditions of the tests.

Two test series were investigated as indicated in the table. Test 3.02.10C-H for Series I and Test 3.09.10O-S for Series II.

8.2.1.5 S-RELAP5 Model Description

8.2.1.5.1 Level Swell

The S-RELAP5 RLBLOCA Revision 3 Methodology has been applied to the development of a model for the ORNL THTF level swell tests. The THTF level swell test is modeled with a hydrodynamic channel and associated heat structures, with boundary conditions modeling the inlet and outlet to the test section. Figure 8.2-8 shows the S-RELAP5 nodalization for the level swell model.

The THTF loop is simulated with an inlet time dependent volume connected to the test section via a time dependent junction. The inlet volume and inlet junction are modeled as time dependent components with fixed boundary conditions, simulating the inlet conditions of the THTF test bundle noted in for these steady state tests.

[

]

Downstream of the test section an exit sink is connected to the test section by a single junction. [

]

8.2.1.5.2 Transient Boiloff

The S-RELAP5 RLBLOCA Revision 3 Methodology has been applied to the development of the model for the ORNL THTF transient boiloff tests.

The S-RELAP5 RLBLOCA Revision 3 Methodology provides a number of enhancements to the RLBLOCA Revision 0 methodology.[

]

Figure 8.2-9 shows the S-RELAP5 nodalization for the transient boiloff model. The model simulates the inlet source with an inlet time dependent volume connected to a branch component via a time dependent junction. These components supply a branch, which subsequently connects to the test section.

[

]

Downstream of the test section is an exit branch connected to a time dependent volume, simulating the exit sink.

[

]

[

]

8.2.1.5.3 Reflood

The S-RELAP5 RLBLOCA Revision 3 Methodology has been applied to the development of the model for the ORNL THTF Reflood tests.

[

]

Figure 8.2-9 shows the S-RELAP5 nodalization for the reflood model. This nodalization is the same as that used for the previous transient boiloff model. The model simulates the inlet source with an inlet time dependent volume connected to a branch component via a time dependent junction. These components supply a branch, which subsequently connects to the test section.

[

]

Downstream of the test section is an exit branch connected to a time dependent volume, simulating the exit sink.

[

]

8.2.1.6 Calculated Results

8.2.1.6.1 Level Swell

Figure 8.2-10 to Figure 8.2-12 show the comparison of the void fraction between the test data and the S-RELAP5 prediction. These results are for test cases 3.09.10j, 3.09.10m, and 3.09.10dd, respectively. Error bars have been included for the test data. In analyzing the results, there are three regions of interest: (1) the pre-CHF region before dryout in the bundle occurs; (2) the transition to dryout region, where the void fraction increases sharply with elevation creating a two-phase mixture; and (3) the post-CHF region, where the bundle is in dryout. The modeling of the void fraction for the level swell tests shows good agreement with the test data.

For the pre-CHF region, there is good agreement between test data and the model for the level swell cases. At the mixture level, the length of this two-phase region is slightly underpredicted by the model (approximately 2-4 inches of bundle length), such that the slope of the void fraction versus elevation is higher for the model. This occurs for each of the three case comparisons. This observation is not significant for this analysis, as it does not affect the location of the mixture level, which is designated as the midpoint of the two-phase mixture.

Figure 8.2-12a and Figure 8.2-12b show S-RELAP5 calculated steam temperatures are slightly higher than the data. Figure 8.2-12c and Figure 8.2-12d show that S-RELAP5 calculated rod surface temperatures above the mixture level are well predicted.

8.2.1.6.2 Transient Boiloff

Comparisons of the transient boiloff THTF test and the S-RELAP5 prediction are shown in Figure 8.2-13 to Figure 8.2-23. Three THTF transient boiloff tests were analyzed, at different elevations for each test. For each figure, the measured THTF data are represented by two curves. Initially the uncertainty is low, due to the fact that the simulator rod is cooled by single phase coolant. Then as the fluid level boils down, a two phase mixture is present, yielding significantly higher uncertainty. These curves represent the two-sided 95% coverage limit for the measured temperature based on the mean and standard deviation extracted from the THTF data. For the S-RELAP5 prediction, upper and lower bound responses are obtained by modeling $\pm 2\sigma$ film boiling heat transfer coefficients. For Figure 8.2-13 through Figure 8.2-22, the calculated results labeled "SR5: lower bound" apply the $+2\sigma$ film boiling heat transfer coefficients and produce lower temperatures; similarly, the calculated results labeled "SR5: upper bound" apply the -2σ film boiling heat transfer coefficients and produce the higher temperatures. This also provides 95 percent coverage of the performance of the film boiling heat transfer. For all the tests analyzed, as noted in the discussion in Section 8.2.1.7.2, S-RELAP5 generally overpredicts the temperature at the lower elevations. At the higher elevations, the model results trend closer to the test data at the peak temperature yet still show a general overprediction of the temperature.

8.2.1.6.3 Reflood

THTF reflood tests were analyzed with S-RELAP5 RLBLOCA Revision 3 Methodology to show the performance of reflood in a fuel bundle at high pressure. Two sets of THTF tests were analyzed.

Figure 8.2-23 to Figure 8.2-28 represent the first set of tests (designated 3.02.10C-H), and Figure 8.2-29 to Figure 8.2-33 the second set (designated 3.09.10O-S).

For the first set of tests (3.02.10C-H), three temperatures are plotted, from three different rods at two different azimuthal locations. These nominal temperature data were taken at the highest elevation in the bundle (Level G). For each test, two S-RELAP5 cases were run to obtain an upper and lower bound response of the film boiling heat transfer. These cases model $\pm 2\sigma$ of the film boiling heat transfer coefficients mean bias which was developed in support of the RLBLOCA Revision 3 Methodology.

For the second set of tests (3.09.10O-S), rod temperatures are benchmarked against data collected by up to six sheathed thermocouples at two azimuthal locations. These nominal temperature data were also taken at the highest elevation in the bundle (Level G). For each test, two S-RELAP5 cases were run with film boiling heat transfer coefficient adjustments as described above. For Figure 8.2-23 through Figure 8.2-33, the calculated results labeled "SR5: lower bound" apply the $+2\sigma$ film boiling heat transfer coefficients and produce lower temperatures; similarly, the calculated results labeled "SR5: upper bound" apply the -2σ film boiling heat transfer coefficients and produce the higher temperatures.

Of interest in the figures is the time and temperature at which quenching occurs at the given elevation, noted by the sudden drop in temperature. As discussed in Section 8.2.1.7.3, the S-RELAP model shows delayed quench times for both sets of tests. The quench temperature is quite well predicted.

8.2.1.7 Discussion of Results

8.2.1.7.1 Level Swell

The level swell benchmark generally shows good agreement with the test data for the three analyzed THTF level swell cases. The void fraction profiles show good agreement with the data with insignificant differences for the three cases. The mixture level is well predicted for all level swell tests. For Tests 3.09.10j and 3.09.10m, vapor temperature and rod surface temperatures were well predicted.

8.2.1.7.2 Transient Boiloff

This analysis investigated the transient dryout bundle response. A range of results is shown by modeling the upper and lower bound of both the measured (THTF) and modeled (S-RELAP5) data. This helps show the band of results that would be expected with 95 percent probability for the sheath thermocouple temperatures for the THTF test data, and 95 percent probability of the film boiling heat transfer in the S-RELAP5 calculation.

From the results at the peak temperatures, S-RELAP5 generally overpredicts the temperature at the lower elevations.

The purpose of this benchmark is to evaluate the degree of conservatism of the steam cooling correlations. These steam-cooling correlations consistently over-predict the peak cladding temperatures, indicating that when high quality steam is present, the heat transfer is conservatively underpredicted.

At the higher elevations, the model results trend closer to the test data at the peak temperature yet still show a general overprediction of the temperature. An exception is Test 3.06.6B Level G (Figure 8.2-19), where the model shows a narrower band of results, with the peak upper bound temperature being underpredicted. However, this case also overpredicts the peak temperature lower bound.

Temperature predictions at Level G for all three cases do not exhibit the expansion of the upper and lower bound envelope seen in the test data. This is exhibited at 5 to 15 seconds for Test 3.03.6AR (Figure 8.2-15) and Test 3.06.6B (Figure 8.2-19) and 25 seconds for Test 3.08.6C (Figure 8.2-22). However, the average of the upper and lower bound measured data (although not specifically plotted here, but evident from the upper and lower bound plots) consistently shows lower temperatures than the average of the predicted upper and lower bound temperatures.

Also of note is that the S-RELAP5 results show a good prediction of the time of the temperature peak with respect to the test data for the range of elevations studied.

From this analysis, the film boiling heat transfer bias applied and the prediction of transient film boiling for the S-RELAP5 RLBLOCA Revision 3 Methodology is shown to be appropriate.

8.2.1.7.3 Reflood

The quenching of a fuel bundle provides an indication of the end of the core heat-up during a LOCA. The S-RELAP5 calculation provides an adequate prediction of the reflood temperature profile. However, there is a consistent delay in the time to quench.

The first test set shows quenching to occur primarily in the range of 0 to 20 seconds after the test data. For Case H (Test 3.02.10H), the model does not show a characteristic quench but rather a continuous reduction in temperature due to reflooding. This case presents the lowest pressure of the series and a low reflood rate, which act to delay the quenching phenomena seen in the other cases.

The second test set shows a longer delay, extending past 20 seconds, for the bundle to quench. These results show that, for the range of uncertainty in the film boiling heat transfer coefficients, S-RELAP5 conservatively delays the quench time. For all tests which experience a quench, the quench temperature has been reasonably calculated.

Table 8.2-1 THTF Level Swell Test Conditions Tests

Parameter	Test 3.09.10j	Test 3.09.10m	Test 3.09.10dd
Bundle power	234.083 ± 12.4731 kWt	224.455 ± 12.1239 kWt	282.543 ± 15.0547 kWt
System pressure	609.340 ± 30.0023 psia (4.20079 ± 0.206836 MPa)	1009.03 ± 30.0023 psia (6.95626 ± 0.206836 MPa)	1173.05 ± 30.0790 psia (8.08700 ± 0.207365 MPa)
Fractional heat loss	0.0516742	0.0422668	0.0298778
Inlet mass flow	634.233 ± 30.1443 lb/hr (0.0799134 ± 0.00379818 kg/s)	656.252 ± 30.4670 lb/hr (0.0826878 ± 0.00383885 kg/s)	972.437 ± 31.3143 lb/hr (0.122527 ± 0.00394560 kg/s)
Outlet mass flow	620.986 ± 42.7734 lb/hr (0.0782442 ± 0.00538945 kg/s)	619.629 ± 35.2779 lb/hr (0.0780733 ± 0.00444501 kg/s)	955.535 ± 67.3208 lb/hr (0.120397 ± 0.00848242 kg/s)
Inlet temperature	405.210 ± 7.00564 ◦ F (480.339 ± 3.89202 K)	394.579 ± 7.00220 ◦ F (474.433 ± 3.89011 K)	356.693 ± 7.00111 ◦ F (453.385 ± 3.88951 K)

Table 8.2-2 Steady-State Conditions Prior to Transient Initiation

Parameter	Tests		
	3.03.6AR	3.06.6B	3.08.6C
Inlet Flow, gpm	285	125	130
Inlet Fluid Temperature, ◦ F	512	526	509
Outlet Fluid Temperature, ◦ F	602	638	618
Bundle Power, MWt	4	2.3	2.4
Outlet Pressure, psia	2065	2165	1870

Table 8.2-3 High-Pressure Reflood Test Matrix

Case	Test Series	Inlet Pressure (psia)	Flooding Velocity (in/s)	Linear Heat Rate (kWt/ft)
3.02.10C	I	400	6.5	0.36
3.02.10D	I	600	5.6	0.25
3.02.10E	I	605	5.4	0.41
3.02.10F	I	1006	1.1	0.27
3.02.10G	I	989	2.8	0.38
3.02.10H	I	303	2.2	0.42
3.09.10O	II	563	4.8	0.62
3.09.10P	II	621	3.6	0.30
3.09.10Q	II	573	2.3	0.31
3.09.10R	II	1065	4.6	0.66
3.09.10S	II	1092	4.0	0.42

Figure 8.2-1 Schematic of ORNL THTF

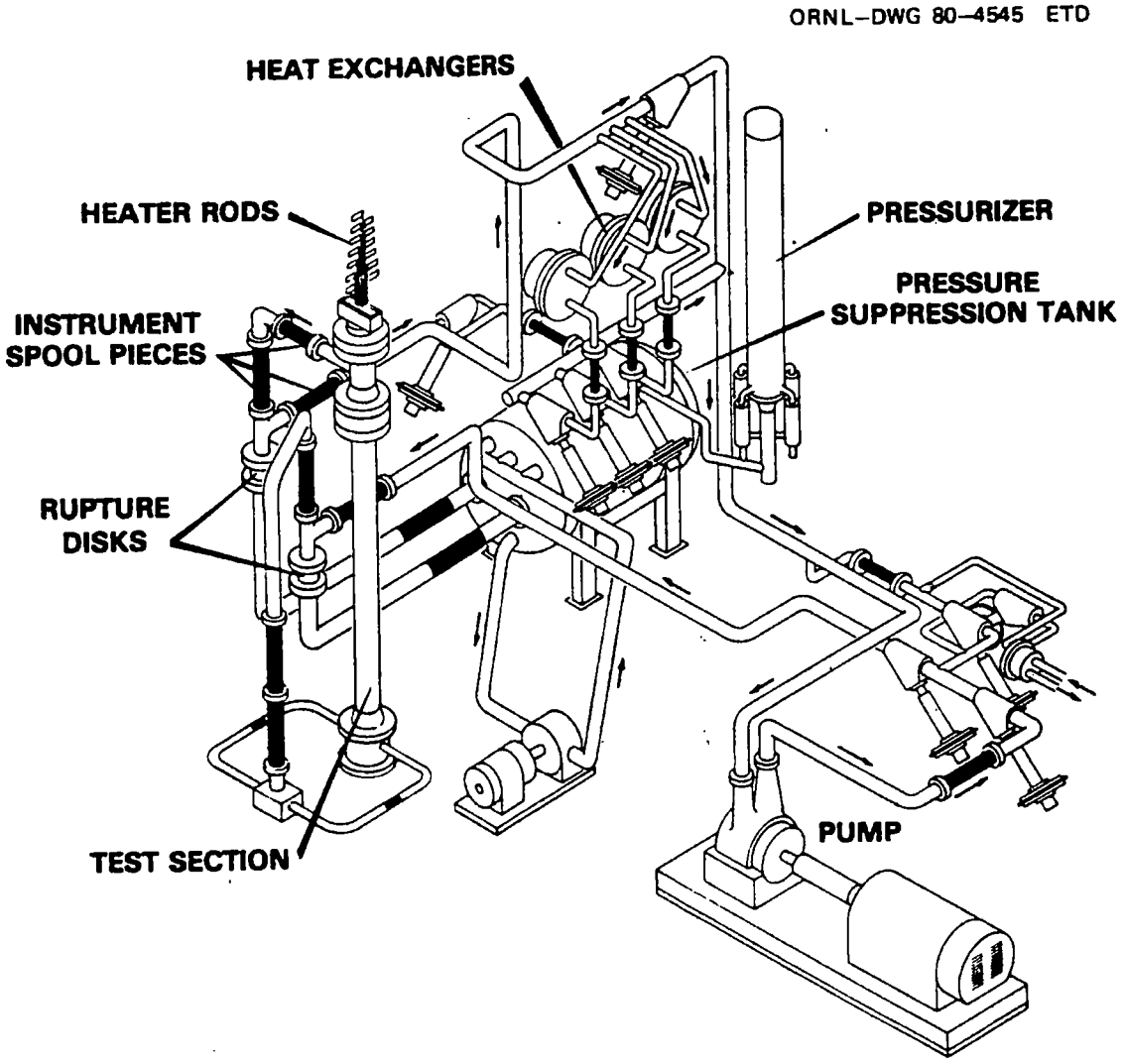

Figure 8.2-2 Diagram of ORNL THTF Test Section

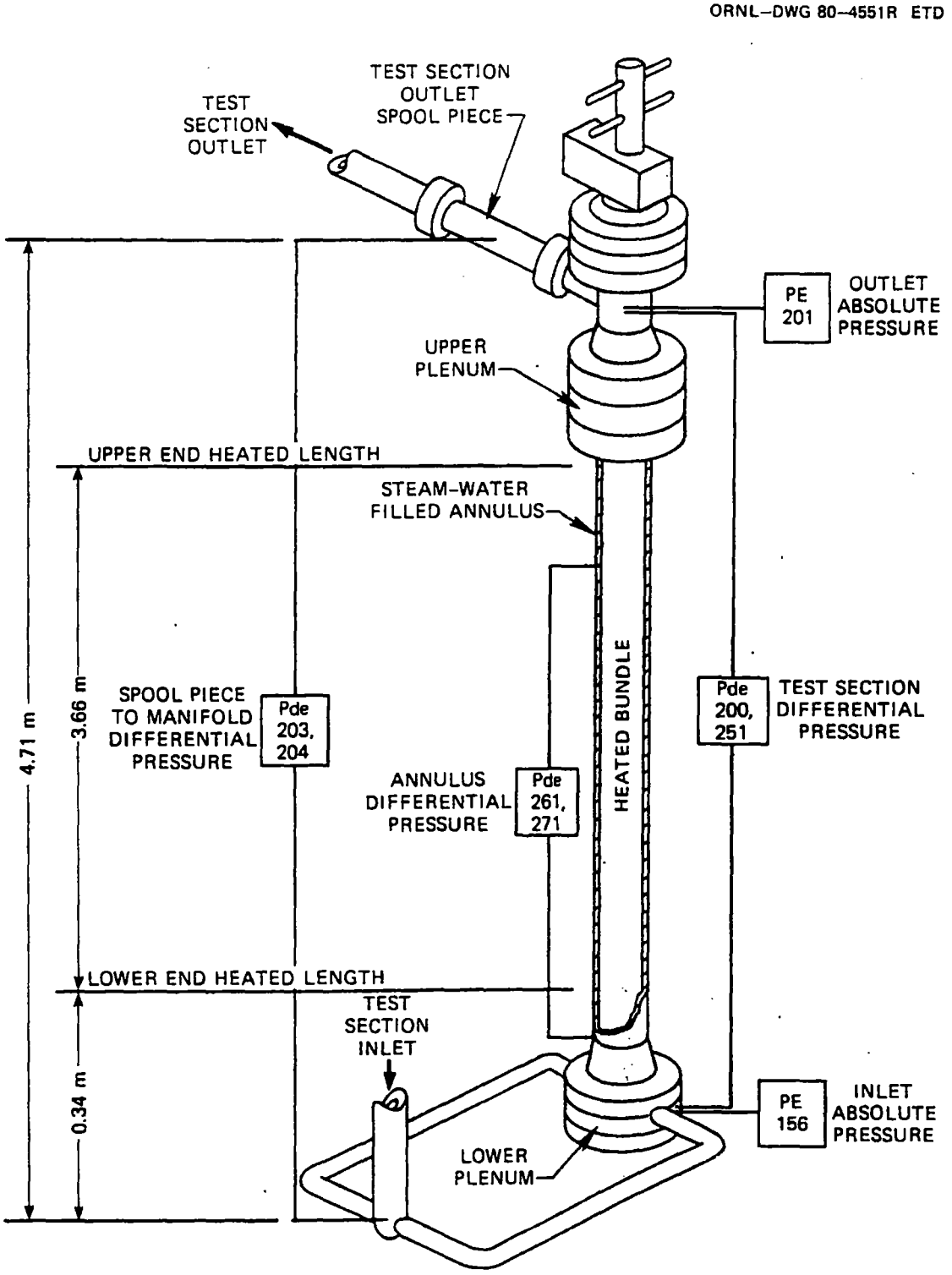

Figure 8.2-3 Diagram of ORNL THTF in Normal Configuration

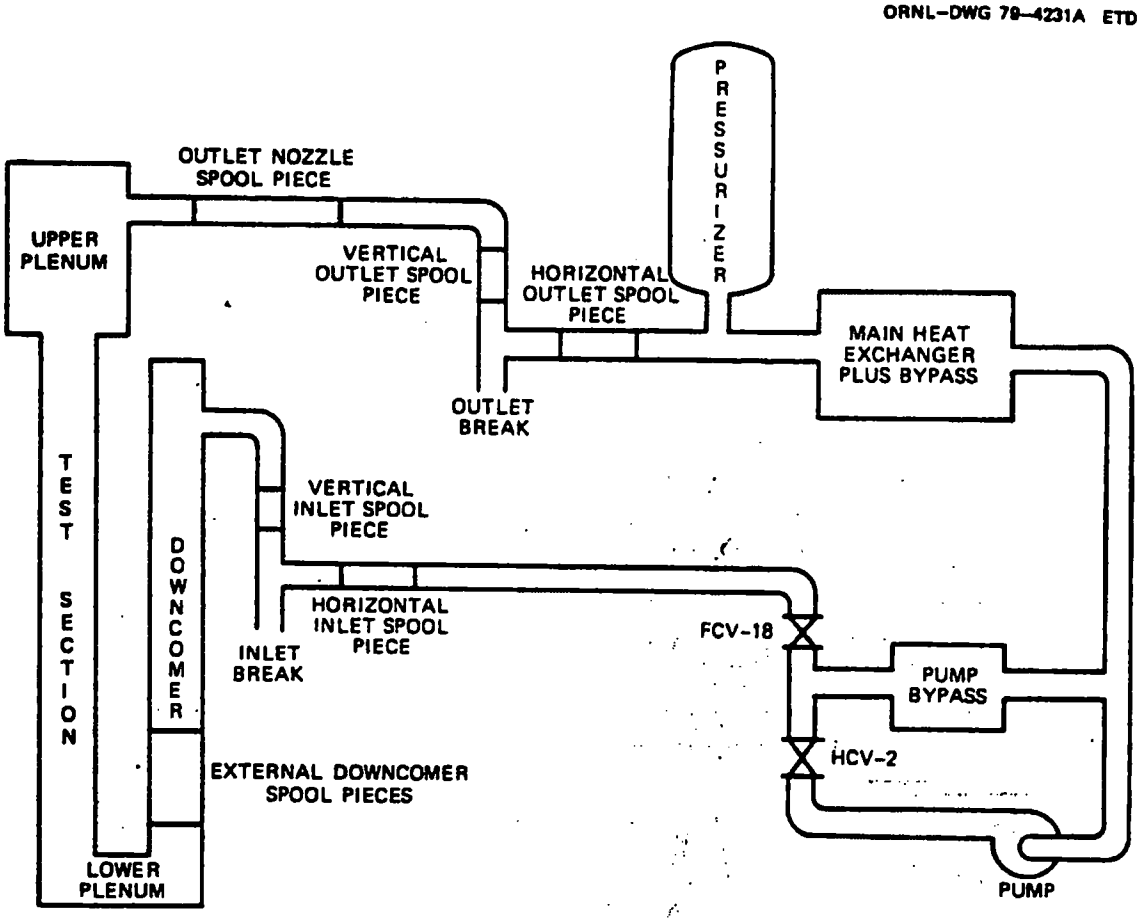

Figure 8.2-4 Diagram of ORNL THTF in Reflood Testing Configuration

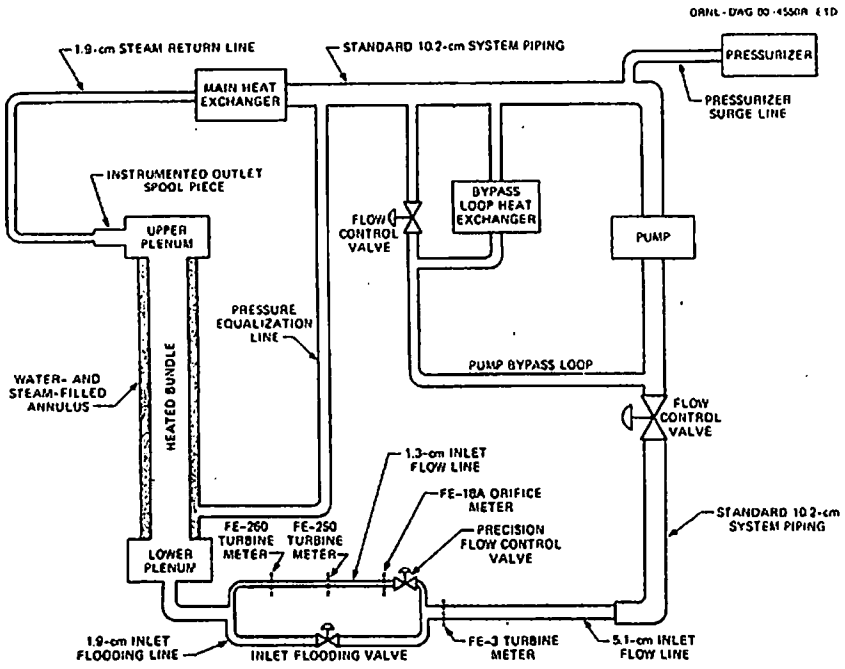

Figure 8.2-5 Section View of Test Section, ORNL THTF

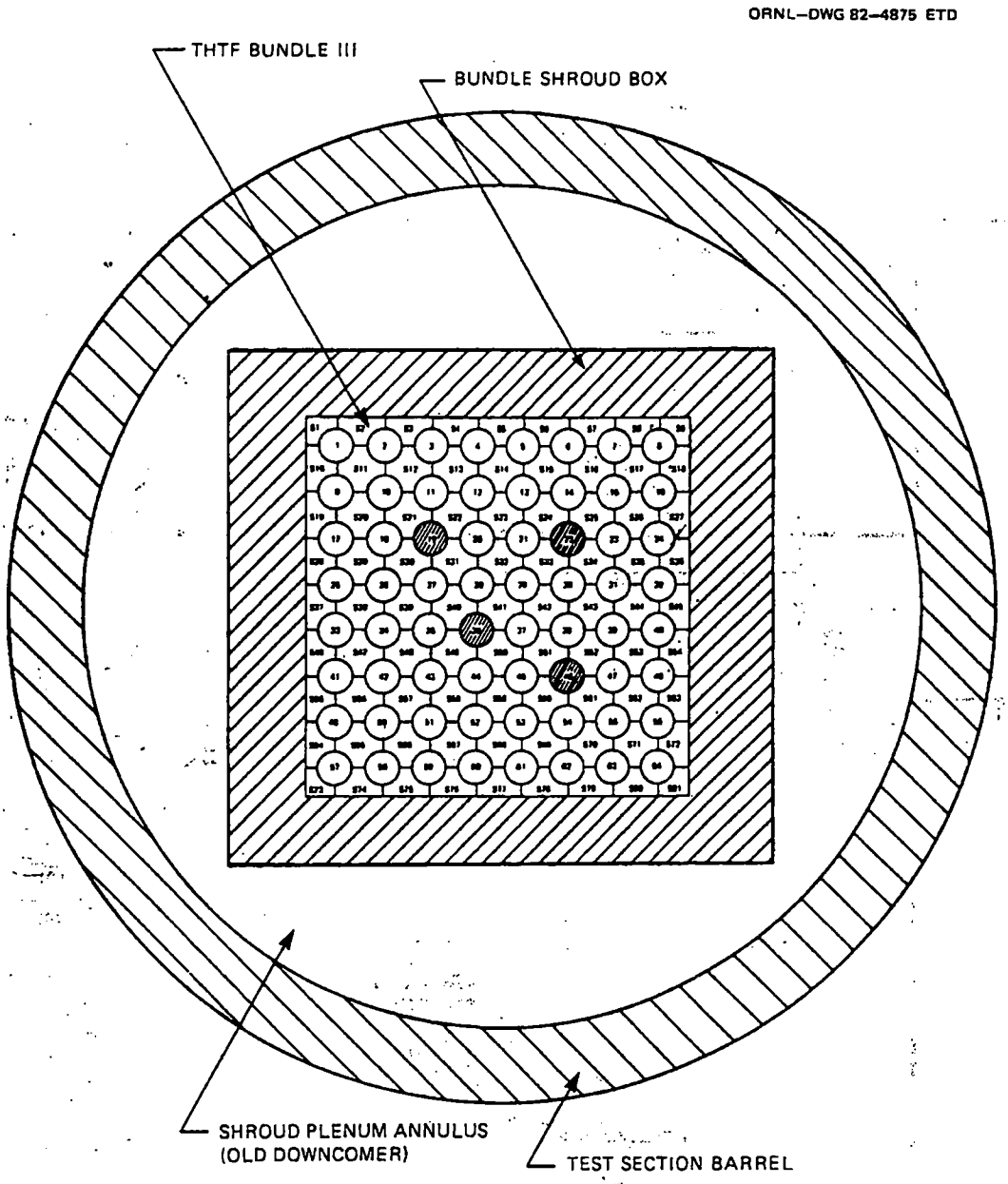

Figure 8.2-6 Location of Thermocouples and Grid Spacers, ORNL THTF

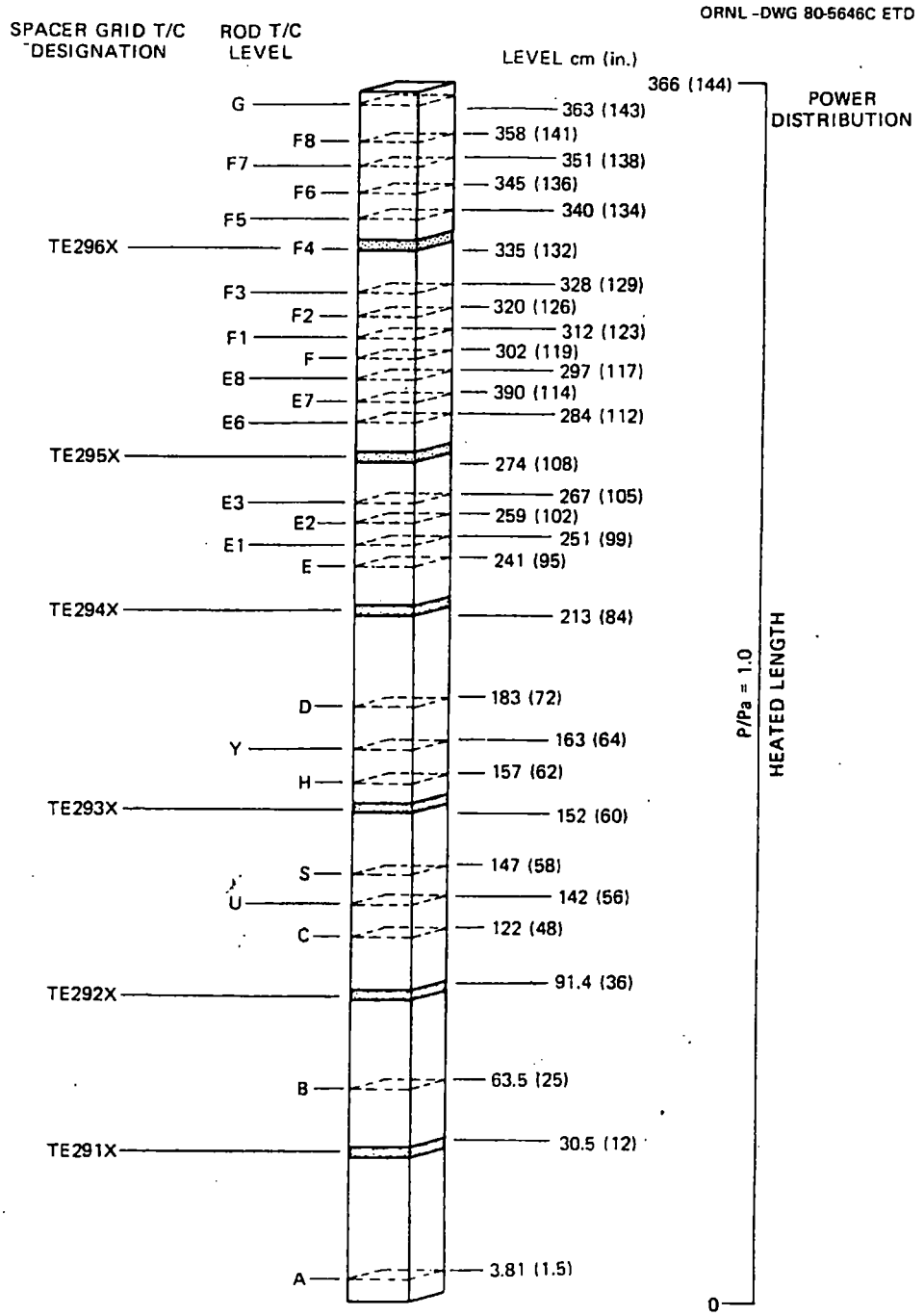

Figure 8.2-7 Cross Section of Fuel Rod Simulator, ORNL THTF

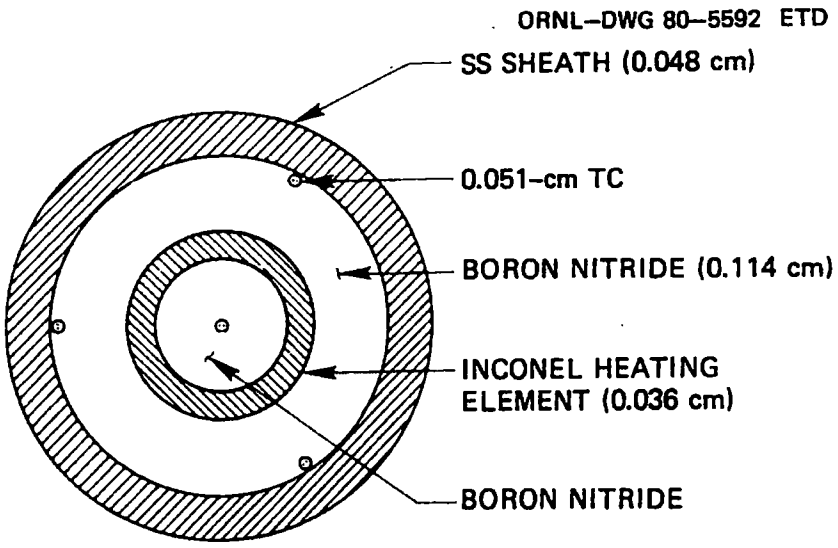

Figure 8.2-8 S-RELAP5 Nodalization of ORNL THTF for Level Swell Test

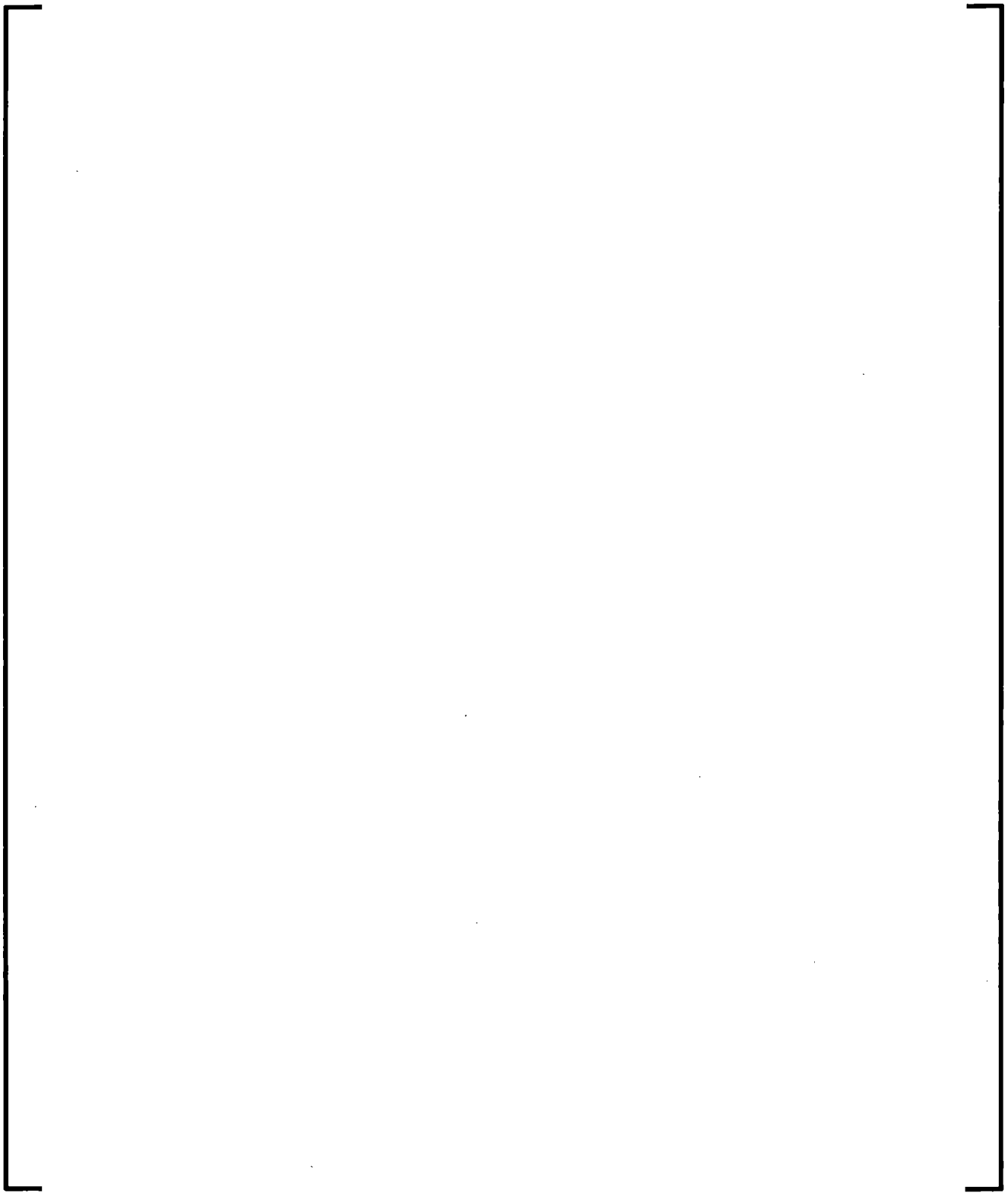

Figure 8.2-9 S-RELAP5 Nodalization of ORNL THTF for Transient Boiloff and Reflood Tests

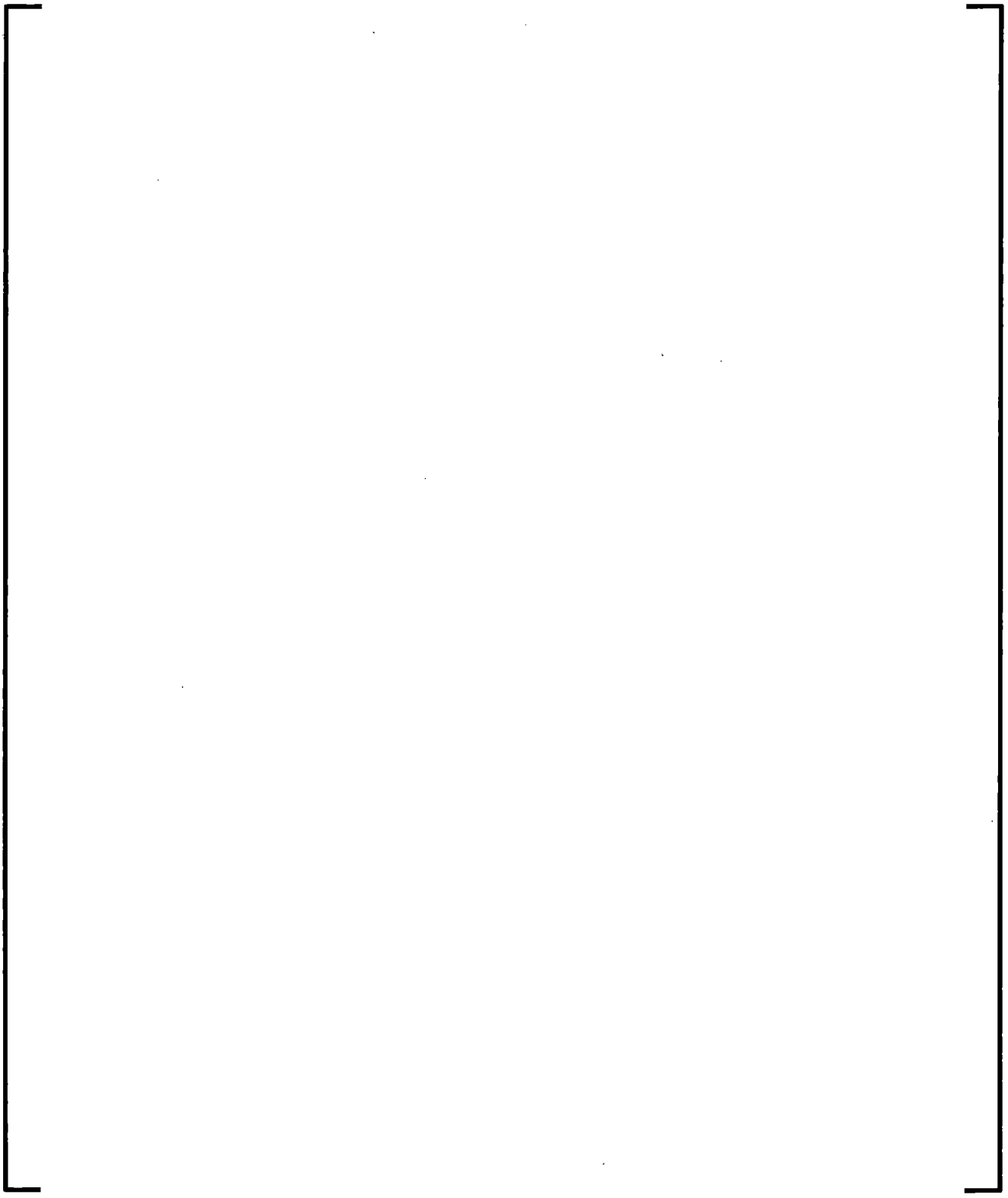

Figure 8.2-10 Void Profile for THTF Test 3.09.10j

Figure 8.2-11 Void Profile for THTF Test 3.09.10m

Figure 8.2-12 Void Profile for THTF Test 3.09.10dd

Figure 8.2-12a Vapor Temperature for THTF Test 3.09.10j

Figure 8.2-12b Vapor Temperature for THTF Test 3.09.10m

Figure 8.2-12c Rod Surface Temperature for THTF Test 3.09.10j

Figure 8.2-12d Rod Surface Temperature for THTF Test 3.09.10m

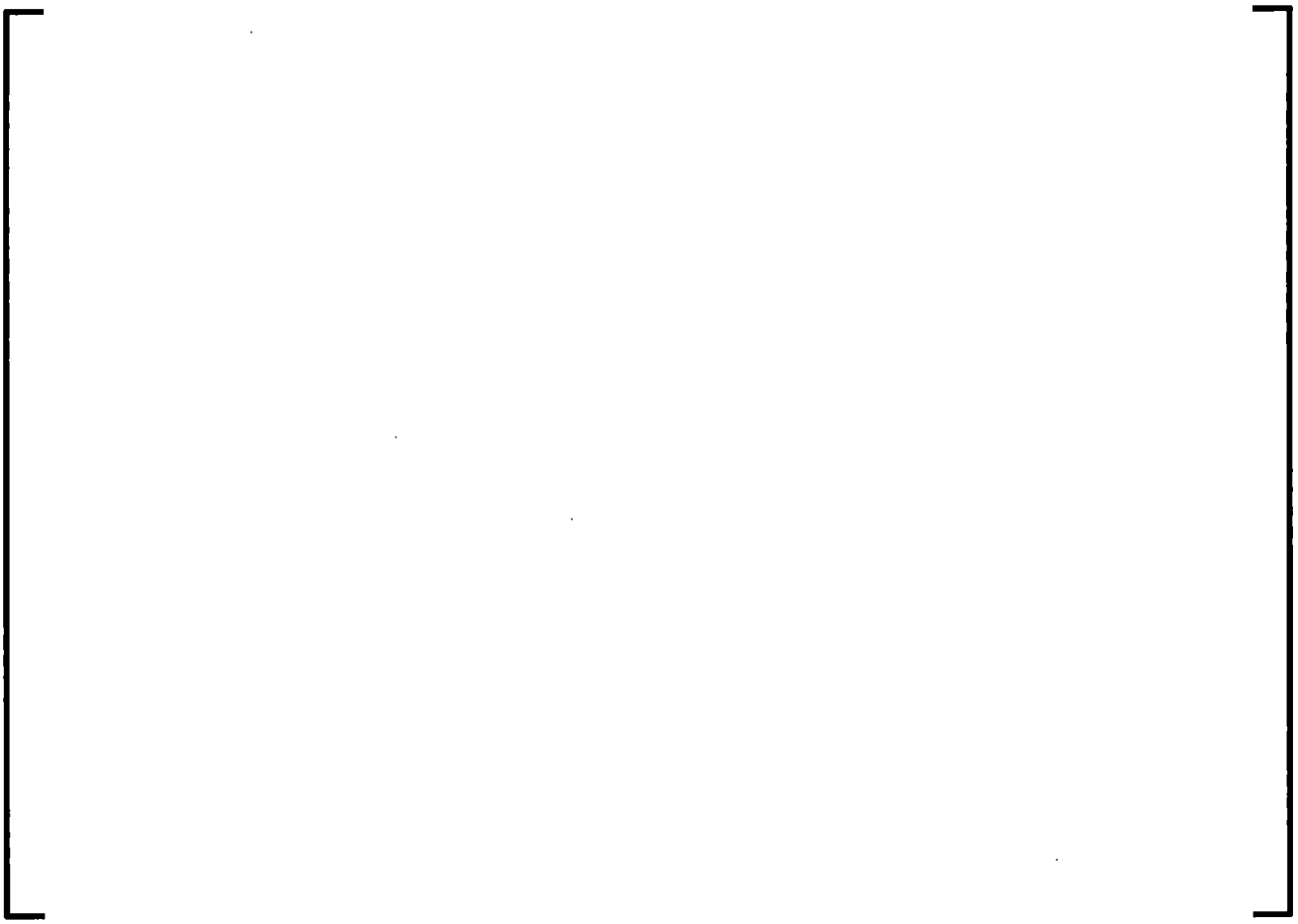

Figure 8.2-13 Temperatures at Level E, Test 3.03.6AR

Figure 8.2-14 Temperatures at Level F, Test 3.03.6AR

Figure 8.2-15 Temperatures at Level G, Test 3.03.6AR

Figure 8.2-16 Temperatures at Level D, Test 3.06.6B

Figure 8.2-17 Temperatures at Level E, Test 3.06.6B

Figure 8.2-18 Temperatures at Level F, Test 3.06.6B

Figure 8.2-19 Temperatures at Level G, Test 3.06.6B

Figure 8.2-20 Temperatures at Level E, Test 3.08.6C

Figure 8.2-21 Temperatures at Level F, Test 3.08.6C

Figure 8.2-22 Temperatures at Level G, Test 3.08.6C

Figure 8.2-23 Temperatures at Level G, Test 3.02.10C

Figure 8.2-24 Temperatures at Level G, Test 3.02.10D

Figure 8.2-25 Temperatures at Level G, Test 3.02.10E

Figure 8.2-26 Temperatures at Level G, Test 3.02.10F

Figure 8.2-27 Temperatures at Level G, Test 3.02.10G

Figure 8.2-28 Temperatures at Level G, Test 3.02.10H

Figure 8.2-29 Temperatures at Level G, Test 3.09.10O

Figure 8.2-30 Temperatures at Level G, Test 3.09.10P

Figure 8.2-31 Temperatures at Level G, Test 3.09.10Q

Figure 8.2-32 Temperatures at Level G, Test 3.09.10R

Figure 8.2-33 Temperatures at Level G, Test 3.09.10S

8.2.2 Bennett Tube Tests

8.2.2.1 Introduction

The Bennett Heated Tube Tests (Reference 8.2-5) were conducted by the UKAEA Research Group to measure the dry-out (or critical heat flux (CHF)) location and the surface temperature profiles in the region beyond the dry-out point. Calculations for Test Case 5-358 and Test Case 5-379 were performed. The main purpose of the assessment is to validate the applicability of the Biasi CHF correlation (Reference 8.2-6 and Section 7.7.4). Post-CHF heat transfer is also examined. The assessment applies to both LBLOCA and SBLOCA.

8.2.2.2 Summary and Conclusions

Two Bennett heated tube tests were assessed. The tests selected are a low-flow test, Case 5-358 (379.7 kg/m^2-s), and a high-flow test, Case 5-379 (3797.4 kg/m^2-s). The calculated CHF positions are in good agreement with the data for these two cases. For the low-mass-flux case, the wall temperatures in the film boiling region are well predicted (reasonable agreement). The calculated temperature rise immediately after CHF is not as high as the measured temperature. For the low-mass-flux case, the calculated temperature continues to rise in the post-CHF region and catches up with the data. For the case of high mass flux, the calculated wall temperature stays rather flat in the post-CHF region and is higher than the data in the top-end region. The mass flux for the high-flow case is well outside the LBLOCA conditions.

The results of this assessment validate the S-RELAP5 correlations for predicting CHF and the point of transition to dry-out.

8.2.2.3 Facility and Test Description

The test tube was a simple heated tube 0.497-in I.D. and 0.625-in O.D. with a total length of 19 ft. Figure 8.2-34 shows the test section along with the construction of the end flanges and current clamps. Twenty-seven thermocouples were attached to the test section (Figure 8.2-35) to measure wall temperatures along the length of the heated tube. Two series of experiments were carried out; in the first, the current clamps were placed to give a heated length of 219 inch, and in the second, the lower busbar connection was moved to just above the joining flange to give a heated length of 144 inch.

The water entered the test section bottom at a pressure adjusted to give a nominal pressure at the outlet (top) of the test section of 1000 psia. The power to the test section was raised until the end thermocouple (No. 27) showed a rapid increase, indicating CHF conditions. Conditions were allowed to steady out and the thermocouple readings were read off on the data logging system together with power input, flow, exit pressure, etc. The power was raised again until the next thermocouple (No. 26) registered a rapid increase in temperature and the readings were taken again. This procedure was repeated until the maximum temperature read by any thermocouple along the test section approached 1400 °F. Some 224 temperature profiles were determined during the experiments.

Two of the tests from the series of 219-in heated length were selected for this assessment. They are Tests 5-358 and 5-379 and their conditions are shown in Table 8.2-4.

8.2.2.4 S-RELAP5 Model Description

The 219-in heated test section [

] A schematic of the nodalization is shown in Figure 8.2-36. [

]

Key input parameters are listed below.

- Tube flow area (ft^2) = 1.3472×10^{-3}
- Total test section length (ft) = 18.25 (219/12)
- Heat structure left coordinate (ft) = 2.070833×10^{-2}
- Heat structure right coordinate (ft) = 2.604167×10^{-2}
- Axial power distribution = 5.479452×10^{-2} for 1.0 ft nodes; 2.739726×10^{-2} for 0.5 ft nodes; 4.109589×10^{-2} for 0.75 ft nodes
- Inlet mass flow rate (lb/s) for Test 5-358 = 0.10478
- Inlet fluid temperature (°F) for Test 5-358 = 482.64, which corresponds to a subcooling of 61.9 °F
- Inlet mass flow rate (lb/s) for Test 5-379 = 1.04782
- Inlet fluid temperature (°F) for Test 5-379 = 530.88, which corresponds to a subcooling of 19.7 °F

8.2.2.5 Calculated Results

Figure 8.2-37 and Figure 8.2-38 present the comparison plots of calculated wall temperatures and data for the two Bennett heated tube tests (Reference 8.2-5), Test 5-358 with a mass flux of 379.7 kg/m2 -s and Test 5-379 with a mass flux of 3797.4 kg/m2 -s. The CHF positions are in good agreement with the data for these two cases. The calculated temperature rise immediately after CHF is not as high as the measured temperature. For the case of high mass flux (Test 5-379), the calculated wall temperature stays rather flat in the post-CHF region and is higher than the data in the top-end region. For the low-mass-flux case (Test 5-358), the calculated temperature continues to rise in the post-CHF region and approaches the data.

8.2.2.6 Discussion of Results

Groeneveld et al. (Reference 8.2-8) reported an assessment of the Biasi CHF correlation (Reference 8.2-6) with the Chalk River Nuclear Laboratories' CHF data bank. According to their results, the Biasi correlation, for the data with constant inlet subcooling, predicts the experimental data well. LBLOCA calculations for the Loss-Of-Fluid Test (LOFT) experiments, and typical Westinghouse 3- and 4-loop plants (References 8.2-9 and 8.2-10) show that the core heat flux exceeds CHF in the mass flux range of 50 to 500 kg/m^2-s during the blowdown period. Also, Leung (Reference 8.2-11) reported that low mass flux (smaller than 200 kg/m^2-s) transient data are best predicted by the Griffith-Zuber (modified Zuber) correlation (Reference 8.2-12).

Therefore, the approach of combining the Biasi and the modified Zuber correlations for CHF computations applies for LOCA calculations.

In the simulation, the Revision 3 RLBLOCA methodology bias of 0.86 on the Biasi CHF correlation was not used. Since this bias is less than 1.0, the use of this bias would have moved the predicted CHF position to slightly below the current position, resulting in the prediction of a slightly higher cladding temperature in the film boiling region. Thus, the Revision 3 EM is slightly conservative in the CHF position prediction.

In summary, the simulation of the Bennett heated tube tests using S-RELAP5 demonstrate that the code will calculate CHF and post-CHF heat transfer reasonably well during a large break LOCA in a PWR.

Table 8.2-4 Test Conditions for Tests 5-358 and 5-379

Parameter	Test 5-358	Test 5-379
Pressure (outlet) (psia)	1000	1000
Power (kW)	113	377
Mass flow, lb/ft^2 -hr (lb/s)	0.28×10^6 (0.10478)	2.8×10^6 (1.04782)
Inlet subcooling, Btu/lb (°F)	75 (61.9)	25 (19.7)

Figure 8.2-34 Diagram of Test Section and Flange Arrangement for the Bennett Heated Tube Tests

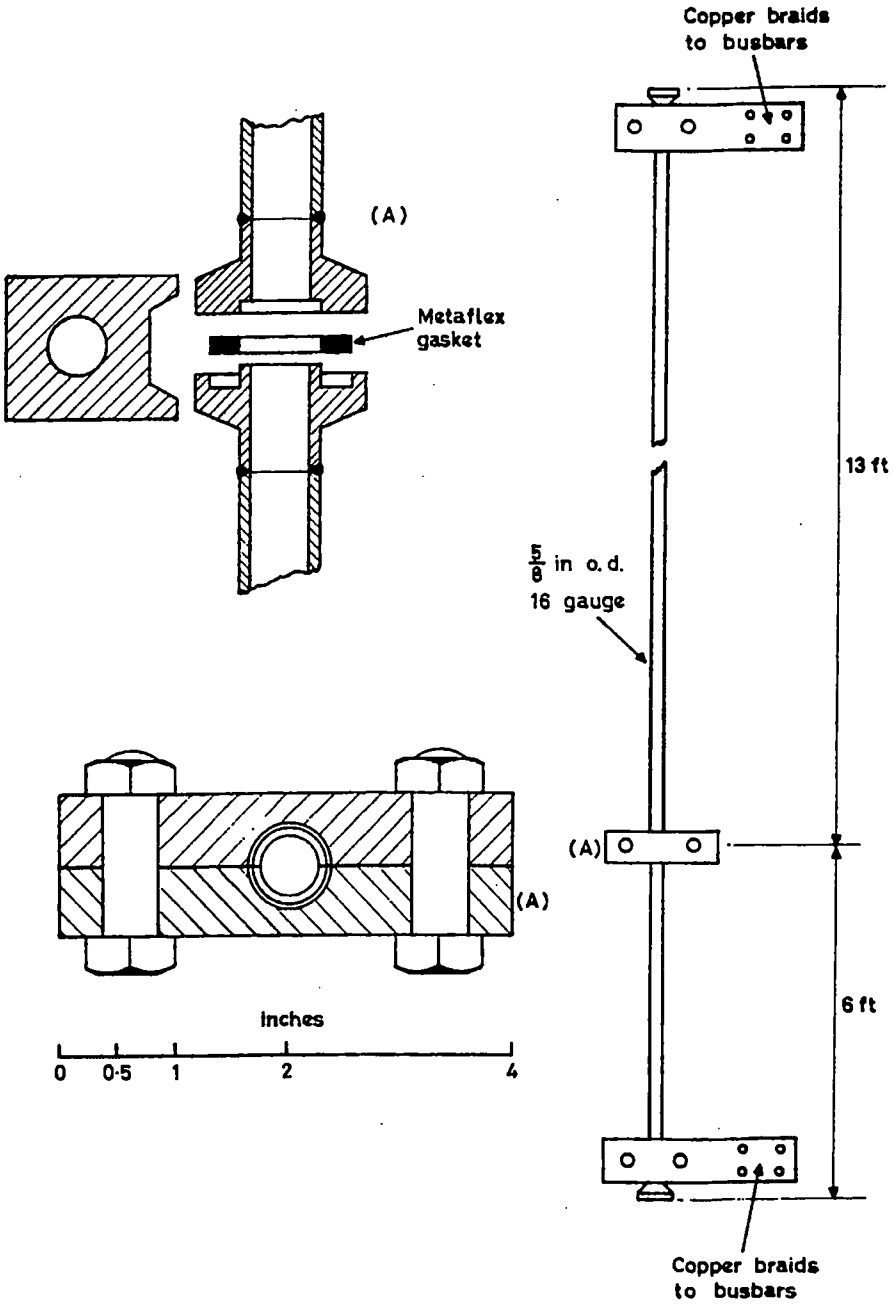

Figure 8.2-35 Arrangement of Thermocouples for the Bennett Heated Tube Tests

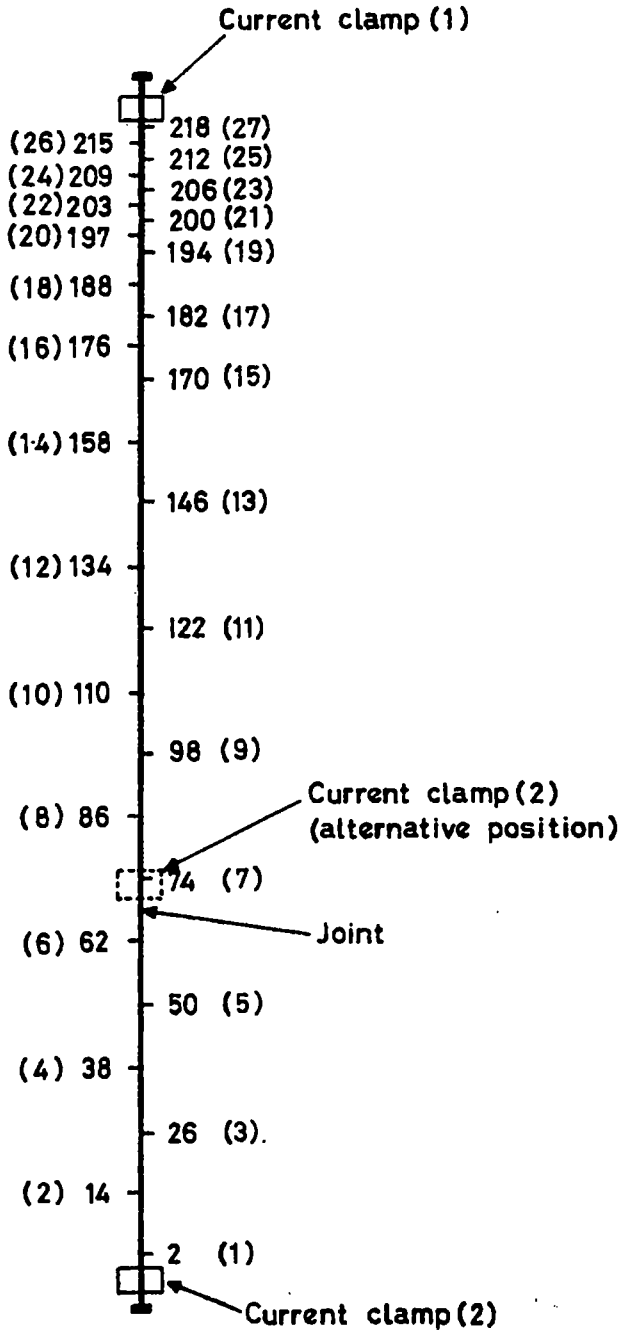

Figure 8.2-36 Nodalization for the Bennett Heated Tube Tests

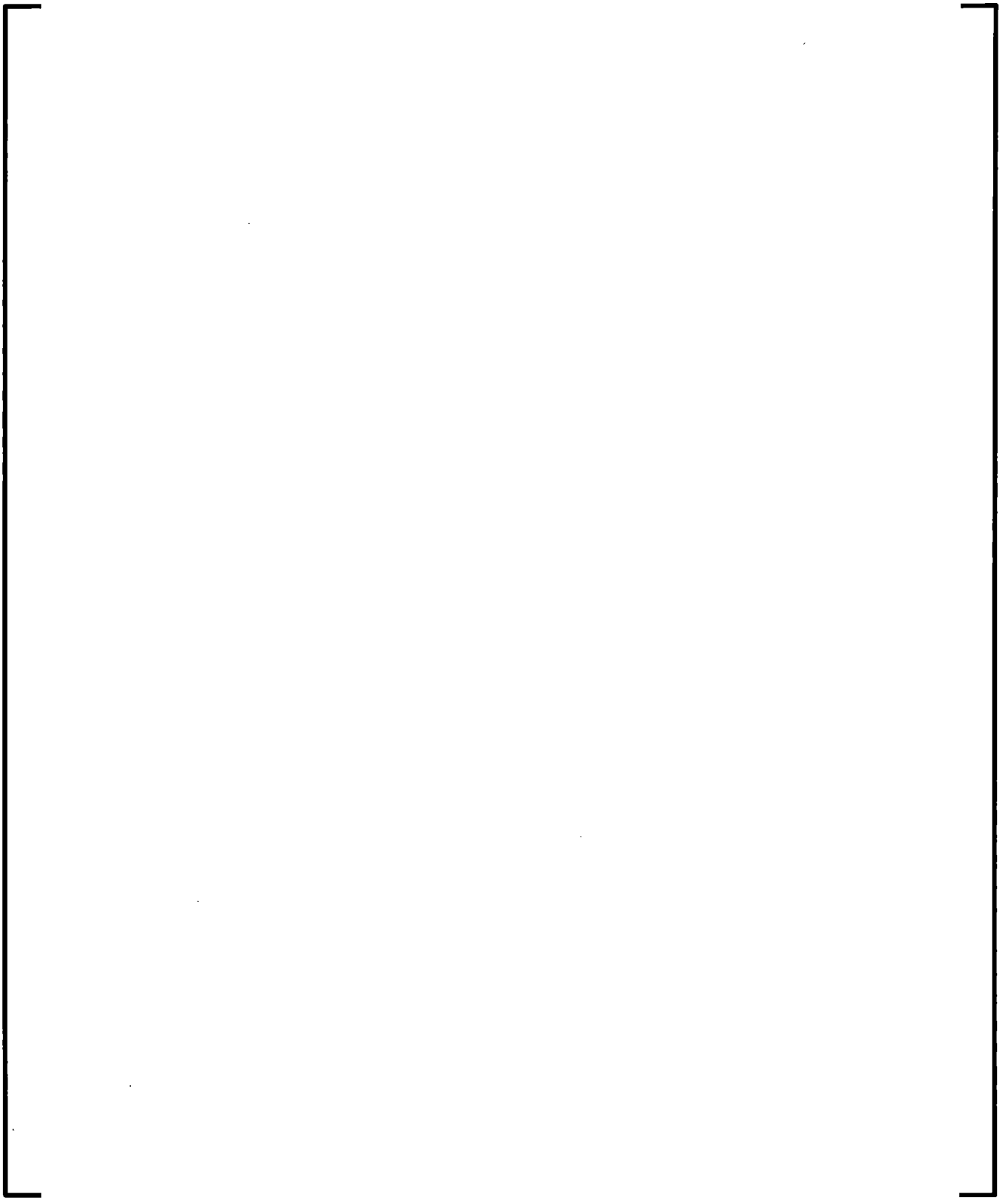

Figure 8.2-37 Wall Temperature Profiles - Bennett Test 5-358

Figure 8.2-38 Wall Temperature Profiles - Bennett Test 5-379

8.2.3 FLECHT-SEASET Tests and FLECHT Low-Flooding Rate Skewed Tests

8.2.3.1 Introduction

Full Length Emergency Core Heat Transfer - System Effects And Separate Effects (FLECHT SEASET) Tests (Reference 8.2-13) and Full Length Emergency Cooling Heat Transfer (FLECHT) Low-Flooding-Rate Skewed Tests (Skewed) (Reference 8.2-21) have been widely used for assessment of system codes to predict reflood heat transfer during a LBLOCA. FLECHT Tests 904 and 4444 and FLECHT SEASET Tests 31701 and 31805 are used in the developmental assessment of COBRA-TRAC (Reference 8.2-14). TRAC-PD2 developers selected FLECHT Tests 4831 and 17201, and FLECHT SEASET Test 31504 for assessment (Reference 8.2-15). Booker also publishes the results of the TRAC-PD2 calculation of FLECHT SEASET Test 31504 (Reference 8.2-16). INL performed calculations of FLECHT SEASET Tests 31504, 31701 and 33436 for the developmental assessment of RELAP5/MOD2 (Reference 8.2-17). Hassan (Reference 8.2-18) assessed RELAP5/MOD2 using FLECHT SEASET Tests 31504 and 31701, and FLECHT Test 4831. Analytis et al. (Reference 8.2-19), assessed RELAP5/MOD2 with FLECHT SEASET Test 34006. FLECHT SEASET Tests 31504 and 31701 are also included in the Code Scaling, Applicability and Uncertainty (CSAU) evaluation matrix (Reference 8.2-20).

The FLECHT SEASET facility used the Westinghouse 17 x 17 geometry for the reference fuel design; the FLECHT facility used the Westinghouse 15 x 15 geometry for the reference fuel design. The forced reflood separate-effect tests use injection or flooding rates that are very demanding for simulations with the realistic system codes. A set of tests have been accepted throughout the industry for code assessment purposes. For LBLOCA reflood conditions, this test selection covers the whole range of pressure, subcooling and flooding rate, and includes cosine and skewed axial power profiles. AREVA NP selected the FLECHT SEASET Tests 31504, 31701, 31302, 31203, 31805, 32013, and 34209, and FLECHT Skewed Tests 13609 and 13914 to validate the reflood modeling capability of S-RELAP5 for realistic large-break loss-of-coolant accident (LBLOCA) methodology.

Table 8.2-5 summarizes the test conditions for the selected tests.

[

]

Time-step and nodalization sensitivity studies were performed using FLECHT SEASET Test 31504 to demonstrate the solution convergence of S-RELAP5 treatment of the reflood transient. FLECHT SEASET Test 31504 was chosen for this purpose because it is a demanding low flooding rate (0.97 inch/s) (2.46 cm/s) test. It is well known that high-flooding-rate tests are easier for the advanced system codes to simulate because of early turnover and no sharp discontinuities in the void distribution.

The important parameters for assessing the code calculation against the measured data are:

- PCT
- cladding surface temperature history
- steam temperatures
- heat transfer coefficients
- differential pressures

- mass inventory
- liquid carryover
- rod quench time

The PCT is one of the required criteria for licensing. The PCT is the maximum value of all cladding temperatures. With the power specified, the cladding surface temperatures at various elevations depend on the heat transfer rates from the surface to the fluid. The fluid conditions, including the steam temperature and void distribution, determine the heat transfer rates. The differential pressures indirectly measure void distribution under the low-flow conditions. The total mass in the test section is an indication of how much of the injection water remains for cooling of the rods and how much is entrained out. The liquid carryover is the amount of liquid entrained out of the test section. The rod quench time depends strongly on the transition boiling correlation used in the code. Information about the eight parameters listed in the previous paragraph provides a basis for understanding the computed results compared with the measured data.

8.2.3.2 Summary and Conclusions

Time-step and nodalization studies were performed using FLECHT SEASET Test 31504. The calculated rod surface temperatures are not sensitive to time-step sizes, particularly in the temperature rise period. The calculated results have some small variations with the node sizes, noticeably in the quench period. The local maximum cladding temperatures (as a function of elevation) computed with different node sizes and different time-step sizes are clustered in an extremely narrow band. This band is much narrower than the corresponding measured data band. Also, the calculation points are distributed in the outer envelope of the measured data.

Data comparisons for all tests calculated were made for the following eight key parameters: (1) PCT, (2) rod surface temperature (or cladding temperature), (3) steam temperature, (4) heat transfer coefficient, (5) differential pressure, (6) mass inventory, (7) liquid carry-over from the test assembly, and (8) rod quench time.

The maximum clad temperature difference (calculated result - measured data) as a function of elevation in the test assembly for all tests calculated is shown in Figure 8.2-39. Considering the variations of the boundary conditions specified in Table 8.2-8 and this figure, the following conclusions are readily apparent:

- As a best-estimate code, S-RELAP5 generally calculated peak cladding temperature (PCT) in good agreement with the measured data.
- S-RELAP5 tends to predict cladding temperatures within a ± 70 Kelvin band.
- S-RELAP5 tends to over-predict with decreasing system pressure.
- S-RELAP5 over-predicts in the case of a top-peaked axial power profile.

The PCT as a function of reflood rate and irrespective of time of occurrence or location is shown in Figure 8.2-40. At the high and low reflood rates, S-RELAP5 under-predicts PCT while agreeing very well with the midrange reflood rates.

The PCT as a function of system pressure, irrespective of time of occurrence or location, is shown in Figure 8.2-41. S-RELAP5 under-predicts the high pressure data while over-predicting the low pressure data. S-RELAP5 correctly predicts the PCT when the system pressure is 40psia.

The PCT as a function of inlet subcooling and irrespective of time of occurrence or location is shown in Figure 8.2-42 . All the calculated results are significantly conservative (calculating a PCT higher than measured), most likely because of the top-peaked axial power profile used in the FLECHT Skewed tests. S-RELAP5 correctly predicts the data trend of increased PCT with increased inlet subcooling.

Rod quench time difference (calculated result − mean of measured data) as a function of elevation in the test assembly is shown in Figure 8.2-43. Using the default Tmin criteria, S-RELAP5 tends to predict quench times within ± 25 s of the averaged data, which is considered acceptable.

8.2.3.3 Facility Description

The FLECHT SEASET test facility (Reference 8.2-13) is a modification of the FLECHT Skewed test facility (Reference 8.2-21). The two test facilities share similar instrumentation configuration. Shown in Figure 8.2-44 is a schematic diagram of the FLECHT SEASET test facility and instrumentation. Some important features common to the two test facilities are as follows:

- A low-mass housing test section
- Upper and lower plenums
- An upper plenum baffle to improve liquid carryover separation
- The pressurized water accumulator
- Injection line flow measurement using three rotameters and a turbine meter
- A close-coupled carryover tank connected to the upper plenum of the test section with a storage capacity of 145 lb (65.8 kg)
- A steam separator with a capacity of 2500 lb/hr (0.315 kg/s) and liquid collection tank with a volume capacity of 21 lb (9.5 kg) to collect liquid entrained in the exhaust line. The steam separator has a storage capacity of approximately 425 lb (193 kg)
- Exhaust piping with a system control valve and an orifice plate flowmeter to measure exhaust steam flow rate
- An electric steam boiler with a capacity of 125 lb/hr (0.016 kg/s) to establish initial loop pressure and temperature

The low-mass housing is designed to minimize the wall effects such that the rods one or more rows away from the housing are representative of any region in a PWR core. The test section dimensions are similar to those of a PWR core fuel element. To preserve proper thermal scaling of the test facility with respect to a PWR, the power-to-flow area ratio is nearly the same as that for a PWR fuel assembly. In this fashion the steam vapor superheat, entrainment, and fluid-flow behavior should be similar to that expected in a PWR for the same boundary conditions.

Differential pressure cells in the test section provided measured data for determining mass balance and bundle void fraction. Low-range (±1 psid (±0.0069 MPa) pressure transducers are used to improve the accuracy of the measured data. The cells are located every 12 inch (0.30 m) along the test section (see Figure 8.2-44). The differential pressure cell manifold is carefully bled to eliminate any trapped air to improve the repeatability of the readings.

Figure 8.2-45 shows a cross section of the FLECHT SEASET test bundle. The bundle is representative of the 17 x 17-type rod geometry and consists of 161 heater rods (93 non-instrumented and 68 instrumented), 4 instrumented thimbles, 12 steam probes, 8 solid triangular fillers, and 8 grids. The triangular fillers are welded to the grids to maintain the proper grid locations. The fillers also reduce the amount of excess flow area from 9.3 to 4.7%. The heater rod is composed of stainless clad and coiled Kanthal wire heating elements, filled with boron nitride. Figure 8.2-46 depicts the material compositions and dimensions of the FLECHT SEASET heater rod. In the instrumented heater rods, thermocouples are located at several different axial locations on the inside wall of the cladding.

Figure 8.2-47 shows a cross section of the FLECHT Skewed test bundle. The bundle is representative of the 15 x 15-type rod geometry and consists of 105 heater rods (55 non-instrumented and 50 instrumented), 4 instrumented and non-instrumented thimbles, 3 steam probes, 12 solid triangular fillers, and 8 grids. The heater rod has the same composition as the FLECHT SEASET heater rod, but has different dimensions. Figure 8.2-48 depicts the material compositions and dimensions of the FLECHT heater rod.

Thermocouples are located at several different axial locations on the inside wall of the cladding.

8.2.3.4 Test Description

The FLECHT and FLECHT SEASET test conditions are based on the reference assumptions applicable for the reflood transient of a hypothetical LBLOCA of a Westinghouse plant. These assumptions are as follows:

- The core hot assembly is simulated in terms of peak power (kW/m) and initial temperatures at the time of bottom of core recovery (BOCREC).
- Decay heat power is based on the draft ANS standard plus 20%.
- The initial rod cladding temperature depends primarily on the full-power linear heating rate at the time of core recovery. For the period from 30 seconds after the initiation of a hypothetical LBLOCA to core recovery, typical results from a worst case analysis yield an initial cladding temperature in the hot assembly of 1600°F (871°C).
- Coolant temperatures are selected to maintain a constant subcooling to facilitate the determination of parametric effects.
- Coolant is injected directly into the test section from the lower plenum for the forced flooding rate tests.

- Upper plenum pressure at the end of blowdown is approximately 20 psia (0.14 MPa) for an ice condenser plant, and about 40 psia (0.28 MPa) for a dry containment plant. The upper plenum pressure is extended to 60 psia (0.42 MPa) for parametric effect.
- The axial power shape built into the heater rod is the modified cosine with a power peak-to-average ratio of 1.66 (FLECHT SEASET Test Series) or a top skewed power peak-to-average ratio of 1.35 at 10 ft (3.048 m) elevation (FLECHT Test Series).

Figure 8.2-49 shows the axial power profile for FLECHT SEASET tests. The power step size is 7.2 inch (183 mm) for the elevations between 24 and 120 inch (610 mm and 3048 mm). The profile is based on a center peaked cosine shape. Figure 8.2-50 shows the axial power profile for FLECHT Skewed tests. The FLECHT Skewed profile shows peak power at 10 ft (3.048 m) elevation. The bundle radial power profiles for both the FLECHT SEASET and FLECHT Skewed tests presented here are approximately uniform. The test conditions for the tests selected are summarized in Table 8.2-8.

The test section, carryover vessel, and exhaust line components are pressurized to the desired system pressure. The coolant in the accumulator is pressurized to 400 psia (2.76 MPa). Water then is injected into the lower plenum until it reaches the beginning of the heated length of the bundle heater rods. Coolant is circulated and drained to ensure that the water in the lower plenum and injection line is at the specified temperature before the run.

Power then is applied to the test bundle and the rods are allowed to heat up. When the temperature in any two designated bundle thermocouples reaches the preset value, the computer automatically initiates flood and controlled power decay. The exhaust control valve regulates the system pressure at the preset value by releasing steam to the atmosphere.

After all the designated heater rods have quenched, as indicated by the rod thermocouples, power to the heater rods is terminated, coolant injection is terminated, and the entire system is depressurized. Water stored in all components is drained and weighed.

8.2.3.5 S-RELAP5 Model Description

The main features of the S-RELAP5 input deck for the assessment of FLECHT SEASET tests and FLECHT Skewed tests are as follows:

[ ]

Figure 8.2-51 shows the nodalization diagrams of the heated test section [

] Only the components required to model the thermal and hydraulic behavior of the forced reflood tests are simulated in the input model. The test section nodalization [

] The initial heat structure temperatures are derived from the data files or the data presented on the data reports. The axial power distribution is obtained from Figure 8.2-49 for the FLECHT SEASET tests and from Figure 8.2-50 for the FLECHT Skewed tests. The power history is input in table form and is obtained from the data files. [ ]

For the heater rods, the bundle option was invoked to specifically use the bundle heat transfer model. [

]

8.2.3.6 Calculated Results

Time-step and nodalization studies are carried out using FLECHT SEASET Test 31504. The calculated rod surface temperatures at the 79 inch elevation [

]

The maximum rod surface temperatures for the calculations and the measured data as a function of test section elevation are plotted in Figure 8.2-54. For a given elevation, the measured data points are from different rod locations (see Figure 8.2-45) and the calculation points cover [ ]. Figure 8.2-54 indicates that the spread of calculation points is much smaller than the spread of measured data, and the calculation points are for the most part, either over the measured data maxima or are distributed in the outer envelope of the measured data points. This means the calculated results are in excellent agreement with respect to the measured data.

The calculated results [

] are used for presenting code-data comparisons. To show possible dependency on flooding rate, pressure, and inlet subcooling, the tests are arranged in different groups. The flooding rate dependency (or sensitivity) is observed from the FLECHT SEASET tests as shown in Table 8.2-5.

The pressure sensitivity is based on the FLECHT SEASET tests as shown in Table 8.2-6.

The FLECHT Skewed tests are used to infer the sensitivity on inlet subcooling as shown in Table 8.2-7. The calculated results for all selected tests are presented below in terms of the eight important parameters identified in Section 8.2.3.1.

8.2.3.6.1 Peak Cladding Temperature

The measured and calculated maximum clad temperature as a function of elevation above the bottom of the test section is provided in Figure 8.2-55 to Figure 8.2-63.

Table 8.2-9 summarizes the PCT results depicted on the figures. The PCTs for the data are the maximums of each measurement channel except for those rods adjacent to disconnected rods or within two rows of the low mass housing. S-RELAP5 calculates the PCT well.

The S-RELAP5 calculated PCT is generally within the measured data and slightly exceeding the data above the 100 inch elevation. The results from the FLECHT Skewed comparisons show [

]

8.2.3.6.2 Rod Surface Temperatures

Figure 8.2-64 to Figure 8.2-99 show the S-RELAP5 calculated temperature at a specified elevation compared with measured temperature near the same elevation. [

] The uncertainties associated with the value of T_{min} used in S-RELAP5 will be discussed in Section 8.4.2. [

]

S-RELAP5 has calculated rod surface temperature in good agreement for the complete transient at all elevations for the high system pressure test, Test 32013, and for elevations below 90 inch for the low pressure test, Test 34209. For the low pressure test, Test 34209, [

]

For the FLECHT Skewed tests, [

]

For FLECHT SEASET Test 31504, the (overall) PCT occurs in the region above, but close to, the mid-plane of the test section. Figure 8.2-74 displays the plots of the calculated and measured surface temperature at the 78-in elevation. The calculated rod surface temperature in the temperature rise period is in good agreement with the measured data.

8.2.3.6.3 Steam Temperatures

Steam temperature is one of the important parameters in determining the heat transfer rate during the temperature rise period. Figure 8.2-100 through Figure 8.2-108 shows the measured and calculated steam temperatures. [

]

[

]

8.2.3.6.4 Differential Pressures

Differential pressure is an indirect measurement of void distribution. Void distribution is an important property for calculating the heat transfer rate. The differential pressure comparison for S-RELAP5 and the tests is shown in Figure 8.2-109 to Figure 8.2-117. The differential applies from the 72- to 84-in. elevations. The calculated data are represented by cntrlvar-300 and the measured data BU-6-7. [

]

[

]

8.2.3.6.5 Heat Transfer Coefficient

The heat transfer coefficient is normally defined with respect to phase or saturation temperature, depending on the heat transfer mode. This definition is used in S-RELAP5, as well as the RELAP5 series of codes. The heat transfer coefficient data are usually deduced from the heat transfer measurements with reference to the saturation temperature. Cntrlvar-311 was defined in the S-RELAP5 input to represent the effective heat transfer coefficient [

] Figure 8.2-118 to Figure 8.2-126 compare the calculated effective heat transfer coefficient. [

]

8.2.3.6.6 Mass Inventory

The total water mass in the test section as a function of transient time is shown in Figure 8.2-127 through Figure 8.2-135. [

]

In those cases that captured the time of power termination, the water accumulation suddenly increased in both the measurements and calculations. The water quickly accumulated in the test section as evaporation and entrainment [

]

8.2.3.6.7 Liquid Carryover

The calculated carryover [

] This parameter is not presented for Test 31504 because AREVA NP does not have the experimental carryover tank level data. This parameter is not presented for Tests 31302 and 31701 because, during the tests the test section upper plenum was seen to flood, invalidating the measured data.

8.2.3.6.8 Rod Quench Time

The mean rod quench time as a function of elevation in the test assembly is shown in Figure 8.2-136 through Figure 8.2-142. As previously mentioned, [

]

8.2.3.7 Discussion of Results

The flow patterns and heat transfer regimes in the test section can be divided into roughly three distinct axial regions for a bottom reflood configuration with low flow rate. (Tests 31504 and 31805 are such tests.) The first region is the low void fraction region below the quench front, more specifically below the point of critical heat flux. The flow regime is slug/bubbly flow, including single-phase liquid. The cladding-to-fluid heat transfer is in nucleate boiling and single-phase liquid convection. The rod surface temperature is nearly constant in time. The heat transfer rate is large and nearly constant in time.

The second region involves medium-to-high void fraction with rapid-cooling and quenching. The flow regime is inverted slug characterized by large drops of liquid (liquid drops with a diameter close to the hydraulic diameter) surrounded by vapor. The rod surface is intermittently wetted and has a very high temperature gradient in the axial direction. The cladding-to-fluid heat transfer is film boiling and transition boiling. The heat transfer rate is quite large and a large amount of vapor is generated. The vapor pushes or entrains liquid upward. The large liquid drops fall back or degenerate into small droplets. The small liquid droplets are entrained further upward by vapor.

The high void fraction water above the quenching region constitutes the third region. The flow regime is dispersed flow (including single-phase vapor) and the cladding-to-fluid heat transfer is dispersed film boiling and convection to vapor. The steam is highly superheated leading to a small heat transfer rate. Liquid droplets vaporize because of the superheated steam and high temperature of the cladding. The cladding surface temperature continues rising until sufficient heat transfer develops to stop the temperature rise.

[

]

In the rapid-cooling period, [

]

The FLECHT SEASET and FLECHT Skewed comparisons shown in this section demonstrate the capacity of the S-RELAP5 code to predict LBLOCA reflood phenomena. Data from these tests are combined with other reflood test data to establish the bias and uncertainties to be used for RLBLOCA as given in Section 8.4.1.

Table 8.2-5 Flooding Rate Dependency

Test	Reflood Rate (in/s : mm/s)
31701	6.10 : 155
31302	3.01 : 76
31203	1.51 : 38
31504	0.97 : 25
31805	0.81 : 21

Table 8.2-6 Pressure Dependency

Test	System Pressure (psia : MPa)
34209	20 : 0.14
31504	40 : 0.28
32013	60 : 0.41

Table 8.2-7 Inlet Subcooling Dependency

Test	System Pressure (psia : MPa)
13609	144 : 80.0
13914	8 : 4.4

Table 8.2-8 FLECHT SEASET, FLECHT Skewed Test Conditions

Run	Pressure (psia)	Peak Power (kW/ft)	Flow Rate (in/s)	Coolant Temp (°F)	Axial Power Profile
FLECHT SEASET Tests Flooding Rate					
31805	40	0.70	0.81	124	Cosine, Center Peak
31203	40	0.70	1.51	126	Cosine, Center Peak
31302	40	0.69	3.01	126	Cosine, Center Peak
31701	40	0.70	6.10	127	Cosine, Center Peak
Pressure Variation					
34209	20	0.72	1.07	90	Cosine, Center Peak
31504	40	0.70	0.97	123	Cosine, Center Peak
32013	60	0.70	1.04	150	Cosine, Center Peak
FLECHT Tests Subcooling Variation					
13609	21	0.70	1.00	87	Skewed, top peak
13914	21	0.70	1.00	223	Skewed, top peak

Table 8.2-9 PCT Results

Run	Data PCT (K)	Data PCT (°F)	S-RELAP5 PCT (K)	S-RELAP5 PCT (°F)
FLECHT SEASET Tests Flooding Rate				
31805	1560	2358	1511	2259
31203	1279	1842	1301	1882
31302	1173	1651	1200	1700
31701	1177	1659	1156	1621
Pressure Variation				
34209	1400	2060	1449	2148
31504	1379	2022	1430	2114
32013	1406	2071	1395	2051
FLECHT Tests Subcooling Variation				
13609	1232	1758	1415	2088
13914	1188	1678	1370	2007

Figure 8.2-39 Maximum Clad Temperature (Calculated - Data) vs. Elevation

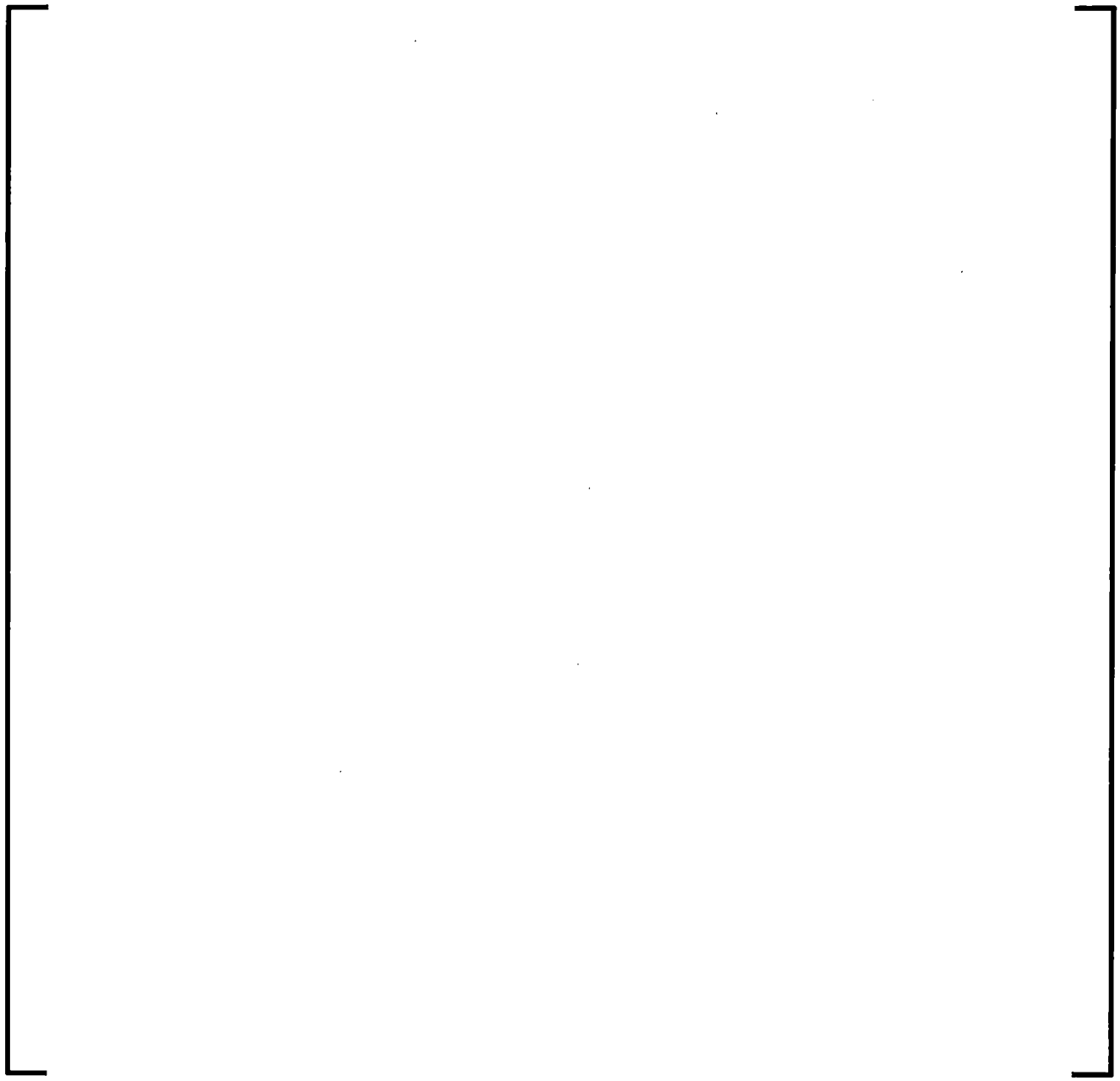

Figure 8.2-40 FLECHT SEASET Test PCT vs. Reflood Rate

Figure 8.2-41 FLECHT SEASET Test PCT vs. System Pressure

Figure 8.2-42 FLECHT Skewed Test PCT vs. Inlet Subcooling

Figure 8.2-43 Mean Rod Quench Time Comparison

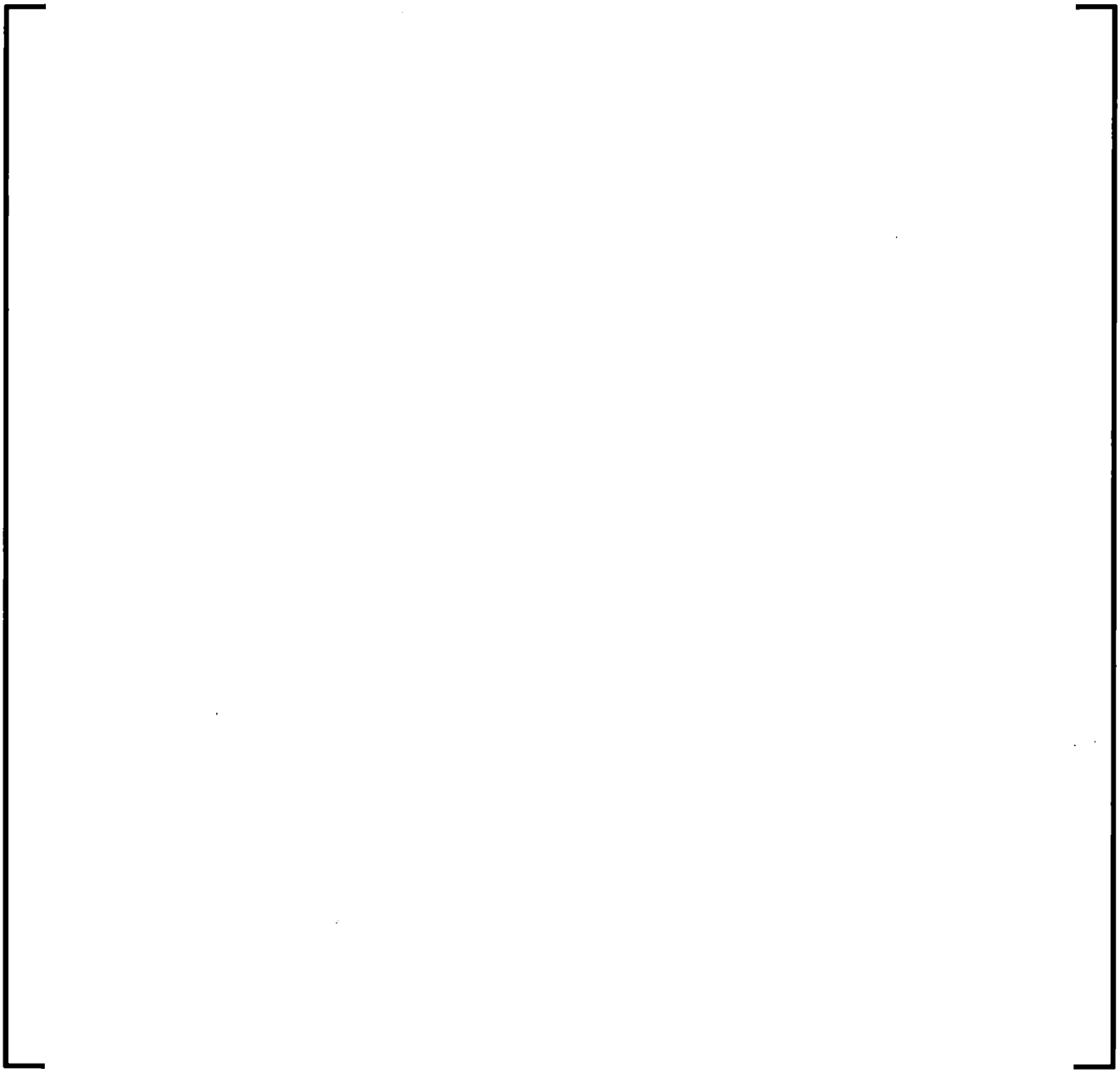

Figure 8.2-44 Schematic Diagram of FLECHT SEASET Test Facility and Instrumentation

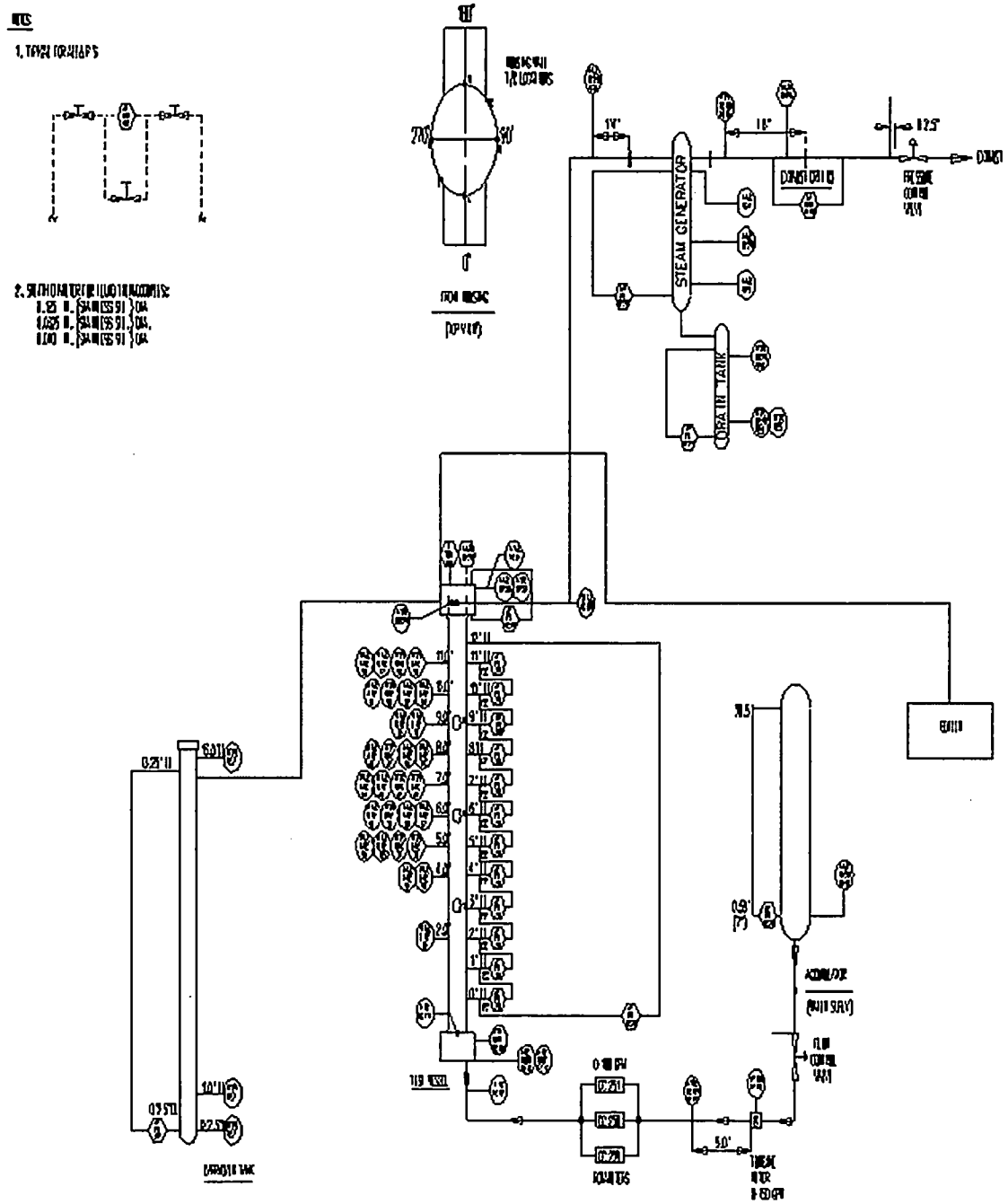

Figure 8.2-45 FLECHT SEASET Bundle Cross Section

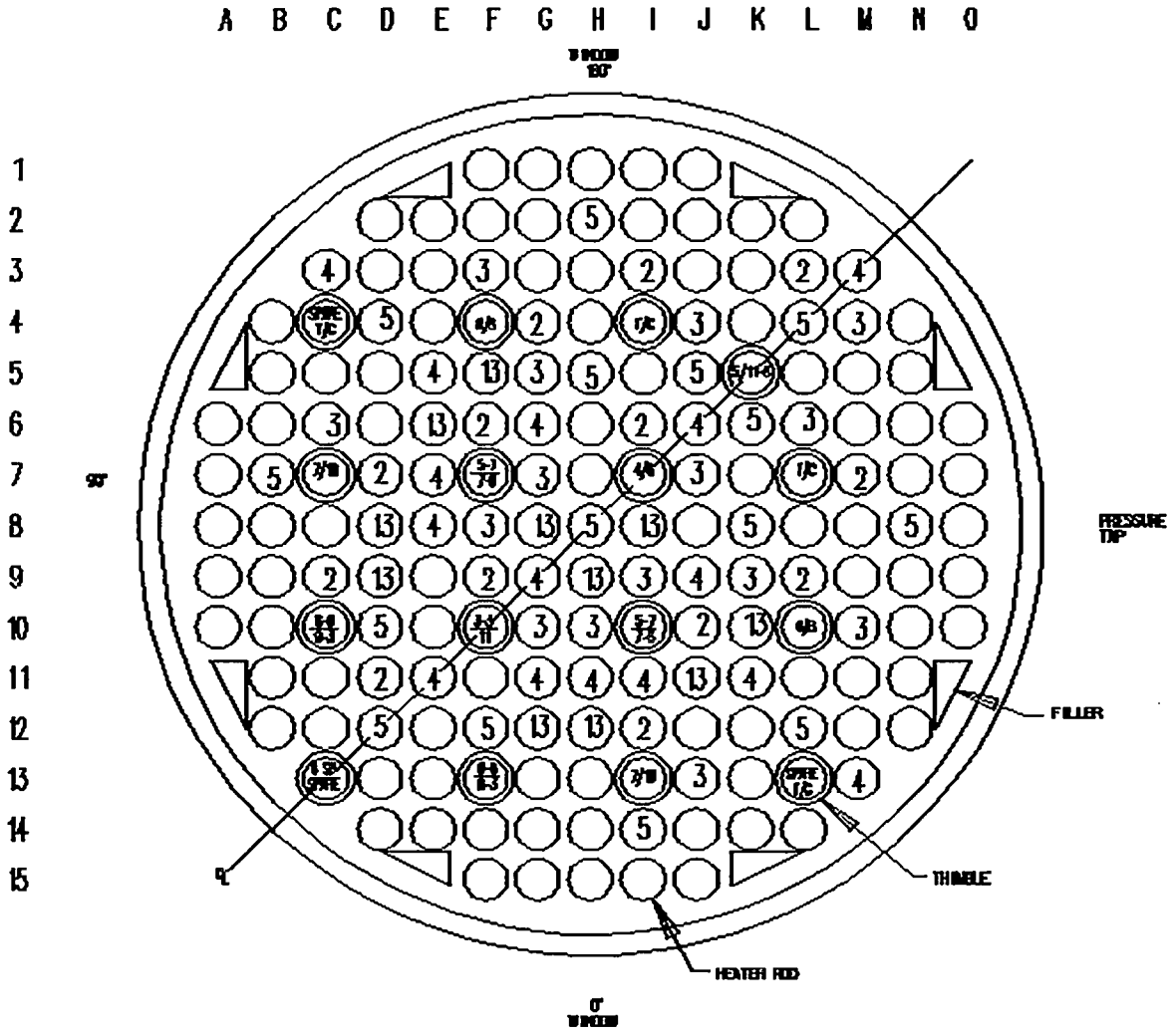

Figure 8.2-46 FLECHT SEASET Heater Rod

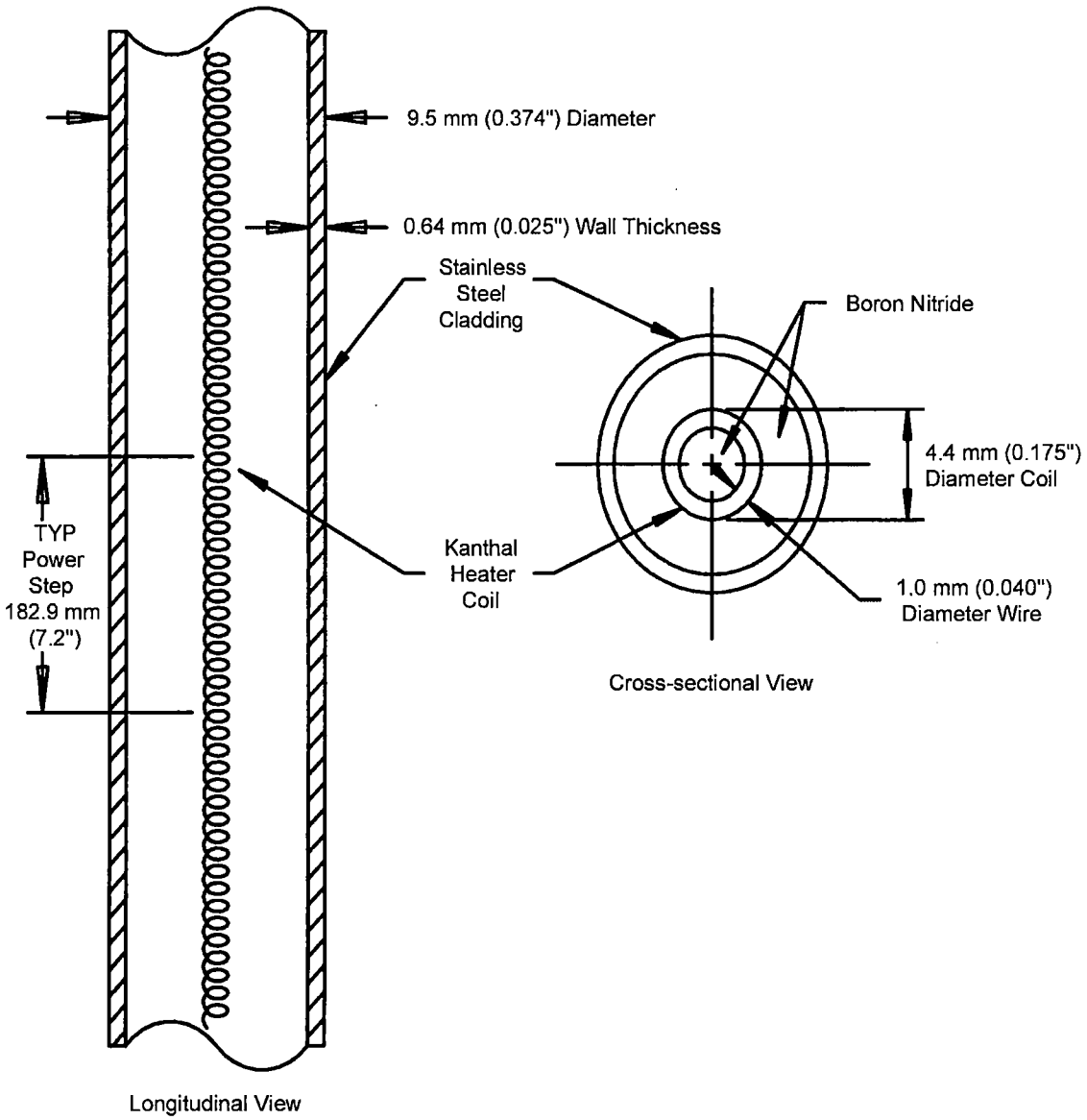

Figure 8.2-47 FLECHT Skewed Test Bundle Cross Section

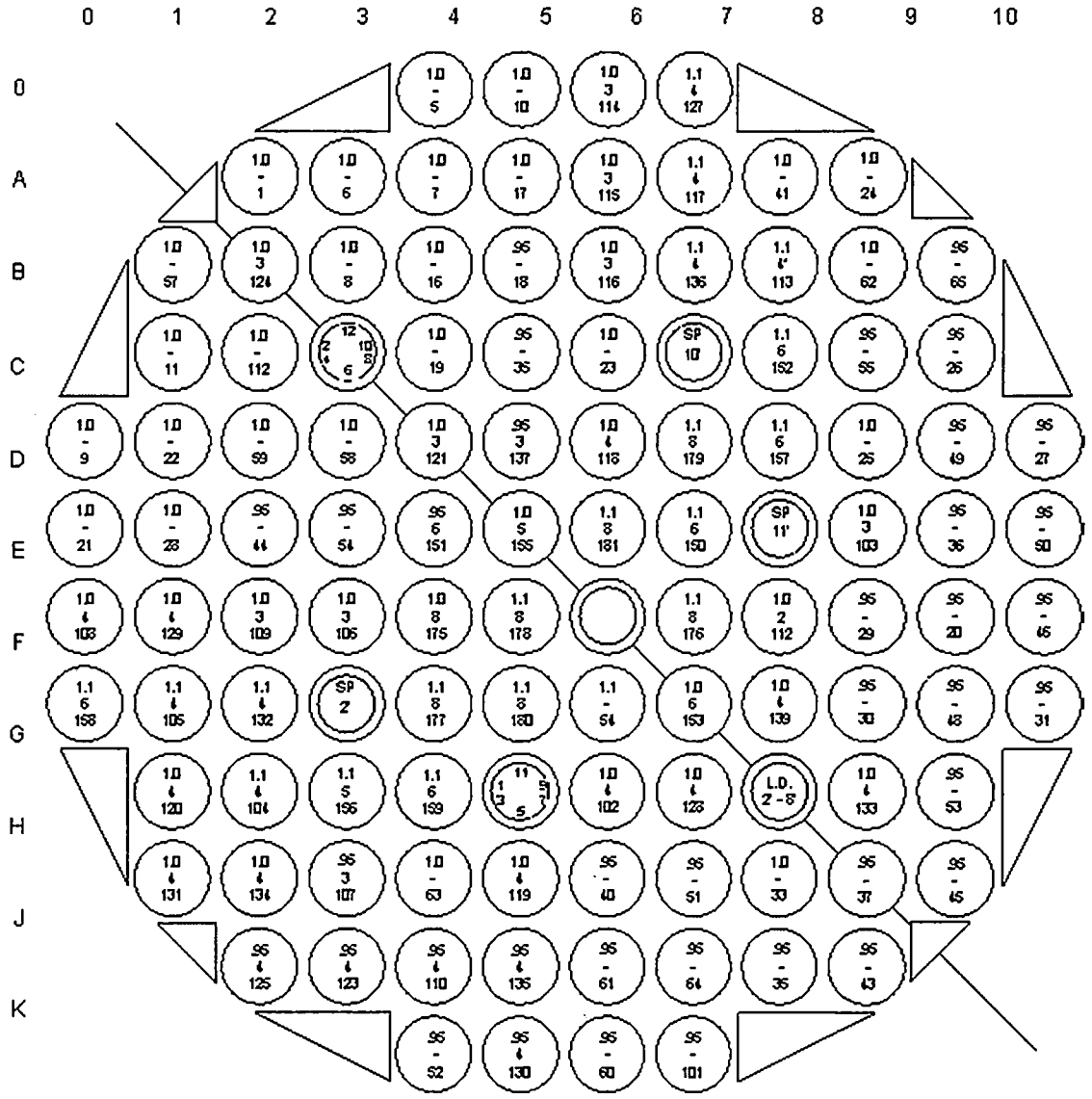

Legend:

1.1, 1.0, .95 Radial Power Distribution
SP Steam Probe
The number in the center denotes:
- 8 Instrumented rod with 8 T/C's at 3', 5', 7', 9', 9.5', 10', 10.5', 11' elevations
- 6 Instrumented rod with 6 T/C's at 1', 4', 6', 8', 10', 11.5' elevations
- 5 Instrumented rod with 5 T/C's at
  - A. 4', 6', 8', 10', 11.5' elevations
  - B. 1', 4', 6', 8', 11.5' elevations
- 4 Instrumented rod with 4 T/C's at 2', 6', 10', 11' elevations
- 3 Instrumented rod with 3 T/C's at
  - A. 2', 6', 10' elevations
  - B. 2', 6', 11' elevations
  - C. 6', 10', 11' elevations
  - D. 2', 10', 11' elevations

* Rod 8B with roughened surfaces at T/C locations

Figure 8.2-48 FLECHT Low Flooding Rate Skew Test Heater Rod

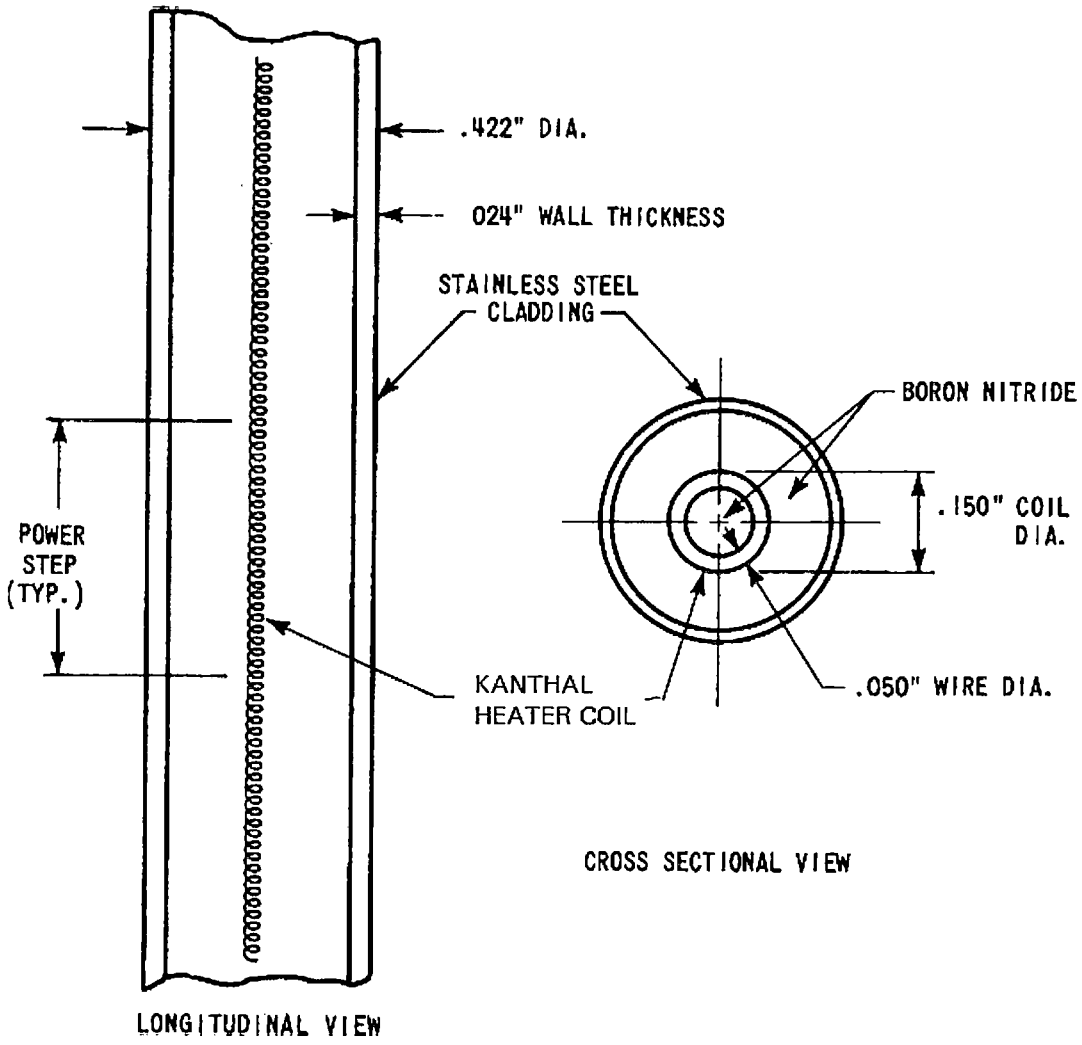

Figure 8.2-49 FLECHT SEASET Axial Power Profile

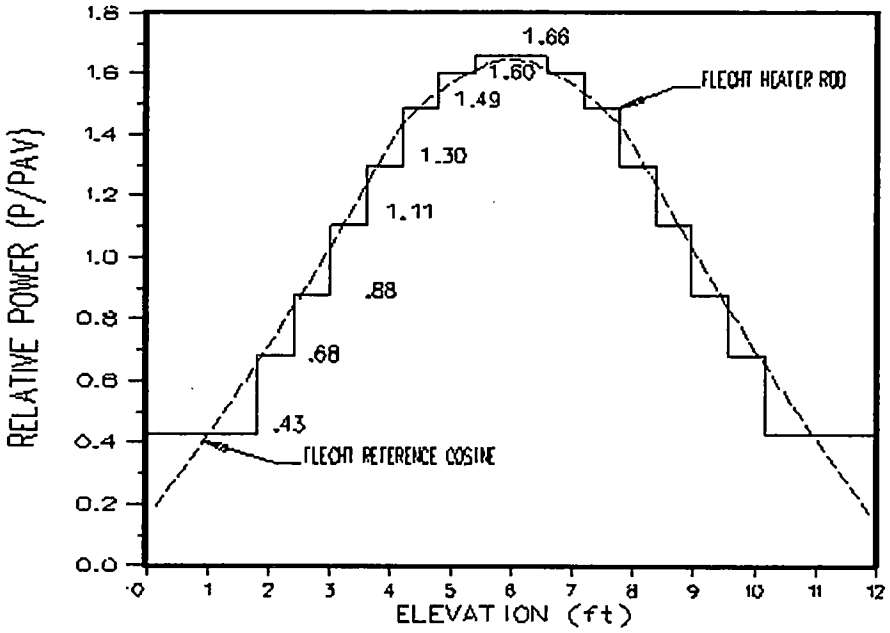

Figure 8.2-50 FLECHT Skewed Axial Power Profile

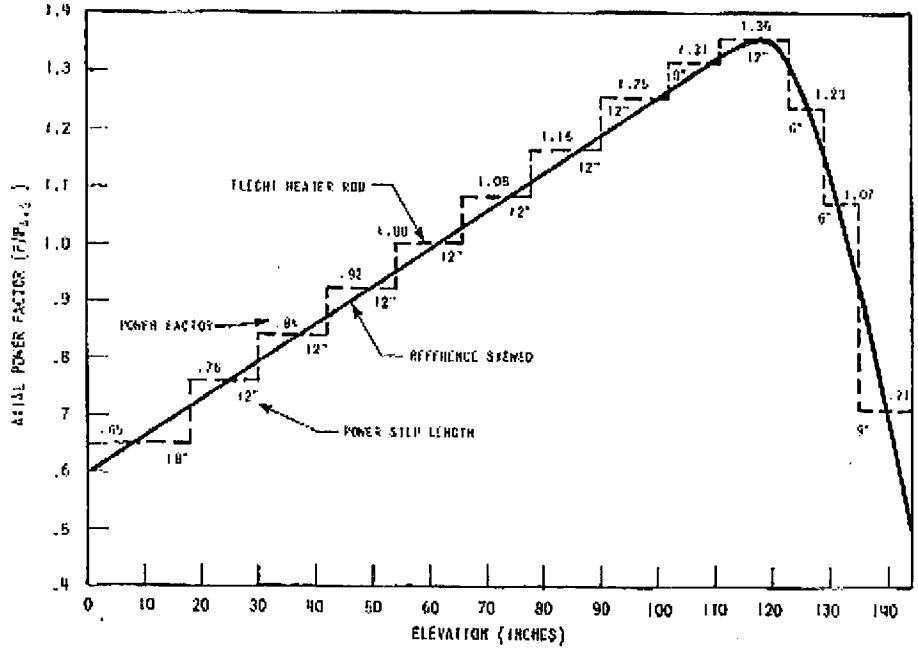

Figure 8.2-51 Bundle Axial Nodalization

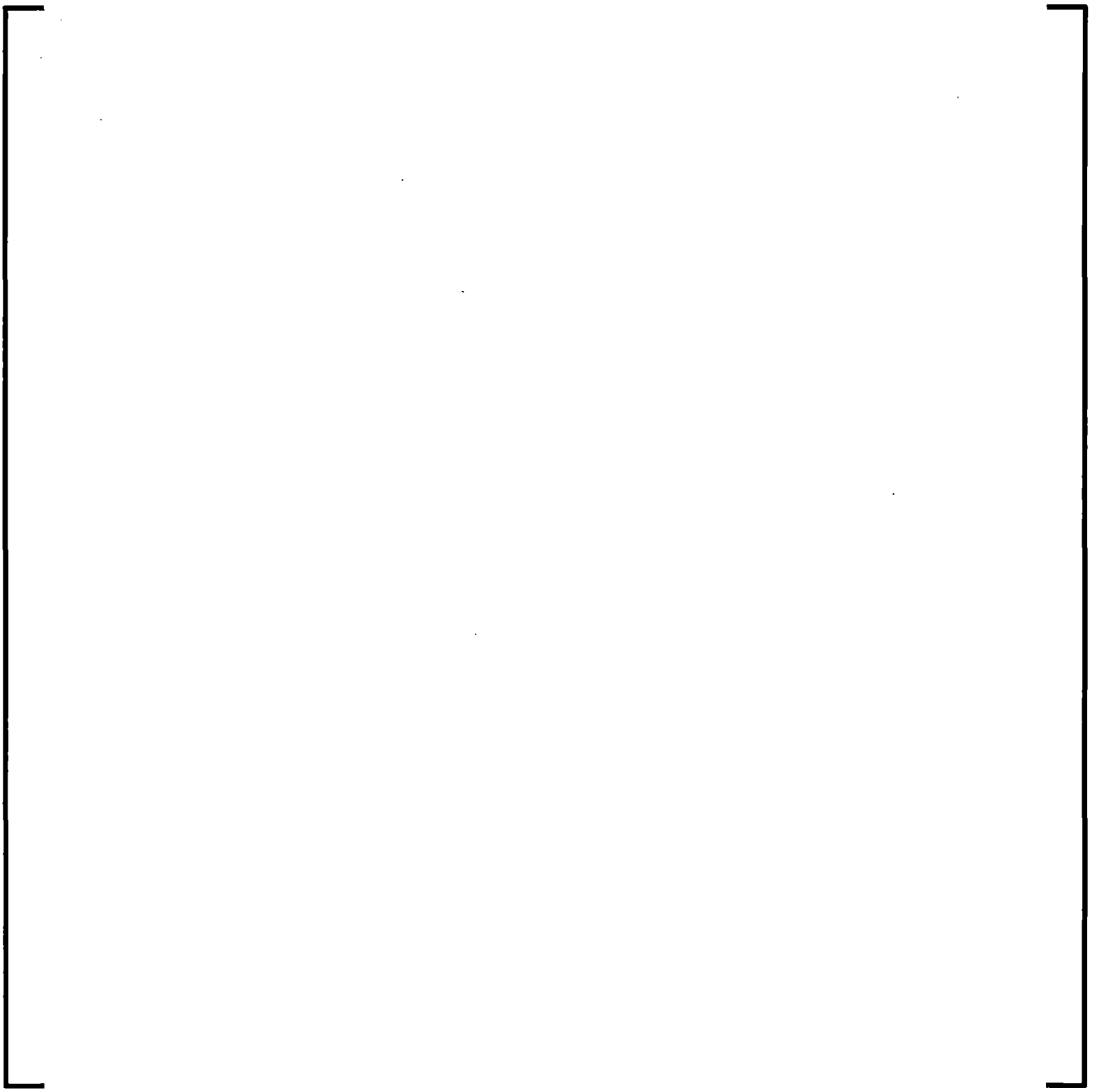

Figure 8.2-52 Calculated Rod Surface Temperatures at 79 Inches for the 20-Volume Test

Figure 8.2-53 Calculated Rod Surface Temperatures at 79 Inches for the 40-Volume Test

Figure 8.2-54 Maximum Cladding Temperatures vs. Axial Elevation, FLECHT SEASET Test 31504

Figure 8.2-55 Maximum Cladding Temperature at All Measured Elevations, FLECHT SEASET Test 31805

Figure 8.2-56 Maximum Cladding Temperature at All Measured Elevations, FLECHT SEASET Test 31504

Figure 8.2-57 Maximum Cladding Temperature at All Measured Elevations, FLECHT SEASET Test 31203

Figure 8.2-58 Maximum Cladding Temperature at All Measured Elevations, FLECHT SEASET Test 31302

Figure 8.2-59 Maximum Cladding Temperature at All Measured Elevations, FLECHT SEASET Test 31701

Figure 8.2-60 Maximum Cladding Temperature at All Measured Elevations, FLECHT SEASET Test 34209

Figure 8.2-61 Maximum Cladding Temperature at All Measured Elevations, FLECHT SEASET Test 32013

Figure 8.2-62 Maximum Cladding Temperature at All Measured Elevations, FLECHT SEASET Test 13609

Figure 8.2-63 Maximum Cladding Temperature at All Measured Elevations, FLECHT SEASET Test 13914

Figure 8.2-64 Calculated and Measured Rod Surface Temperatures at 48 inch, FLECHT SEASET Test 31805

Figure 8.2-65 Calculated and Measured Rod Surface Temperatures at 48 inch, FLECHT SEASET Test 31504

Figure 8.2-66 Calculated and Measured Rod Surface Temperatures at 48 inch, FLECHT SEASET Test 31203

Figure 8.2-67 Calculated and Measured Rod Surface Temperatures at 48 inch, FLECHT SEASET Test 31302

Figure 8.2-68 Calculated and Measured Rod Surface Temperatures at 48 inch, FLECHT SEASET Test 31701

Figure 8.2-69 Calculated and Measured Rod Surface Temperatures at 48 inch, FLECHT SEASET Test 34209

Figure 8.2-70 Calculated and Measured Rod Surface Temperatures at 48 inch, FLECHT SEASET Test 32013

Figure 8.2-71 Calculated and Measured Rod Surface Temperatures at 36 inch, FLECHT SEASET Test 13609

Figure 8.2-72 Calculated and Measured Rod Surface Temperatures at 36 inch, FLECHT SEASET Test 13914

Figure 8.2-73 Calculated and Measured Rod Surface Temperatures at 78 inch, FLECHT SEASET Test 31805

Figure 8.2-74 Calculated and Measured Rod Surface Temperatures at 78 inch, FLECHT SEASET Test 31504

Figure 8.2-75 Calculated and Measured Rod Surface Temperatures at 78 inch, FLECHT SEASET Test 31203

Figure 8.2-76 Calculated and Measured Rod Surface Temperatures at 78 inch, FLECHT SEASET Test 31302

Figure 8.2-77 Calculated and Measured Rod Surface Temperatures at 78 inch, FLECHT SEASET Test 31701

Figure 8.2-78 Calculated and Measured Rod Surface Temperatures at 78 inch, FLECHT SEASET Test 34209

Figure 8.2-79 Calculated and Measured Rod Surface Temperatures at 78 inch, FLECHT SEASET Test 32013

Figure 8.2-80 Calculated and Measured Rod Surface Temperatures at 60 inch, FLECHT SEASET Test 13609

Figure 8.2-81 Calculated and Measured Rod Surface Temperatures at 60 inch, FLECHT SEASET Test 13914

Figure 8.2-82 Calculated and Measured Rod Surface Temperatures at 90 inch, FLECHT SEASET Test 31805

Figure 8.2-83 Calculated and Measured Rod Surface Temperatures at 90 inch, FLECHT SEASET Test 31504

Figure 8.2-84 Calculated and Measured Rod Surface Temperatures at 90 inch, FLECHT SEASET Test 31203

Figure 8.2-85 Calculated and Measured Rod Surface Temperatures at 90 inch, FLECHT SEASET Test 31302

Figure 8.2-86 Calculated and Measured Rod Surface Temperatures at 90 inch, FLECHT SEASET Test 31701

Figure 8.2-87 Calculated and Measured Rod Surface Temperatures at 90 inch, FLECHT SEASET Test 34209

Figure 8.2-88 Calculated and Measured Rod Surface Temperatures at 90 inch, FLECHT SEASET Test 32013

Figure 8.2-89 Calculated and Measured Rod Surface Temperatures at 84 inch, FLECHT SEASET Test 13609

Figure 8.2-90 Calculated and Measured Rod Surface Temperatures at 84 inch, FLECHT SEASET Test 13914

Figure 8.2-91 Calculated and Measured Rod Surface Temperatures at 111 inch, FLECHT SEASET Test 31805

Figure 8.2-92 Calculated and Measured Rod Surface Temperatures at 111 inch, FLECHT SEASET Test 31504

Figure 8.2-93 Calculated and Measured Rod Surface Temperatures at 111 inch, FLECHT SEASET Test 31203

Figure 8.2-94 Calculated and Measured Rod Surface Temperatures at 111 inch, FLECHT SEASET Test 31302

Figure 8.2-95 Calculated and Measured Rod Surface Temperatures at 111 inch, FLECHT SEASET Test 31701

Figure 8.2-96 Calculated and Measured Rod Surface Temperatures at 111 inch, FLECHT SEASET Test 34209

Figure 8.2-97 Calculated and Measured Rod Surface Temperatures at 111 inch, FLECHT SEASET Test 32013

Figure 8.2-98 Calculated and Measured Rod Surface Temperatures at 108 inch, FLECHT SEASET Test 13609

Figure 8.2-99 Calculated and Measured Rod Surface Temperatures at 108 inch, FLECHT SEASET Test 13914

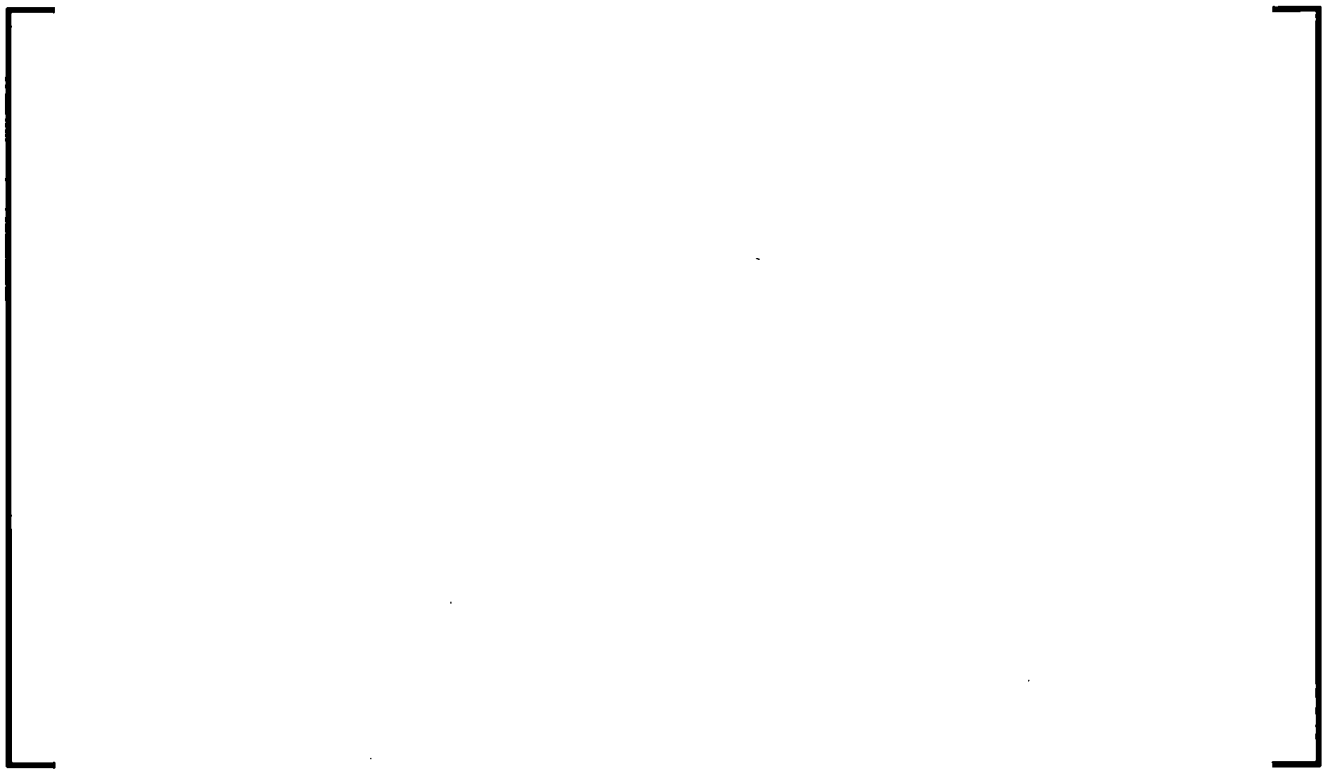

Figure 8.2-100 Steam Temperatures Calculated at 75.6 inch and Measured at 72 inch, FLECHT SEASET Test 31805

Figure 8.2-101 Steam Temperatures Calculated at 75.6 inch and Measured at 72 inch, FLECHT SEASET Test 31504

Figure 8.2-102 Steam Temperatures Calculated at 75.6 inch and Measured at 72 inch, FLECHT SEASET Test 31203

Figure 8.2-103 Steam Temperatures Calculated at 75.6 inch and Measured at 72 inch, FLECHT SEASET Test 31302

Figure 8.2-104 Steam Temperatures Calculated at 75.6 inch and Measured at 72 inch, FLECHT SEASET Test 31701

Figure 8.2-105 Steam Temperatures Calculated at 75.6 inch and Measured at 72 inch, FLECHT SEASET Test 34209

Figure 8.2-106 Steam Temperatures Calculated at 75.6 inch and Measured at 72 inch, FLECHT SEASET Test 32013

Figure 8.2-107 Steam Temperatures Calculated at 82.8 inch and Measured at 84 inch, FLECHT SEASET Test 13609

Figure 8.2-108 Steam Temperatures Calculated at 82.8 inch and Measured at 84 inch, FLECHT SEASET Test 13914

Figure 8.2-109 Calculated and Measured Differential Pressures Between 72 and 84 inch, FLECHT SEASET Test 31805

Figure 8.2-110 Calculated and Measured Differential Pressures Between 72 and 84 inch, FLECHT SEASET Test 31504

Figure 8.2-111 Calculated and Measured Differential Pressures Between 72 and 84 inch, FLECHT SEASET Test 31203

Figure 8.2-112 Calculated and Measured Differential Pressures Between 72 and 84 inch, FLECHT SEASET Test 31302

Figure 8.2-113 Calculated and Measured Differential Pressures Between 72 and 84 inch, FLECHT SEASET Test 31701

Figure 8.2-114 Calculated and Measured Differential Pressures Between 72 and 84 inch, FLECHT SEASET Test 34209

Figure 8.2-115 Calculated and Measured Differential Pressures Between 72 and 84 inch, FLECHT SEASET Test 32013

Figure 8.2-116 Calculated and Measured Differential Pressures Between 72 and 84 inch, FLECHT SEASET Test 13609

Figure 8.2-117 Calculated and Measured Differential Pressures Between 72 and 84 inch, FLECHT SEASET Test 13914

Figure 8.2-118 Comparison of Calculated and Measured Heat Transfer Coefficient, FLECHT SEASET Test 31805

Figure 8.2-119 Comparison of Calculated and Measured Heat Transfer Coefficient, FLECHT SEASET Test 31504

Figure 8.2-120 Comparison of Calculated and Measured Heat Transfer Coefficient, FLECHT SEASET Test 31203

Figure 8.2-121 Comparison of Calculated and Measured Heat Transfer Coefficient, FLECHTSEASET Test 31302

Figure 8.2-122 Comparison of Calculated and Measured Heat Transfer Coefficient, FLECHT SEASET Test 31701

Figure 8.2-123 Comparison of Calculated and Measured Heat Transfer Coefficient, FLECHT SEASET Test 34209

Figure 8.2-124 Comparison of Calculated and Measured Heat Transfer Coefficient, FLECHT SEASET Test 32013

Figure 8.2-125 Comparison of Calculated and Measured Heat Transfer Coefficient, FLECHT SEASET Test 13609

Figure 8.2-126 Comparison of Calculated and Measured Heat Transfer Coefficient, FLECHT SEASET Test 13914

Figure 8.2-127 Accumulated Water Mass in the Test Section, FLECHT SEASET Test 31805

Figure 8.2-128 Accumulated Water Mass in the Test Section, FLECHT SEASET Test 31504

Figure 8.2-129 Accumulated Water Mass in the Test Section, FLECHT SEASET Test 31203

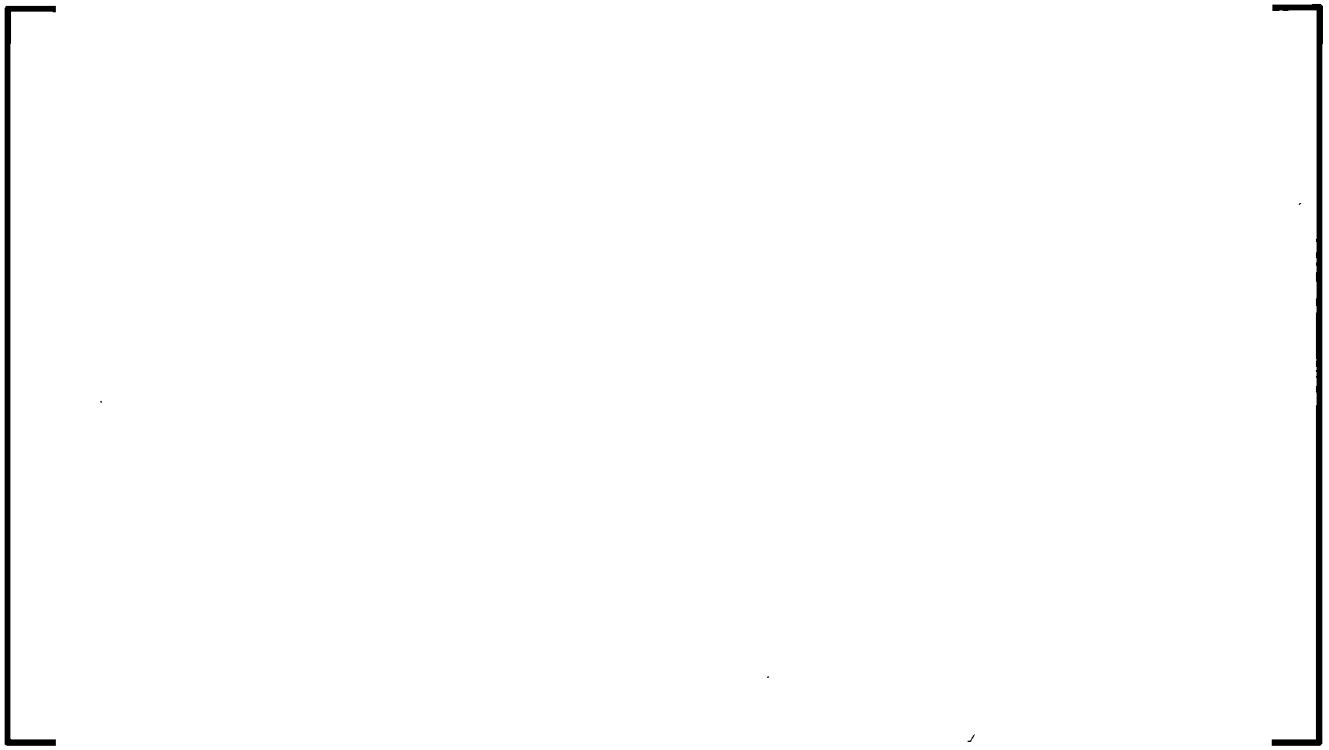

Figure 8.2-130 Accumulated Water Mass in the Test Section, FLECHT SEASET Test 31302

Figure 8.2-131 Accumulated Water Mass in the Test Section, FLECHT SEASET Test 31701

Figure 8.2-132 Accumulated Water Mass in the Test Section, FLECHT SEASET Test 34209

Figure 8.2-133 Accumulated Water Mass in the Test Section, FLECHT SEASET Test 32013

Figure 8.2-134 Accumulated Water Mass in the Test Section, FLECHT SEASET Test 13609

Figure 8.2-135 Accumulated Water Mass in the Test Section, FLECHT SEASET Test 13914

Figure 8.2-136 Average Rod Quench Time, FLECHT SEASET Test 31805

Figure 8.2-137 Average Rod Quench Time, FLECHT SEASET Test 31203

Figure 8.2-138 Average Rod Quench Time, FLECHT SEASET Test 31504

Figure 8.2-139 Average Rod Quench Time, FLECHT SEASET Test 31302

[ ]

Figure 8.2-140 Average Rod Quench Time, FLECHT SEASET Test 31701

Figure 8.2-141 Average Rod Quench Time, FLECHT SEASET Test 34209

Figure 8.2-142 Average Rod Quench Time, FLECHT SEASET Test 32013

8.2.4 FLECHT-SEASET Steam Cooling

8.2.4.1 Introduction

The purpose of this section is to assess the S-RELAP5 vapor convection heat transfer used in the "bundle option" heat transfer model (See Section 7.7.8) developed for reflood modeling in S-RELAP5. The vapor convection [

] Applied along with this model are [

] This assessment uses temperature data from Reference 8.2-22 for validation of the bundle option heat transfer model and will determine [

] for single phase vapor heat transfer.

8.2.4.2 Summary and Conclusions

The FLECHT-SEASET steam cooling tests 32753, 36160, 36261, 36362, 36463, 36564, 36766, and 36867 were simulated by S-RELAP5 using the bundle model option. The ranges of conditions of the tests were; temperatures between 280 and 400 °F, Reynolds Numbers between 3,000 and 20,000, and a pressure of approximately 40 psia. [

]

In summary, the FLECHT-SEASET steam cooling tests 32753, 36160, 36261, 36362, 36463, 36564, 36766, and 36867 were simulated by S-RELAP5 using the bundle model option and the results were compared to measured data. The uncertainty of the data comparisons was determined. [

]

8.2.4.3 Facility Description and Test Procedure

The facility description is fully discussed in Section 8.2.3.3, and will not be presented here. The test procedure (Reference 8.2-22) for the forced convection steam flow tests was initiated by pressurizing and preheating the rod bundle and associated piping with steam from the steam generator separate effects test boiler. Since the boiler produced saturated steam at 0.69 MPa (100 psia), the steam pressure was reduced across a central valve so that slightly superheated steam entered the test section. Once the test section had been heated above the saturation temperature, the rod power was turned on to a preset value and the rods were heated up to steady-state or near-steady-state conditions.

Data was obtained as the rods heated up to the steady-state conditions. The duration of the test was limited by the maximum number of data scans which could be recorded by the data acquisition computer storage disk; tests typically lasted 1400 seconds. As discussed later in Reference 8.2-22, 1400 seconds was not always sufficient for a true steady state to be achieved. After the test was complete, the power was turned off. The recorded data were processed onto computer tape, and the power and flow were reset for the next test.

8.2.4.4 S-RELAP5 Model Description

The input model is based on the standard input model (discussed in Section 8.2.3.5 and is shown in Figure 8.2-51,) [

] The initial conditions of pressure, inlet flow rate, inlet flow temperature and power were taken from Reference 8.2-22, and are listed in Table 8.2-10.

8.2.4.5 Discussion of Results

The cases were run to steady conditions, as shown in Figure 8.2-143. The resulting temperature comparisons are shown in Figure 8.2-144. [

]

In summary, the FLECHT-SEASET steam cooling tests 32753, 36160, 36261, 36362, 36463, 36564, 36766, and 36867 were simulated by S-RELAP5 [

]

Table 8.2-10 Input Parameters for Steam Cooling Tests

Run Number	Steam Temperature °F	Inlet Mass Flow lb/s	System Pressure psia	Average Power kW
32753	269	0.800	40	0.05826
36160	292	0.810	39	0.05289
36261	287	0.655	39	0.04291
36362	280	0.400	39	0.02643
36463	273	0.243	40	0.01589
36564	271	0.188	40	0.01258
36766	267	0.120	40	0.00803
36867	267	0.117	39	0.00670

Figure 8.2-143 FLECHT-SEASET Steady State Temperatures

[ ]

Figure 8.2-144 Comparison of S-RELAP5 with FLECHT-SEASET Steam Cooling Tests

8.2.5 Assessment of Heat Transfer in FLECHT-SEASET Test 31504

8.2.5.1 Introduction

The post-CHF heat transfer model [

] The discussion of those results is given in Section 8.4.1.3.

Presented here is a description of the input deck, [

] from FLECHT-SEASET Test 31504 (Reference 8.2-25).

8.2.5.2 Summary and Conclusions

The FLECHT-SEASET input decks were modified to include rod to rod radiation by adding a radiation enclosure model to the existing 161-rod bundle. The cases were executed and a post-CHF heat transfer probability distribution was generated. [

] This indicates that when the S-RELAP5 post-CHF heat transfer model is applied to LBLOCA plant analysis, the total amount of heat transfer is appropriate.

8.2.5.3 S-RELAP5 Model Description

The application of the heat transfer uncertainties [

]

[ ] were added to the otherwise unchanged (except for numbering) S-RELAP5 input model discussed in Section 8.2.3.5. A new [ ] that differs from [ ] A new [ ] that differs from the original [ ] This amount was determined by comparison with results presented in Reference 8.2-26. For this analysis, [ ] The [ ] was applied [ ] The [ ] This arrangement is meant to achieve best estimate response and is also similar in application to the plant model. Finally, control variables were added to compute the desired heat transfer quantities [ ]

For this analysis, [

] given in Section 8.4.1.3.

8.2.5.4 Discussion of Results

The amount of [

]

Test 31504, documented in NUREG/CR-2256 (Reference 8.2-26). In that analysis, the rod temperature distribution, steam temperature, component temperatures and liquid droplet concentrations from measured data were used to compute the total effective heat transfer from reverse conduction and the total effective radiation heat flux. From that analysis, the researchers presented the ratio of convective heat transfer to total heat transfer at 20 s intervals from 80 to 200 s.

The [

]

Consequently, the ratio of convective heat transfer to total heat transfer at 100 s (time of PCT) was determined to be the figure of merit for comparison. From preliminary sensitivity studies, [

] The results from Test 31504 are shown in Figure 8.2-145. The data were estimated from Figure 6-12 in Reference 8.2-26.

The total heat transfer coefficient is presented in Figure 8.2-146 and the total convection heat transfer coefficient is presented in Figure 8.2-147. Also in Figure 8.2-146 are the measured heat transfer coefficients estimated from Figures H-6 on page H-5 from Reference 8.2-26. The measurements are from three separate rods while the estimates are from the estimated maximum and minimum heat transfer coefficients from 50 to 200 s. [

]

[

]

Figure 8.2-145 Ratio of Convective to Total Heat Transfer, Calculated and Measured

Figure 8.2-146 Total Heat Transfer Coefficient, Calculated and Measured

Figure 8.2-147 Convective Heat Transfer Coefficient

8.2.6 PDTF SMART

8.2.6.1 Introduction

The Product Development Test Facility (PDTF) Small Array Reflood Test (SMART) tests (References 8.2-27 and 8.2-28,) were performed by AREVA to show that the HTP spacer was thermodynamically equivalent to a mixing-vane-type spacer with respect to reflood and PCT. The purpose of the facility was primarily to demonstrate equivalence between differing fuel designs and not to demonstrate the performance of either. That being said, a reasonable benchmark of the reflood test results does offer insight as to the range of capability of the S-RELAP5 code in simulating reflood behavior.

8.2.6.2 Facility and Test Description

The PDTF SMART tests were similar to the FLECHT-SEASET tests, but performed in an AREVA facility. The test assemblies were 6x6, full-height, simulated PWR assemblies. The rod diameter and pitch were characteristic of AREVA's 15x15 PWR fuel design. The test assembly had a uniform radial power distribution and a chopped cosine axial power distribution. Details of the assembly cross-section and the rod cross-section are provided in Figure 8.2-153 and Figure 8.2-154, respectively. The tests simulated five different flooding conditions. Of the five flooding rate conditions, four were constant-flooding-rate tests and one was a variable-flooding-rate test. The constant-flooding-rate tests had flooding rates of 0.6, 1.0, 2.0, and 4.0 inch/s. The variable-flooding-rate tests started at 8.0 in/s and ramped rapidly to a constant 1.0 inch/s flooding rate. The 0.6 inch/s tests were terminated prematurely; therefore, they were eliminated for the verification and validation of S-RELAP5. The tests selected for the simulation are listed in Table 8.2-1.

8.2.6.3 S-RELAP5 Model Description

Detailed S-RELAP5 input models for these analyses were constructed [ ] by following the RLBLOCA input guidelines (see Appendix A). The general model nodalization is shown in Figure 8.2-155 and the assembly nodalization is shown in Figure 8.2-156. The models include heat structures for [ ] Thermal-hydraulically, the lower plenum is modeled as a time-dependent volume that feeds a time-dependent junction to the vessel inlet. The vessel is modeled [ ] The outlet to the atmosphere is modeled as a time-dependent volume. [

]

Two S-RELAP5 models were developed; one with HTP spacer grids and one with mixing-vane type spacers. Since the test bundle is small, [

]

8.2.6.4 Calculated Results

Figure 8.2-148 shows the PCT for each of the benchmarks. Figure 8.2-149 through Figure 8.2-152 show the maximum cladding temperature as a function of elevation and independent of time for all four benchmarks and the two test sets. [

]

In summary, from the simulation of the PDTF SMART reflood tests, it can be concluded that the S-RELAP5 code can adequately predict the core thermal-hydraulic behavior during the reflood phase of a LBLOCA.

Figure 8.2-148 shows the PCT for each of the four benchmarks and for the tests with the HTP and the mixing vane (FOCUS) spacers. As can be seen, the predicted PCTs are in good agreement with the test data. Figure 8.2-149 through Figure 8.2-152 show the maximum cladding temperature as a function of elevation and independent of time for the benchmarks and the two test sets. [

]

Table 8.2-11 PDTF SMART Tests Chosen for S-RELAP5 Verification and Validation

Test Designator	Test Description
KH01A	HTP spacer test with constant flooding rate of 4 inch/s
KH01B	HTP spacer test with constant flooding rate of 4 inch/s (repeat experiment of KH01A)
KH02A	HTP spacer test with constant flooding rate of 2 inch/s
KH02B	HTP spacer test with constant flooding rate of 2 inch/s (repeat experiment of KH02A)
KH03A	HTP spacer test with constant flooding rate of 1 inch/s
KH03B	HTP spacer test with constant flooding rate of 1 inch/s (repeat experiment of KH03A)
KH05A	HTP spacer test with variable flooding rate from 8 to 1 inch/s
KV01A	FOCUS spacer test with constant flooding rate of 4 inch/s
KV02A	FOCUS spacer test with constant flooding rate of 2 inch/s
KV02B	FOCUS spacer test with constant flooding rate of 2 inch/s (repeat experiment of KV02A)
KV03A	FOCUS spacer test with constant flooding rate of 1 inch/s
KV03B	FOCUS spacer test with constant flooding rate of 1 inch/s (repeat experiment of KV03A)
KV05A	FOCUS spacer test with variable flooding rate from 8 to 1 inch/s
KV05B	FOCUS spacer test with variable flooding rate from 8 to 1 inch/s (repeat experiment of KV05A)

Figure 8.2-148 Comparison of Predicted PCT and Measured Data

Figure 8.2-149 MCT vs. Elevation for 4 inch/s Flooding Rate Test

Figure 8.2-150 MCT vs. Elevation for 2 inch/s Flooding Rate Test

Figure 8.2-151 MCT vs. Elevation for 1 inch/s Flooding Rate Test

Figure 8.2-152 MCT vs. Elevation for Variable 8-1 inch/s Flooding Rate Test

Figure 8.2-153 Assembly Cross Section

Figure 8.2-154 Rod Cross Section

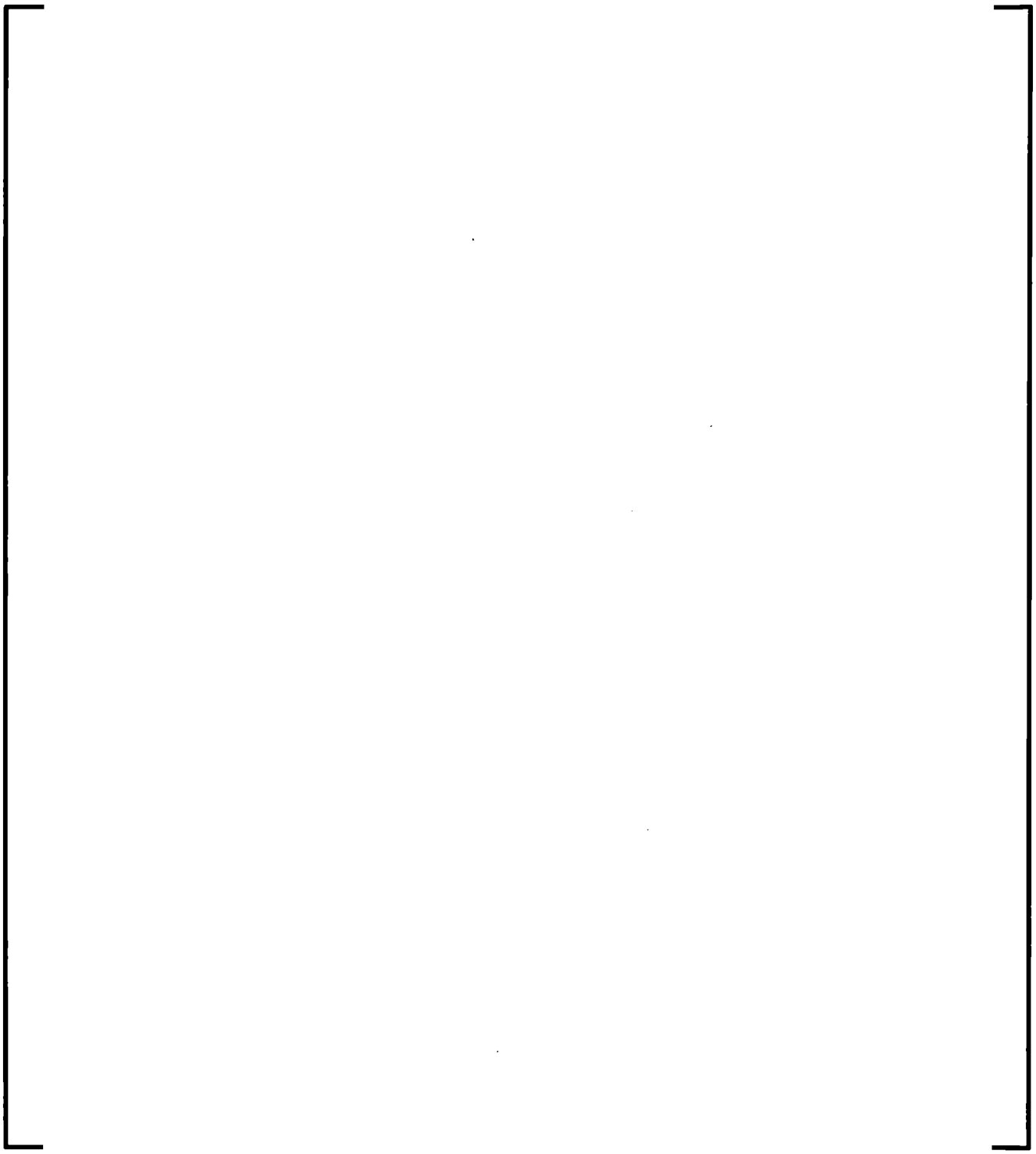

Figure 8.2-155 General Model Nodalization

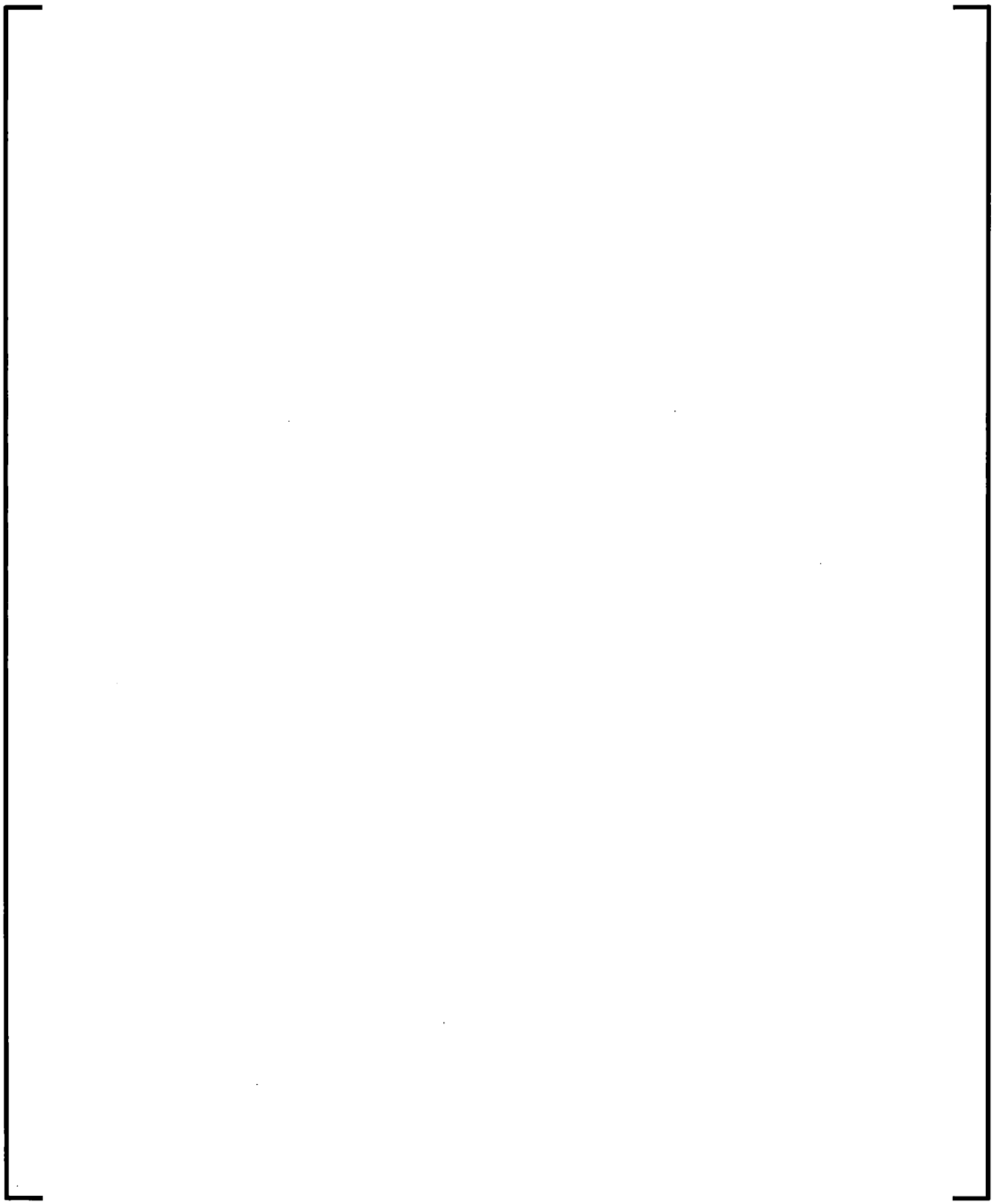

Figure 8.2-156 Assembly Nodalization

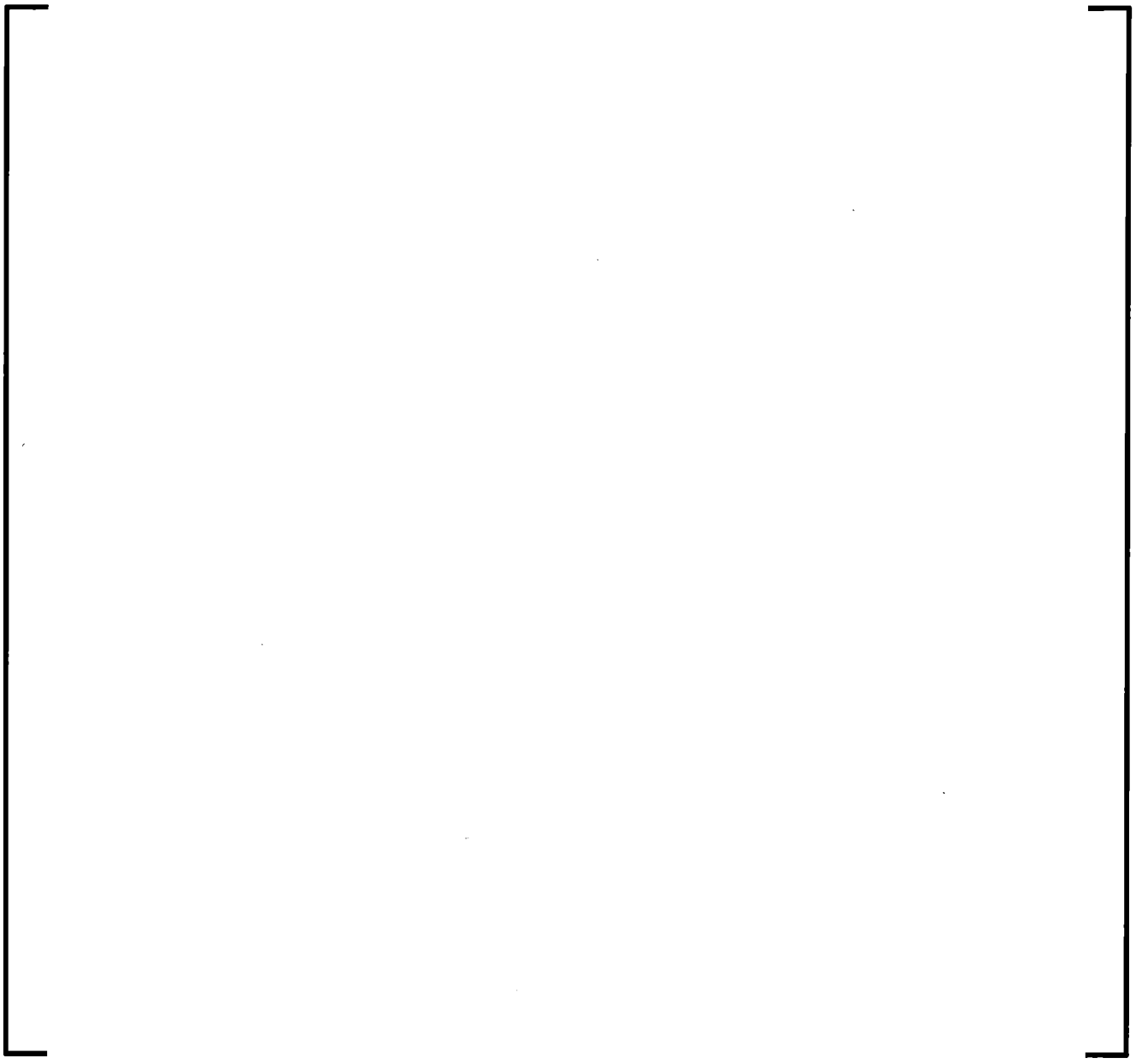

8.2.7 Marviken Full-Scale Critical Flow Tests

8.2.7.1 Introduction

The assessment of the Marviken Full-Scale Critical Flow Tests (Reference 8.2-29) was performed to assess the capability of the S-RELAP5 code to predict large-scale critical flow phenomena and to determine the uncertainty associated [

] The Marviken Full-Scale Critical Flow Test data are used in Code Scaling, Applicability, and Uncertainty methodology (Reference 8.2-20) to determine the critical flow multipliers and uncertainties for TRAC-PF1/MOD1 break flow model (Reference 8.2-30). The test data also are widely used in assessing critical flow models of various system codes.

During critical flow, the fluid velocity at the break location, or other restrictions can exceed the local sound speed which causes the fluid flow rate to become insensitive to downstream pressure changes. Of particular importance are choking conditions at pipe break locations where fluid at high pressure-temperature conditions is subject to large decreases in pressure. [

]

[

]

Only [ ]

using the Marviken test benchmarks. [

] The code assessment selected nine tests (2, 6, 8, 16, 17, 20, 22, 24 and 25).

[

] It should be noted that the data provided by the nine Marviken tests selected cover the region between 0 and 30% void fraction.

8.2.7.2 Summary and Conclusions

The calculated critical flow mass fluxes and the measured values [

]

The overall critical flow [

] Thus, the critical flow model [ ]

The application will use a mean value of 0.0083 and a standard deviation of 0.0798 for the subcooled to a two-phase void fraction below 30 percent. The bias factor to be used is 1 - 0.0083 = 0.9917.

Reference 8.2-31, Section 6.1.2, states that the maximum extended mass flux error in two fluid code simulations of Marviken is on the order of ±20%; while the Marviken data report (Reference 8.2-29) gives a mass flux error of ±15%. Thus, [

] indicating excellent agreement.

8.2.7.3 Facility and Test Descriptions

The Marviken Full-Scale Critical Flow Tests have been conducted as a multi-national project at the Marviken Power Station in Sweden 8.2-29. The test facility (Figure 8.2-157) consists of four major components: a full-scale BWR vessel, a discharge pipe attached to the bottom of the vessel, a test nozzle connected to the downstream end of the discharge pipe, and a rupture disk assembly attached to the downstream end of the nozzle. A detailed description is found in Reference 8.2-29 of the test facility, procedures and results. The Marviken test data has been widely used in assessing critical flow models of various system codes.

The pressure vessel originally was a part of the Marviken nuclear power plant. Of the original vessel internals, only the peripheral part of the core superstructure, the cylindrical wall, and the bottom of the moderator tank remain. Gratings are installed at three levels in the lower part of the vessel to prevent the formation of vortices that might enter the discharge pipe. The vessel has an inside diameter of 5.22 m and is 24.55 m high as measured from the vessel bottom to the top of the top cupola. The net available internal volume is 420 m^3.

The discharge pipe consists of seven elements: an axisymmetric inlet section, a connection piece, two pipe stools, two instrumentation rings, and an isolation ball valve. The internal diameters of the connection piece, pipe stools, and instrumentation rings are all 752 mm. The flow path through the ball valve contains a fairly abrupt diameter change of 30 mm. The axial distance from the discharge pipe entrance to the end of the discharge pipe (nozzle entrance) is 6.3 m.

The test nozzle connects to the lower end of the discharge pipe. The nozzle consists of a rounded entrance section followed by a test section of different inside diameters and various length-to-diameter (L/D) ratios for different tests (Figure 8.2-158). Nozzles of four different diameters are used in the tests: 200 mm, 300 mm, 500 mm, and 509 mm. The range of the L/D ratio varies from 0.3 to 3.7 for different tests.

The rupture disc assembly attaches to the downstream end of the test nozzle. The assembly contains two identical rupture discs. The test was initiated by overpressurizing the volume between the discs. This over-pressurization caused the outer disc to fail, which subsequently resulted in the failure of the inner disc. Failure of the discs was designed to occur along the entire periphery so that they were completely removed from the nozzle exit.

Water initially filled up the system, and then drained to a specific level in the vessel. A warm-up process was applied to produce a temperature profile in the vessel. A sketch of a typical vessel temperature profile is shown in Figure 8.2-159. The steam dome was at 5 MPa saturated conditions. The water level was between 16.5 m and 20 m in the vessel. The liquid region consisted of a saturation zone, a transition zone, and a zone of relatively constant subcooling. The initial subcooling in the lower vessel relative to steam dome temperature was varied for different tests. The measurement recording system was started approximately 180 seconds before the test began. The test was terminated when the ball valve began to close or when steam entered the discharge pipe.

Nine tests are selected for this assessment, Tests 2, 6, 8, 16, 17, 20, 22, 24, and 25. The nozzle diameters and length-to-diameter ratios (L/D) for the nine tests are listed in Table 8.2-12.

8.2.7.4 S-RELAP5 Model Description

Figure 8.2-160 illustrates the S-RELAP5 nodalization for the assessment of the Marviken Full-Scale Critical Flow Tests. The vessel is represented [

]

[

]

The [ ]

while the [

] A subcooled discharge coefficient of [

] is used to get the appropriate depressurization effect at the nozzle. The [

] is used for computing the critical mass flow rate at the break.

The break junction flows into the time-dependent volume component, which is set at 1 atmosphere pressure. The initial conditions for the tests are derived from the electronic data files. A [ ] steady-state run (without the break) is carried out to balance the pressure in the vessel and the pipe. The break is initiated at the beginning of the transient restart run. The transient calculation is terminated in accordance with the data range of each particular test.

8.2.7.5 Calculated Results

Figure 8.2-161 through Figure 8.2-169 show the code-to-data comparisons of the fluid (liquid) temperatures in the nozzle entrance region. The good agreement for all tests indirectly indicates that the initial temperature profiles in the system are appropriately set up.

Figure 8.2-170 through Figure 8.2-178 show the code-to-data comparisons of mass flow rates at the break. The calculations agree very well with the data. [

]

For the critical flow uncertainty computation, the calculations and data [

] Figure 8.2-179 shows the calculated mass flux versus data. The data [ ] and they show very good agreement between the code calculated values and the measured data.

[

]

The results are summarized in Table 8.2-13 and a graphical illustration of the break flow uncertainty is presented in Figure 8.2-180.

8.2.7.6 Discussion of Results

The [ ] is used to calculate the critical flow in the two-phase region for the Marviken Full-Scale Critical Flow Tests. To be consistent with this assessment, [ ] used in all RLBLOCA analyses. This requirement is implemented in the Input Development Guidelines (Appendix A).

The calculated critical flow mass fluxes depend on the conditions upstream of the break. In turn, the upstream conditions are influenced by many code sub-models. If the upstream conditions are not accurately calculated, the effects of these other sub-models propagate into the uncertainty of the critical flow model.

Two factors can strongly affect the break upstream conditions. The first, [

] This may shorten the subcooled choking period considerably and make calculated results and data out of sync. (Note that the test was terminated when the steam entered the discharge pipe.) [

] as shown by the comparison of calculated and measured liquid temperatures at the nozzle entrance (Figure 8.2-161 through Figure 8.2-169). Secondly, [

] This is particularly important for the tests with short nozzles. [

] This break nodalization scheme works well for all nozzle sizes.

The critical flow model is not scale dependent. The model is successfully applied for small- or large-scale facilities as shown in the assessments for Semiscale (Section 8.3.2), LOFT (Section 8.3.1), and Marviken (current section).

Table 8.2-12 Test Nozzle Dimensions

Test Number	Diameter (D, mm)	L/D
2	300	3.0
6	300	1.0
8	509	3.1
16	500	3.6
17	300	3.7
20	500	1.5
22	500	1.5
24	500	0.3
25	300	1.7

Table 8.2-13 Summary of Results

[
]

Figure 8.2-157 Marviken Test Facility Diagram

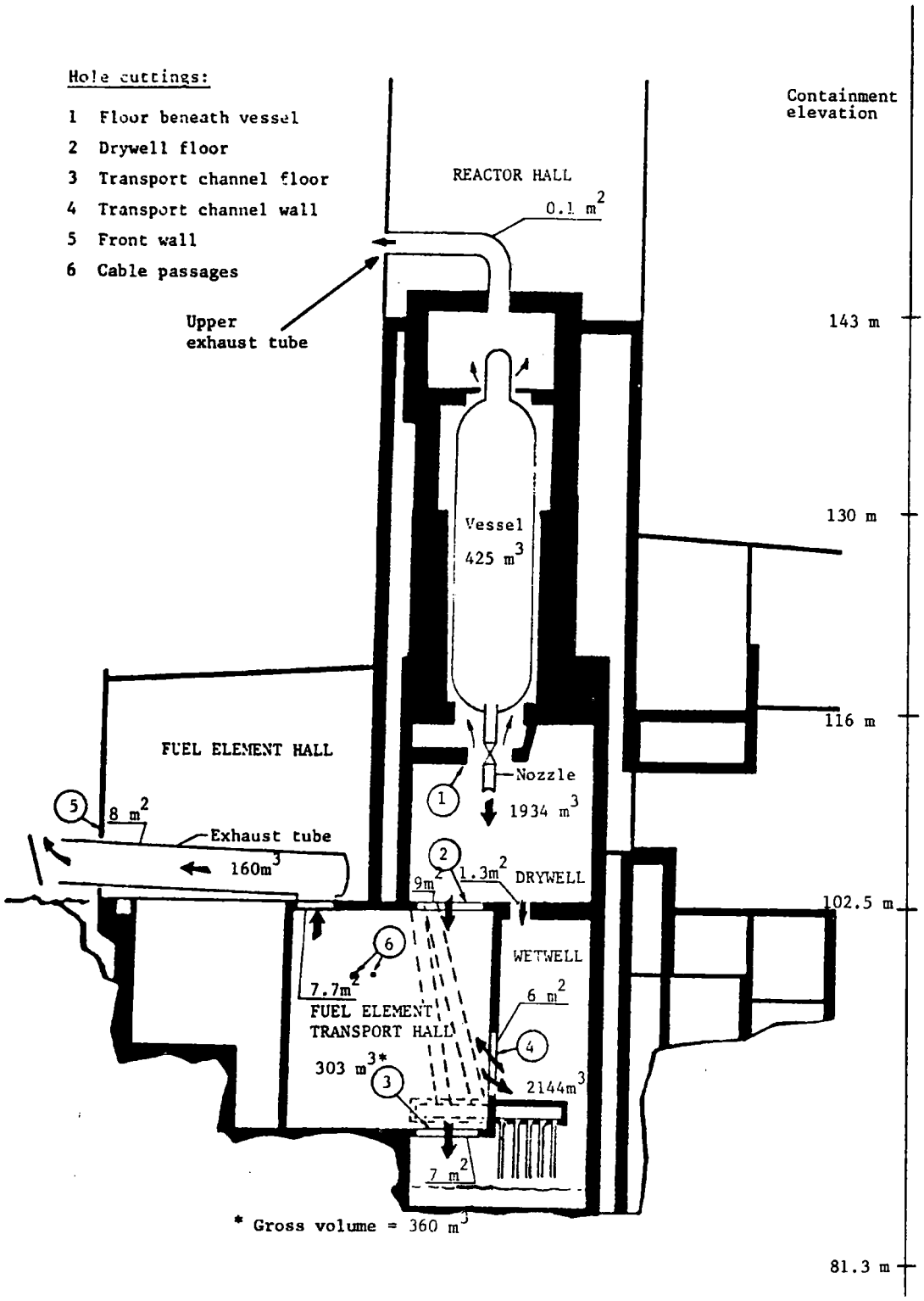

Figure 8.2-158 Marviken Test Nozzle

Note: All dimensions are in millimeters
at room temperature.

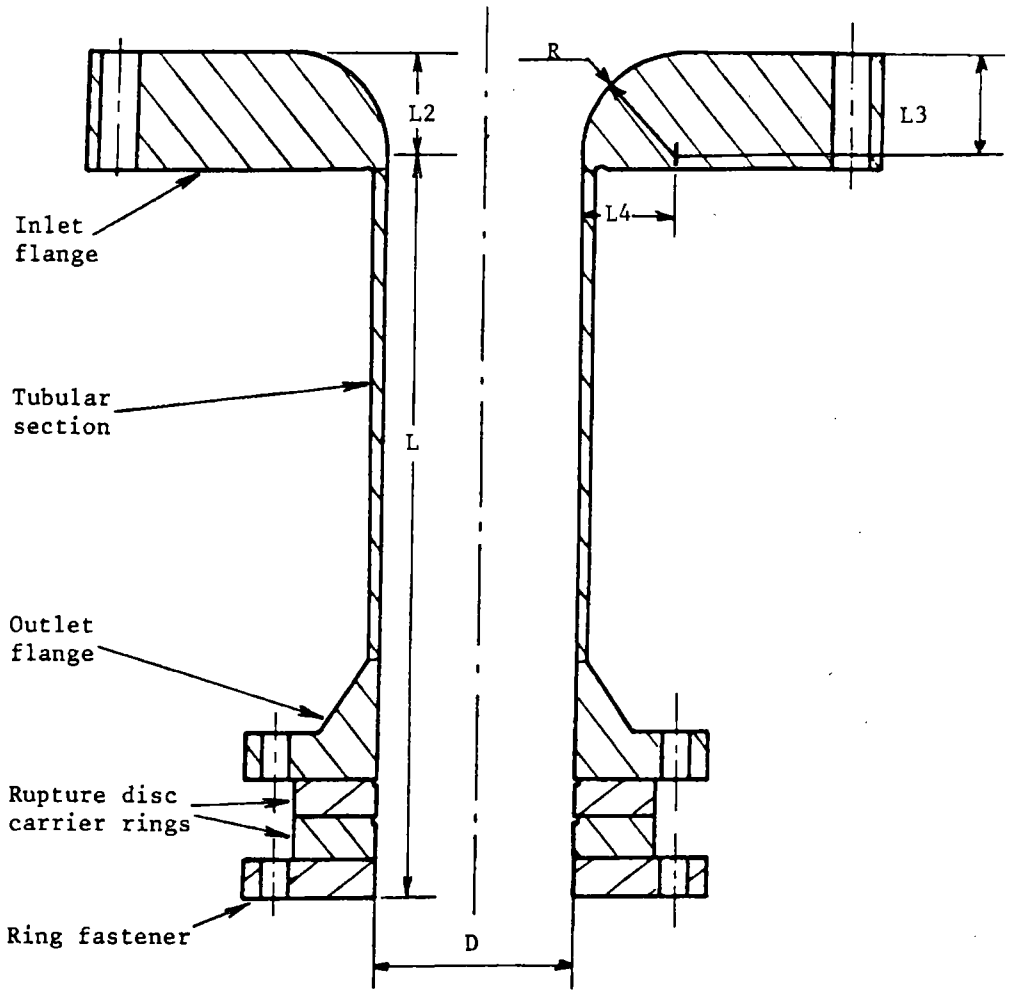

Figure 8.2-159 Typical Temperature Profile

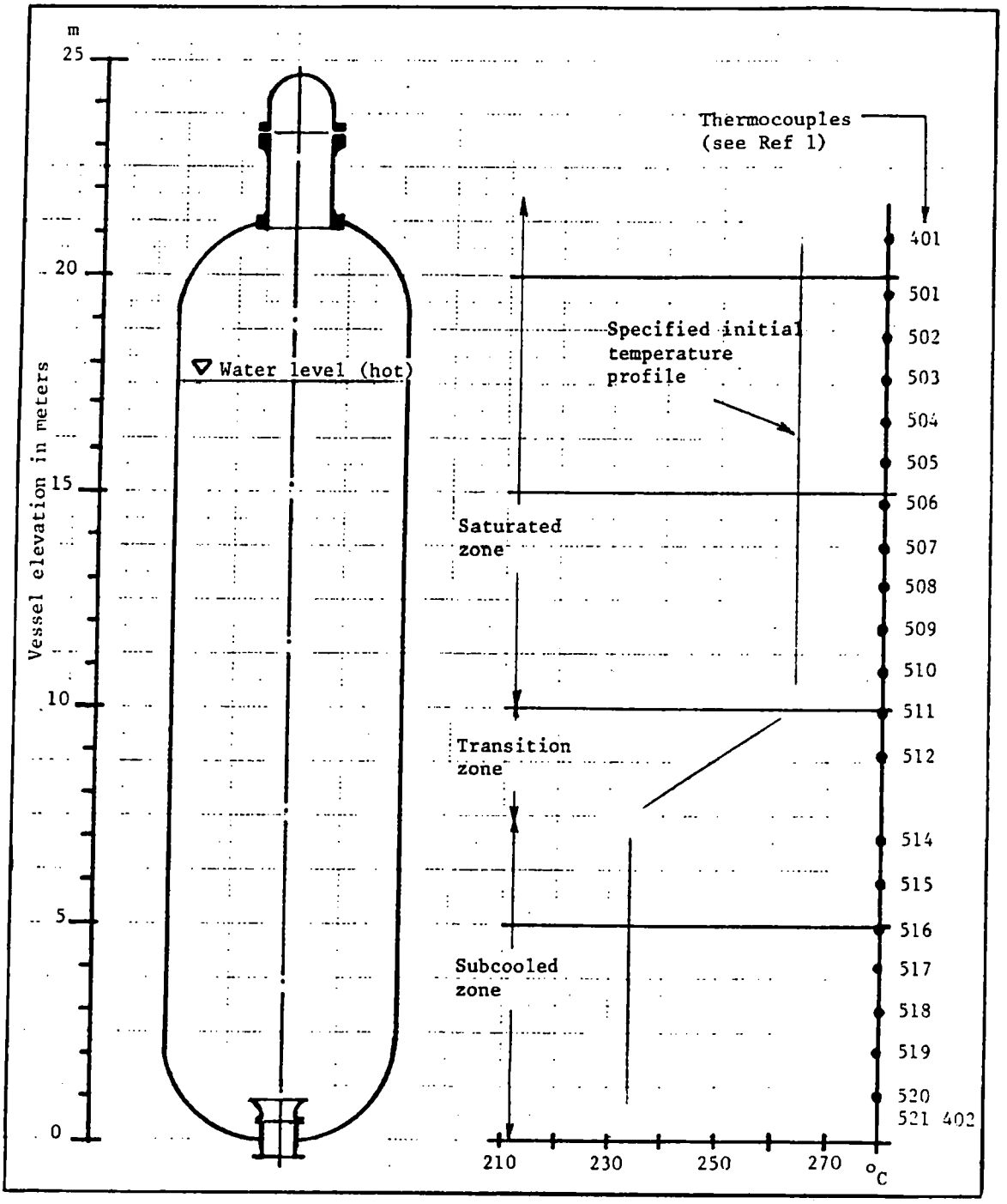

Figure 8.2-160 Nodalization for Marviken Tests

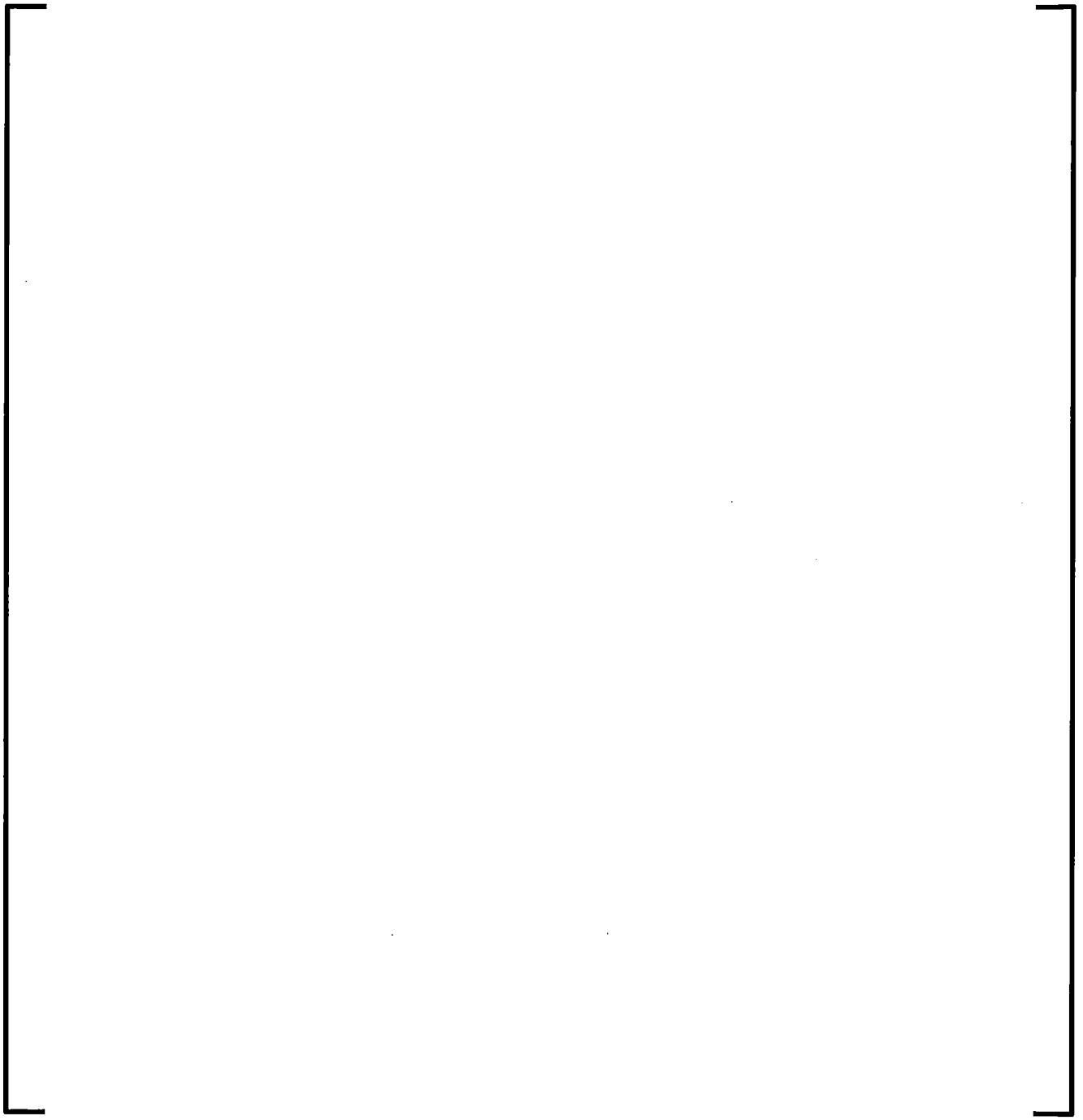

Figure 8.2-161 Fluid Temperature Comparison at the Nozzle Entrance, Marviken Test 2

Figure 8.2-162 Fluid Temperature Comparison at the Nozzle Entrance, Marviken Test 6

Figure 8.2-163 Fluid Temperature Comparison at the Nozzle Entrance, Marviken Test 8

Figure 8.2-164 Fluid Temperature Comparison at the Nozzle Entrance, Marviken Test 16

Figure 8.2-165 Fluid Temperature Comparison at the Nozzle Entrance, Marviken Test 17

Figure 8.2-166 Fluid Temperature Comparison at the Nozzle Entrance, Marviken Test 20

Figure 8.2-167 Fluid Temperature Comparison at the Nozzle Entrance, Marviken Test 22

Figure 8.2-168 Fluid Temperature Comparison at the Nozzle Entrance, Marviken Test 24

Figure 8.2-169 Fluid Temperature Comparison at the Nozzle Entrance, Marviken Test 25

Figure 8.2-170 Break Mass Flow Comparison at the Nozzle Entrance, Marviken Test 2

Figure 8.2-171 Break Mass Flow Comparison at the Nozzle Entrance, Marviken Test 6

Figure 8.2-172 Break Mass Flow Comparison at the Nozzle Entrance, Marviken Test 8

Figure 8.2-173 Break Mass Flow Comparison at the Nozzle Entrance, Marviken Test 16

Figure 8.2-174 Break Mass Flow Comparison at the Nozzle Entrance, Marviken Test 17

Figure 8.2-175 Break Mass Flow Comparison at the Nozzle Entrance, Marviken Test 20

Figure 8.2-176 Break Mass Flow Comparison at the Nozzle Entrance, Marviken Test 22

Figure 8.2-177 Break Mass Flow Comparison at the Nozzle Entrance, Marviken Test 24

Figure 8.2-178 Break Mass Flow Comparison at the Nozzle Entrance, Marviken Test 25

Figure 8.2-179 Comparison of Calculated and Measured Mass Fluxes (All Nine Marviken Tests)

Figure 8.2-180 Break Flow Uncertainty, Marviken Tests

8.2.8 GE Level Swell Test 1004-3

8.2.8.1 Introduction

The GE Level Swell Test 1004-3 is essentially a small-break blowdown of a vertical vessel 14 ft high and 1 ft in diameter. The vessel was initially pressurized to 1011 psi and filled with saturated water up to the 10.4 ft elevation. The void fraction distribution was measured axially in the test. This assessment provides a test of the two-fluid interphase models in predicting the flow regimes and void fraction distributions that occur under depressurization conditions. The purpose is to assess the capabilities of S-RELAP5 to predict void fraction distribution behavior primarily for SBLOCA. The GE Level Swell Test facility is not typical of nuclear power plant geometry, so modeling did not follow the RLBLOCA guidelines. However, reasonable node sizes were chosen such that S-RELAP5 was able to predict the void fraction distribution appropriately.

8.2.8.2 Summary and Conclusions

Measured versus calculated void fraction distributions are compared at two transient times, 40 and 100 seconds, using results from S-RELAP5. The calculated results are very similar and compare well with the data. The void fractions calculated by S-RELAP5 are within the range of experimental uncertainty, therefore signifying excellent agreement. The calculated [

] The results indicate that, for this slow transient condition, the two-fluid interphase friction model implemented in S-RELAP5 is applicable.

8.2.8.3 Facility and Test Description

The GE Small Vessel Level Swell Test Facility (Reference 8.2-32) consists of a 1-ft (0.3048 m)-diameter, 14-ft (4.2672 m)-long, vertically oriented cylindrical pressure vessel, a blowdown line containing an orifice, and a suppression pool at atmospheric conditions. Figure 8.2-181 is a schematic of the main test components. The vessel is initially pressurized at 1011 psi and filled with saturated water up to 10.4 ft (3.1699 m) elevation. The break orifice (3/8 inch. (0.009525 m) ID) is located within the 2-in (0.0508 m)- diameter Schedule 80 blowdown pipe at the top of the vessel. During the test, system pressure is measured by means of a pressure transducer at the top of the vessel and differential pressures are taken over 2-ft (0.6096 m) vertical intervals along the vessel. The differential pressure measurements are converted to mean void fraction data at each level by assuming hydrostatic conditions exist at all times.

8.2.8.4 S-RELAP5 Model Description

The vessel is modeled [

] The nodalization scheme is shown in Figure 8.2-182. This nodalization scheme is similar to that used [

]

[

] The initial pressure is 1011 psi. The trip valve (break) opens at time >0.07 s to start the blowdown.

8.2.8.5 Calculated Results

Figure 8.2-183 and Figure 8.2-184 are comparison plots of void fraction profiles at t=40 seconds and t=100 seconds. The calculated results compare well with the data. The void fractions calculated by S-RELAP5 are within the range of experimental uncertainty (excellent agreement).

The calculated [

] . The void distribution within mixture region is in very good agreement with the measured void fractions at both t=40 seconds and t=100 seconds indicating that, for this slow transient condition, the two-fluid interphase friction model implemented in S-RELAP5 is valid.

8.2.8.6 Discussion of Results

The key model affecting this assessment is the interphase friction for the bubbly and slug flows. The calculated void fractions by S-RELAP5 for these two flow regime regions are within the data uncertainty range. This confirms the applicability of interphase friction correlations described in Sections 7.6.2.1 and 7.6.2.2. The changes made to the interphase friction models for EMF-2103 Rev. 3 [

] was expected for this assessment. The results for this assessment indicate that the two-fluid model performs very well, and as expected, the change observed in the calculated assessment was insignificant.

The jump of void fraction from about 0.4 to about 0.99 within neighboring volumes distinctly defines the location of a two-phase mixture level. The interphase friction models for slug flow, vertical stratification, and annular-mist flow (see Sections 7.6.1.1.3, 7.6.2.2, 7.6.2.3, and 7.6.2.6) work harmoniously to produce a smooth, but sharp transition from a low-void-fraction region to a very-high-void-fraction region.

In a non-equilibrium code such as S-RELAP5, the phase exchange (vapor generation) process during a blowdown is calculated through the use of an interphase heat transfer model. The calculated liquid and vapor (steam) temperatures are close to the saturation temperature. This shows that the interphase heat transfer sub-models described in Section 7.6.4, particularly those for the meta-stable state conditions, are appropriate and adequate for treating the depressurization phenomena.

Figure 8.2-181 GE Small Blowdown Vessel

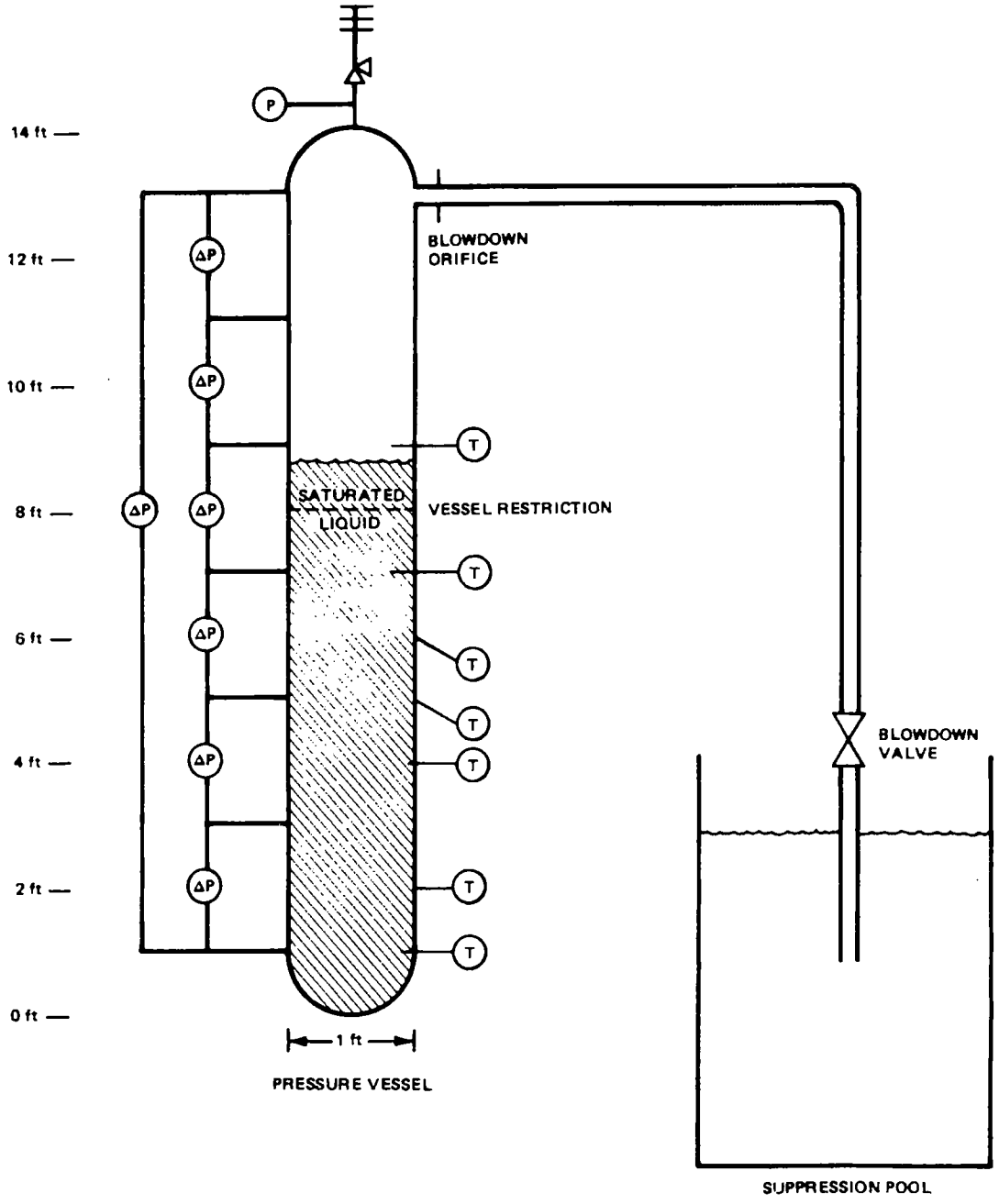

Figure 8.2-182 Nodalization for 1 ft GE Test 1004-3

Figure 8.2-183 Void Profiles at 40 Seconds for the 1 ft GE Test 1004-3

Figure 8.2-184 Void Profiles at 100 Seconds for the 1 ft GE Test 1004-3

8.2.9 Upper Plenum Test Facility

8.2.9.1 Introduction

UPTF was operated by Kraftwerk Union AG (KWU) where several separate and integral effects tests were conducted under the 2D/3D Program. UPTF was designed to simulate a German four-loop, 3900 MWt PWR primary system. It was intended to provide a full-scale simulation of thermal-hydraulic behavior in the primary system during the end-of-blowdown, refill, and reflood phases of a PWR LBLOCA. [

]

The reactor vessel, the core barrel, and the greater part of the vessel internals were a full-sized representation of a PWR, as were the four hot and cold legs that simulated three intact loops and one broken loop. The reactor core, steam generators, and coolant pumps were replaced bysimulators. Steam produced in a real core during refill/reflood, and the water entrained by this steam, were simulated by steam and water injection sources in the core simulator. Steam production on the primary side of an actual intact-loop steam generator was simulated by injecting steam into the steam generator simulator. The system was capable of simulating both cold and hot leg breaks, including ECC water injection into both intact and broken cold legs and hot legs and into the downcomer. Additional details of the test facility are given in Section 8.2.9.2. The specific tests assessed with S-RELAP5 include selected runs from the following test series: Tests 6, 7, 8, 10, 12, and 29. [

]

8.2.9.2 Facility Description

This section documents the assessment of S-RELAP5 using the Upper Plenum Test Facility (UPTF). The UPTF was operated by Kraftwerk Union AG (KWU) where several separate effects and integral tests were run in support of the 2D/3D Program. The UPTF was designed to simulate a German four loop 3,900 MWt pressurized water reactor (PWR) primary system, similar in size and geometry as a Westinghouse four-loop PWR. The facility was intended to provide a full-scale simulation of thermal-hydraulic behavior in the primary system during the end-of-blowdown, refill, and reflood phases of a PWR large break loss-of-coolant accident (LBLOCA). The tests simulated scenarios applicable to U.S. PWRs.

Tests 6, 7, 8, 10, 11 (not explicitly simulated), 12 and 29 were used for the assessment of S-RELAP5 in providing primary system behavior, such as cold leg condensation, limiting countercurrent flow at the upper tie plate and upper plenum regions, and countercurrent flow in the downcomer.

8.2.9.2.1 System Description

The reactor vessel, the core barrel, and the greater part of the reactor vessel internals are a full-sized representation of a PWR, as were the four hot and cold legs that simulated three intact loops and one broken loop. The reactor core, steam generators, and coolant pumps were represented by simulators. The thermal-hydraulic feedback of the reactor containment was also simulated.

Schematic diagrams of the UPTF facility are shown in Figure 8.2-185 through Figure 8.2-187.

System boundary conditions were preprogrammed, and then implemented through an automated process control system. Steam produced in a real core during refill/reflood and the water entrained by the steam was simulated by steam and water injection sources in the core simulator. Steam production on the primary side of an actual intact-loop steam generator was simulated by injecting steam into the steam generator simulator.

The facility was capable of simulating both cold- and hot-leg breaks, including ECC water injection into both intact and broken cold legs, the hot legs and the downcomer.

8.2.9.2.2 Main Components

Test Vessel

The dimensions of the test vessel (Component 1 in Figure 8.2-185) were identical with those of the reactor pressure vessel of the reference PWR plant (Grafenrheinfeld plant), similar to a Westinghouse four-loop PWR plant. An exception was that the vessel wall thickness was thinner than that in an actual PWR because of the lower operating pressure.

The vessel and loop geometry were full size. There were 193 fuel assemblies, with each assembly having a 16 x 16 array of fuel pin simulators. The dummy fuel assembly region was about 3 feet long, including the fuel pins, the upper tie plate (UTP), and the end box. The fuel pin simulators have no internal heat sources; therefore, the thermal effect of core power was simulated by injecting steam beneath the dummy fuel assemblies. Seventeen inlet pipes for steam and water injection penetrated through the lower plenum and lower core regions, and, along with associated structure, occupied much of the volume in those regions. The steam-water inlet pipes fed 193 steam-water mixers, each of which injected steam or a steam-water mixture into a separate fuel assembly.

The upper plenum internals (61 control rod guide tubes and 16 support columns) were identical to the reference PWR reactor (Grafenrheinfeld plant). The downcomer annulus, which was formed by the vessel wall and the core barrel, had a gap width that varied from 0.25 m (0.82 ft) in the lower part down to 0.21 m (0.69 ft) in the upper part.

Intact Loops

The loop geometry and cross section areas corresponded to the reference PWR plant (Grafenrheinfeld plant). The pump simulators (Component 4 in Figure 8.2-185) were designed to maintain proper hydraulic resistance and were capable of being blocked when test conditions required.

The steam generator simulators (Component 2 in Figure 8.2-185) were designed to duplicate evaporation and condensation on the primary side of an actual PWR steam generator. Each steam generator simulator contained 31 cyclone separators that separated and collected entrained water from steam-water flow entering the steam generators via the hot legs.

Broken Loop

The broken loop (Loop IV in Figure 8.2-185) simulator consisted of a steam generator simulator, a pump simulator, and associated piping. The steam generator included 44 cyclone separators. The hot leg and the cold leg connect to the containment simulator through independent lines (Components 5a and 5b in Figure 8.2-185). Each leg had its own break valve. The main portion of the broken cold leg connected the test vessel to the containment simulator through the fully open break valve and a water separator.

A secondary portion of the cold leg ended in the pump simulator and connected, via a Y-joint, to the main portion of the cold leg at a site between the downcomer and the break valve.

Containment Simulator

The containment simulator (Component 6 in Figure 8.2-185) was intended to reproduce the containment pressure boundary. It consisted of an upper dry well and a lower suppression chamber. The path from the broken leg to the containment simulator was complex, with an intervening cyclone separator (Component 3b in Figure 8.2-185) to remove water from the break flow.

ECC System

The ECC system was configured to allow water and nitrogen injection directly into the intact cold legs or hot legs (Components 8 and 9 in Figure 8.2-185). The rate of water and nitrogen injection could be controlled separately and could support a wide range of injection rates.

Test Instrumentation and Controls

Comprehensive test instrumentation was used in the UPTF. AREVA has used these data to define the system boundary conditions and to provide a basis for comparing these assessment calculations. The UPTF used a control system to establish boundary conditions that were representative of prototypic plant conditions.

Figure 8.2-185 Upper Plenum Test Facility, Primary System

1	Test Vessel	4	Pump Simulator	9	ECC-Injection Nozzles (Hot Leg)
2	Steam Generator Simulator (Intact Loop)	5a	Break Valve (Hot Leg)	10	Core Simulator Injection Nozzle
3a	Steam Generator Simulator (Broken Loop)	5b	Break Valve (Cold Leg)	11	Test Vessel Drainage Nozzle
3b	Water Separator (Broken Loop Hot Leg)	6	Containment Simulator	12	Steam Injection Nozzle
3c	Drainage Vessel for Hot Leg	7	Surgeline-Nozzle	13	Drainage Nozzle
3d	Drainage Vessel for Cold Leg	8	ECC-Injection Nozzles (Cold Leg)		

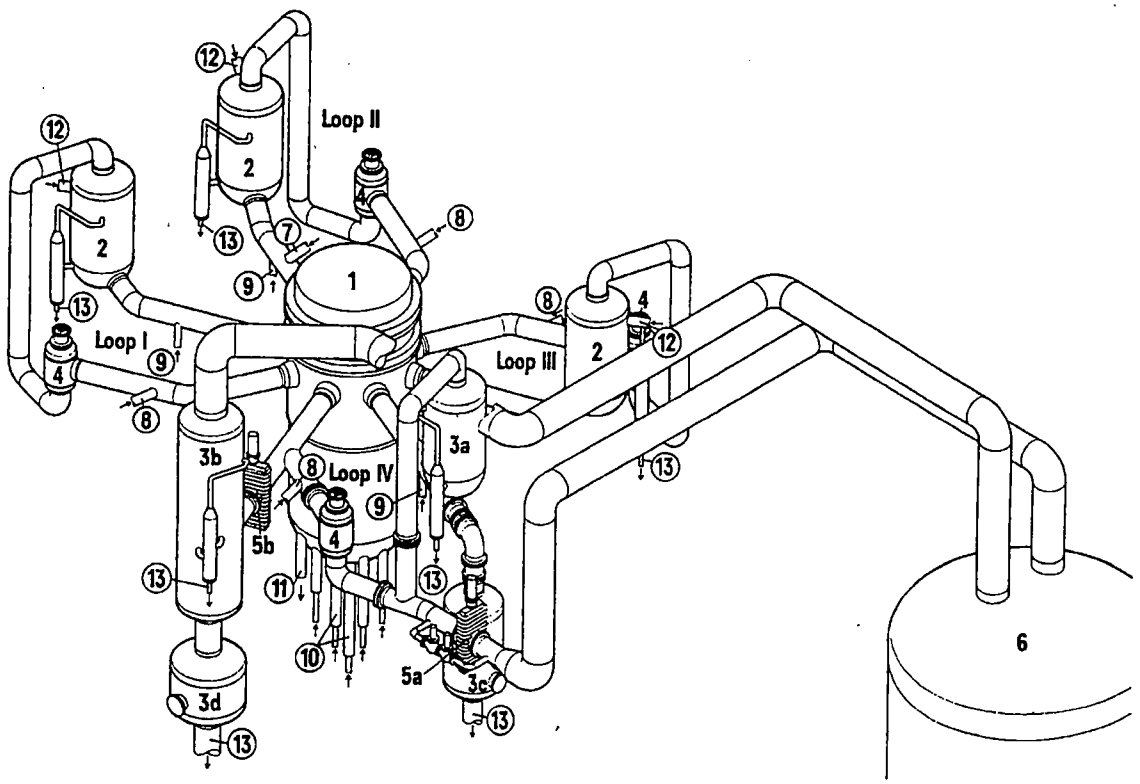

Figure 8.2-186 Upper Plenum Test Facility, Vessel Assembly

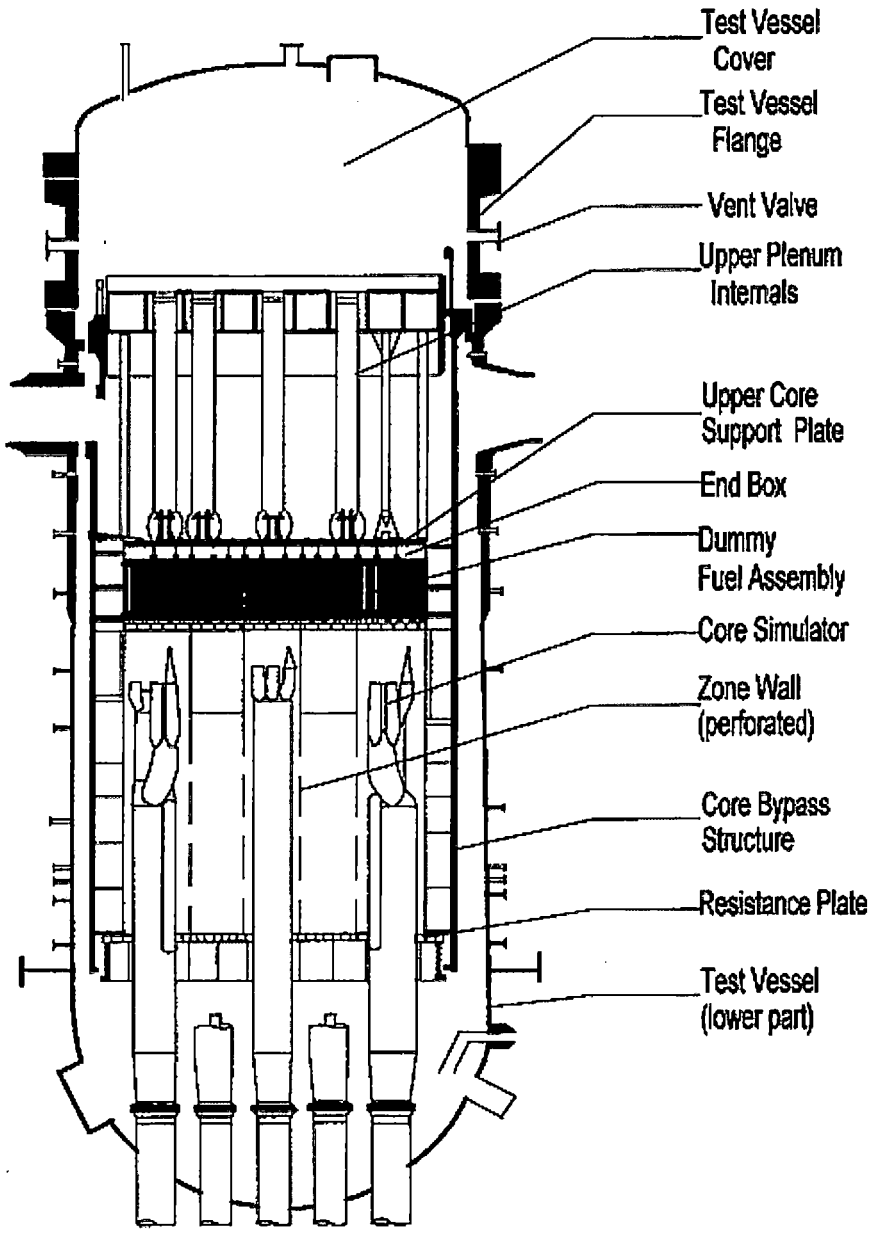

Figure 8.2-187 Upper Plenum Test Facility, Primary System Internals

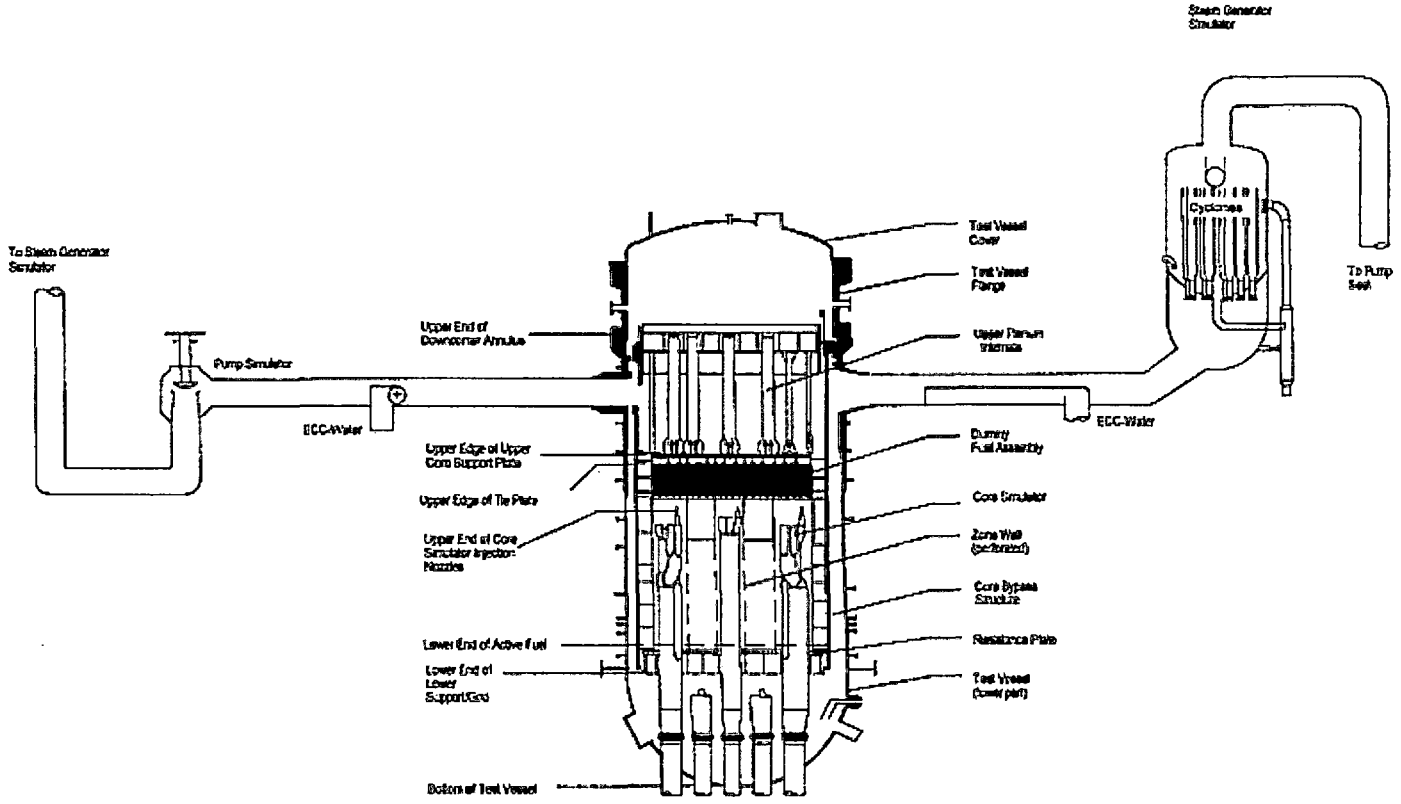

8.2.9.3 UPTF Tests 6 and 7

UPTF Tests 6 and 7 were designed to examine downcomer countercurrent flow behavior during refill, emergency core coolant (ECC) bypass and lower plenum refill following a large break LOCA in a PWR with cold-leg ECC injection. The interaction between the steam flowing out from the core and the water flowing in from the ECC injection plays a key role in determining the rate at which the ECC water is able to refill the lower plenum. The tests were analyzed to demonstrate the ability of S-RELAP5 to self-limit countercurrent flow in the downcomer and predict reasonable refill behavior, including ECC bypass, when compared to experimental data.

8.2.9.3.1 Summary and Conclusions

S-RELAP5 simulations of UPTF Tests 6 and 7 were performed to simulate the downcomer penetration and ECC bypass behaviors displayed by these tests. The results of these simulations indicate that S-RELAP5 conservatively underestimates the rate of lower plenum refill and conservatively overestimates the rate of ECC bypass, which will result in a conservative bottom of core recovery time during a PWR large break LOCA. These conservative estimates are provided [

] due to the ability of the code to self-limit counter-current flow.

8.2.9.3.2 Test Description (UPTF Tests 6 and 7)

UPTF Tests 6 and 7 were separate-effects tests (SET) that investigated the countercurrent flow of steam and ECC water in the downcomer during a postulated large break of a cold-leg pipe in a PWR. These investigations focused on steam-water flow phenomena in the intact cold legs, the downcomer, and the lower plenum during the refill phase of an LBLOCA. The objective of these tests was to obtain test data for a complete flooding curve in a full-scale down-comer. The area of investigation for these downcomer SETs encompassed the intact-loop cold legs and associated ECC injection system, the cold leg of the broken loop from the vessel to the containment, the downcomer, and the lower plenum. Simulating these UPTF tests demonstrates the ability of the S-RELAP5 code to self-limit countercurrent flow in the downcomer and to predict the refill behavior described by the experimental data, including ECC bypass.

Both Tests 6 and 7 were run as quasi-steady-state experiments; however, the procedure for conducting the two experiments differed. The runs for Test 6 were initiated with little or no water in the lower plenum at the beginning of the test and were continued until the lower plenum was nearly full of water. The change in the level of water in lower plenum was used to determine the amount of ECC penetrating to the lower plenum. The runs for Test 7 were initiated with the lower plenum partially filled with water. A lower plenum drain valve, operated by a level-controller, was used to limit the water level to a maximum value of 1.9 m (6.2 ft), which is 78% of the way to the top of the lower plenum at an elevation of 2.43 m (8.0 ft). The flow rate of water drained from the lower plenum was measured and could be used (along with changes in the lower plenum water level) to determine the amount of water entering the lower plenum from the downcomer. This procedure allowed the test period to be extended beyond what was possible with the procedure used for Test 6 and permitted each run to be set up as a series of separate phases, each with different flow conditions.

Another difference between the two tests was the nitrogen injection in the ECC flow. For all of the runs in Test 6, nitrogen was injected into each cold leg along with the ECC water to simulate dissolved nitrogen in the ECC water. No nitrogen was injected during Test 7.

Runs 131, 132, 133, 135, and 136 from Test 6 and Phase IV of Run 203 from Test 7 were selected to be simulated using S-RELAP5 for this analysis. Table 8.2-14 lists the main test parameters for these six runs. All of these runs used symmetric ECC injection with approximately 485 kg/s (1070 lb_m /s) of water injected into each intact cold leg. The total flow rate of steam injected into the core simulator and steam generator simulators varied between runs, from a maximum of 436 kg/s (961 lb_m /s) for Run 135 to a minimum of 51 kg/s (112 lb_m /s) for Run 203/Phase IV.

The drain flow from the lower plenum allowed Test 7 to be performed at a lower steam flow rate (and correspondingly higher ECC penetration rate) than was possible with the procedure used for Test 6.

During the runs with higher steam flow, the core steam injection had to be augmented with steam injection into the steam generator simulators to obtain the required total steam flow. During the runs with lower rates of steam flow (Run 136 and Run 203/Phase IV) the core steam injection alone was sufficient to provide the required flow.

The test features specific to Test 6 are summarized below:

- Symmetric ECC injection into each intact cold leg with nitrogen gas included
- ECC mass flow rate nearly constant at about 485 kg/s (1070 lbm /s) in each intact loop
- Total steam flow rates ranging from 102 kg/s (225 lb_m /s) to 436 kg/s (961 lb_m /s)
- ECC water subcooling varying from 26 °C (47 °F) to 59 °C (106 °F)
- Separate run for each test in the series
- Vessel structures initialized to steam temperature

- No lower plenum drain flow

The features specific to Run 203/Phase IV of Test 7 are the following:

- Symmetric ECC injection into each intact cold leg with no nitrogen gas
- ECC water mass flow rate nearly constant at 485 kg/s (1070 lbm /s) in each intact loop
- Low total steam flow rate of 51 kg/s (112 lb_m/s) with no steam injected into the steam generator simulators
- Low ECC water subcooling of 2 °C (4 °F)
- Run performed as a sequence of phases
- Vessel structures initialized to steam temperature
- Lower plenum drained during the test

For both Test 6 and 7, the UPTF had the following configuration:

- The hot leg break valve was closed
- The cold leg break valve was open during the entire test
- All pump simulators were closed
- All vent valves were closed
- The core simulator steam injection system was activated
- The core simulator water injection system was not activated
- The control valves of the ECC control system were preset

The following systems were used for only one of the tests:

- The steam generator simulator steam injection system - Test 6 only
- The nitrogen injection into the ECC water - Test 6 only
- The test vessel drainage system - Test 7 only

Both tests were conducted by initially warming the primary system with steam to the approximate temperature of the steam to be injected during the test to minimize steam condensation on the walls. The primary system was then filled with low-pressure steam. To begin each run, steam flow from the core and (if necessary) the steam generators was started, further pressurizing the primary system. This was followed shortly thereafter by ECC injection into the intact cold legs.

8.2.9.3.3 S-RELAP5 Model Description (UPTF Tests 6 and 7)

The S-RELAP5 input deck for UPTF Tests 6 and 7 was developed from the facility data in accordance with the S-RELAP5 RLBLOCA PWR modeling guidelines (Appendix A). Facility specifications and test conditions were obtained from reports (References 8.2-34, 8.2-35, 8.2-36, and 8.2-37) and supplied by the UPTF research team (Siemens AG, UB KWU). The development of this input model required several deviations from the RLBLOCA guidelines, which are described in detail in the following sections. In general,

[

] while the representations of the [

]

Hydraulic Nodalization - Tests 6 and 7

The nodalization of the S-RELAP5 model used to simulate Tests 6 and 7 is diagrammed in Figure 8.2-188. This model consists of [

] The following features of this system model, which are of special significance to the Test 6 and 7 analyses, will be discussed in more detail in the remainder of this section:

[

]

- Drainage of the lower plenum is included when required.
- Steam injection sources are connected to the core simulator and steam generator simulators.
- Downcomer-to-upper-head and downcomer-to-hot-leg leakage paths are included to simulate known leak paths in the test facility.
- The hot and cold legs are included as separate entities because the recirculation pump simulators are completely blocked.

[ ]

Two-Dimensional Downcomer

[

] Figure 8.2-189

displays a top-down view of the downcomer and an "unwrapped" view of the S-RELAP5 cylindrical shell model of the downcomer hydraulic volumes. The orientation of the downcomer is established by the location of the cold-leg and hot-leg connections identified on the third row of nodes. A nodal cell identifier is displayed in each cell.

[

]

For consistency with the RLBLOCA model, [

]

Lower Head

The lower head is modeled [

]

[

]

Lower Plenum Drain Flow

Time-dependent volume 810 and time-dependent junction 805 are used to simulate the drain flow during Test 7. Component 810 provides the outlet pressure boundary condition for the drain flow. The lower plenum drain junction (component 805) represents four outlet pipes that connect the lower plenum (component 014) to the water collecting tank and associated piping (time-dependent volume 810). In the simulation of Run 203 of Test 7, the liquid flow rate in component 805 is taken to be a boundary condition, with the flow determined from the drainage measured during the test. This drain flow is deactivated during Test 6 consistent with the conditions of the test.

Core Steam Injection

Time-dependent volume 660 and time-dependent junction 665 were included in the system model to permit the injection of steam into the core simulator. This injection is considered to be upward and is located [

] Volume 660 controls the thermodynamic condition of the steam injected into the core simulator, and junction 665 controls the steam mass flow rate into the core simulator. The temperature, quality, and mass-flow tables required for these components were obtained from experimental data.

Vessel Leak Paths

Two leak paths in the UPTF vessel allow steam to leak directly from the core region to the broken cold leg, thereby bypassing the normal downcomer flow path. The first path is through gaps where the hot legs join the core barrel wall. These gaps are 0.16 inch wide, and extend around the perimeter of each hot leg pipe. These gaps allow steam to leak directly from the upper plenum to the top of the downcomer and from there to the broken cold leg.

The second leak path is at the joint between the core assembly support flange and the ledge in the reactor vessel that supports the core assembly. This path permits steam to leak directly from the upper head to the top of the downcomer and, hence, to the broken cold leg.

These leak paths are modeled in the S-RELAP5 model of the UPTF [

]

KWU ran a series of tests to determine the leak rate through these leak paths as documented in Reference 8.2-38. In these tests, the lower part of the vessel was filled with water deep enough to block the normal flow path from the core to the downcomer. Steam was then injected into the core at a low flow rate and allowed to escape through the two leak paths. The total steam injection rate and pressures in the upper plenum and upper downcomer regions were measured and used to calculate loss coefficients for these two leak paths, which are used in the model.

Intact Loop Hot Leg

The three intact hot legs [

]

The intact steam generator simulators, crossover leg piping, and pump simulator inlets are not modeled in detail, because their only role in the system is to serve as a reservoir for steam injected into the steam generator simulators (in Test 6 only). Therefore, these components [

]

Steam injection to the steam generator simulators is modeled by component 670, a time-dependent volume that is connected to branch component 220 by a time-dependent junction (no. 675). The junction controls the rate of steam injection into the steam generator simulator, and the volume controls the thermodynamic condition of this steam. The temperature, quality, and mass-flow tables required for these components were obtained from experimental data.

Broken Loop Hot Leg

As with the hot leg of the intact loop, most of the components of the broken loop – the steam generator simulator, crossover piping, and pump simulator inlet – do not need to be modeled in detail, because their only role in the system is to serve as a reservoir for steam injected into the vessel system. Therefore, [

]

Intact Loop Cold Legs

Each of the three intact cold legs is modeled [

] ECC water and nitrogen gas are injected into these legs from a set of six time-dependent volumes and six time-dependent junctions, with one volume/junction pair used for the injection of each fluid (water or nitrogen) into each of the three legs. In each pair, the volume controls the thermodynamic condition of the injection fluid, and the junction connects the volume to the cold leg and controls the mass flow rate. Volumes 710, 720, and 730 and junctions 715, 725, and 735 deliver ECC water to the cold legs. Volumes 711, 721, and 731 and junctions 716, 726, and 736 deliver nitrogen gas. The pressure, temperature, quality, and mass-flow tables required for these components were obtained from experimental data.

Broken Loop Cold Leg

The broken loop cold leg (BCL) is modeled [

] which connect the downcomer to the water separator.

[

]

The main consideration in modeling this cold leg is to match the calculated downcomer pressure history to the measured downcomer pressure history. The actual thermal-hydraulic conditions between the downcomer and the containment do not play a significant part in these calculations except for the role that they have in determining the downcomer pressure.

[

] to establish the pressure boundary condition at the location of the water separator. The pressure table for component 750 was obtained from experimental data. The broken cold leg outlet boundary condition is discussed further in the sub-section Initial Conditions and Boundary Conditions.

Heat Structures

Heat structure models [

] These structures are important because they span the region where the primary steam/water (S/W) interaction occurs. The vessel structures that are modeled include [

]

Initial Conditions and Boundary Conditions

The initial conditions for the S-RELAP5 model of the UPTF consisted primarily of pressure and temperature data and were obtained from the Quick Look Reports for Tests 6 and 7 (References 8.2-34 and 8.2-36). All flows were initialized to zero, consistent with the stagnant conditions at the beginning of each test.

The following source and sink boundary conditions are required for Test 6 and 7:

- Source for the steam injection into the core simulator
- Source for the steam injection into the steam generator simulators
- Sources for the ECC water and nitrogen injection
- Sink for the broken-loop cold leg flow
- Sink for the lower plenum water drain

In the S-RELAP5 model of Tests 6 and 7, these sources and sinks are represented by time-dependent volume components and time-dependent junction components as described in sub-section Hydraulic Nodalization - Tests 6 and 7. The time-dependent tabular data required for these boundary condition components were obtained from KWU test data files and were verified by comparison with the data shown graphically in the KWU Experimental Data Reports for Tests 6 and 7 (References 8.2-35 and 8.2-37). The sensors that supplied the fluid conditions and flow rates for the boundary conditions are listed in and are described in Reference 8.2-39.

The boundary conditions at the BCL outlet, the core simulator steam injection source, and the lower plenum drain flow outlet are more complex than the other boundary conditions and are described below in greater detail.

Broken Loop Cold Leg Boundary Condition

The method used to simulate the BCL outlet boundary condition was developed to provide an accurate representation of pressure within the downcomer. The downcomer pressure determines the subcooling of the ECC water and the density of the steam flowing up the downcomer, which in turn affects the interfacial shear between the upflowing steam and the downflowing ECC water. Since this interfacial shear determines the flooding characteristics of the downcomer, verifying that the code correctly reproduce these characteristics is one of the primary objectives of the S-RELAP5 analyses of UPTF Tests 6 and 7.

Test data are available to establish a pressure boundary condition either at the lowest part of the water separator, from sensor JEA05CP001, or at a site between the water separator and the downcomer, from sensor JEC04CP21 (Reference [8.2-39]). [

]

Core Simulator Steam Injection

Component 660 serves as the source for steam injected into the core simulator. Test data obtained from system pressure and temperature sensors show the steam in the delivery lines to the core steam injection nozzles to be very nearly saturated, hence the thermodynamic state of the steam in component 660 was specified to be saturated steam with a specified temperature history.

Lower Plenum Drain Flow Boundary Condition

The lower plenum drain flow was activated only for simulation of Run 203 of Test 7, in which drain flow from the bottom of the lower plenum was used to maintain the lower plenum liquid level at an acceptable elevation. In the S-RELAP5 model, a time-dependent junction was used to simulate the pumped drain flow. The flow rates measured during the test was used to specify this boundary condition.

8.2.9.3.4 Simulations and Comparison with Experimental Results (UPTF Tests 6 and 7)

S-RELAP5 assessment calculations of UPTF Tests 6 and 7 were performed using the RBLOCA guideline recommended nodalization scheme (see Appendix A), except for the deviations noted in sub-section Hydraulic Nodalization - Tests 6 and 7. These calculations included simulations of Runs 131, 132, 133, 135 and 136 from Test 6 and Run 203 from Test 7.

As discussed in following sections, the following general observations were found to be true of both the experiments and their corresponding S-RELAP5 simulations.

- There was very little water delivery to the downcomer and lower plenum during the period in which the intact cold legs filled with ECC water. Only after the cold legs were completely filled to a quasi-steady-state level did a significant amount of ECC penetration to the downcomer and lower plenum begin.
- When ECC penetration to the lower plenum did occur, the rate of that penetration tended to vary inversely with the rate of steam flow in the downcomer.
- In the experiments, during the period of ECC penetration, water from cold legs 2 and 3 (opposite the broken cold leg) tended to penetrate directly downward to the lower plenum, while water from cold leg 1 (immediately adjacent to the broken cold leg) tended to bypass to the broken cold leg. The S-RELAP5 results do not clearly indicate the source of the water that is entrained to the broken cold leg.
- Highly unstable flow conditions were present in the downcomer during the entire period of ECC injection.

Test 6 - Chronology of Events

UPTF Test 6 consisted of a series of five quasi-steady-state separate effects runs that investigated the countercurrent flow of vapor and ECC water in the downcomer of a full-scale prototypic PWR. These runs were initiated with no water inventory in the lower plenum. Steam was injected through the core simulator and steam generator simulators (except during Run 136, which did not use steam injection into the steam generators). The steam injection rate was constant during each run, but differed between runs. The injection rate of ECC water was nearly identical for all runs, with a constant flow rate of approximately 485 kg/s (1070 lbm /s) injected into each of the three intact loops, resulting in a nearly symmetric source of water to the downcomer.

To demonstrate the overall predictive capabilities of the S-RELAP5 code, the chronology of key events in the Test 6 runs are described below, and the ability of S-RELAP5 to adequately simulate the test results during each phase of the test sequence are demonstrated. Figure 8.2-190 to Figure 8.2-229 graphically compare the S-RELAP5 results to the test results for key quantities in the five runs from Test 6. The runs are presented in order of decreasing steam flow rate (given in Table 8.2-14), starting with Run 135 with a steam flow rate of 436 kg/s (961 lbm /s) and ending with Run 136 with a steam flow rate of 102 kg/s (225 lbm /s).

Initiation of Steam Flow

The first figure for each run shows the steam injection to the core and steam generator simulators. In each run, steam injection begins approximately 30 seconds after the initiation of the test, spikes briefly, then subsides to nearly steady values. After 40 seconds of elapsed time in Runs 135, 131, and 132, the steam flow rate declines gradually for the next 30 to 50 seconds. It then drops quite rapidly as the test facility's steam supply system becomes depleted. Since Runs 133 and 136 use lower flow rates, the steam supply system has an adequate capacity to maintain a near-steady flow rate throughout the entire run. The measured steam flow (Reference 8.2-34) is used as a boundary condition for the S-RELAP5 analysis (as described in the sub-section Initial Conditions and Boundary Conditions).

The second figure in each set shows the pressure at the top of the downcomer. In all of these figures, the pressure rises abruptly from its steady initial value when the steam injection begins. Approximately 15 seconds later, the pressure increase becomes less stable as condensation increases when ECC water begins to enter the downcomer. The pressure continues to rise until steam flow begins to reduce, after which time the pressure decreases until the steam is exhausted. The comparisons shown in these figures demonstrate the adequacy of the selected broken-loop outlet boundary conditions (which are described in the sub-section Initial Conditions and Boundary Conditions).

These figures show a series of large oscillations in the downcomer pressure calculated by S-RELAP5. These oscillations, which are not evident in the test results, are a limitation of S-RELAP5. Referring to Figure 8.2-188, as the collapsed liquid level in the bottom node of the lower plenum approaches the boundary [

] the steam, rather than being diverted through [

] much as in a manometer, causing the pressure to drop. Preliminary undocumented analyses indicated that [

] Additionally, since a steam flow of this magnitude and duration seems unlikely during a plant analysis, the model limitation was accepted.

Initiation of ECC Injection

The third figure shows the rate of total ECC water injection (Reference 8.2-34). In each case, the ECC injection begins approximately 42 seconds into the run and quickly rises to a constant value of approximately 1460 kg/s (3220 lbm /s), which is divided equally among the three intact cold legs. Like the steam flow, this flow rate is also specified explicitly as a boundary condition in S-RELAP5.

The fourth figure shows the temperature of the liquid inside the broken cold leg (adjacent to the break), and the fifth figure shows the temperature of the liquid in the lower head. In both set of figures, the temperatures measured in the test differ significantly from the temperatures calculated by S-RELAP5 at the beginning of the test, because initially both regions contain only steam. Thus, the thermocouple in the test facility reports the steam temperature, whereas the liquid temperature provided by S-RELAP5 is the saturation temperature. This beginning period is not used in the assessment.

Both the measured and calculated temperatures begin to change as the steam injection begins. Finally, after the initiation of ECC injection, liquid flows into the two regions, first to the broken cold leg, then to the lower head, and the liquid temperature predicted by S-RELAP5 agrees relatively well with the temperatures measured in the test, indicating that the condensation rates in the cold legs and downcomer are being adequately calculated by S-RELAP5.

Filling of the Lower Plenum

The next two figures for each run are a comparison – showing both the S-RELAP5 results and the test data (Reference 8.2-34) – of the level of water and liquid mass inventory of the lower plenum. As noted above, the ECC injection starts at approximately 42 seconds. Both experimental data and code prediction show a delay of 10 to 13 seconds after the start of ECC injection before the lower plenum begins to rapidly refill. The delay is due to the ECC water filling the cold legs to a quasi-steady-state level, bypassing the downcomer, and flowing to the broken loop. The total flow of water and steam out of the break in the cold leg during the refill phase is shown in the final figure of each run, which compares the mass calculated by S-RELAP5 to the measured test data taken from Reference 8.2-40. In each case of Test 6, S-RELAP5 conservatively overestimates the mass that flows through the cold leg break.

Rapid ECC penetration to the lower plenum lasts for approximately 15 seconds, during which time the lower plenum mass inventory increases roughly linearly with time. The figures show that the S-RELAP5 calculation consistently underpredicts the high refill rate that was observed during the test. The rate at which the lower plenum fills during this period was used to determine the ECC penetration rate for each run, as discussed in the sub-section Test 6 - ECC Penetration Flow Rate.

The period of rapid filling ends as the gap between the water level in the lower plenum and the lower edge of the core barrel shrinks, leading to an increase in the outward steam velocity from the lower plenum to the downcomer and a corresponding increase in entrainment of liquid from the lower plenum to the downcomer, as discussed above under Initiation of ECC Injection. This sweep-out effect is overestimated by S-RELAP5 and is the source of the sudden increases and decreases in the calculated liquid levels.

Eventually, the calculated lower plenum inventory levels off at an equilibrium value when the rate at which water is swept out matches the rate at which ECC water flows into the lower downcomer from above.

Test 6 - ECC Penetration Flow Rate

As the lower plenum fills, the slope of the mass inventory curve (Figure 8.2-196, Figure 8.2-203, Figure 8.2-212, Figure 8.2-220, and Figure 8.2-228) provides a measure of the rate at which ECC water penetrates the downcomer to the lower plenum. To be useful, this slope must be evaluated during an appropriately chosen time interval, referred to here as the evaluation period, which determines the time span over which the region is filled at a roughly constant rate. A separate evaluation period is determined for each run using the following method, which is based on the method described in Reference 8.2-34:

- The evaluation period begins when the water level in the lower plenum exceeds 0.6 m (1.97 ft).

- The steam injection rate is required to remain steady until the end of the end of the period. This condition is taken here to mean that the rate of steam injection is required to remain above 90% of its nominal rate during the entire evaluation period. It is applicable only for Runs 131 and 135, when the steam injection steadily decreased during the test.
- The end of the evaluation period is conservatively chosen to maximize the flow rate, provided that the duration of the evaluation period is at least 6 seconds, but not longer than 15.5 seconds.

This method yields the evaluation periods in Table 8.2-16. For comparison, the evaluation periods used by KWU to analyze their test data are also included in this table, and they are similar to the evaluation periods used for the S-RELAP5 results.

The beginning of the evaluation period is the first of two quantities that are used to assess the results of the S-RELAP5 calculations. The time at which the water level in the lower plenum exceeds 0.6 m (1.97 ft) as calculated by S-RELAP5 and as determined from the test measurements were compared. The difference between these two times – called the relative end of bypass, because it marks the transition from water bypassing the downcomer to ECC penetration of the lower plenum – is also provided in Table 8.2-16 for all five runs of Test 6. The S-RELAP5 result is conservatively delayed relative to the test results of the two cases with the highest rate of steam flow (Runs 135 and 131). For the remaining three runs of Test 6, the time predicted by the S-RELAP5 model either matches or is close to the time reported for the test results (within one second).

The second quantity that is used to assess the results of the calculation is the ECC penetration rate to the lower plenum. Since the lower plenum was not drained during Test 6, this quantity is the simply the rate of change of the mass inventory in the lower plenum, which is determined from the increase in liquid mass in the lower plenum over the evaluation period. The values calculated from the S-RELAP5 results are presented in along with the flow rates reported by KWU (Reference 8.2-34) for each test.

Test 7 – Simulation

As described in Section 8.2.9.3.2, Run 203 of Test 7 consisted of a series of distinct phases, each with a different set of flow conditions. Although the entire run was simulated with S-RELAP5, only the results of Phase IV were analyzed, because this phase was the only part of the test that used the same pattern of ECC injection as that used during the runs of Test 6. The analysis of this phase augments and extends the results from the analysis of Test 6 to lower steam flow conditions.

Unlike the runs in Test 6, Run 203 was initiated with water in the lower plenum, which was drained during the run to maintain a near constant level of water. The rate of drainage from the lower plenum was measured and recorded, providing a means to determine the amount of ECC penetration to the lower plenum. The evaluation period used by KWU for their analysis, 290 to 330 seconds into the run, was also used to analyze the numerical results for S-RELAP5.

Figure 8.2-230 to Figure 8.2-233 show several key quantities for Run 203: the lower plenum drainage rate, the steam injection rate, the downcomer pressure, and the ECC injection rate. These figures show that the boundary conditions of the simulation faithfully reproduce the conditions of the test. The comparisons of the results for the temperatures of the liquid in the broken cold leg and lower head, in Figure 8.2-234 and Figure 8.2-235, show that the measured and calculated values closely agree for most of the test, particularly in Phase IV, indicating that the condensation model used in the S-RELAP5 model is adequate for this test. The water level in the lower plenum, shown in Figure 8.2-236, was approximately constant during the evaluation period in Phase IV. S-RELAP5 slightly underpredicts the flow through the cold leg break during the test, as shown in Figure 8.2-238; however, the S-RELAP5 estimate is close to the values for the measured flow during Phase IV obtained from Reference 8.2-40, and the rate of flow out of the break is roughly the same during this phase of the test.

Because water is allowed to drain from the lower plenum, the ECC penetration rate to the lower plenum is the sum of the rate of change of lower plenum mass inventory and the rate at which water flows through the drain. The former rate is determined from the slope of the mass inventory curve; the latter rate is taken to be the average value of the reported drain flow during the evaluation period. The ECC penetration rates are given in Table 8.2-17.

Discussion of ECC Penetration to Lower Plenum

Since the steam in the downcomer flows in the opposite direction as the ECC water exiting the cold legs, it is expected that the ECC penetration to the lower plenum should decrease as the steam flow rate increases. The results in , which are also shown in Figure 8.2-239, generally exhibit this trend. [

]

S-RELAP5 underestimates the downcomer penetration rate during all six runs, which indicates that the code provides conservatively low estimates of the lower plenum refill. This evidence is further supported by the graphs of the upper level and mass inventory of the liquid in the lower plenum, which show that S-RELAP5 consistently underpredicts these quantities. Even the least conservative result, the rate of downcomer penetration predicted by S-RELAP5 for the low-steam-flow conditions of Phase IV of Run 203, is acceptable in that it matches the test results. Nevertheless, it is unclear whether the interaction of the draining of the lower head and the observed sweep-out effect in this part of the model has influenced the results for this particular run.

The results of this study suggest a general pattern of downcomer flow behavior that depends on the steam flow. In all cases, at least some of the ECC water from the cold leg adjacent to the break (belonging to loop 1) bypasses the downcomer and flows directly to the broken cold leg and out of the system. This bypass is evident by comparing the ECC injection from all three loops to the rate at which water penetrates the downcomer and flows into the lower plenum.

The ability of S-RELAP5 to accurately simulate this pattern of two-phase flow behavior demonstrates the ability of the code to model important refill phenomena. Several of these phenomena are discussed below.

Downcomer multi-dimensional effects

The calculated distribution of steam and ECC water flowing through the downcomer are consistent with the results from the tests. Although the highly separated flows in the downcomer are challenging to simulate with system codes such as S-RELAP5, [ ] have successfully reproduced these flows as the results demonstrate.

Downcomer countercurrent flow

The tests encompassed a wide range of steam flow rates and two-phase flow conditions, including countercurrent flow. The code provided estimates of the penetration of ECC water to the lower plenum that were either conservative or acceptable for the entire range of conditions.

Downcomer condensation and non-equilibrium flow

The estimates of downcomer penetration of ECC water encompassed a wide range of ECC subcooling (and downcomer condensation rates). The overall agreement between the measured and calculated temperatures in the broken cold leg and lower head indicates that the cold leg condensation model used in these calculations provides acceptable condensation rates in the cold legs and downcomer. Thus, [ ] calculate condensation in the downcomer due to the interaction of steam and ECC water.

Downcomer entrainment and deentrainment

The code provided reasonable predictions of the entrainment of ECC water to the broken leg during both the cold leg fill period and the lower plenum refill period.

Lower plenum sweep-out

The [ ]
caused
S-RELAP5 to overestimate the sweep-out effect in this region. While this is a non-physical phenomenon, it occurs under conditions that are not expected to be reproduced during plant analyses.

The results of these simulations of UPTF Tests 6 and 7 indicate that S-RELAP5 conservatively estimates the rate of lower plenum refill and the rate of ECC bypass, which will result in a conservative bottom of core recovery time during a PWR large break LOCA. These conservative estimates are provided [ ] due to the ability of the code to self-limit counter-current flow.

Table 8.2-14 Parameters for UPTF Tests 6 and 7

	Test 6 Runs					Test 7
	135	**131**	**132**	**133**	**136**	**203/IV**
Downcomer Pressure (kPa)	1130	978	727	543	360	337
Water Level (m)	0	0	0	0	0	2.0
Vessel Inventory (kg)	0	0	0	0	0	17070
Steam Injection (kg/s)						
Total	436	396	295	202	102	51
Steam Generator, per Loop	30	30	30	30	0	0
ECC Injection Flow (kg/s)	480	483	491	493	490	490
ECC Temperature (°C)	129	120	115	119	114	133
ECC Subcooling (°C)	56	59	52	36	26	2
Nitrogen Injection (kg/s)	1.03	1.01	1.03	1.02	1.03	0
Downcomer Pressure (psia)	164	142	105	79	52	49
Water (ft)	0	0	0	0	0	6.6
Vessel Inventory (lb_m)	0	0	0	0	0	37600
Steam Injection (lb_m)						
Total	961	873	650	445	225	112
Steam Generator, per Loop	66	66	66	66	0	0
ECC Injection, per Loop (lb_m/s)	1058	1065	1082	1087	1080	1080
ECC Temperature (°F)	264	248	239	246	237	271
ECC Subcooling (°F)	101	106	94	65	47	4
Injection Flow Rate (lb_m/s)	2.3	2.2	2.3	2.2	2.3	0

Table 8.2-15 Boundary Conditions for UPTF Tests 6 and 7

Steam Injection to core simulator	
Boundary Condition Components:	TMDPV 660, TMDPJ 665
Temperature Sensors (average):	JKG01CT002, JKG03CT002
Flow Sensors (sum):	CJKG01CF001H, CJKG03CF001H
Steam injection to steam generator simulator	
Boundary Condition Components:	TMDPV 670, TMDPJ 675
Temperature Sensors (average):	JEC01CT13, JEC02CT13, JEC03CT13
Flow Sensors (sum):	CQHA05CF012, CQHA05CF021, CQHA05CF022
ECC liquid injection to loop 1	
Boundary Condition Components:	TMDPV 710, TMDPJ 715
Temperature Sensor:	JNG26CT001
Flow Sensor:	CJNG26CF001
Pressure:	Test 6 Quick Look Report, page 33
ECC liquid injection to loop 2	
Boundary Condition Components:	TMDPV 720, TMDPJ 725
Temperature Sensor:	JNG27CT001
Flow Sensor:	CJNG27CF001
Pressure:	Test 6 Quick Look Report, page 33
ECC liquid injection to loop 3	
Boundary Condition Components:	TMDPV 730, TMDPJ 735
Temperature Sensor:	JNG21CT001
Flow Sensor:	CJNG21CF001
Pressure:	Test 6 Quick Look Report, page 33
Nitrogen injection to loop 1	
Boundary Condition Components:	TMDPV 711, TMDPJ 716
Temperature Sensor:	QJB02CT001
Flow Sensor (1/3 for each loop):	CQJB20CF001H
Pressure:	QJB02CP001
Nitrogen injection to loop 2	
Boundary Condition Components:	TMDPV 721, TMDPJ 726
Temperature Sensor:	QJB02CT001
Flow Sensor (1/3 for each loop):	CQJB20CF001H
Pressure:	QJB02CP001
Nitrogen injection to loop 3	
Boundary Condition Components:	TMDPV 731, TMDPJ 736

Temperature Sensor:	QJB02CT001
Flow Sensor (1/3 for each loop):	CQJB20CF001H
Pressure:	QJB02CP001
Lower plenum drain flow	
Boundary Condition Components:	TMDPV 810, VALVE 805
Pressure:	105 Pa
Flow Sensor:	CKTA06CF001H
Broken cold leg break	
Boundary Condition Components:	TMDPV 750
Pressure:	JEC04CP21

Table 8.2-16 Evaluation Periods Used to Determine the Rate of Downcomer Flow for UPTF Test 6

Run	Evaluation Period (s)		Relative End of Bypass (s)
	KWU	S-RELAP5	
135	59.0 - 65.0	70.5 - 76.5	-11.5
131	59.5 - 70.5	62.5 - 72.0	-3.0
132	57.0 - 65.5	57.0 - 63.0	0.0
133	55.0 - 66.0	54.0 - 65.0	1.0
136	51.5 - 67.0	50.5 - 61.5	1.0

Table 8.2-17 Downcomer Penetration Results of UPTF Tests 6 and 7

Run	Steam Flow (kg/s)	ECC Injection (kg/s)			Downcomer Penetration (kg/s)		
		Loop 1	Loop 2	Loop 3	KWU	S-RELAP5	Difference
135	436	480	480	481	548	70	478
131	396	478	485	488	570	269	301
132	295	494	489	489	898	776	122
133	202	499	486	493	975	678	297
136	102	494	488	489	875	776	99
203	51	493	485	487	1031	1009	22
Run	Steam Flow (kg/s)	ECC Injection (kg/s)			Downcomer Penetration (kg/s)		
		Loop 1	Loop 2	Loop 3	KWU	S-RELAP5	Difference
135	961	1058	1058	1060	1208	154	1054
131	873	1054	1069	1076	1257	593	664
132	650	1089	1078	1078	1980	1711	269
133	445	1100	1071	1087	2150	1495	655
136	225	1089	1076	1078	1929	1711	218
203	112	1087	1069	1074	2273	2224	49

Figure 8.2-188 S-RELAP5 Nodalization of the UPTF for Tests 6 and 7

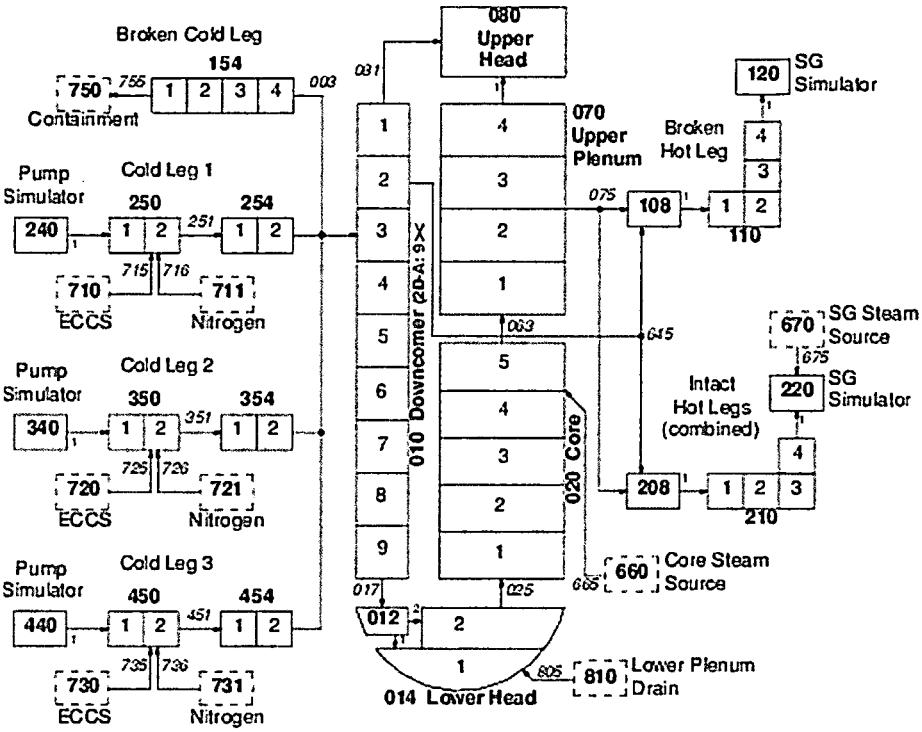

Figure 8.2-189 Nodalization of the Downcomer

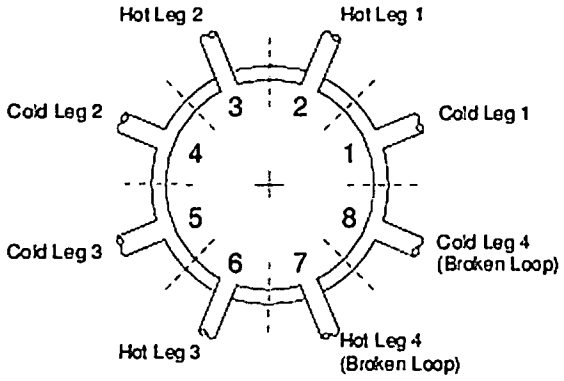

	1	2	3	4	5	6	7	8
1	010010100	010020100	010030100	010040100	010050100	010060100	010070100	010080100
2	010010200	010020200	010030200	010040200	010050200	010060200	010070200	010080200
3	Loop 1 C 010010300	Loop 1 H 010020300	Loop 2 H 010030300	Loop 2 C 010040300	Loop 3 C 010050300	Loop 3 H 010060300	Loop 4 H 010070300	Loop 4 C 010080300
4	010010400	010020400	010030400	010040400	010050400	010060400	010070400	010080400
5	010010500	010020500	010030500	010040500	010050500	010060500	010070500	010080500
6	010010600	010020600	010030600	010040600	010050600	010060600	010070600	010080600
7	010010700	010020700	010030700	010040700	010050700	010060700	010070700	010080700
8	010010800	010020800	010030800	010040800	010050800	010060800	010070800	010080800
9	010010900	010020900	010030900	010040900	010050900	010060900	010070900	010080900

Figure 8.2-190 Total Steam Injection Rate for Test 6 Run 135

Figure 8.2-191 Downcomer Pressure for Test 6 Run 135

Figure 8.2-192 Total ECC Water Injection Rate for Test 6 Run 135

Figure 8.2-193 Broken Cold Leg Liquid Temperature for Test 6 Run 135

Figure 8.2-194 Lower Head Liquid Temperature for Test 6 Run 135

Figure 8.2-195 Lower Plenum Liquid Level for Test 6 Run 135

Figure 8.2-196 Lower Plenum Liquid Mass Inventory for Test 6 Run 135

Figure 8.2-197 Total Cold Leg Break Flow for Test 6 Run 135

Figure 8.2-198 Total Steam Injection Rate for Test 6 Run 131

Figure 8.2-199 Downcomer Pressure for Test 6 Run 131

Figure 8.2-200 Total ECC Water Injection Rate for Test 6 Run 131

Figure 8.2-201 Broken Cold Leg Liquid Temperature for Test 6 Run 131

Figure 8.2-202 Lower Head Liquid Temperature for Test 6 Run 131

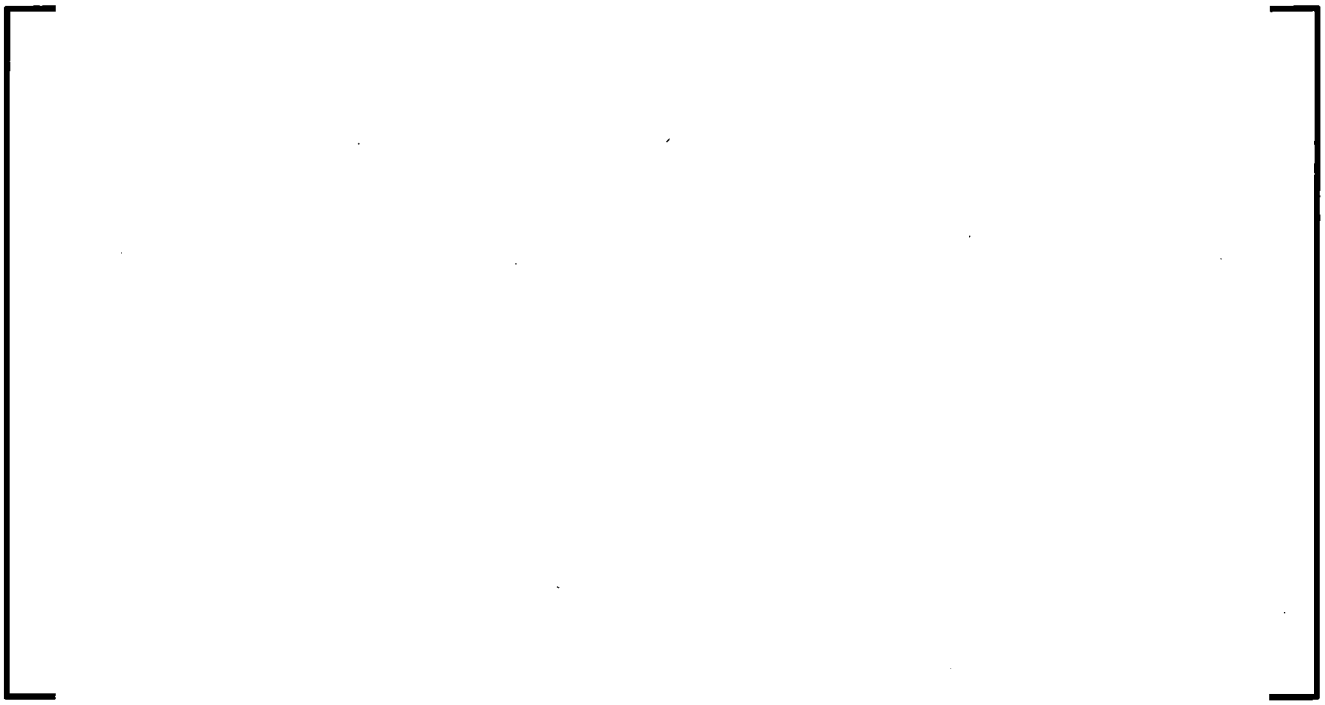

Figure 8.2-203 Lower Plenum Liquid Level for Test 6 Run 131

Figure 8.2-204 Lower Plenum Liquid Mass Inventory for Test 6 Run 131

Figure 8.2-205 Total Cold Leg Break Flow for Test 6 Run 131

Figure 8.2-206 Total Steam Injection Rate for Test 6 Run 132

Figure 8.2-207 Downcomer Pressure for Test 6 Run 132

Figure 8.2-208 Total ECC Water Injection Rate for Test 6 Run 132

Figure 8.2-209 Broken Cold Leg Liquid Temperature for Test 6 Run 132

Figure 8.2-210 Lower Head Liquid Temperature for Test 6 Run 132

Figure 8.2-211 Lower Plenum Liquid Level for Test 6 Run 132

Figure 8.2-212 Lower Plenum Liquid Mass Inventory for Test 6 Run 132

Figure 8.2-213 Total Cold Leg Break Flow for Test 6 Run 132

Figure 8.2-214 Total Steam Injection Rate for Test 6 Run 133

Figure 8.2-215 Downcomer Pressure for Test 6 Run 133

Figure 8.2-216 Total ECC Water Injection Rate for Test 6 Run 133

Figure 8.2-217 Broken Cold Leg Liquid Temperature for Test 6 Run 133

Figure 8.2-218 Lower Head Liquid Temperature for Test 6 Run 133

Figure 8.2-219 Lower Plenum Liquid Level for Test 6 Run 133

Figure 8.2-220 Lower Plenum Liquid Mass Inventory for Test 6 Run 133

Figure 8.2-221 Total Cold Leg Break Flow for Test 6 Run 133

Figure 8.2-222 Total Steam Injection Rate for Test 6 Run 136

Figure 8.2-223 Downcomer Pressure for Test 6 Run 136

Figure 8.2-224 Total ECC Water Injection Rate for Test 6 Run 136

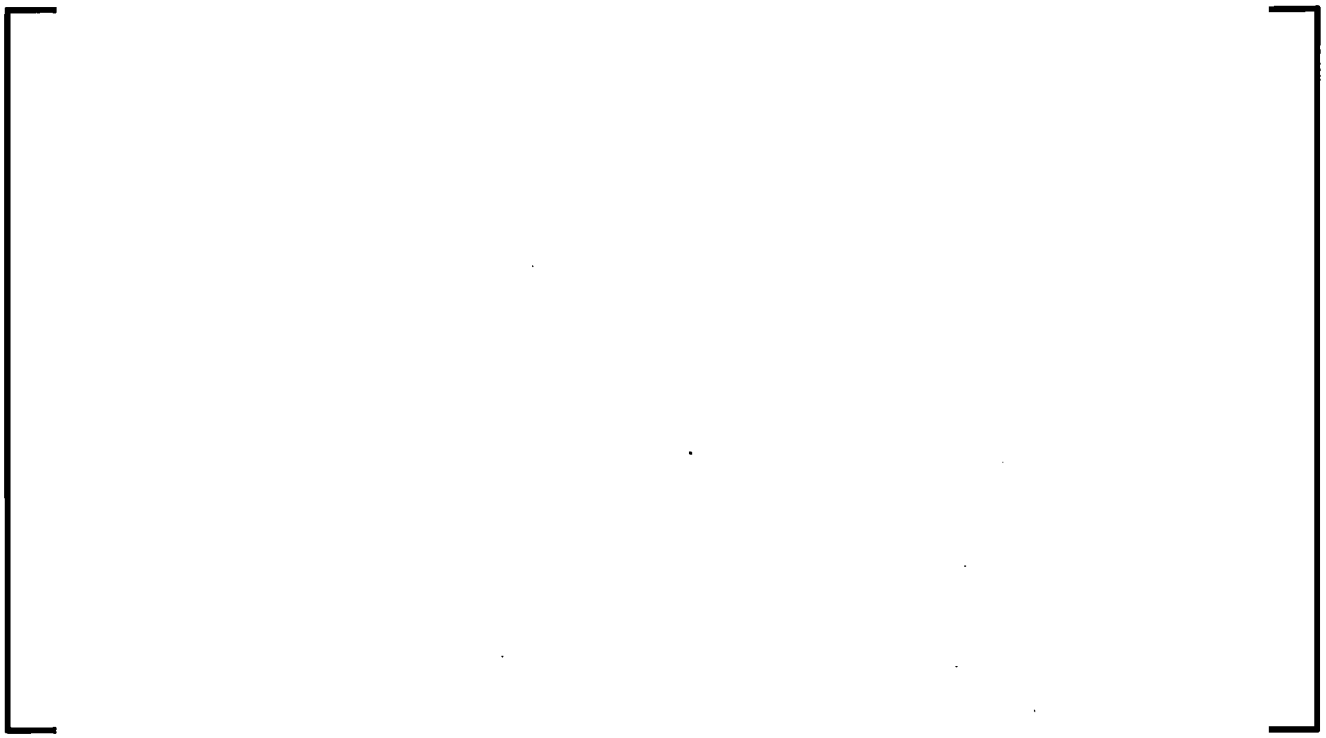

Figure 8.2-225 Broken Cold Leg Liquid Temperature for Test 6 Run 136

Figure 8.2-226 Lower Head Liquid Temperature for Test 6 Run 136

Figure 8.2-227 Lower Plenum Liquid Level for Test 6 Run 136

Figure 8.2-228 Lower Plenum Liquid Mass Inventory for Test 6 Run 136

Figure 8.2-229 Total Cold Leg Break Flow for Test 6 Run 136

Figure 8.2-230 The Rate of Lower Head Drainage Flow for Test 7 Run 203

Figure 8.2-231 Total Steam Injection Rate for Test 7 Run 203

Figure 8.2-232 Downcomer Pressure for Test 7 Run 203

Figure 8.2-233 Total ECC Water Injection Rate for Test 7 Run 203

Figure 8.2-234 Broken Cold Leg Liquid Temperature for Test 7 Run 203

Figure 8.2-235 Lower Head Liquid Temperature for Test 7 Run 203

Figure 8.2-236 Lower Plenum Liquid Level for Test 7 Run 203

Figure 8.2-237 Lower Plenum Liquid Mass Inventory for Test 7 Run 203

Figure 8.2-238 Total Cold Leg Break Flow for Test 7 Run 203

Figure 8.2-239 ECC Downcomer Penetration Rate for All Six Runs in Tests 6 and 7

8.2.9.4 UPTF Test 8

UPTF Test 8 was one of the tests used for the S-RELAP5 simulation as part of the cold-leg condensation model development. UPTF Test 8 was performed under the 2D/3D program to investigate the thermal-hydraulic behavior of emergency core cooling (ECC) water injection in the cold legs during the end-of-blowdown, refill, and reflood phases of a postulated LOCA. Test 8 was performed by isolating intact Loop 1 at the pump simulator, opening intact Loop 3 to stabilize the pressure drop between the upper plenum and the downcomer, opening the break valves in the broken loop, injecting steam into the test vessel, and varying ECC water injection into the intact Loop 2 cold leg. Test 8 consisted of two runs, (Runs 111 and 112), which differed by the value of the resistance to flow applied in the pump simulator of intact Loop 2. The variation in resistance resulted in a different steam rate into the intact Loop 2 (Reference 8.2-41).

8.2.9.4.1 Summary and Conclusions

In summary, from the simulation of UPTF Test 8 using S-RELAP5, it can be concluded that with the use of the cold leg condensation model, S-RELAP5 will correctly calculate the temperature of the water entering the downcomer (DC) during the reflooding phase of a LOCA in a PWR. Excellent agreement is seen between S-RELAP5 calculated downcomer entrance temperatures and corresponding UPTF test data.

8.2.9.4.2 Test Description (UPTF Test 8)

Test 8 was performed by isolating intact Loop 1 at the pump simulator, opening intact Loop 3 to stabilize the pressure drop between the upper plenum and the downcomer, opening the break valves in the broken loop, injecting steam into the test vessel, and varying ECC water injection into the intact Loop 2 cold leg. The S-RELAP5 model consisted of only the principal portion of the system relevant to the UPTF Test 8; that being the piping from the second loop steam generator simulator to the pump simulator (including loop seal), the pump simulator, and the cold-leg piping from the pump simulator to the vessel downcomer.

A schematic of this portion of Loop 2 with some key measurement instrumentation locations is given in Figure 8.2-240. The downcomer pressure measurement shown in Figure 8.2-240 (JAA01CP002L) is located at the Loop 1 cold leg outlet and not the Loop 2 cold leg outlet.

Each Test 8 run consisted of two parts. Part 1 involves cold-leg ECC injection lasting to approximately 240 seconds into the test. Part 2, immediately following Part 1, involved hot-leg ECC injection. Only Part 1 involving cold-leg ECC injection is considered in this assessment, to validate the cold leg condensation model developed in Section 8.4.2. For Part 1, the initial pressure of the system was approximately 380 kPa. For Run 111, the pump simulator of Loop 2 was set to correspond to a form loss factor Kloss=18 and the test was initiated at about 23 seconds. For Run 112, the pump simulator of Loop 2 was set to correspond to a form loss factor Kloss=10 and the test was initiated at about 20 seconds. The effect of the lower form loss factor Kloss was to have a slightly higher steam flow rate into Loop 2 (about a 10 percent higher flow).

The ECC injection rate was stepped down in increments every 30 seconds from an initial value of 600 kg/s to nearly 0 kg/s at the end of the cold-leg injection part of the test. After an approximate 20 second test initialization period, the tests were started. Upon initiation of the test, steam injection to the test vessel was started at rate of about 100 kg/s, and ECC injection into the Loop 2 cold leg was started at a rate of about 600 kg/s.

Immediately after initiation of ECC injection, a subcooled plug of liquid was formed at the injection point, as indicated by having all of the thermocouples in a temperature stalk measure subcooled liquid temperatures. Thermocouples upstream from the plug all measured steam temperatures. As the ECC injection rate was decreased to about 250 kg/s at about 90 seconds, oscillations in the cold-leg temperature became more pronounced. When the ECC injection rate reaches about 200 kg/s at about 120 seconds, the top thermocouple of the temperature stalk near the ECC injection point consistently measures the steam temperature, indicating fully developed horizontal stratified flow in the cold leg. The flow remained stratified in the cold leg throughout the additional reductions in ECC injection rate until the cold-leg injection part of the test was terminated at about 230 seconds. Table 8.2-19 and Table 8.2-20 outline the test conditions for both runs (from Table 4-1, Figure 4-4a and Figure 4-4b of Reference 8.2-42).

8.2.9.4.3 S-RELAP5 Model Description (UPTF Test 8)

Figure 8.2-241 shows the S-RELAP5 model nodalization corresponding to the simplified single-loop UPTF configuration shown in Figure 8.2-240. A model driven by a simple single-leg boundary condition will adequately assess the condensation and flow regime characteristics in the cold leg of Test 8, where ECC water was injected into the intact Loop 2 cold leg.

Hydraulic Nodalization - Test 8

The cold leg piping for Loop 2 from the pump discharge piping to the downcomer is modeled according to the RLBLOCA methodology guidelines. These include the following:

- The cold leg condensation model is applied to [

  ] The values used for these multipliers are those specified in Sections 8.2.10 and 8.4.2.
- The cold leg condensation model is described in detail in Section 8.4.2. The basic hydraulic nodalization is shown in Figure 8.2-241.

Initial Conditions and Boundary Conditions

For the single-loop UPTF configuration shown in Figure 8.2-240, the following Test 8 experimental data were used to establish the required boundary conditions for both Runs 111 and 112:

- Cold-leg inlet steam flow rate
- Cold-leg inlet steam temperature
- ECC injection water flow rate
- ECC injection water temperature
- Cold-leg outlet (downcomer) pressure

In certain cases, the extracted boundary condition data were smoothed. In all cases the data were re-sampled and reformatted into an S-RELAP5 table to produce 180 data points. outlines the thermocouple locations in the cold leg for temperature stalk number 4 (Section 7.3 and Figure 4-7 of Reference 8.2-39) which are used when comparing S-RELAP5 predictions with UPTF Test results to evaluate cold leg condensation.

For S-RELAP5 Components 200 and 210, the cold-leg inlet temperature and steam flow rate boundary conditions used the UPTF data (Reference 8.2-41) from sensors JEC02CT001 and CJEC02CF001, respectively. For S-RELAP5 Components 100 and 110, the ECC water temperature and flow rate boundary conditions used the UPTF data (Reference 8.2-41) from sensors JNG27CT001 and CJNG27CF001, respectively. For S-RELAP5 Component 004, the cold-leg outlet-pressure boundary condition used the UPTF data (Reference 8.2-41) from sensor JAA01CP002L for the downcomer pressure channel. The boundary conditions of the test are used to examine the ability of the code to model these parameters.

8.2.9.4.4 Simulation and Comparison with Experimental Results (UPTF Test 8)

Figure 8.2-242 and Figure 8.2-243 compare key run boundary condition inputs (steam flow rate) the ECC injection rate for Run 111 and Run 112. These figures show the relationship between the boundary conditions for the two runs and demonstrate that both runs are similar.

Run 111

Figure 8.2-244 through Figure 8.2-248 compare the S-RELAP5 boundary conditions and the measured data from which the boundary conditions were derived. These plots demonstrate that the boundary conditions are input correctly into S-RELAP5.

Figure 8.2-249 through Figure 8.2-253 provide an overview of the S-RELAP5 results for Run 111, showing the calculated flow regime and the cold-leg mass flow rate, fluid temperatures, vapor generation rate, and vapor void fraction for the run. Figure 8.2-249 displays the flow regime in the cold leg. The cold-leg section (Volume 318) closest to the ECC injection point exhibits slug flow between 20 and 180 seconds; afterwards the flow transitions to annular mist. This is consistent with the UPTF experimental data (Figure 4-4a from Reference 8.2-42) where the flow transitioned from slug flow to stratified flow after 150 seconds. The S-RELAP5 run displays annular mist [

] Figure 8.2-250

displays the S-RELAP5 calculated mass flow in Volume 318; the step changes in the flow rate are consistent with the ECC flow input as shown in Figure 8.2-243. The temperature in the cold leg in the ECC mixing branch and cold leg sections downstream from the ECC injection point are shown in Figure 8.2-251. The temperature in Volumes 320 of the cold leg rises until reaching saturation. Volume 318 displays a similar trend until 180 seconds where heat up no longer occurs; this is the same point where the flow regime changes from slug flow to annular mist in the S-RELAP5 model. Figure 8.2-252 displays the calculated vapor generation rate for the three cold leg volumes after the ECC injection location. Most of the condensation occurs near the ECC injection location. The vapor void fraction in the cold leg volume downstream from the ECC injection point (Volume 320) is shown in Figure 8.2-253. The void fraction is around 0.6 during the slug flow regime and increases towards 1.0 when the flow begins to transition to stratified flow.

Figure 8.2-254 and Figure 8.2-255 compare the S-RELAP5 simulation and the test facility data from UPTF Test 8 Run 111. Figure 8.2-254 displays the UPTF data in thermocouple stalk number four located downstream from the ECC injection point (Figure 4-7 of Reference 8.2-35). The measurement data for the cold leg bottom (A390 at 25 mm) to the centerline of the cold leg (A387 at 325 mm) is plotted. During both the accumulator injection period and the pumped injection period the S-RELAP5 run results agree well with the test data. The UPTF data of the cold leg temperature at the top (A391 at 625 mm) of temperature stalk number 5 (near the ECC injection location) was plotted along with the S-RELAP5 predicted flow regime for Volume 318 in Figure 8.2-255. The temperature was taken to indicate the flow regime in the test for comparison with the S-RELAP5 predicted flow regimes and agree well with the slug flow regime noted in the test data from 30 to 120 seconds. The cold leg top temperature from the UPTF data reached the steam temperature (A900) at 120 seconds. The flow regime transitioned from slug flow to annular mist at 180 seconds [

] consistent with Figure 4-4a of Reference 8.2-42 where the flow in the UPTF transitions out of slug flow after 150 seconds.

Run 112

Similarly for Run 112, Figure 8.2-256 through Figure 8.2-260 show the boundary conditions for S-RELAP5 were developed accurately from the measured data.

Figure 8.2-261 through Figure 8.2-265 display the S-RELAP5 results for the run including calculated flow regime, and the cold leg mass flow rate, fluid temperatures, vapor generation rate and vapor void fraction for the run. Figure 8.2-267 shows the S-RELAP5 calculated flow regimes in the cold leg volumes. Volume 318 (ECC mixing branch) transitions between slug and annular mist flow until 180 seconds since the non-stratified flow option is selected in the ECC injection node. The stratified flow seen after 120 seconds in Figure 4-4b of Reference 8.2-42 is not predicted in this volume [

] The next volume downstream from the ECC injection location (volume 320-01) alternates between bubbly and horizontal stratified flow until 160 seconds, where the flow transitions completely to stratified flow. This is consistent with the UPTF test data in Figure 4-4b of Reference 8.2-42. Figure 8.2-262 displays the calculated mass flow in the ECC mixing branch; the oscillations in the flow are consistent with alternating flow regimes in the volume. The liquid and steam temperatures in Volume 320 are shown to increase to saturation in Figure 8.2-263. The liquid temperature in Volume 318 heats up until 180 seconds when the flow transitions from slug flow to an annular mist flow regime. The vapor generation rate in Figure 8.2-264 oscillates in Volume 318 as the flow regime changes between slug and annular mist. Figure 8.2-265 displays the void fraction in the cold leg downstream from the ECC injection location, with a lower void fraction until 160 seconds. The lower void fraction indicates the slug flow regime in the cold leg. After 160 seconds the void fraction increases consistent with the transition to stratified flow.

Figure 8.2-266 and Figure 8.2-267 display the comparison between the calculated S-RELAP5 results and test data for the cold-leg fluid temperature and the cold-leg flow regime, respectively. Figure 8.2-266 plots the S-RELAP5 temperature along with the UPTF temperature data from thermocouples at the centerline of the cold leg (375 mm) until the bottom of the cold leg (25 mm). The code is able to predict the temperature within the thermocouple test data. Figure 8.2-267 plots the flow regime at the ECC mixing branch along with the UPTF data from temperature stalk number 5 (Figure 4-7 of Reference 8.2-35). The UPTF data from the thermocouple at the top of the cold leg (A391 at 625 mm from Figure 4-7 in Reference 8.2-35) shows the temperature begins to approach saturation at around 120 seconds. The flow alternates between slug flow and annular mist flow until 150 seconds, after which it transitions completely to annular mist. At this point it is not stratified flow [

] These results are consistent with the UPTF data where during the time period from 120 seconds to 150 seconds the flow becomes stratified (Figure 4-4b from Reference 8.2-42).

In summary, the comparisons of S-RELAP5 results for Run 111 and Run 112 with UPTF test data are in good agreement and the code predicts the cold leg condensation correctly. These results show that with the use of the cold leg condensation model, S-RELAP5 will correctly calculate the temperature of the water entering the DC during the reflooding phase of a LOCA in a PWR.

Table 8.2-18 UPTF/S-RELAP-5 Model Cross Reference Test 8

Channel	Sensor	Component	Description
A900	JEC02CT001	TMDPVOL 200	Cold Leg Inlet Steam Temperature Boundary Condition
C590	CJEC02CF001	TMDPJUN 210	Cold Leg Inlet Steam Flow Boundary Condition ECC
A889	JNG27CT001	TMDPVOL 100	Water Temperature Boundary Condition ECC Water
C668	CJNG27CF001	TMDPJUN 110	Flow Boundary Condition
A1289	JAA01CP002L	TMDPVOL 4	Cold Leg Outlet Pressure Boundary Condition Cold
A387	JEC02CT043		Leg Centerline (375 mm) Temperature Cold Leg
A388	JEC02CT044		Temperature at 250 mm
A389	JEC02CT045		Cold Leg Temperature at 125 mm
A390	JEC02CT046		Cold Leg Bottom (25 mm) Temperature
A391	JEC02CT051		Cold Leg Top (625 mm) Temperature

Table 8.2-19 UPTF Test 8 Run 111 Conditions

Phase-Part	P (kPa)	W_g (kg/s)	W_l (kg/s)	Steam ΔT_{sup} (°C)	Liquid ΔT_{sub} (°C)
I	405	38	600	1	110
II	405	36	400	1	110
III	405	34.5	250	1	110
IV	405	34.5	200	1	110
V	405	33	150	1	110
VI	405	32.5	90	1	110
VII	405	31	15	1	110

Table 8.2-20 UPTF Test 8 Run 112 Conditions

Phase-Part	P (kPa)	W_g (kg/s)	W_l (kg/s)	Steam ΔT_{sup} (°C)	Liquid ΔT_{sub} (°C)
I	400	34	60	2	110
II	400	35	400	2	110
III	400	31	250	2	110
IV	400	32	200	2	110
V	400	31	150	2	110
VI	400	30	87	2	110
VII	400	29	18	2	110

Figure 8.2-240 UPTF Test 8 Cold Leg Loop Configuration

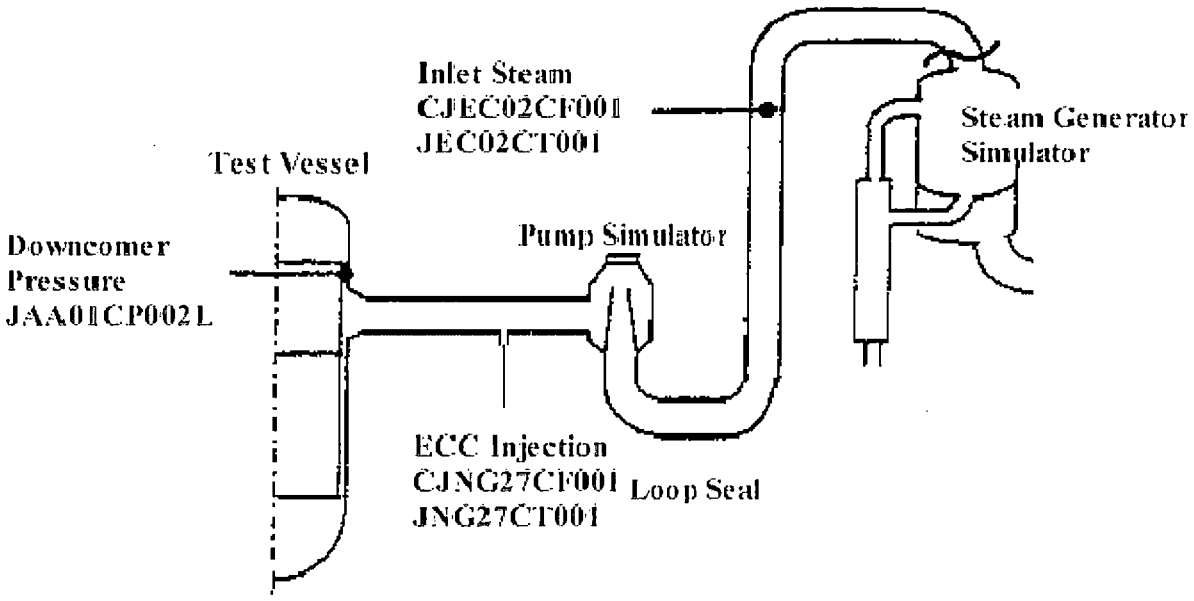

Figure 8.2-241 UPTF Test 8 S-RELAP5 Nodalization

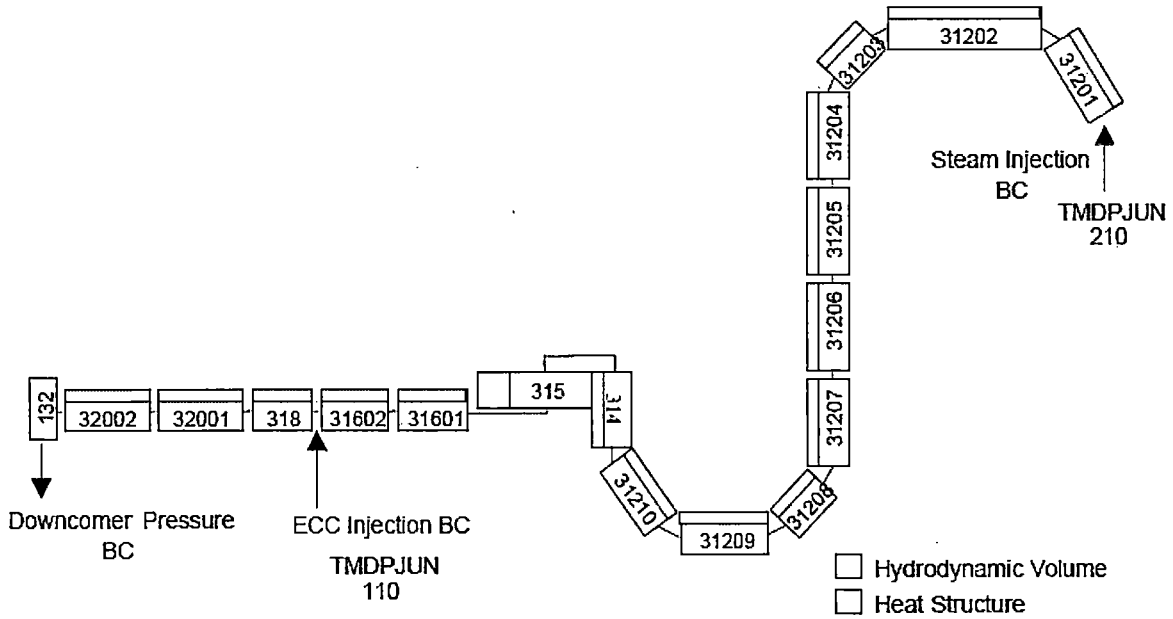

Figure 8.2-242 Run Comparison of Steam Flow Boundary Condition, UPTF Test 8

Figure 8.2-243 Run Comparison of ECC Injection, UPTF Test 8

Figure 8.2-244 Steam Flow Boundary Condition, UPTF Test 8 Run 111

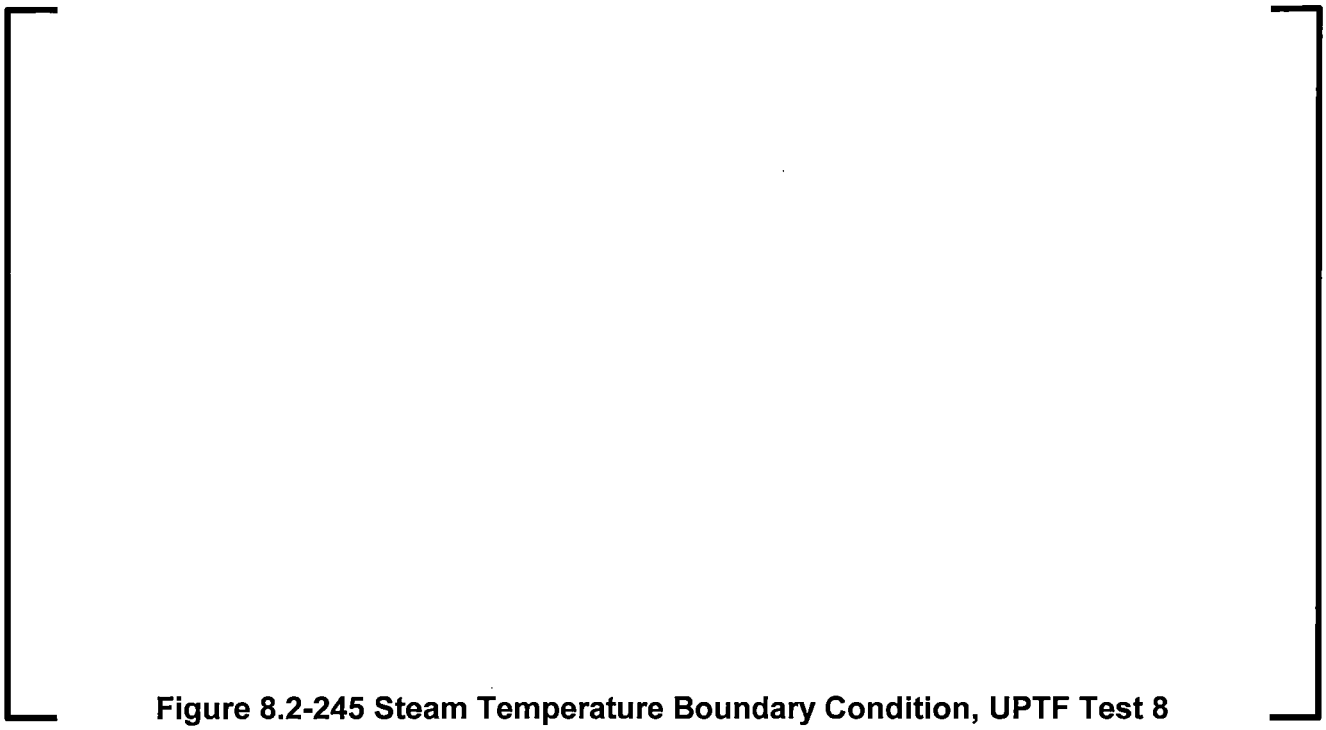

Figure 8.2-245 Steam Temperature Boundary Condition, UPTF Test 8 Run 111

Figure 8.2-246 ECC Water Flow Boundary Condition, UPTF Test 8 Run 111

Figure 8.2-247 ECC Water Temperature Boundary Condition, UPTF Test 8 Run 111

Figure 8.2-248 Downcomer Pressure Boundary Condition, UPTF Test 8 Run 111

Figure 8.2-249 S-RELAP5 Calculated Flow Regime, UPTF Test 8 Run 111

Figure 8.2-250 S-RELAP5 Calculated Mass Flow, UPTF Test 8 Run 111

Figure 8.2-251 S-RELAP5 Calculated Temperature, UPTF Test 8 Run 111

Figure 8.2-252 S-RELAP5 Calculated Vapor Generation Rate, UPTF Test 8 Run 111

Figure 8.2-253 S-RELAP5 Calculated Vapor Void Fraction, UPTF Test 8 Run 111

Figure 8.2-254 UPTF Data/S-RELAP5 Temperature Comparison, UPTF Test 8 Run 111

Figure 8.2-255 UPTF Data/S-RELAP5 Flow Regime Comparison, UPTF Test 8 Run 111

[ ]

Figure 8.2-256 Steam Flow Boundary Condition, UPTF Test 8 Run 112

[ ]

Figure 8.2-257 Steam Temperature Boundary Condition, UPTF Test 8 Run 112

Figure 8.2-258 ECC Water Flow Boundary Condition, UPTF Test 8 Run 112

Figure 8.2-259 ECC Water Temperature Boundary Condition, UPTF Test 8 Run 112

Figure 8.2-260 Downcomer Pressure Boundary Condition, UPTF Test 8 Run 112

Figure 8.2-261 S-RELAP5 Calculated Flow Regime, UPTF Test 8 Run 112

Figure 8.2-262 S-RELAP5 Calculated Mass Flow, UPTF Test 8 Run 112

Figure 8.2-263 S-RELAP5 Calculated Temperature, UPTF Test 8 Run 112

Figure 8.2-264 S-RELAP5 Calculated Vapor Generation Rate, UPTF Test 8 Run 112

Figure 8.2-265 S-RELAP5 Calculated Vapor Void Fraction, UPTF Test 8 Run 112

Figure 8.2-266 UPTF Data/S-RELAP5 Temperature Comparison, UPTF Test 8 Run 112

Figure 8.2-267 UPTF Data/S-RELAP5 Flow Regime Comparison, UPTF Test 8 Run 112

8.2.9.5 UPTF Tests 10 and 12

UPTF Test 10 Run 080 and Test 12 Run 014 also were specifically designed to simulate upper core, upper plenum, and hot-leg fluid flow behavior during the reflood phase of a RLBLOCA transient. These tests differed from Test 10 Run 081 and Test 29 in that flow was allowed between the downcomer and core region and Test 12 included nitrogen injection. Analysis of these tests demonstrates the ability of S-RELAP5 to properly limit countercurrent flow at the upper tie plate (UTP) and upper plenum regions of a PWR during the LBLOCA reflood phase. This limiting of downflow into the core is important because water downflow into the core region provides a source of additional core cooling and reduces the likelihood of water carryout to the steam generators with the associated steam binding effects.

8.2.9.5.1 Summary and Conclusions

The key parameters to be compared between S-RELAP5 simulations and test results are the downflow of water to the lower vessel region, Kutateladze countercurrent flow parameters calculated at the junctions between the upper plenum and core, and the upper plenum pressure. Reduced downflow of water to the lower vessel generally is considered to have a conservative effect because it leads to less core cooling.

For both tests, data and S-RELAP5 calculations were compared [

] from the RLBLOCA input development guideline (Appendix A). The S-RELAP5 code is demonstrated to conservatively limit the water downflow in the countercurrent flow mode. The code predictions show conservative predictions relative to the data (adequate agreement) in both tests.

The calculated UPTF water downflow also was compared with the S-RELAP5 calculated water downflow. The results show that overall (co-current and countercurrent) S-RELAP5 conservatively underpredicts downflow. The results are consistent with the UPTF results, which indicate breakthrough of ECC liquid near the hot-leg upper plenum junction. The S-RELAP5 results are based on describing the core-to-upper-plenum junction with the fuel bundle UTP area consistent with the current RLBLOCA method.

With respect to upper plenum pressure, the S-RELAP5 calculated upper plenum pressure and the measured data comparisons indicate that the S-RELAP5 code slightly underpredicts the pressure for all cases.

The final observation is that the presence of nitrogen in the system does not appear to have a significant impact on CCFL. One of the differences between Test 12 Run 014 and Test 10 Run 080 is that nitrogen was injected into the system in Test 12 Run 014. Results show that the presence of the nitrogen in the system does not affect either the S-RELAP5 calculation or the UPTF experimental results for CCFL.

Therefore the S-RELAP5 modeling is deemed adequate because it yields conservative results.

8.2.9.5.2 Test Description (UPTF Tests 10 and 12)

For Test 10 Run 080, the hot-leg break valve (loop 4) was open, the cold-leg break valve was closed, the pump simulators were closed, steam was injected into the test vessel, ECC water was injected into the intact hot legs, steam was injected into the intact steam generators, and the test vessel drainage system was activated during the test. The initial pressure of the system was about 385 kPa (56 psi). The test consisted of two phases using different ECC modes with a period in between for draining the upper plenum.

As described in Reference 8.2-43, UPTF Test 10 Run 080 was performed to examine countercurrent flow through the UTP and to examine co-current water downflow. The lower plenum was filled with water to a level of 1.2 m (3.94 ft) (Reference 8.2-43, pg. 30). Steam was injected into the core as shown in Figure 8.2-271 and Figure 8.2-272. Subcooled water was injected into the intact hot legs, as shown in Figure 8.2-276 and Figure 8.2-277. The boundary conditions set up countercurrent flow of steam and water through the UTP, as well as regions of co-current water downflow.

For Test 12 Run 014, the hot- and cold-leg break valves were opened, the pump simulators were closed, steam was injected into the test vessel, ECC water and nitrogen were injected into the intact hot legs, steam was injected into the intact steam generators, and the test vessel drainage system was activated during the test. The initial pressure of the system was about 660 kPa (96 psi).

As described in Reference 8.2-44, UPTF Test 12 Run 014 was performed to examine countercurrent flow between the UTP and the upper plenum. The water level in the lower vessel at the start of the test was low enough (0.56 m (1.84 ft)) to allow steam to flow from the core to the downcomer and broken cold leg. Steam was injected into the core as shown in Figure 8.2-284 and Figure 8.2-285. Subcooled water was injected into the intact hot legs as shown in Figure 8.2-288 and Figure 8.2-289. These boundary conditions set up countercurrent flow of steam and water through the UTP.

8.2.9.5.3 S-RELAP5 Model Description (UPTF Tests 10 and 12)

The S-RELAP5 input model is the same as that used in Revision 0 of the RLBLOCA methodology for the Test 10 Run 080 and Test 12 Run 014 assessments. Since the primary purpose of this simulation is to evaluate the CCFL between the core and upper plenum, the upper core region and the upper plenum nodalization followed the guidelines. [

]

A simplified modeling approach is used to model the remaining part of the test facility. The use of [ ] was not required in this input model. Figure 8.2-268 and Figure 8.2-269 present S-RELAP5 nodalization diagrams

for the model used in the assessment of Test 10 Run 080 and Test 12 Run 014. The model uses time-dependent volumes (components 680 and 690) connected to both the intact and broken hot legs, respectively, to provide a transient pressure boundary condition at the hot legs to be the same as that observed in the tests. The steam generator simulators are not modeled.

Initial Conditions and Boundary Conditions

Figure 8.2-268 shows that pressure boundary conditions are used on the combined intact hot leg (time-dependent volume sink, component 680), the broken hot leg (time-dependent volume sink, component 690), and the broken cold leg (time-dependent volume sink, component 750). The boundary condition input is taken from corresponding UPTF test data. The use of the boundary conditions eliminates the need to model the UPTF steam generator and pump simulators in the S-RELAP5 model. As shown in Figure 8.2-268 and Figure 8.2-269, flow and state property boundary conditions are used for the injection of steam into the core (time-dependent volume sources, components 660, 661, 662, 670, 671, and 672, and the associated time-dependent junctions) and combined intact hot leg (time-dependent volume sources, components 652 and 656 and the associated time-dependent junctions). The boundary condition input is taken from corresponding UPTF test data.

Table 8.2-21 provides a cross reference from the UPTF data channels and sensors to the S-RELAP5 components for building the boundary condition file and generating comparison plots with calculation results. Boundary conditions were generated for the lower plenum drain, core steam injection, core water injection, broken cold-leg pressure, intact hot-leg pressure, broken-loop hot-leg pressure, intact hot-leg ECC water injection, intact hot-leg steam injection, and nitrogen injection for Test 12. Figure 8.2-270 through Figure 8.2-279 compare the S-RELAP5 boundary conditions and data for Test 10 Run 080; Figure 8.2-283 through Figure 8.2-293 compare the boundary conditions and data for Test 12 Run 014.

8.2.9.5.4 Simulations and Comparison with Experimental Data (UPTF Tests 10 and 12)

[

]

Figure 8.2-280 through Figure 8.2-282 compare the S-RELAP5 predictions to the UPTF experimental results for Test 10 Run 080. Figure 8.2-280 presents a plot of Kutateladze parameters calculated from the S-RELAP5 results compared to the UPTF correlation. The comparison shows that S-RELAP5 is correctly limiting liquid downflow as is shown by the linear upper limit of $\sqrt{K_g^*}$. This is based [

] specified in the RLBLOCA guidelines (Appendix A). Figure 8.2-280 clearly shows that the S-RELAP5 calculation is conservative relative to the UPTF correlation.

Figure 8.2-281 compares the S-RELAP5 upper plenum pressure calculation to the measured UPTF upper plenum pressure. The two are shown to be in good agreement.

Figure 8.2-282 compares the S-RELAP5 calculated downflow to downflow calculated using UPTF test data. The downflow in the UPTF test was derived from data sensors for the test vessel level, the downcomer level, and the lower plenum drain rate. The comparison shows that the overall downflow (countercurrent and cocurrent) calculated by S-RELAP5 trends the UPTF data, but conservatively underpredicts the data (adequate agreement). This prediction is based on a core to upper plenum junction specification consistent with the UTP.

Figure 8.2-294 through Figure 8.2-296 compare the S-RELAP5 predictions to the UPTF experimental results for Test 12 Run 014. Figure 8.2-294 presents a plot of Kutateladze parameters calculated from the S-RELAP5 results compared to the UPTF correlation. The comparison shows that S-RELAP5 is correctly limiting liquid downflow as is shown by the linear upper limit of $\sqrt{K_g^*}$. The S-RELAP5 calculation is based [

] specified in the RLBLOCA guidelines (Appendix A).

Figure 8.2-294 clearly shows that the S-RELAP5 calculation is conservative relative to the UPTF correlation.

Figure 8.2-295 compares the S-RELAP5 upper plenum pressure calculation to the measured UPTF upper plenum pressure. The two are shown to be in good agreement.

Figure 8.2-296 compares the S-RELAP5 calculated downflow to downflow calculated using UPTF test data. The downflow in the UPTF test was derived from data sensors for the test vessel level, the downcomer level, and the lower plenum drain rate, as was done in the assessment for the Revision 0 RLBLOCA methodology. The comparison shows that the overall downflow (countercurrent and cocurrent) calculated by S-RELAP5 trends the UPTF data, but conservatively underpredicts the data. This prediction is based on a core to upper plenum junction specification consistent with the UTP.

The final observation is that there does not appear to be a significant impact on CCFL from the presence of nitrogen in the system. One of the differences between Test 12 Run 014 and Test 10 Run 080 is that nitrogen was injected into the system for Test 12 Run 014. Comparison of Figure 8.2-280 with Figure 8.2-294 indicates that the presence of the nitrogen in the system did not affect either the SRELAP5 calculation or the UPTF experimental results for CCFL.

Table 8.2-21 UPTF/S-RELAP5 Model Cross Reference Test 10 Run 080 and Test 12 Run 014

Channel	Sensor	Component	Description
A3	JEC03CP11	TMDPVOL 680	Hot leg pressure loop 3
A4	JEC04CP11	TMDPVOL 690	Hot leg pressure loop 4
A5	JEC04CP21	TMDPVOL 750	Cold leg pressure broken loop 4
A3	JEC03CP11	TMDPVOL 652	Hot leg pressure loop 3
C575	CQHA05CF012	TMDPJUN 654	Steam generator steam injection flow loop 3
C576	CQHA05CF021	TMDPJUN 654	Steam generator steam injection flow loop 2
C577	CQHA05CF022	TMDPJUN 654	Steam generator steam injection flow loop 1
A913	JKG01CT002	TVOL 660,661,662	Temperature of steam injection into core simulator pipe 1
A914	JKG03CT002	TVOL 660,661,662	Temperature of steam injection into core simulator pipe 3
A891	QHA01CT003	TVOL 660,661,662	Temperature of steam injection into core simulator
C624	CJKG01CF001H	TABLE 665	Flow of steam injection into core simulator pipe 1
C626	CJKG03CF001H	TABLE 665	Flow of steam injection into core simulator pipe 3
C662	CJKG30CF001	TABLE 665	Flow of steam injection into core simulator
A697	JNG02CP001	TMDPVOL 656	Pressure of ECC ACCUMULATOR LOOP 2
A883	JNG22CT001	TMDPVOL 656	Hot leg ECC injection temperature loop 3
C664	CJNG22CF001	TABLE 658	Hot leg ECC injection flow loop 3
C666	CJNG25CF001	TABLE 658	Hot leg ECC injection flow loop 2
C665	CJNG24CF001	TABLE 658	Hot leg ECC injection flow loop 1
A686	QJB02CP001	TMDVOL 710	Nitrogen pressure
A867	QJB02CT001	TMDVOL 710	Nitrogen temperature
C579	CQJB20CF001H	TMDJUN 712	Nitrogen flow
C580	CKTA06CF001H	TMDJUN 805	Lower plenum drain rate
A679	JAA01CP001L	P-184030100	Upper plenum pressure
C839	C2A08:58PC09		Test vessel liquid level
C841	CJAA01CL003		Downcomer liquid level

Figure 8.2-268 S-RELAP5 Nodalization for UPTF Tests 10 and 12

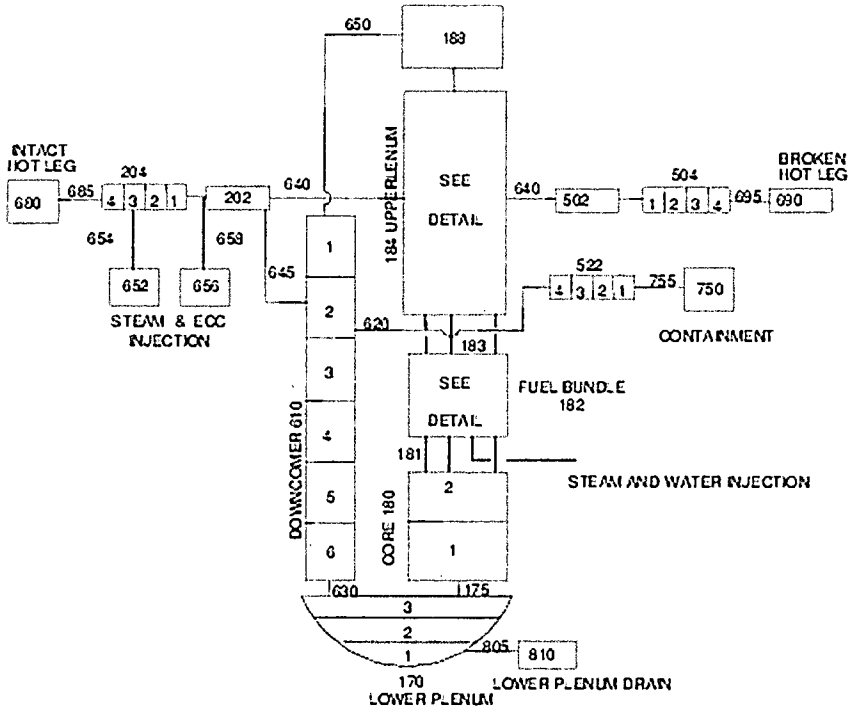

Figure 8.2-269 S-RELAP5 Nodalization Details

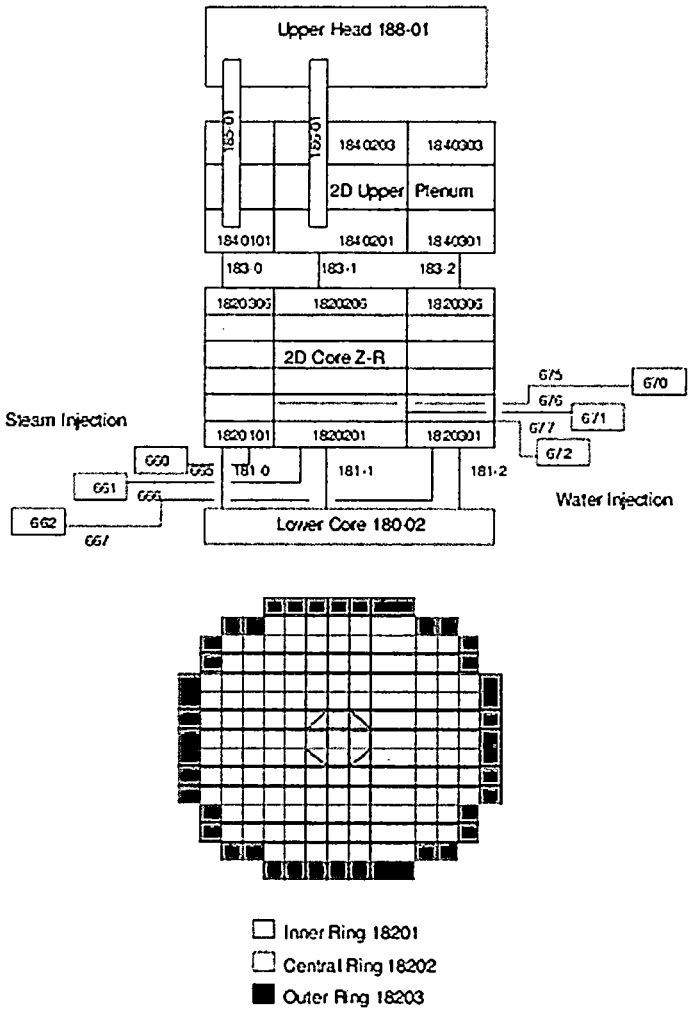

Figure 8.2-270 Lower Plenum Drain Flow Boundary Condition Test 10 Run 080

Figure 8.2-271 Core Steam Injection Temperature Boundary Condition Test 10 Run 080

Figure 8.2-272 Core Steam Flow Boundary Condition Test 10 Run 080

Figure 8.2-273 Broken Cold Leg Pressure Boundary Condition Test 10 Run 080

Figure 8.2-274 Combined Intact Hot Leg Pressure Boundary Condition Test 10 Run 080

Figure 8.2-275 Broken Hot Leg Pressure Boundary Condition Test 10 Run 080

Figure 8.2-276 Hot Leg ECC Temperature Boundary Condition Test 10 Run 080

Figure 8.2-277 Hot Leg ECC Flow Boundary Condition Test 10 Run 080

Figure 8.2-278 Hot Leg Steam Injection Pressure Boundary Condition Test 10 Run 080

Figure 8.2-279 Hot Leg Steam Injection Flow Boundary Condition Test 10 Run 080

Figure 8.2-280 Calculated Kutateladze Parameters Test 10 Run 080

Figure 8.2-281 Upper Plenum Pressure Comparison Test 10 Run 080

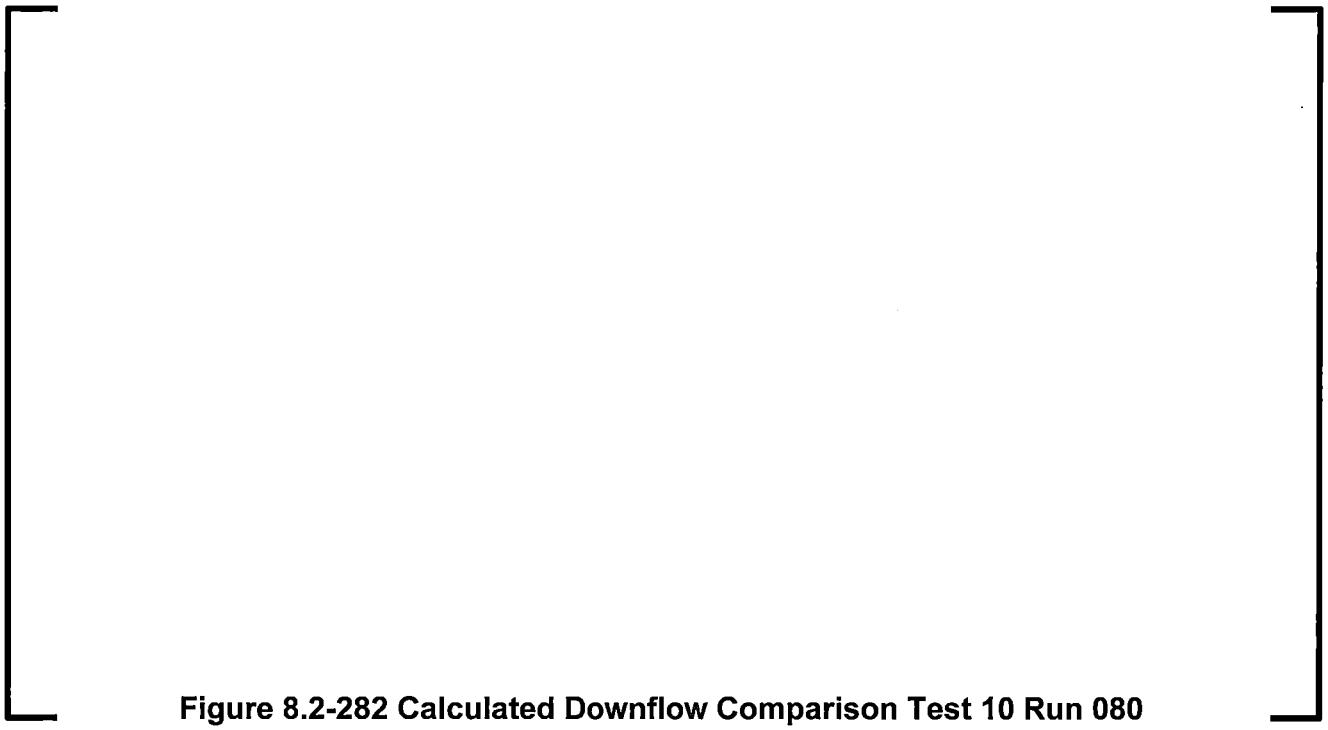

Figure 8.2-282 Calculated Downflow Comparison Test 10 Run 080 (m=1.0, c=1.8)

Figure 8.2-283 Lower Plenum Drain Flow Boundary Condition Test 12 Run 014

Figure 8.2-284 Core Steam Injection Temperature Boundary Condition Test 12 Run 014

Figure 8.2-285 Core Steam Flow Boundary Condition Test 12 Run 014

Figure 8.2-286 Broken Cold Leg Pressure Boundary Condition Test 12 Run 014

Figure 8.2-287 Broken Hot Leg Pressure Boundary Condition Test 12 Run 014

Figure 8.2-288 Hot Leg ECC Temperature Boundary Condition Test 12 Run 014

Figure 8.2-289 Hot Leg ECC Flow Boundary Condition Test 12 Run 014

Figure 8.2-290 Hot Leg Steam Injection Pressure Boundary Condition Test 12 Run 014

Figure 8.2-291 Hot Leg Steam Injection Flow Boundary Condition Test 12 Run 014

Figure 8.2-292 Nitrogen Injection Temperature Boundary Condition Test 12 Run 014

Figure 8.2-293 Nitrogen Injection Flow Boundary Condition Test 12 Run 014

Figure 8.2-294 Calculated Kutateladze Parameters Test 12 Run 014

Figure 8.2-295 Upper Plenum Pressure Comparison Test 12 Run 014

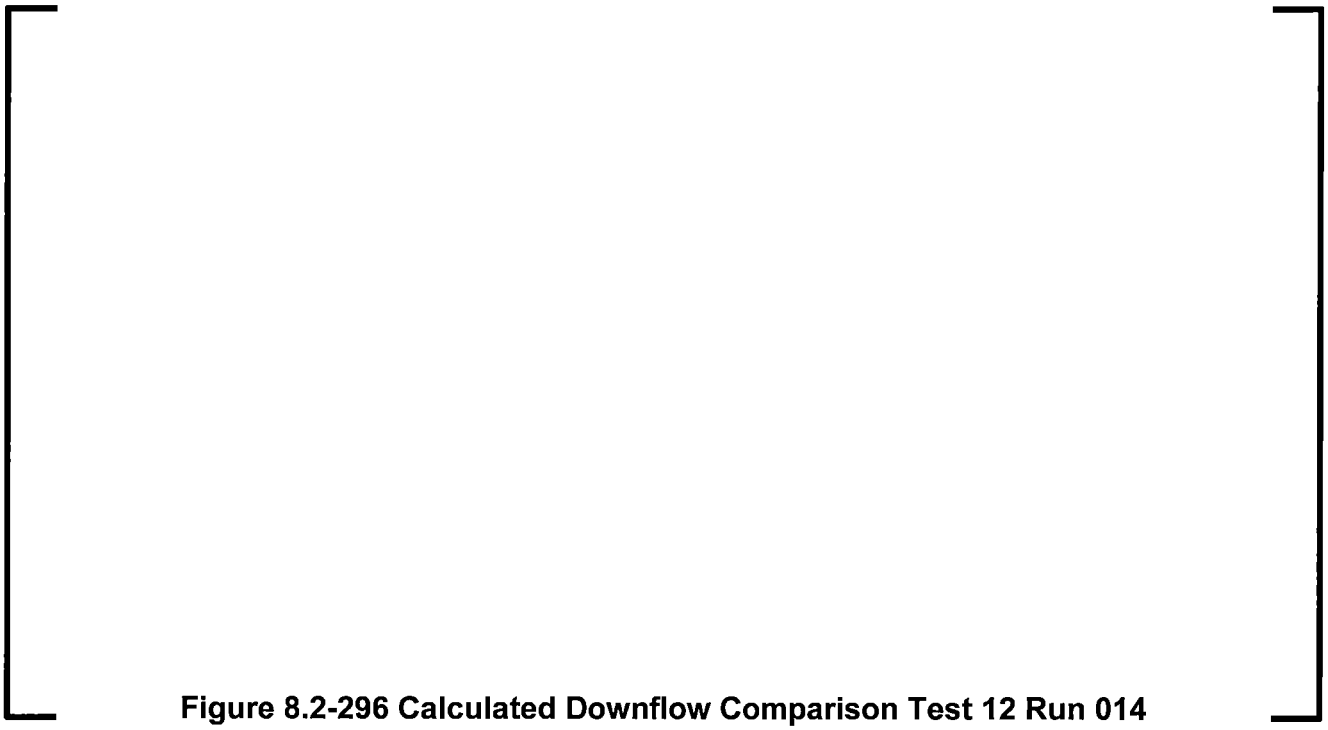

Figure 8.2-296 Calculated Downflow Comparison Test 12 Run 014 (m=1.0, c=1.8)

8.2.9.6 UPTF Tests 10B and 29B

UPTF Test 10, Run 081 (Test 10B), and Test 29, Runs 211 and 212 (Test 29B), were analyzed to provide specific S-RELAP5 input modeling guidelines for the hot leg and steam generator inlet plenum regions. This was to ensure adequate prediction of the liquid entrainment to the steam generator tube region, and to limit countercurrent flow at the UTP during the reflood phase of a postulated LBLOCA. These tests were separate effect tests specifically designed under the 2D/3D program to investigate water mass distribution in the upper plenum, hot leg, and steam generator inlet plenum, and tube regions during reflood. Limiting water down flow into the core is important because it provides a source of additional core cooling and reduces the likelihood of water carryout to the steam generators. Water carryover to the steam generators is directly related to the prediction of steam binding, which results from liquid vaporization in the steam generator tubes.

8.2.9.6.1 Summary and Conclusions

The results of the simulation of Tests 10B and 29B show that S-RELAP5 will conservatively predict liquid entrainment to the steam generator tube region and the countercurrent flow at the upper core tie plate (UTP) of a PWR during the LBLOCA reflood phase.

Based on the results of the evaluations of Tests 10B and 29B, modeling guidelines (Appendix A.1.3.6.1.2) are provided for incorporation into the S-RELAP5 input modeling guidance for PWR large break LOCA transients. These specific modeling options promote entrainment of liquid to the STGR tube region and limit liquid downflow from the upper plenum to the core region.

8.2.9.6.2 Test Description (UPTF Tests 10B and 29B)

For Tests 10B and 29B, the UPTF system was configured to simulate the reflood phase of a cold leg break PWR LBLOCA. For these tests, the lower plenum and lower downcomer were filled with water to block steam flow directly from the core to the downcomer and cold legs. A mixture of steam and water was injected into the core simulator to simulate reflood steam generation and water entrainment. The injected steam and entrained water then flowed to the hot legs via the upper core support plate and upper plenum. From the hot legs, the steam/water mixture flowed into the steam generator simulator inlet plenum and from there to the cyclone separators where water was separated from the mixture. The separated water was stored and measured in holding tanks, while the steam (and any unseparated water droplets) flowed onward through the pump simulators, intact cold legs, upper downcomer and broken cold leg, and flowed out the break into the containment simulator. Each test consisted of a sequence of phases using different steam and water injection rates. Test 10B was a 300 second transient consisting of four different flow phases. The conditions for the four phases of this test are given in Table 8.2-22 .

Test 29B Runs 211 and 212 were 900 second transients consisting of six different flow phases. Each phase consisted of a period of constant steam and water flow rates, followed by a period of no flow. The first two phases of Run 211 and last three phases of Run 212 were flawed. Consequently, the S-RELAP5 predictions will be compared to Run 212 data from Phases 1 and 2 (0 through 300 seconds), and Run 211 data from Phases 3 through 6 (300 through 900 seconds). The test parameters for the six phases in combined Run 212/211 are shown in Table 8.2-23.

The specific LBLOCA reflood phenomena addressed by UPTF Tests 10B and 29B benchmarks are:

- Steam generator steam binding
- Upper plenum two-phase flow

- Core-to-upper plenum countercurrent flow
- Upper plenum, hot leg, and steam generator inlet plenum entrainment and deentrainment

8.2.9.6.3 S-RELAP5 Model Description (UPTF Tests 10B and 29B)

The S-RELAP5 input models for UPTF Tests 10B and 29B were developed from UPTF facility data, facility specifications, and data reports provided by the UPTF research team (References 8.2-45 through 8.2-48).

Hydraulic Nodalization - Tests 10B and 29B

Nodalization diagrams for the Test 10B and 29B S-RELAP5 system model are shown in Figure 8.2-297 and Figure 8.2-298. Significant model details for the Test 10B and 29B analyses include:

- Water and steam injection sources are connected to the core simulator region.
- A greatly simplified cold-leg model is used because the cold legs play only a minor role in these simulations.
- Upper core region modeling uses specialized nodalization to simulate the injection of steam and water.
- Upper plenum modeling is in accordance with standard guidelines.
- The intact hot legs are lumped into one set of nodes and the broken loop hot leg and other set. Both provide an exit path for the injected steam-water mixture. The sink and pressure boundary conditions are modeled as a time dependent volume at the outlet junction of steam generator (STGR) simulator lower steam/water separator.
- [

]

- [

]

- [

]

- [

]

- [

]

Initial Conditions and Boundary Conditions

Initial conditions for the S-RELAP5 model of Tests 10B and 29B consisted primarily of the pressure and temperature data from (References 8.2-45 and 8.2-46). All flows were initialized to zero, consistent with the stagnant conditions that prevailed at the initiation of each test.

The boundary condition sources and sinks required for Test 10B and 29B analyses were as follows:

- Source for core simulator steam injection
- Source for core simulator water injection

[5] [

]

- Sink for intact hot-leg outlet flow
- Sink for broken hot-leg outlet flow
- Sink for broken cold-leg outlet flow
- Sink for lower plenum water drain

These boundary conditions were applied by means of time-dependent volume components and time-dependent junction components as described earlier in Section 8.2.9.6.3. The time-dependent tabular data required for the boundary conditions was obtained from KWU test data files and is shown graphically in the KWU Experimental Data Reports for Tests 10 and 29 (References 8.2-47 and 8.2-48). The sensors that supplied the fluid conditions and flow rates for the boundary conditions are listed in Table 8.2-24 and are described in Reference 8.2-39. Select boundary conditions are compared in Figure 8.2-299 and Figure 8.2-300 for Test 10B and Figure 8.2-301 through Figure 8.2-305 for Test 29B. These figures depict input and should not be interpreted as indicating capability of the code to predict phenomena.

8.2.9.6.4 Simulations and Comparison with Experimental Results (UPTF Tests 10B and 29B

Figure 8.2-306, Figure 8.2-307 and Figure 8.2-310 present plots of Kutateladze parameters at the core exit calculated from the S-RELAP5 results for UPTF Test 10 Run 080, Test 10 Run 081 and Test 29, respectively. Values, that were calculated using the UPTF correlation (which was developed using the UPTF CCFL tests), are also shown in these figures. The figures clearly show S-RELAP5 calculates conservative liquid down flow relative to the UPTF correlation.

Figure 8.2-309 and Figure 8.2-312 show the liquid carryover to the steam generators for UPTF Tests 10 and 29, respectively. Again, both plots clearly show S-RELAP5 generally overpredicts the carryover of liquid to the steam generators.

The following general observations can be made regarding the S-RELAP5 simulations of Tests 10B and 29B.

- Overall the predictions of total water carryover to the steam generator simulators indicate that the code overpredicts (adequate agreement with data) the liquid carryover to the steam generators. This is conservative because it will result in an overprediction of steam binding, which in turn will reduce the reflood flooding rate.
- Overall the predictions of total fallback to the lower plenum region also were shown to be conservative in that the fallback to the core was underpredicted (adequate agreement with data). This is consistent with the overprediction of liquid carryover to the steam generators because more liquid will be present in the upper plenum to be carried over to the steam generators.

Based on the results of the evaluations of Tests 10B and 29B, the following modeling guidelines are provided for incorporation into the S-RELAP5 input modeling guidance for PWR large break LOCA transients:

[

]

[6] [

]

These specific modeling options promote entrainment of liquid to the STGR tube region and limit liquid downflow from the upper plenum to the core region and they are incorporated in the input development guidelines (Appendix A).

In summary, it can be concluded that S-RELAP5 will calculate acceptable liquid entrainment to the steam generator tube region and countercurrent flow at the upper core tie plate for a PWR during the reflood phase of a LBLOCA.

Table 8.2-22 Test Phase Parameters for Test 10B

Phase	StartTime (s)	EndTime (s)	SteamInjectionRat (kg/s) (lbm/s)	WaterInjectionRate (kg/s) (lbm/s)
1	35	75	125 276	60 132
2	75	135	125 276	16 35
3	135	196	110 243	16 35
4	195	255	87 192	16 35

Table 8.2-23 Test Phase Parameters for Test 29B

Phase	StartTime (s)	EndTime (s)	SteamInjectionRat (kg/s) (lbm/s)	WaterInjectionRate (kg/s) (lbm/s)
1	35	175	102 225	140 309
2	175	320	87 192	153 337
3	320	465	100 221	90 198
4	465	615	85 187	101 223
5	615	770	101 223	47 104
6	770	900	85 187	63 139

Table 8.2-24 Application of Boundary Conditions for Tests 10B and 29B

Boundary Condition Components	Sensor	Description
TMDPV 660, 661, 662 and TMDPJ 665,666,667	Temperature: JKG01CT002, JKG03CT002 and QHA01CT003 (average) Flow: CJKG01CF001H, CJKG03CF001H and CJKG30CF001 (sum)	Steam injection to core simulator
TMDPV 670,671, 672 and TMDPJ 675,676, 677	Pressure: JKF01CP002 Temperature: JKF01CT004 Flow: CJKF01CF001	Water injection to core simulator
TMDPV 230	Pressure: JEC01CP11, JEC02CP11, JEC03CP11 and JEC04CP11 (average)	Pressure sink for lumped intact hot leg
TMDPV 130	Pressure: JEC01CP11, JEC02CP11, JEC03CP11 and JEC04CP11 (average)	Pressure sink for broken hot leg
TMDPV 750	Pressure: JEC04CP21	Pressure sink for broken cold leg
TMDPV 810 and VALVE 805	Pressure: Arbitrary sink pressure of 1.0E5 Pa was used. Control system provided flow regulation.	Lower plenum drain flow

Figure 8.2-297 S-RELAP5 Nodalization for UPTF Tests 10B and 29B

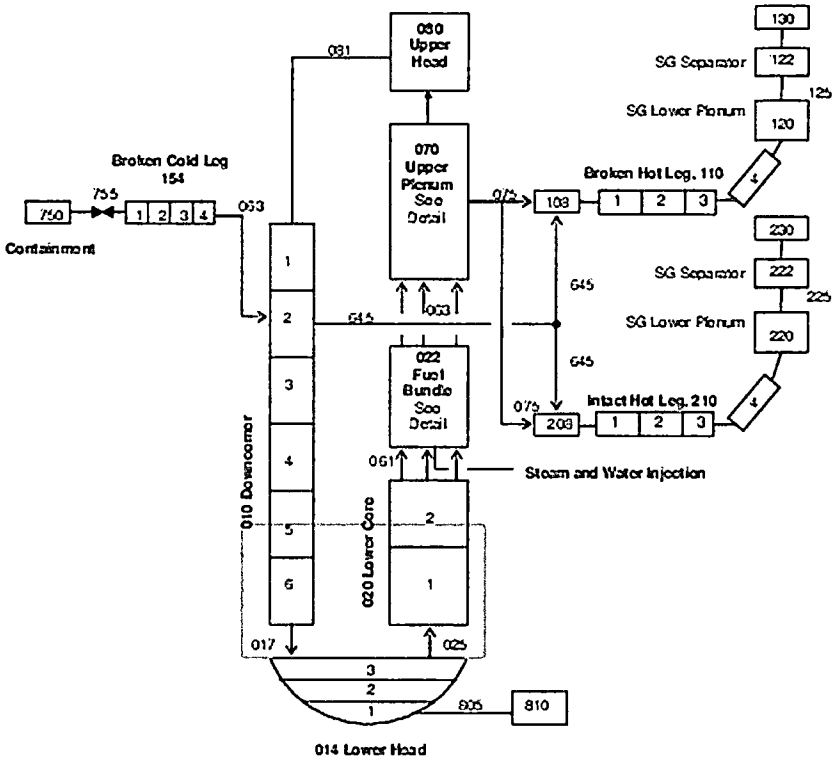

Figure 8.2-298 S-RELAP5 Nodalization Details

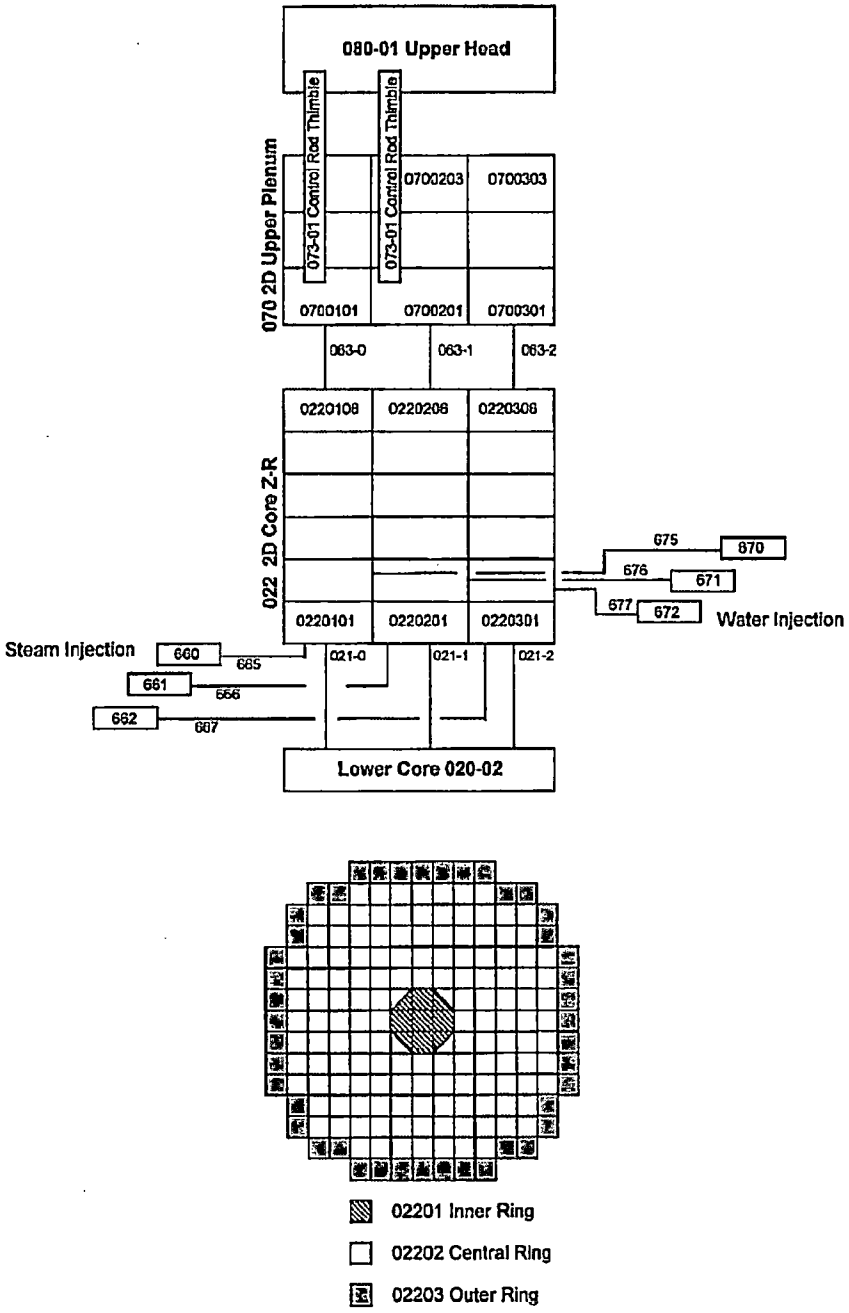

Figure 8.2-299 Core Steam Flow Boundary Condition Test 10B

Figure 8.2-300 Core Water Flow Boundary Condition Test 10B

Figure 8.2-301 Intact Hot Legs Pressure Boundary Condition Test 29B

Figure 8.2-302 Broken Hot Leg Pressure Boundary Condition Test 29B

Figure 8.2-303 Broken Cold Leg Pressure Boundary Condition Test 29B

Figure 8.2-304 Core Steam Flow Boundary Condition Test 29B

Figure 8.2-305 Core Water Flow Boundary Condition Test 29B

Figure 8.2-306 Countercurrent Flow of Steam and Water UPTF Test 10 Run 080

Figure 8.2-307 Countercurrent Flow of Steam and Water Test 10B Run 081

Figure 8.2-308 Upper Plenum Pressure Test 10B

Figure 8.2-309 Water Carryover to Steam Generators Test 10B

Figure 8.2-310 Countercurrent Flow of Steam and Water Test 29B Run 212/211

Figure 8.2-311 Upper Plenum Pressure Test 29B

Figure 8.2-312 Cumulative Water Carryover to Steam Generators Test 29B

8.2.9.7 UPTF Test 11

UPTF Test 11 is a series of quasi-steady-state SETs conducted under the 2D/3D program to investigate countercurrent flow of steam and saturated water in the hot leg of a PWR under LBLOCA conditions. The test consisted of a series of flow conditions to map out countercurrent flow curves at two different pressure conditions, 0.3 MPa (low pressure case) and 1.5 MPa (high pressure case). Also under the 2D/3D program, MPR Associates (Reference 8.2-49) developed a Wallis form CCFL correlation by using a least square fit to the data. The MPR CCFL correlation [ ] coefficients are: [ ] For Revision 3, [ ] Since the CCFL correlation was developed from UPTF Test 11 data, the assessment of the phenomena is best performed with independent data. Therefore, the UPTF Test 11 assessment was not performed as part of the Revision 3 methodology assessments. However, since other UPTF CCFL assessments demonstrated that the code calculated CCFL replicates the input parameters used in the analysis, further assessment is unnecessary. The UPTF test facility is full-scale. Therefore, the CCFL model developed from the UPTF Test 11 is to be applied [ ]

8.2.10 Westinghouse/EPRI One-Third Scale Test

8.2.10.1 Introduction

One of the important phenomena identified in a pressurized water reactor (PWR) large-break loss-of-coolant accident (LBLOCA) is the mixing of emergency core cooling system (ECCS) water and steam in the cold leg during the accumulator and pumped safety injection phases of the LBLOCA. The controlling parameter is the interfacial condensation heat transfer coefficient, whose impact on the peak cladding temperature (PCT) calculation needs to be evaluated. To meet this need, the uncertainty range in the interfacial condensation heat transfer coefficient for the mixing process must be determined based on assessment against relevant data. In this assessment, data from 23 benchmark tests in the Westinghouse (W)/Electric Power Research Institute (EPRI) one-third (1/3) scale study (Reference 8.2-50) were selected. These data have been determined to be appropriate and representative of the conditions encountered in the accumulator and pumped safety injection phases of a PWR LBLOCA.

This section documents assessment results and the evaluation of a model for the multiplier on the interfacial heat transfer coefficient. The assessment results will be used to support the overall application of the realistic LBLOCA methodology including the implementation in S-RELAP5 of condensation model discussed in Section 8.4.2.

8.2.10.2 Summary and Conclusions

S-RELAP5 has been assessed against the following 23 benchmark tests selected from the W/EPRI 1/3 scale condensation experiments: 5-18, 5-23, 5-24, 5-25, 5-27, 5-30, 5-33, 5-34, 5-48, 5-52, 5-53, 5-57-1, 5-60, 6-41, 6-65, 6-67, 6-69, 6-73, 6-83, 6-88-1, 6-93, 6-95, and 6-99. A figure of merit was defined that approximately represents [

]

interfacial condensation heat transfer coefficient. The figure of merit was used to assess the ability of S-RELAP5 to predict interfacial heat transfer during the ECC/steam mixing process. Results, based on 23 data points, show [

] (good agreement). This indicates that S-RELAP5 slightly over predicts the interfacial condensation heat transfer coefficient in the ECC/steam mixing process.

8.2.10.3 Facility Description

Figure 8.2-313 is a schematic of the test facility. The principal portion of the test apparatus was the simulated cold leg, fabricated from 10.42-in inside diameter (I.D.) straight pipe. Two injection points were provided so the pipe lengths downstream of the injection point were equivalent to typical PWR scaled and full lengths. In a typical W PWR, the cold leg pipe length downstream of the injection point is about 16 ft, or 6×D, where D is the cold leg I.D., typically 2.7 ft. In the W 1/3 scale test, the full length is approximately 15.6 ft, and the scaled length is 6 ft, which is approximately 7×D. The injection line had an I.D. of 3.325 inch.

Superheated steam from the boiler flowed through the inlet surge tank and an inlet flow chamber before entering the test section. The inlet flow chamber was designed to yield a uniform velocity profile entering the test section. Cold water from the storage tank was allowed to enter the test section through either injection point. The effluent fluid exited the test section into the outlet surge tank. The surge tanks upstream and downstream of the test section helped maintain constant pressure boundary conditions for circumstances where large pressure oscillations occurred inside the test section. An air tank was connected to the outlet chamber of the test section and was used to control the desired test section pressure. The test section was fitted at the top and bottom with thermocouples to provide temperature data for both the vapor and liquid phase in the case of stratified flow inside the test section. Pressure drops along the test section were also measured.

In the present study, the focus is on the [

] The capability of S-RELAP5 in predicting the interfacial condensation heat transfer in the mixing of ECCS water and steam can therefore be assessed by comparing [

]

8.2.10.4 S-RELAP5 Model Description

Figure 8.2-314 shows the nodalization diagram. The simulations in this study model the surge tanks and the test section. The nodalization of the test section is consistent with the RLBLOCA methodology guidelines. A time-dependent volume (component 100) represents the steam source. A time-dependent junction (component 105) specifies the desired steam flow rate. The superheated steam flows through the inlet surge tank (component 110), the 8-in schedule 40 piping (component 120), and the inlet flow chamber (component 130). The simulated cold leg section has a pipe (component 140), a branch (component 142), and another pipe (component 180) with two nodes. The ECC injection uses a time-dependent junction (component 155). The condensation model is used in the ECC injection and cold leg nodes downstream of the injection node. The desired water temperature is specified at a time-dependent volume (component 150). A single junction (component 185) connects the test section outlet to the outlet surge tank (component 190). A time-dependent volume (component 200) specifies the back pressure. Air is modeled in this boundary node in order to allow air flow back into the test sections (which was observed in some of the high ECC injection tests).

Reference 8.2-50 provides no information on the initial state because the tests were intended to be steady-state tests. In the simulation, the system is assumed to be initially filled with single-phase steam (superheated) flowing at the desired steam flow rate, temperature, and pressure. ECC water at the desired liquid temperature and flow rate is then injected (at 5 s into the transient) at junction 155. The transient was run until a reasonably steady state is achieved.

8.2.10.5 Calculations

Twenty-three runs were assessed of which 13 correspond to the pumped safety injection phase and the other 10 correspond to the accumulator injection phase. Otherwise, all 23 tests used the same input model except for the values of inlet temperature, inlet flow rate, and system pressure, all of which are test-specific. Table 8.2-25 gives the flow conditions for each test.

The condensation model described in Section 8.4.2 [

]

The use of a noncondensable state exit boundary condition enabled the modeling of air in the test section in test cases where air may have been present. This boundary condition is based on examinations of the W/EPRI test data in Reference 8.2-50, which indicate some W/EPRI tests had a surge of air from the exit surge tank back into the test section.

The test section was nodalized such that [

] This approach allows [

]

Table 8.2-25 lists the range of test conditions used for this assessment study. As mentioned in the introduction, the W 1/3-scale tests were performed to assess the ECC/steam mixing process during the reflood-accumulator and reflood-safety injection period in a typical PWR LBLOCA scenario. The previous assessment examined a referenced Westinghouse 3-loop PWR for a typical LBLOCA scenario and confirmed the appropriateness of the W/EPRI data, and, in particular, the use of the test matrix in Table 8.2-25 . The test matrix for this study includes all 19 tests from Reference 8.2-50 plus four more tests to give more complete coverage at higher temperatures. The four additional tests fall within the range of conditions for the previous 19 tests.

In the Revison 0 assessment the accumulator injection period for the typical plant was from approximately 10 to 50 seconds (Reference 8.2-51). Low-pressure safety injection and high pressure safety injection were initiated at around 45 seconds. The primary pressure during the reflood phase was about 40 to 50 psia.

The liquid and vapor phasic mass fluxes in the cold leg during the accumulator injection period were about 400 and 10 lb/ft^2-s, respectively, and about 50 and 10lb/ft^2-s, respectively, during the reflood safety-injection period. In the Revision 0 sample calculation, the liquid temperatures in the intact cold legs (Loops 2 and 3) remained subcooled by about 70 °F, and the vapor temperatures remained superheated by about 270 °F. The predominant flow regime during both the reflood-accumulator and reflood-safety injection periods were horizontal stratified flow. This was the case in either the mixing volume or in the last volume of the cold leg.

Table 8.2-26 compares the relevant flow conditions from the Revision 0 sample calculation to the test matrix. An examination of Table 8.2-26 shows the range of conditions considered in the test matrix is similar to the range in the sample calculation. Hence, the test matrix selected for this study is appropriate for the present assessment and can be used to determine the uncertainty associated with the code's capability to predict the ECC/steam mixing process during the reflood period of a LBLOCA.

8.2.10.6 Results

The primary model output sought in this study is the effluent liquid temperature, i.e., the liquid phase temperature at the exit of the test section. For all cases run, the thermal hydraulic variables showed no signs of oscillations at 100 seconds. Thus, the effluent temperature at 100 seconds is used for comparison to the measured data.

Table 8.2-27 compares the calculated and measured effluent temperatures for liquid and vapor in all 23 benchmark cases. The information from Table 8.2-27 is plotted in Figure 8.2-315.

8.2.10.7 Determination of Multiplier and Range

[

]

8.2.10.8 Conclusions

The ability of S-RELAP5 in simulating the ECC/steam mixing process during the reflood phase of a LBLOCA has been assessed, using data from the W 1/3-scale test. The test conditions have been compared against typical plant calculations and shown to be representative of the expected conditions during the accumulator injection and pumped safety injection periods of a typical LBLOCA. The model used a nodalization scheme that was consistent with plant nodalization of the cold leg. The following conclusions are drawn:

1. The results based on the figure of merit R used for evaluating [

   ] show there is acceptable agreement between the code calculations and the W/EPRI test data.

2. Based on the 23 W/EPRI benchmark test cases, [

] indicates that the code has a slight tendency to over predict the interfacial condensation heat transfer.

3. The level of agreement between the calculated values and the measured values shows the S-RELAP5 code capably predicts interfacial condensation heat transfer. This study validates the use of S-RELAP5 for similar thermal-hydraulic applications and supports Revision 3 of the RLBLOCA methodology.

Table 8.2-25 Test Conditions of Westinghouse 1/3 Scale Assessment

Run No.	Pressure (psia)	Steam Temp. (°F)	Steam Flow (lb/s)	ECC Temp. (°F)	ECC Velocity (ft/s)
5-18	22.2	251	3.058	120	12.61
5-23	50.0	285	6.114	118	12.38
5-24	49.7	285	6.114	121	16.49
5-25	50.1	504	6.125	87	4.08
5-27	34.5	505	6.095	85	12.28
5-30	23.6	504	6.094	83	8.20
5-33	49.5	505	6.125	119	12.29
5-34	49.6	506	6.109	120	16.51
5-48	45.9	509	6.388	148	16.01
5-52	22.5	238	1.418	118	4.03
5-53	22.0	237	1.430	120	6.05
5-57-1	50.2	505	6.172	122	2.01
5-60	21.8	490	3.091	117	4.15
6-41	39.7	510	6.434	151	41.00
6-65	22.1	506	6.435	150	70.18
6-67	22.2	506	6.432	125	72.07
6-69	22.4	502	6.442	125	40.20
6-73	21.8	506	4.475	151	70.48
6-83	21.9	520	6.390	147	70.55
6-88-1	21.7	515	6.415	122	40.65
6-93	22.0	503	6.495	100	70.56
6-95	50.1	504	6.390	151	40.75
6-99	50.1	501	6.405	124	69.94

Table 8.2-26 Comparison of Plant and Test Conditions for ECC/Steam Mixing Process, Westinghouse/EPRI

Condition	Typical Plant	Test Matrix, in
Liquid flux in reflood-accumulator period (lb/ft^2-s)	400	200 to 430
Vapor flux in reflood-accumulator period (lb/ft^2-s)	10	10
Liquid flux in reflood-safety injection period (lb/ft^2-s)	50	12 to 100
Vapor flux in reflood-safety injection period (lb/ft^2-s)	10	5 to 10
System pressure (psia)	40 to 50	22 to 50
Flow regime	horizontal stratified	horizontal stratified
Vapor temperature (°F)	500 in intact loops	490 to 520
ECC temperature (°F)	90	85 to 151

Table 8.2-27 Comparison of Effluent Temperature for the Plant-Consistent Model, Westinghouse/EPRI

Run No.	Liquid, Data (°F)	Liquid, Calculated (°F)	Vapor, Data (°F)	Vapor, Calculated (°F)

Table 8.2-28 [ ] Interfacial Condensation Heat Transfer Model in S-RELAP5, Westinghouse/EPRI

Run No.	[ ]
5-18	
5-23	
5-24	
5-25	
5-27	
5-30	
5-33	
5-34	
5-48	
5-52	
5-53	
5-57-1	
5-60	
6-41	
6-65	
6-67	
6-69	
6-73	
6-83	
6-88-1	
6-93	
6-95	
6-99	

Figure 8.2-313 Schematic of Westinghouse ECC Injection Test Facility

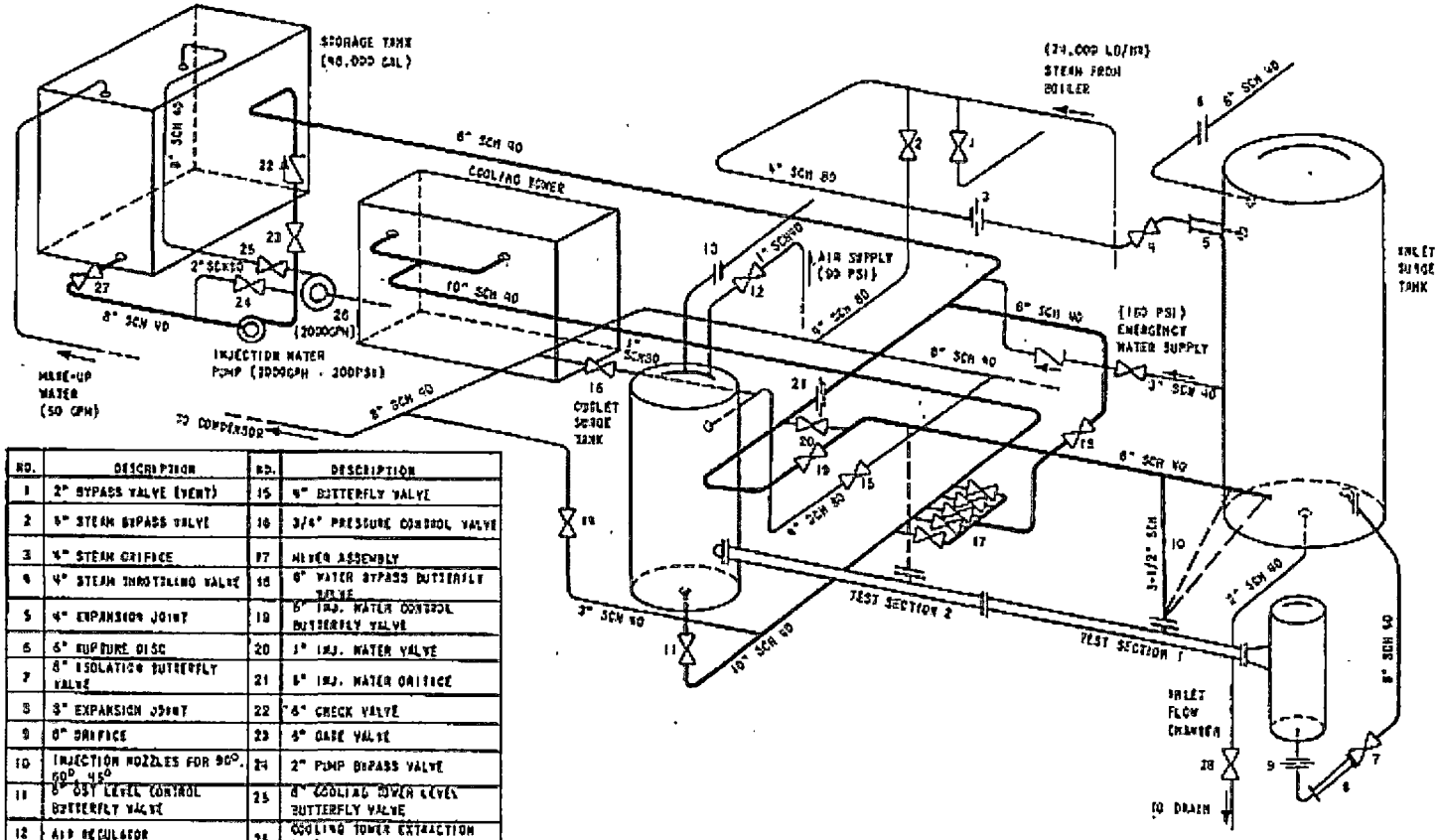

NO.	DESCRIPTION	NO.	DESCRIPTION
1	2" BYPASS VALVE (VENT)	15	8" BUTTERFLY VALVE
2	6" STEAM BYPASS VALVE	16	3/4" PRESSURE CONTROL VALVE
3	4" STEAM ORIFICE	17	MIXER ASSEMBLY
4	4" STEAM THROTTLING VALVE	18	6" WATER BYPASS BUTTERFLY VALVE
5	4" EXPANSION JOINT	19	6" INJ. WATER CONTROL BUTTERFLY VALVE
6	6" RUPTURE DISC	20	1" INJ. WATER VALVE
7	6" ISOLATION BUTTERFLY VALVE	21	6" INJ. WATER ORIFICE
8	3" EXPANSION JOINT	22	6" CHECK VALVE
9	6" ORIFICE	23	6" GATE VALVE
10	INJECTION NOZZLES FOR 90°, 60°, 45°	24	2" PUMP BYPASS VALVE
11	8" DST LEVEL CONTROL BUTTERFLY VALVE	25	6" COOLING TOWER LEVEL BUTTERFLY VALVE
12	AIR REGULATOR	26	COOLING TOWER EXTRACTION PUMP
13	4" RUPTURE DISC	27	8" BUTTERFLY VALVE
14	3" VALVE	28	2" DRAIN VALVE

Figure 8.2-314 Nodalization Diagram, Westinghouse/EPRI 1/3 Scale Test

Figure 8.2-315 Comparison of Calculated and Measured Effluent Temperature

8.2.11 FRIGG-2 Axial Void Distribution Tests

8.2.11.1 Introduction

The FRIGG-2 void distribution experiments were performed in the FRIGG Loop Facility in the late 1960's (Reference 8.2-52). The test section for this series of experiments, consisting of 36 heated rods, was designed to give a full-scale simulation of a boiling channel for the Marviken reactor. In 27 of these tests, the void distribution was measured by the multi-beam gamma method. The pressure of the loop in the tests was about 50 bars (5 MPa), the inlet subcooling varied from ~2 °C to ~22 °C, the mass fluxes varied from ~700 to ~1500 kg/(m^2/s), and the heat fluxes varied from ~21 to ~67 W/cm^2.

The purpose of this assessment is to validate the S-RELAP5 subcooled boiling model and interphase friction model for pre-Critical-Heat-Flux (pre-CHF) flow regimes at relatively high pressures which are typical of SBLOCA conditions. The tests were performed under steady-state conditions and the axial void distribution data are well-suited for the purpose of this validation. Calculations were performed for all 27 tests.

8.2.11.2 Summary and Conclusions

Calculations of 27 FRIGG-2 axial void distribution tests produce excellent code-data comparisons. In plots of the calculated versus the measured void fraction, the points are scattered around and close to the diagonal line, indicating good agreement between the code and the measurements. The 174 measured void fractions from the test were compared to values calculated by S-RELAP5. [

] The results confirm the applicability of S-RELAP5 interphase friction model for the pre-CHF flow regimes, particularly the slug flow regime, to the core geometry.

Strong subcooled boiling phenomena are present in about 8 of the 27 tests. For these subcooled boiling cases, the curve of void fraction vs. elevation has the expected s-like shape. The calculated void fractions are slightly below the data but are generally within the uncertainty of measurement. These results confirm the applicability of S-RELAP5 subcooled boiling model at relatively high pressures.

8.2.11.3 Facility and Test Description

Figure 8.2-316 shows the layout of the test loop of the FRIGG Loop Facility. The loop can be operated in both forced and natural circulation modes.

The test section configuration is shown in Figure 8.2-317. It was designed to give a full scale simulation of a boiling channel for the Marviken reactor. The test section consisted of a circular shroud encompassing 37 rods. Thirty-six of these rods contained heaters and were arranged in circular rings around the remaining rod, which was located in the center of the shroud and was unheated. As depicted in Figure 8.2-318, the inner ring had 6 rods, the middle ring had 12 rods, and the outer ring had 18 rods. Eight spacers held the rods in place, seven of which were located inside the test section. Figure 8.2-317 includes the axial positions of these spacers. The input deck for the S-RELAP5 model of the test section channel was prepared using the geometrical data in Table 8.2-29. Figure 8.2-316 shows that an open riser section, which was connected to a steam separator, was located above the test section. When steam was produced in the test section, the loop pressure was regulated by spraying cold water into a spray condenser. The inlet subcooling was controlled by feeding water from the cooling circuit into the upper part of the downcomer. The power to the heated rods was uniform both axially and radially from ring to ring. Most of the heat was produced in the 0.8 mm stainless steel canning of the rods.

The tests yielded measurements that include the two-phase-flow pressure drop, the axial and radial void distribution, the burnout in steady state, the natural circulation mass velocity, the stability limit, and details of the system during transient conditions. The estimated uncertainties of these measurements are given in Table 8.2-30.

This study considers only the average axial void distribution, which was determined by the multi-beam gamma method. Measurements were taken at eight void gauge stations, seven of which were inside the test section. The axial positions of these stations are shown in Figure 8.2-317. The void measurement uncertainty stated above is based on data taken from a Plexiglas mockup of the rod bundle was used to determine the accuracy of the void measurements. Twenty-seven tests with axial void distribution data are available for code-measurement comparison. All 27 were conducted at a pressure of about 50 bar (5 MPa). In this series of tests, the inlet subcooling varies from ~2 °C to ~22 °C, the mass fluxes vary from ~700 to ~1500 kg/(m^2s), and the heat flux varies from ~21 to ~67 W/cm^2. The parameters used for each test are given in Table 8.2-31.

8.2.11.4 S-RELAP5 Model Description

The S-RELAP5 nodalization for the FRIGG-2 Tests is shown in Figure 8.2-319 and Figure 8.2-320. A simple input modeling approach was used to develop the S-RELAP5 input model. Since these tests simulated the pre-CHF void distribution in the bundle, the RLBLOCA guidelines are not used in the input model development. Component number 001 is the test section. This region, spanning a length of 4.375 m, [

] The riser above the test section is modeled up to the lower end of the perforated part of the riser, where the pressure was measured (i.e., [

]). This portion of the riser [

]

The [ ] is connected to a time-dependent node (component number 210) which represents the measured system pressure, through a single junction (component number 200). The flow of water into the test section is modeled by a time-dependent node (component number 110) and a time-dependent junction (component number 100). The 36 heated rods are modeled [

]

The boundary conditions, including the values of heat flux used for the heat structures representing the rods, used for the 27 tests are given in Table 8.2-31.

8.2.11.5 Results

This assessment uses the void fraction reported by S-RELAP5 to evaluate its subcooled boiling and interphase friction models.

Representative cases shown in Figure 8.2-321 to Figure 8.2-330 compare the void fraction calculated by S-RELAP5 along the length of the test section to the values measured at the gauge stations. The regularly spaced local decreases that appear in what would otherwise be a monotonically increasing S-RELAP5 calculated void profile, result from the form losses that are applied in the model to represent the spacers. These losses reduce the fluid velocity at the spacer junction. Since the velocity of the fluids increases with elevation (as the fluids are heated), the velocity downstream of the spacers is higher than the velocity upstream, and thus, the void fraction must be lower downstream so that the product of the liquid fraction and the liquid velocity is approximately the same flowing into, and out of the junction, so that mass is conserved (the conversion to steam is insignificant over the spacer height). The gas phase plays a much smaller role in this balance of mass, because its density is substantially smaller than that of the liquid phase.

Figure 8.2-321 to Figure 8.2-325 show five cases with conditions that allowed subcooled boiling to persist for a considerable length of the test section (taken here to be a situation in which the temperature of the liquid phase is ~0.5 °C or more below the saturation temperature in over half of the test section). Therefore, these tests provide a good evaluation of the S-RELAP5 subcooled boiling model. Their void fraction profiles have the characteristic S-shape that is typical of this type of test. In general, the code tends to underpredict the void fraction; however, most of the estimates are within the uncertainty of the measurements. Overall, the code models the subcooling boiling phenomena well with good to excellent agreement between the calculated and measured values.

Figure 8.2-326 to Figure 8.2-330 show five cases in which subcooled boiling is not significant. The code's predictions for these tests better match the measured void fraction than the results for the subcooled boiling cases.

The calculated and measured void fractions are compared directly in Figure 8.2-331, which shows the measured void fraction along the x -axis and the value predicted by S-RELAP5 at the location of the measurement (gauge station) along the y -axis. Thus, a point located on the diagonal line indicates that the measured and calculated values agree. The measurement uncertainty is indicated by a horizontal line at each point.

[ ]

Figure 8.2-332 shows [

] In addition, a histogram of the data is provided at the top of the graph along [

] There is a good agreement between the histogram and distribution curve, which indicates that the deviation (discrepancy between the calculated and measured values) [

]

The statistical parameters, [

] In any case, these results show a good agreement between the code's prediction and the measured results, which implies that the physical phenomena (e.g., subcooled boiling) are well modeled.

Figure 8.2-333 shows the same plot of [

] Their values are given in Table 8.2-32. S-RELAP5 tends to underpredict slightly the void fraction at most values, but particularly at very low values (< 0.1) and at high values (> 0.666). Nevertheless, it should be emphasized that these differences are small, and the results show very good agreement between calculated and measured values.

8.2.11.6 Discussion of Results

The FRIGG-2 axial void distribution experiment is a useful benchmark for validating the S-RELAP5 subcooled boiling model, and pre-CHF (or wetted wall) interphase friction model at relatively high pressures. The void fraction in a subcooled volume is mainly determined by two processes: vaporization on the wall, and condensation in the bulk fluid (see Sections 7.6.4 and 7.7.3.2). The results of the tests with significant subcooling demonstrate the suitability of the subcooled boiling model, and indicate a noticeable improvement when the new methodology is used. The interphase friction model (Section 7.6.4) most strongly determines the axial void distribution profile. The code-measurement comparisons for all cases validate the pre-CHF interphase friction model at relatively high pressures.

All tests were performed under pre-CHF, steady-state conditions. Under such conditions, the flow regimes along the wetted wall consist of bubbly, slug, and annular-mist flow. For the core geometry, bubbly flow is usually present only below a void fraction of ~0.05, and only Test 313030 has conditions that are sufficient to produce annular-mist flow (in the top six nodes of the test section). Therefore, slug flow is the dominant flow regime in the pre-CHF region for the core geometry. The results of this assessment confirm that using slug flow to represent the flow through the core under these conditions is a reasonably good approximation of the physical flow (see Section 7.6.2.8 for further discussion). They also indicate that the local two-fluid interphase friction model can perform as well as the drift-flux model under steady-state conditions (Sections 7.6 and 7.6.2.8).

Table 8.2-29 Test Section Dimensions, FRIGG Loop Facility

Number of heated rods	36
Heated length (m)	4.375
Heat rod, OD (m)	0.0138
Unheated center rod, OD (m)	0.02
Shroud, ID (m)	0.1595
Number of spacers	7

Table 8.2-30 Measurement Uncertainties, FRIGG-2 Tests

Void fraction	±2.5%
Pressure	±0.3 bar (0.03 MPa)
Temperature	±0.5 °C
Mass Flux	±20.0 kg/m^2 -s
Power	±2.5%

Table 8.2-31 Parameters, FRIGG-2 Void Distribution Experiments

Test No.	Pressure (bars)	Inlet Subcooling (K)	Heat Flux (W/cm^2)	Mass Flux (kg/m^2-s)
313001	49.6	5.0	22.0	1492
313003	49.6	2.6	22.0	1096
313004	49.8	3.7	22.0	1103
313005	49.8	3.7	22.0	1110
313006	50.0	3.7	22.0	729
313007	50.0	11.7	22.0	1110
313008	50.0	4.3	43.9	1471
313009	50.0	4.4	43.6	1107
313010	50.0	4.6	43.6	687
313012	49.7	4.2	20.9	1457
313013	49.7	4.6	42.9	1120
313014	49.7	11.0	42.9	1163
313015	49.7	11.0	42.7	1163
313016	49.6	19.3	42.6	1208
313017	49.6	2.4	64.4	1464
313018	49.7	3.7	64.3	1124
313019	49.5	8.6	64.3	1177
313020	49.7	22.4	64.6	1159
313024	49.7	4.2	21.6	858
313027	50.0	4.9	41.3	886
313030	50.0	5.1	66.7	823
313034	50.0	4.6	22.0	1012
313037	50.0	4.4	43.9	1026
313040	50.0	4.4	22.0	792
313043	50.0	3.5	43.9	823
313056	49.9	9.5	43.9	918
313060	49.4	10.5	21.5	792

Table 8.2-32 Comparison of Calculated and Measured Void Fraction, FRIGG-2 Tests

[
]

Figure 8.2-316 Schematic of FRIGG Loop System

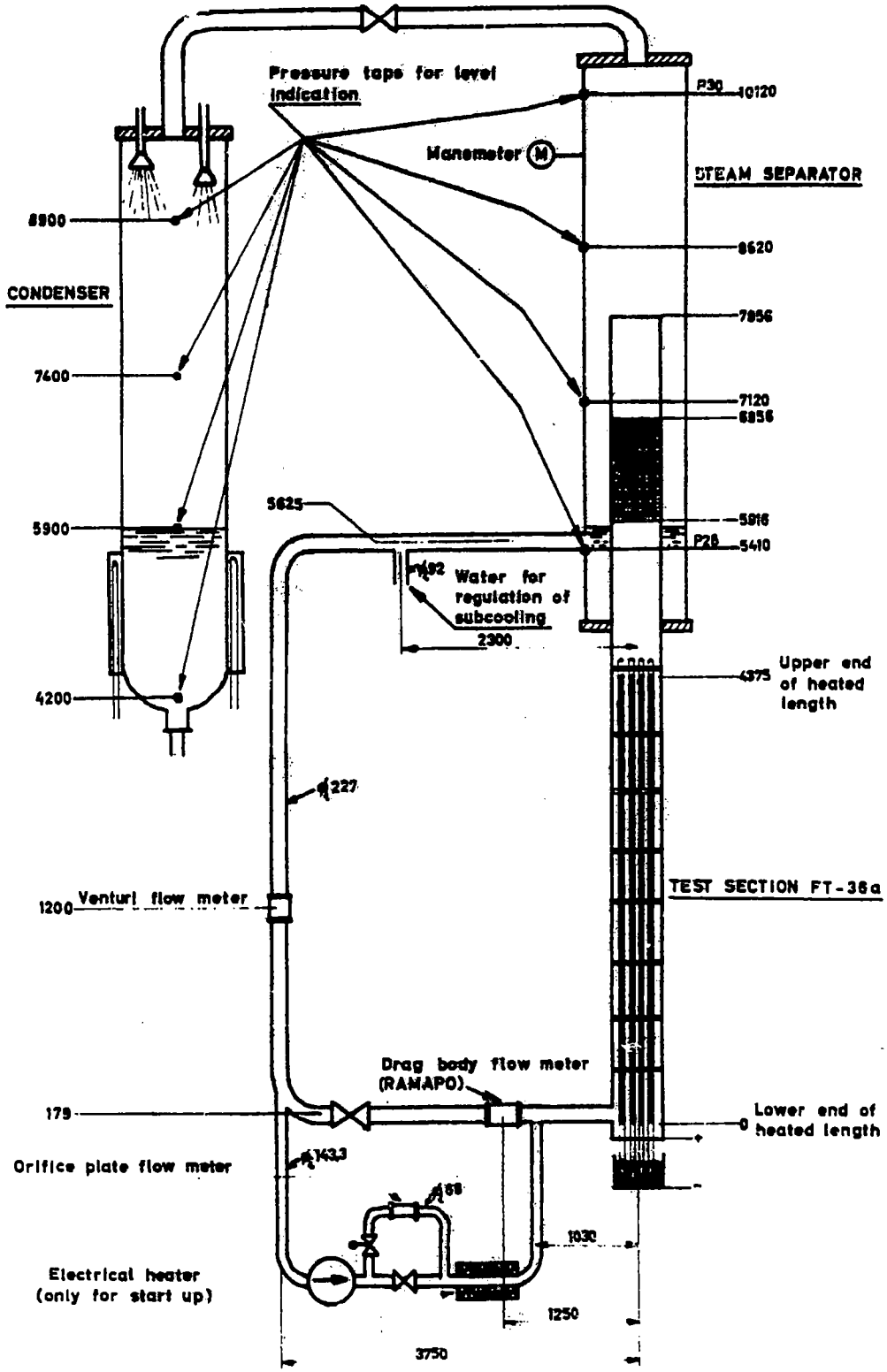

Figure 8.2-317 FRIGG Loop Test Section

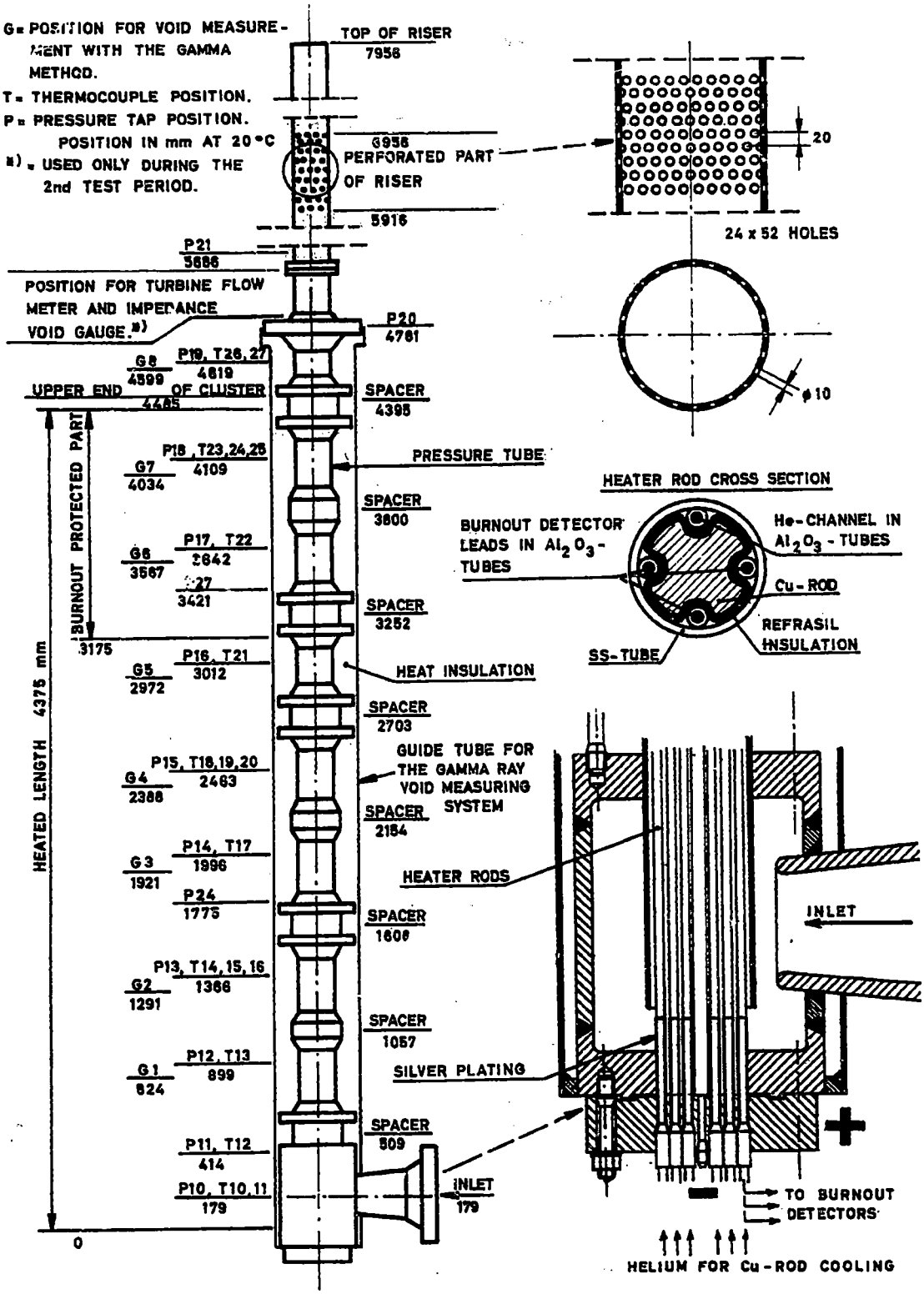

Figure 8.2-318 Cross Section of FRIGG-2 Test Assembly

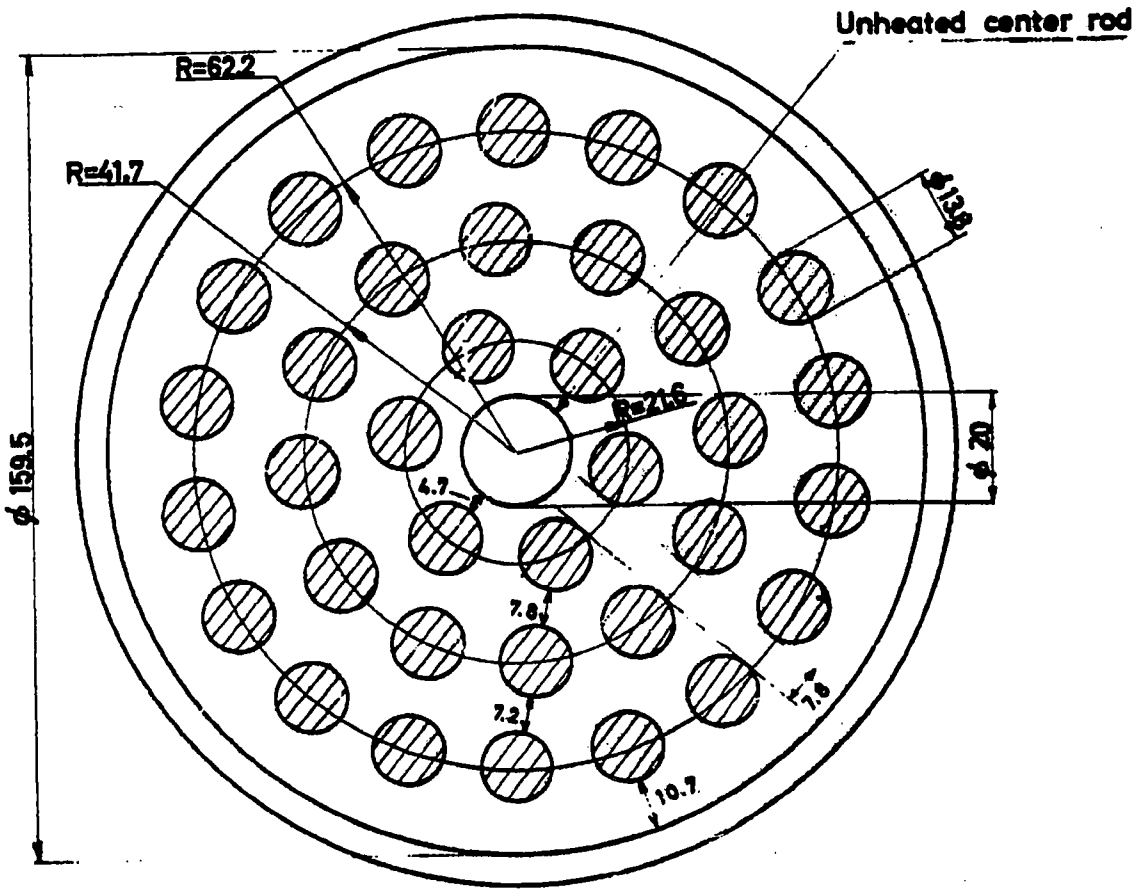

Figure 8.2-319 Nodalization for FRIGG-2 Void Distribution Tests

Figure 8.2-320 Nodalization of the Test Section, FRIGG-2

Figure 8.2-321 Comparison of Calculated and Measured Void Fraction, FRIGG-2 Test 313007

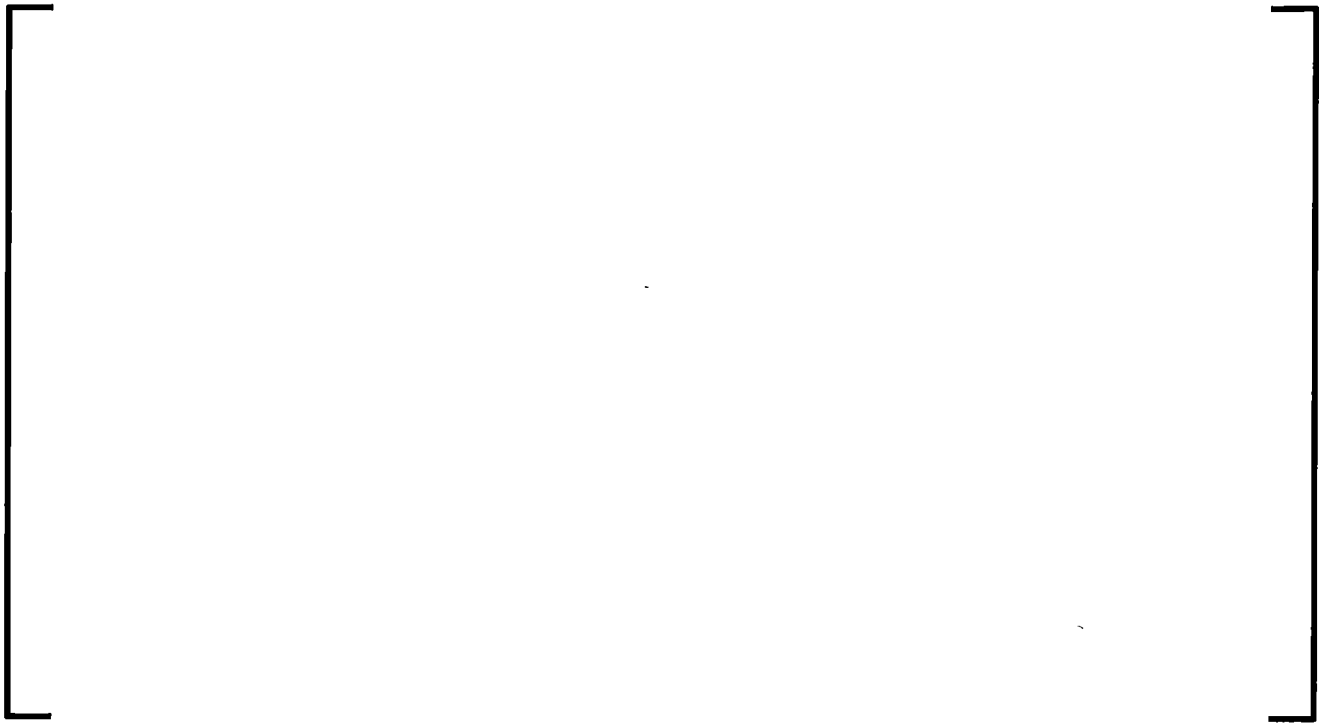

Figure 8.2-322 Comparison of Calculated and Measured Void Fraction, FRIGG-2 Test 313014

Figure 8.2-323 Comparison of Calculated and Measured Void Fraction, FRIGG-2 Test 313016

Figure 8.2-324 Comparison of Calculated and Measured Void Fraction, FRIGG-2 Test 313020

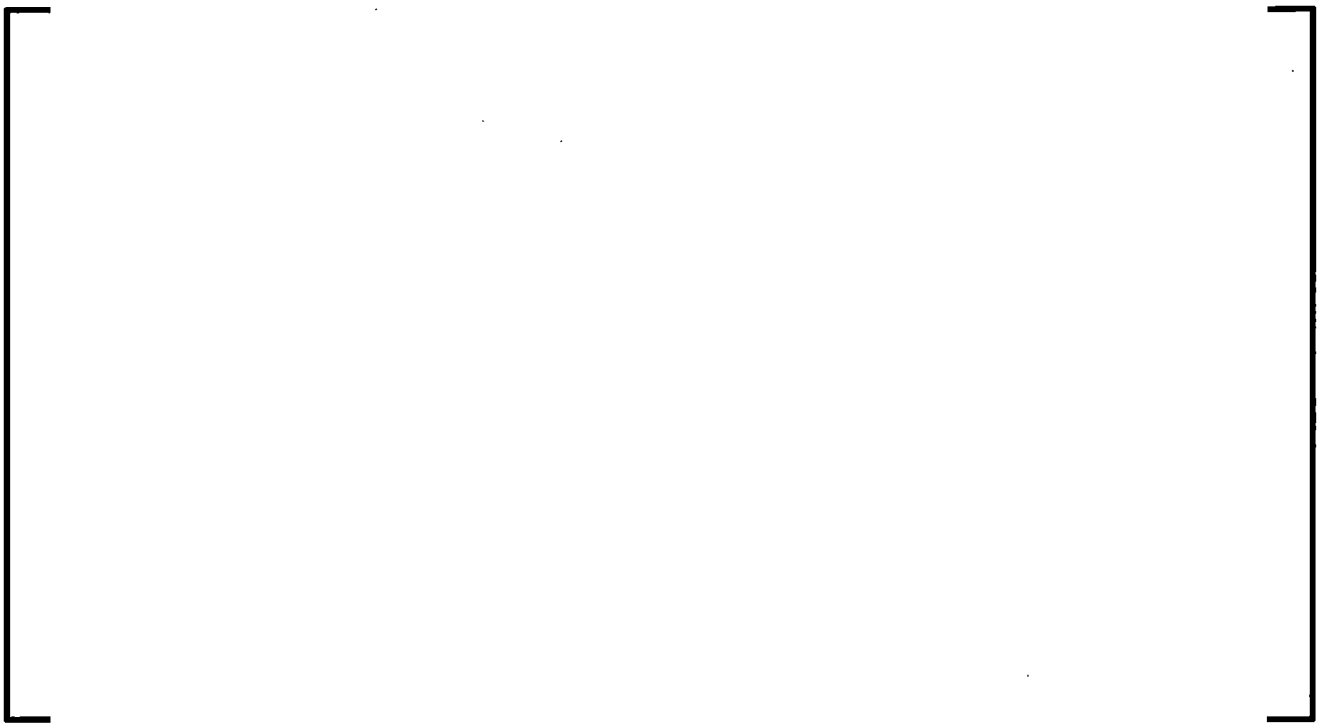

Figure 8.2-325 Comparison of Calculated and Measured Void Fraction, FRIGG-2 Test 313060

Figure 8.2-326 Comparison of Calculated and Measured Void Fraction, FRIGG-2 Test 313010

Figure 8.2-327 Comparison of Calculated and Measured Void Fraction, FRIGG-2 Test 313013

Figure 8.2-328 Comparison of Calculated and Measured Void Fraction, FRIGG-2 Test 313017

Figure 8.2-329 Comparison of Calculated and Measured Void Fraction, FRIGG-2 Test 313019

Figure 8.2-330 Comparison of Calculated and Measured Void Fraction, FRIGG-2 Test 313030

Figure 8.2-331 Comparison of the measured void fraction to the value calculated by S-RELAP5 for all 27 FRIGG-2 tests

Figure 8.2-332 Difference between the measured void fraction and the value calculated by S- RELAP5 (calculated value minus measured value) for all 27 FRIGG-2 tests

Figure 8.2-333 Difference between the measured void fraction and the value calculated by S- RELAP5 (calculated value minus measured value) in ten regions of void fraction

8.2.12 SCTF Core-II Tests

8.2.12.1 Introduction

The Slab Core Test Facility (SCTF) Core-II Test Series was undertaken in part to obtain information that could be used to validate thermal hydraulic models in best estimate, Loss of Coolant Accident (LOCA) evaluation models. The intent of these benchmarks is to use the SCTF-II test series to assess the accuracy of the S-RELAP5 computer code. Six tests from a series of twenty-seven were chosen, representing a diverse sample of behaviors, to evaluate the performance of the RLBLOCA EM and the S-RELAP5 computer code during reactor vessel (RV) reflooding. The study objectives were (1) to assess the capability of S-RELAP5 to simulate both forced and gravity reflood transients, and (2) to study the effect of radial nodalization on reflood behavior.

8.2.12.2 Summary and Conclusions

A comprehensive assessment of the SCTF Core-II reflood experiment was performed. Six tests from the experimental program were selected for the study. The assessment was performed in two phases. Phase I assessed the capability of S-RELAP5 in both forced and gravity reflood counterpart simulations. Phase II studied the effect of radial power split and nodalization.

The tests were designed to have a long period of adiabatic heatup. The heaters were powered up, the adiabatic heatup occurred, and the safety injection started. The adiabatic heatup period is well predicted proving that the thermal properties of the heater rod fill materials and the input power are appropriate to calculate heatup behavior using S-RELAP5.

S-RELAP5 is capable of simulating both forced and gravity reflood transients. The PCT results for the forced and gravity reflood counterpart tests - Tests S2-11 and S2-AC1 and Tests S2-10 and S2-SH1 - show good agreement with the data. The radial power split and nodalization study indicates limited S-RELAP5 sensitivity to the core assembly modeling scheme and radial power distribution; supporting the modeling variations for plant-consistent radial core nodalization. Several observations can be made:

1. For the gravity case with high flooding rate (S2-AC1), all the three parameters, PCT, the time of the PCT (t_{PCT}) and the quench time (t_q), were well predicted. In general, the cladding temperature profile comparisons are good, especially at the mid-core elevations.

2. For the gravity reflood with low flooding rate (S2-SH1), t_{PCT} is predicted to occur sooner than the data for certain elevations. This is consistent with the earlier results for the counterpart Test S2-10. The cladding temperature cooldown is predicted to continue without a second heatup, whereas the data show a second peak which is turned around only after the LPCI coolant starts to penetrate the core. Thus, for the low flooding rate condition, S-RELAP5 reasonably predicts enhanced core cooling as a result of accelerated core flooding.

3. For low ACC flooding rate tests (S2-10 and S2-SH1), the cladding temperature predictions were slightly higher at bottom assembly elevations and slightly lower peaks were observed at higher elevations, compared to the data. With the low ACC flooding rates, the mixture level rises rather calmly to fill the lower low-powered assembly elevations. As the level rises through the higher-powered upper sections of the core, [

] resulting in slightly lower cladding temperature peaks. Although the cladding temperature peaks are predicted to be lower at t_{PCT}, the rate of cladding temperature cooldown and the subsequent progression of the quench front is delayed in the upper core locations. A prolonged quench front predicted by the code is attributed to the higher void fractions prevailing in the upper sections of the core.

4. The high ACC flooding rate tests (S2-11 and S2-AC1) were simulated extremely well by S-RELAP5. The predictions matched the data, depicting good agreement. With high ACC flooding rate, higher injection velocities prevent [

] contributes to the accurate code predictions of the cladding temperature profiles and the quench behavior. The time to quench the entire core is well captured.

5. The effect of core radial power split does not have a significant impact on the results, particularly on the cladding temperature responses. For the two tests considered, Test S2-17 simulates a flat radial power profile, and Test S2-18 simulates a steep radial power profile. For Test S2-18, the two nodalizations yielded about the same cladding temperature responses for most node elevations. In particular, the individual nodalization yielded slightly higher cladding temperatures than did the nominal nodalization at most elevations. The upper core nodes showed some differences in the cladding temperature profile for the two nodalization schemes. However, the results support the use of the plant-consistent radial nodalization as the sensitivity to core noding scheme is minimal. In summary, the results of the core radial power split and nodalization sensitivity study indicate that S-RELAP5 is capable of handling such model variations aptly and these conditions do not seem to adversely affect code performance.

The results demonstrate that S-RELAP5 can properly simulate reflood phenomena during a postulated large-break loss-of-coolant accident (LBLOCA). The following summarizes the key results:

- S-RELAP5 can simulate both forced and gravity reflood transients. The results for the counterpart tests, Tests S2-11 and S2-AC1, and Tests S2-10 and S2-SH1, have good agreement with data. For high and low flooding rates, the peak cladding temperature (PCT) was predicted within 50 °F or less of the test data (good agreement). The predicted time of PCT occurrence compared well with the data demonstrating good agreement. The quench front in general was predicted to be delayed, at high elevations.

- Core nodalization representing finer radial power distribution does not have a beneficial impact on improving phenomenological results, particularly the cladding temperature responses. For the two tests considered, Test S2-17 simulates a flat radial power profile and Test S2-18 simulates a steep radial power profile. All nodalizations yielded about the same cladding temperature responses for both tests. These results support the use of the RLBLOCA EM-consistent nodalization.

- Two radial nodalizations were used for Test S2-18: a nominal nodalization and [ ] See Section 8.2.12.4.6 for additional details.

8.2.12.3 Facility and Test Description

The SCTF-II test program (References 8.2-53 and 8.2-54,) is designed to investigate the two-dimensional (2-D) thermal-hydraulic behavior in the reactor pressure vessel during the reflood phase of an LBLOCA in a PWR. To meet this objective, SCTF-II simulates a full-radius slab section of a PWR with eight bundles arranged in a row. The heating power for each bundle can be independently controlled.

In the SCTF-II test, the following two test modes were adopted: (1) a gravity feed mode with the emergency core cooling (ECC) injection into the cold leg, and (2) a forced feed mode with ECC injection into the lower plenum (the bottom of the downcomer being closed). The gravity feed mode can be considered as an integral test which includes the coupled phenomena to predict reflood rate and reflood heat transfer. The forced feed mode can be characterized as a separate effect test to decouple the phenomena affecting reflood rate and focus only on reflood heat transfer phenomena. Use of data from the two test modes permits the assessment of the capability to predict two different sets of phenomena somewhat separately and in integral combination.

Although the gravity feed mode is considered to be a simulation closer to an actual reactor, the boundary conditions at the core inlet (mass flow rate and subcooling) are affected because of parameter changes (e.g., change of system pressure and of core heating, etc.). Therefore, investigating the effect of a parameter change on the 2-D thermal-hydraulic behavior in the pressure vessel, the forced feed test mode was adopted to obtain accurate boundary conditions at the core inlet. Justifying the validity of the forced-feed mode is necessary because a solid system in that mode might change the thermal-hydraulic behavior in the pressure vessel including the 2-D behavior.

A schematic diagram of SCTF-II (Reference 8.2-53) is shown in Figure 8.2-334. The primary coolant loop consists of a hot leg equivalent to four actual hot legs, a steam/water (S/W) separator in place of four actual steam generators, an intact cold leg equivalent to three intact cold legs, a broken cold leg on the pressure vessel side, and a broken cold leg on the S/W separator side. The two broken cold legs are connected to two containment tanks as shown in Figure 8.2-334.

The SCTF-II pressure vessel simulates a full-radius slab section of a 1,100 MWe PWR. The scaling ratio of flow area is 1:21 of a referenced PWR, whereas the height of each component is preserved.

The simulated core consists of eight bundles arranged in a row with full radial width. Each bundle consists of 234 heater rods and 22 non-heated rods arranged in a 16 x 16 array. The outer diameter and the heated length of the heater rods are 10.7 mm and 3,660 mm, respectively. The dimension and arrangement pitch of the rods are based on those of a 15 x 15 fuel rod bundle for a Westinghouse-type PWR (Reference 8.2-53).

The SCTF-II reflood program consisted of a series of tests. The first set of tests covered "gravity flood" conditions, in which communication occurred between the downcomer and the lower plenum, and the hydrostatic downcomer-to-core head provided the driving force for flow into the bottom of the core. The second set of tests considered "forced flood" conditions in which the vessel downcomer was sealed off from the lower plenum and a predetermined water flow rate was forced into the bottom of the core via the lower plenum.

Six tests from the SCTF Core-II reflood experiment were analyzed to assess forced reflood versus gravity reflood, and the effects of radial power distribution and radial nodalization during the reflood phase of a LBLOCA. The primary tests that were modeled in the calculation assessments were two "gravity flood" tests (Tests S2-SH1 and S2-AC1), and two "forced flood" tests (Tests S2-10 and S2-11). The radial power distribution study (Tests S2-17 and S2-18), was performed with "forced flood" conditions. The assessment matrix is summarized as follows:

- Forced versus Gravity Reflood (Phase I). In this assessment phase, two sets of counterpart tests were chosen to study the differences between forced and gravity reflood. The first set is made up of Tests S2-11 and S2-AC1, and the second set consists of Tests S2-10 and S2-SH1. A nominal nodalization [

]

The S2-SH1 test is the SCTF-II gravity-flood base-case test. During Test S2-SH1, the downcomer was not blocked from the lower plenum (i.e., there was hydraulic communication between the lower plenum and downcomer). A combination of lower plenum injection and cold leg injection was used in Test S2-SH1.

Test S2-AC1 differs from Test S2-SH1 in the accumulator core coolant (ACC) injection rate and duration.

The S2-10 test is the SCTF-II forced-flood base case. In Test S2-10, ECC was injected into the lower plenum only, with no hydraulic communication between the lower plenum and the downcomer. The ECC injection rate was specified to match the core inlet flow rate achieved in the gravity feed test.

Test S2-11 differs from S2-10 in that a high ACC flow rate was used.

- Effect of Radial Nodalization (Phase II). In this assessment phase, two tests were chosen to study the effect of radial nodalization and radial power split on reflooding behavior. These tests are S2-17 and S2-18. Test S2-17 represents a flat radial core power distribution. Two radial nodalizations were used for Test S2-18: a nominal nodalization, and [ ] See Section 8.2.12.4.6 for additional details.

Table 8.2-23 shows the test conditions for each of the test configurations examined.

8.2.12.4 S-RELAP5 Model Description

Figure 8.2-335 is a schematic of the nodalization used for the SCTF-II facility. The nodalization scheme and the model flags were selected to be consistent with the S-RELAP5 RLBLOCA, Revision 3 methodology. The modeling of the downcomer, lower plenum, core, upper plenum, and upper head is summarized here.

[ ]

SCTF hot leg geometry is atypical. Its inside geometry is elliptical with its height (major axis) close to the inside diameter of a typical 4-loop PWR. The width (minor axis) is very narrow to preserve the volume flow area scaling of a 4-loop PWR. [

] In SCTF there is no active steam generator. A steam water separator is used to simulate the primary side of the steam generator. The inlet chamber represents the inlet plenum of four scaled steam generators. The outlet chamber collects the liquid that is entrained from the inlet chamber.

For the purpose of core nodalization sensitivity, an alternate core model was developed based on [

]

- The RLBLOCA multipliers used are the same as those listed in Sections 8.2 and 8.3. Any deviations are stated and justified.
- The break valves in the cold legs (Components 505 and 580) are initially set closed. They open at time zero and become fully open in 1.8 seconds, consistent with the test.
- [

]

- For all tests, except S2-11 and S2-AC1, the core heat structures were almost at the saturation temperature of the surrounding steam at the initial system pressure (Reference 8.2-53). [

  ] For Tests S2-11 and S2-AC1, the hot bundle cladding temperature at time zero varied along the heated length and was above saturation (Reference 8.2-53). There is no information regarding this initial heat-up process before the start of the transient test. In this study, the initial axial hot rod cladding temperature distribution is based on data. When the transient simulation starts at t=0, [

  ] This simple approach is adequate for the present study because the rod undergoes a nearly-adiabatic heatup prior to reflood initiation, and therefore, the initial radial temperature profile has very little impact on the cladding response at reflood.

- For the forced reflood tests, the water level is prescribed only in the lower plenum volume. The downcomer is isolated from the lower plenum and assumed to contain saturated vapor. For the gravity reflood tests, the water level is prescribed in both the lower plenum and downcomer volume, because the downcomer communicates with the lower plenum.

- For all cases, the following [ ]

[

]

- To get acceptable liquid entrainment out of the S/W separator inlet plenum, the following input modeling recommended in the UPTF Tests 10B and 29B benchmarks (see Section 8.2.9) is utilized.

[

]

- Since all the heated rods are represented by an average rod and there are no rod arrays simulated, the rod-to-rod radiation model is not used.
- The cold leg condensation model (described in Section 8.4.2) is used in the intact cold leg. For all cases, [

]

[7] [

]

- [

]

To study the radial power distribution effect, Test S2-18 was also simulated using [

]

Specific modeling changes implemented to the S-RELAP5 test models are discussed in the following sections. The heat structure modeling scheme representing the different bundle configurations is summarized in Table 8.2-34.

8.2.12.4.1 Test S2-11 Input Model

- The initial temperature distribution for the HR region is approximated by the initial temperature data measurements, which are shown in Table 8.2-35. All other heat structures are assigned an initial temperature of 411 K (average core wall temperature, Reference 8.2-53, Table 8.2-35).
- The ECC injection is via the lower plenum. The injection flow rate and temperature are given in Table 8.2-36: Injection started at 122.5 seconds and terminated at 155.0 seconds. It then was switched to low pressure coolant injection (LPCI) at 155.0 seconds, which lasted to the end of the transient.
- Initial water level in the lower plenum is 1.58 m. The lower plenum initial conditions are shown in Table 8.2-37.

8.2.12.4.2 Test S2-10 Input Model

- The initial temperature of all heat structures is assigned an initial temperature of 392 K (Reference 8.2-53, Table B-2). [

]

The ECC injection is via the lower plenum. The injection flow rate and temperature are given in Table 8.2-38. ACC injection started at 143 seconds and terminated at 225.0 seconds. It then was switched to LPCI injection at 225.0 seconds (225.5 in the simulation) which lasted to the end of the transient.

- The initial water level in the lower plenum is 1.56 m. The lower plenum initial conditions are shown in Table 8.2-39.

8.2.12.4.3Test S2-AC1 Input Model

This is the counterpart test to S2-11 with gravity feed reflood.

- The downcomer was NOT blocked off.
- The initial temperature distribution for the HR is approximated by the initial temperature data measurement, which are summarized in Table 8.2-40. All other heat structures are assigned an initial temperature of 410 K (Reference 8.2-53, Table B-2).
- The ECC injection is via the lower plenum and the intact cold leg. The injection flow rate and temperature are given in Table 8.2-41.
- The initial water level in the lower plenum is 1.56 m. The lower plenum initial conditions are given in Table 8.2-42.
- The initial water level in the downcomer is assumed to be the same as that in the lower plenum and is shown in Table 8.2-43. NOTE: Because the lower plenum is not blocked off, the initial water level covers the downcomer portion for hydrostatic balance.

8.2.12.4.4Test S2-SH1 Input Model

This is the counterpart test to Test S2-10 with gravity feed reflood.

- The downcomer was NOT blocked.
- All heat structures are assigned an initial temperature of 393 K (Reference 8.2-53, Table B-2).
- The ECC injection is via the lower plenum and the intact cold leg. The injection flow rate and temperature are given in Table 8.2-44.
- The initial water level in the lower plenum is 1.56 m. The lower plenum initial conditions are given in Table 8.2-45.
- The initial water level in the downcomer is assumed to be the same as that in the lower plenum and is shown in Table 8.2-46. NOTE: Because the lower plenum is not blocked off, the initial water level should cover the downcomer portion for hydrostatic balance.

8.2.12.4.5Test S2-17 Input Model

- All heat structures are assigned an initial temperature of 394 K (Reference 8.2-53, Table B-2).
- The ECC injection is via the lower plenum. The injection flow rate and temperature are given in Table 8.2-47. ACC injection started at 135 seconds and terminated at 205.0 seconds. It then was switched to LPCI injection at 205.0 seconds which lasted to the end of the transient.
- The initial water level in the lower plenum is 1.56 m. The lower plenum initial conditions are shown in Table 8.2-48.

8.2.12.4.6 Test S2-18 Input Model

- For this test configuration, [

  ] are modified to reflect the consistent bundle order for this test.

- [

  ]

- All heat structures are assigned an initial temperature of 393 K (Reference 8.2-53, Table B-2).
- The ECC injection is via the lower plenum. The injection flow rate and temperature are given in Table 8.2-49. ACC injection started at 113.5 seconds and terminated at 260.0 seconds. It then was switched to LPCI injection at 260.0 seconds which lasted to the end of the transient.
- The initial water level in the lower plenum is 1.58 m. The lower plenum initial conditions are shown in Table 8.2.50.

8.2.12.5 Results

8.2.12.5.1 Phase I Assessment Results: Forced versus Gravity Reflood

This phase studied the comparison between forced and gravity reflooding for the same test conditions. Nominal [ ] nodalization was used. The cladding temperature plots at the elevation of 3.62 m are not included in the discussions presented below as at this top-most elevation the comparisons are of less importance from the standpoint of criteria or phenomenon.

First consider the test pair S2-11 and S2-AC1. The flooding rates during ACC and LPCI reflood are 17.4 cm/s and 1.6 cm/s for Test S2-11, and 25.8 cm/s and 1.6 cm/s for Test S2-AC1, respectively (Table B-3, Reference 8.2-53). These tests represent the highest combined injection rate in the SCTF-II test matrix. Figure 8.2-336 through Figure 8.2-348 show the results for Test S2-11. Figure 8.2-336 through Figure 8.2-344 depict the cladding temperature responses for Test S2-11. The calculated responses show excellent agreement with the data reproducing the peak cladding temperature time and magnitude extremely well. Figure 8.2-345 shows the core pressure comparison, displaying good agreement. The pressure in the vessel increases at the point of ECC injection because of steam generation. The extent of pressurization depends on the rate of steam venting through the hot leg. The comparison indicates that the loop resistance is appropriately represented. Figure 8.2-346 shows the core void fraction. The calculated results exhibit oscillations, which are typical of reflood simulation. The overall behavior for this set of tests follows the data trend. Figure 8.2-347 confirms that the appropriate ACC/LPCI flow rates were applied by the model. The core differential pressure prediction indicates good agreement with the data, as illustrated in Figure 8.2-348.

Figure 8.2-349 through Figure 8.2-363 show the calculated and measured responses for Test S2-AC1. In general, the agreement between calculation and data is comparable to that observed in Test S2-11; the prediction of quench front behavior may be somewhat improved relative to Test S2-11. In particular, the cladding temperature predictions display excellent agreement with the data at all elevations, except for the two topmost locations where the predicted cladding temperature profiles and peak deviate from the data and do not follow the heating trend shown by the measurements. Quench time along the heated length is well predicted at all elevations except for the two topmost locations. Although the peak fuel assembly pressure was overpredicted by 0.04 MPa (Figure 8.2-359), there is good agreement with the measured data for the test.

Next consider the test pair S2-10 and S2-SH1. The flooding rates during ACC and LPCI reflood are 3.7 cm/s and 1.8 cm/s for Test S2-10, and 6.6 cm/s and 1.6 cm/s for Test S2-SH1, respectively (Table B-3, Reference 8.2-53). These tests represent the lowest combined injection rate in the SCTF-II test matrix. Figure 8.2-364 to Figure 8.2-377 show the comparisons for Test S2-10, and Figure 8.2-378 to Figure 8.2-392 for Test S2-SH1. The calculation is in good agreement with the data for both tests.

The PCT and quench time information, which were observed in the phase I assessments, are presented in Table 8.2-51. In general, the quench time predictions at higher locations did not always compare reasonably well with the data. Considering the fact that the quench response at the top elevations is not a key behavior (being removed from the PCT location), a comparison of the quench time at the 2.76 m elevation is presented as a representative location. As shown in Table 8.2-51, the comparison between measured and predicted quench times at the 2.76 m elevation shows some deviation, however, the difference can be deemed acceptable. For Test S2-10 and Test S2-SH1, the PCTs were slightly under-predicted relative to the mean, but remained within the data range (see Table 8.2-51). For S2-SH1, the cladding temperature predictions start an earlier decline compared to the data; thus resulting in an early PCT time prediction. For Test S2-10, a somewhat similar behavior was observed.

Referring back to Table 8.2-51, the S-RELAP5 predicted PCTs compare reasonably with the measured PCT data for most elevations, with PCT differences ranging from 1.5 K to 15 K (Case S2-10: 15 K, Case S2-11: 5.5 K, Case S2-AC1: 1.5 K, and Case S2-SH1 11.5 K).

The core differential pressure for Test S2-10 (see Figure 8.2-377) shows a pressure spike at about 150 seconds, which corresponds to the ACC/LPCI injection initiation time. This behavior is attributed to S-RELAP5 boundary condition initialization and is expected not to have any downstream implication during the time of PCT and quenching.

8.2.12.5.2Phase II Assessment Results: Effect of Radial Power Distribution

Phase II studied the effect of radial power split on the reflood behavior during a postulated LBLOCA event. Two tests selected for the study were Test S2-17 and Test S2-18. The ACC flooding rate for S2-17 is about half that for S2-18, while the LPCI flooding rates are about the same for both tests. The major difference between these two tests is in the core power distribution. Test S2-17 has uniform power across the core (all at 890 kW). Test S2-18 has a significant radial power tilt, with the peak bundle power (1210 kW) about twice as much as the peripheral bundle power (676 kW). The total power level for the two tests is almost the same (7120 kW for S2-17 versus 7118 kW for S2-18). The distribution of radial power renders these two tests ideal for a core radial power study.

In addition, a core radial nodalization sensitivity study was performed for Test S2-18. Two radial nodalization schemes were used: the nominal nodalization [

] The input model for the individual bundle nodalization was developed from the base model having the nominal nodalization. Three primary modifications were required:

Core Component

[

]

Upper Plenum Component

[

]

Core Heat Structures Component

[

]

Comparisons between S-RELAP5 predictions and data for Test S2-17 are shown in Figures Figure 8.2-393 to Figure 8.2-406. The figures depict cladding heatup behavior and other key parameters. A similar set of plots for Test S2-18 are presented in Figure 8.2-407 to Figure 8.2-420, showing predictions from the nominal and [

] As for the Phase I assessment results, the cladding temperature plots at the elevation of 3.62 m are not included; at this top-most elevation, the comparisons are of less importance from the standpoint of criteria or phenomenon. The PCT and quench time information, which were encountered in the phase II assessments, are presented in Table 8.2-52. Both tests show the PCT is under-predicted and the bundle quench time is over predicted relative to the test data. The predicted time of PCT shows good agreement with the test data.

Referring back to Table 8.2-52, the S-RELAP5 predicted PCTs compare reasonably with the measured PCT data, with PCT differences ranging from 0 K to 30 K [Case S2-17: 30 K, data range not available, Case S2-18 (nominal nodalization): 28 K, Case S2-18 [ ] 0 K].

The core differential pressure for Tests S2-17 and S2-18 (see Figure 8.2-406 and Figure 8.2-420) shows pressure spikes at about 150 seconds, which corresponds to the ACC/LPCI injection initiation time. This behavior is attributed to S-RELAP5 boundary condition initialization and is expected not to have any downstream implication during the time of PCT and quenching.

The different radial nodal meshes can potentially result in different hydraulic responses through the core. The Test S2-18 comparison figures (Figure 8.2-407 through Figure 8.2-420), show that [

] The 8-channel model better predicts the core void fraction than does the 4-channel model. In light of the similar cladding temperature responses, it is concluded that the impact of radial nodalization on the hydraulic response is minimal. In particular, the fluid conditions seen by the hot rod must be able to produce the similar cladding temperature responses. These results confirm that radial modeling differences do not significantly affect predictions, and therefore the nominal nodalization should be adequate to represent the PCT response for a typical plant situation. Additionally, the study pertaining to the radial power split demonstrates that the S-RELAP5 code can reasonably predict both flat and steep radial power profiles.

8.2.12.5.3SG Tube-Inlet Interfacial Drag

As discussed in Section 8.2.12.4, an S/W separator is used to simulate the primary side of the steam generator. The inlet chamber represents the inlet plenum of four scaled steam generators. The outlet chamber collects the liquid that is entrained from the inlet chamber. In the tests, the liquid level in the outlet chamber is measured. This collected liquid represents the mass that will be entrained in the tube region during the LOCA in a scaled PWR. The S-RELAP5 predicted water level in the S/W separator region is compared with the measured data to evaluate [

]

Figure 8.2-421 through Figure 8.2-426 present the S/W separator region S-RELAP5 calculated collapsed water level comparison with the measurements for the six SCTF-II test cases being studied, S2-11, S2-AC1, S2-10, S2-SH1, S2-17 and S2-18. Reasonable agreement is observed for all cases at the time of about 350-450 seconds, which represents the period when the quenching of the peak power node takes place. Considering the a-typicality of the SCTF hot leg and the approximation used in modeling the hot leg in the S-RELAP5 input model, these results demonstrate that the S-RELAP5 code is capable of predicting acceptable entrainment behavior for plant cases during the reflooding phase of the LOCA.

Additionally, differential pressures between the upper plenum and the top of the downcomer, which represents the 7847 mm pressure tap, are depicted in Figure 8.2-427 through Figure 8.2-432. These ΔP comparisons display reasonable to acceptable agreement between the measured data and the predicted results.

---

[8] [

]

Table 8.2-33 Test Data for SCTF-II Tests Modeled

Test Number	S2-AC1	S2-SH1	S2-10	S2-11	S2-17	S2-18
Core Pressure, kPa	200	200	200	200	200	200
Containment Tank II Pressure, kPa	200	200	200	200	200	200
Lower Plenum Water Level, m	1.56	1.56	1.56	1.58	1.56	1.58
Average Core Wall Temperature at Midplane, K	410	393	392	411	394	393
Peak Bundle Average Temperature at Midplane, K	490	395	395	500	395	395
SWS Side Broken Cold Leg Orifice, Diameter, mm	86	86	86	86	86	86
Intact Cold Leg Orifice, Diameter, mm	180	180	180	180	180	180
Pump Simulator Orifice Diameter, mm	174	174	174	174	174	174
Vent Valve Blocked?	Yes	Yes	Yes	Yes	Yes	Yes
Downcomer Blocked?	No	No	Yes	Yes	Yes	Yes
Water Extraction System On?	No	No	No	No	No	No
Bundle Power kW:						
No. 1,2	887	891	891	887	890	1210[1]/ 1068[2]
No. 3,4	944	948	948	942	890	1068
No. 5,6	900	903	903	900	890	676
No. 7,8	815	818	818	816	890	676
Total	7092	7120	7120	7090	7120	7118
ECC Water Temperature, K						
ACC	360	355	360	365	375	370
LPCI	352	352	380	375	375	380
ACC Flow Rate, kg/s						
Lower Plenum	78.3	20.0	11.2	52.8	12.5	25.9
Intact Cold Leg	0.	0.	0.	0.	0.	0.
Upper Plenum	0.	0.	0.	0.	0.	0.
LPCI Flow Rate, kg/s						
Lower Plenum	0.	0.	0.	0.	0.	0.
Intact Cold Leg	4.8	4.9	5.6	4.9	6.0	4.9
Steam Injected to Pump Simulator Intact Cold Leg, kg/s	0.0	0.0	0.0	0.0	0.0	0.0
Start of Power Supply to Core, s	0.0	0.0	0.0	0.0	0.0	0.0

Test Number	S2-AC1	S2-SH1	S2-10	S2-11	S2-17	S2-18
Start of ECC Injection, s						
ACC	123	143	143	122.5	135	113.5
LPCI	143	198	225	155	205	260
Duration of ECC Injection, s						
ACC	20	55	82	32.5	70	146.5
LPCI	900	900	918	667.5	930	353.5
Start of Core Power Decay, s	126	183	183	124.5	177	115.5
Power Decay Curve:						
ANS X	1.0	1.02	1.02	1.02	1.02	1.02
+ACTINIDES X	1.0	1.02	1.02	1.02	1.02	1.02
+DN Effect X	1.0	0.	0.	0.	0.	0.
From Reactor Time, s	30	40	40	40	40	40
BOCREC, s	124	146	146	124	138	115.5
Maximum Core Inlet Subcooling, K	32	23	N/A	28	16	21.9
ACC Flooding Rate, cm/s	25.8	6.6	3.7	17.4	4.1	7.0
LPCI Flooding Rate, cm/s	1.6	1.6	1.8	1.6	2.0	1.6
Maximum Clad Temperature at BOCREC, K	1077	1076	1078	1079	1033	1092
Maximum Clad Temperature, K	1085	1166	1168	1085	1080	1116
Time of Maximum Clad Temperature, s	127	251.5	193.5	125.5	180	125
Time of Whole Core Quench, s	510.5	638.5	564	458.5	540	500
Start of Steam Supply to Pump Simulator of Intact Leg, s	N/A	N/A	N/A	N/A	N/A	N/A

Notes:

1. Bundle Number 1 is at 1210 kW.
2. Bundle Number 1 is at 1068 kW.

Table 8.2-34 S-RELAP5 Heat Structure and Assembly Arrangements

Tests S2-10, S2-11and S2-17

Heat Structure Number	Associated Core Volume Channel	Assemblies Represented	Designator

Tests S2-18 (Nominal Model)

Heat Structure Number	Associated Core Volume Channel	Assemblies Represented	Designator

Tests S2-18 (8-Channel Core Model)

Heat Structure Number	Associated Core Volume Channel	Assemblies Represented	Designator

Table 8.2-35 Initial Cladding Temperature Distribution (HA Region), SCTF-II Test S2-11

Elevation (m)	Initial Temperature (K)	Heat Structure No.
0.110	425	1 - 6
0.520	449	7 - 10
0.950	488	11 - 18
1.38	512	19 - 22
1.735	522	23, 24
1.905	525	25 - 28
2.330	518	29 - 32
2.760	481	33 - 40
3.190	452	41 - 44
3.620	405	45 - 48

Table 8.2-36 ECC Injection Flow Rate, SCTF-II Test S2-11

Time (s)	Injection Flow (kg/s)	Liquid Temperature (K)
0.0	0.0	N/A
122.5	52.8	365 (ACC)
155.0	52.8	365 (ACC)
155.1	4.9	375 (LPCI)
700.0	4.9	375 (LPCI)

Table 8.2-37 Lower Plenum Initial Conditions, SCTF-II Test S2-11

Component no.	Length (m)	Quality	
014-1	0.500	0.0	All liquid
014-2	1.113	3.66e-5	Corresponds to 1.58 m level

Table 8.2-38 ECC Injection Flow Rate, SCTF-II Test S2-10

Time (s)	Injection Flow (kg/s)	Liquid Temperature (K)
0.0	0.0	N/A
143.0	11.2	360 (ACC)
225.0	11.2	360 (ACC)
225.5	5.6	380 (LPCI)
1143.0	5.6	380 (LPCI)

Table 8.2-39 Lower Plenum Initial Conditions, SCTF-II Test S2-10

Component no.	Length (m)	Quality	
014-1	0.500	0.0	All liquid
014-2	1.113	5.99e-5	Corresponds to 1.56 m level

Table 8.2-40 Initial Cladding Temperature Distribution (HA Region), SCTF-II Test S2-AC1

Elevation (m)	Initial Temperature (K)	Heat Structure No.
0.110	408	[redacted]
0.520	426	
0.950	461	
1.38	495	
1.735	513	
1.905	520	
2.330	525	
2.760	508	
3.190	465	
3.620	399	

Table 8.2-41 ECC Injection Flow Rate, SCTF-II Test S2-AC1

Time (s)	Injection Flow (kg/s)	Liquid Temperature (K)
0.0	0.0	N/A
123.0	52.8	360 (ACC)
143.0	52.8	360 (ACC)
>143.0	0.0	N/A
0.0	0.0	N/A

Table 8.2-42 Lower Plenum Initial Conditions, SCTF-II Test S2-AC1

Component no.	Length (m)	Quality	
014-1	0.500	0.0	All liquid
014-2	1.113	5.99e-5	Corresponds to 1.56 m level

Table 8.2-43 Downcomer Level Initial Conditions, SCTF-II Test S2-AC1

Component no.	Length (m)	Quality	
012-01	0.500	0.0	All liquid
010-09	0.372	0.0	All liquid
010-08	1.225	9.34e-4	Corresponds to 1.56 m level

Table 8.2-44 ECC Injection Flow Rate, SCTF-II Test S2-SH1

Time (s)	Injection Flow (kg/s)	Liquid Temperature (K)
0.0	0.0	N/A
143.0	20.0	355 (ACC)
198.0	20.0	355 (ACC)
>198.0	0.0	N/A

Table 8.2-45 Lower Plenum Initial Conditions, SCTF-II Test S2-SH1

Component no.	Length (m)	Quality	
014-1	0.500	0.0	All liquid
014-2	1.113	5.99e-5	Corresponds to 1.56 m level

Table 8.2-46 Downcomer Level Initial Conditions, SCTF-II Test S2-SH1

Component no.	Length (m)	Quality	
012-01	0.500	0.0	All liquid
010-09	0.372	0.0	All liquid
010-08	1.225	9.34e-4	Corresponds to 1.56 m level

Table 8.2-47 ECC Injection Flow Rate, SCTF-II Test S2-17

Time (s)	Injection Flow (kg/s)	Liquid Temperature (K)
0.0	0.0	N/A
135.0	12.5	375 (ACC)
205.0	12.5	375 (ACC)
205.5	6.0	375 (LPCI)
1135.0	6.0	375 (LPCI)

Table 8.2-48 Lower Plenum Initial Conditions, SCTF-II Test S2-17

Component no.	Length (m)	Quality	
014-1	0.500	0.0	All liquid
014-2	1.113	5.99e-5	Corresponds to 1.56 m level

Table 8.2-49 ECC Injection Flow Rate, SCTF-II Test S2-18

Time (s)	Injection Flow (kg/s)	Liquid Temperature (K)
0.0	0.0	N/A
113.5	25.9	370 (ACC)
260.0	25.9	370 (ACC)
260.5	4.9	380 (LPCI)
1148.0	4.9	380 (LPCI)

Table 8.2.50 Lower Plenum Initial Conditions, SCTF-II Test S2-18

Component no.	Length (m)	Quality	
014-1	0.500	0.0	All liquid
014-2	1.113	3.66e-5	Corresponds to 1.58 m level

Table 8.2-51 Phase I Assessment Results, SCTF-II Tests

		S2-10	S2-11	S2-AC1	S2-SH1
PCT(K)	S-RELAP5	1126.0	1069.0	1067.0	1112.0
	Data (min/max)	1114/1168	1042/1085	1052/1085	1081/1166
	Data (mean)	1141.0	1063.5	1068.5	1123.5
Time of PCT(s)	Data	193.5	125.5	127.0	251.5
	S-RELAP5	180.0	125.0	125.0	175.0
Quench Time (s)	Data (elev 2.76 m)	520.0	425.0	465.0	570.0
	S-RELAP5	572.0	445.0	480.0	625.0

Table 8.2-52 Phase II Assessment Results, SCTF-II Tests

		S2-17 nominal nodalization	S2-18 nominal nodalization	S2-18 [ ]
PCT(K)	S-RELAP5	1050.0	1048.0	1076.0
	Data (min/max)	1080.0	1036/1116	1036/1116
	Data (mean)	data spread not avail.	1076.0	1076.0
Time of PCT(K)	Data	180.0	125.0	125.0
	S-RELAP5	173.0	128.0	123.0
Quench Time (s)	Data (elev. 2.76 m)	498.0	455.0	455.0
	S-RELAP5	570.0	570.0	570.0

Figure 8.2-334 Schematic of Slab Core Test Facility (SCTF-II)

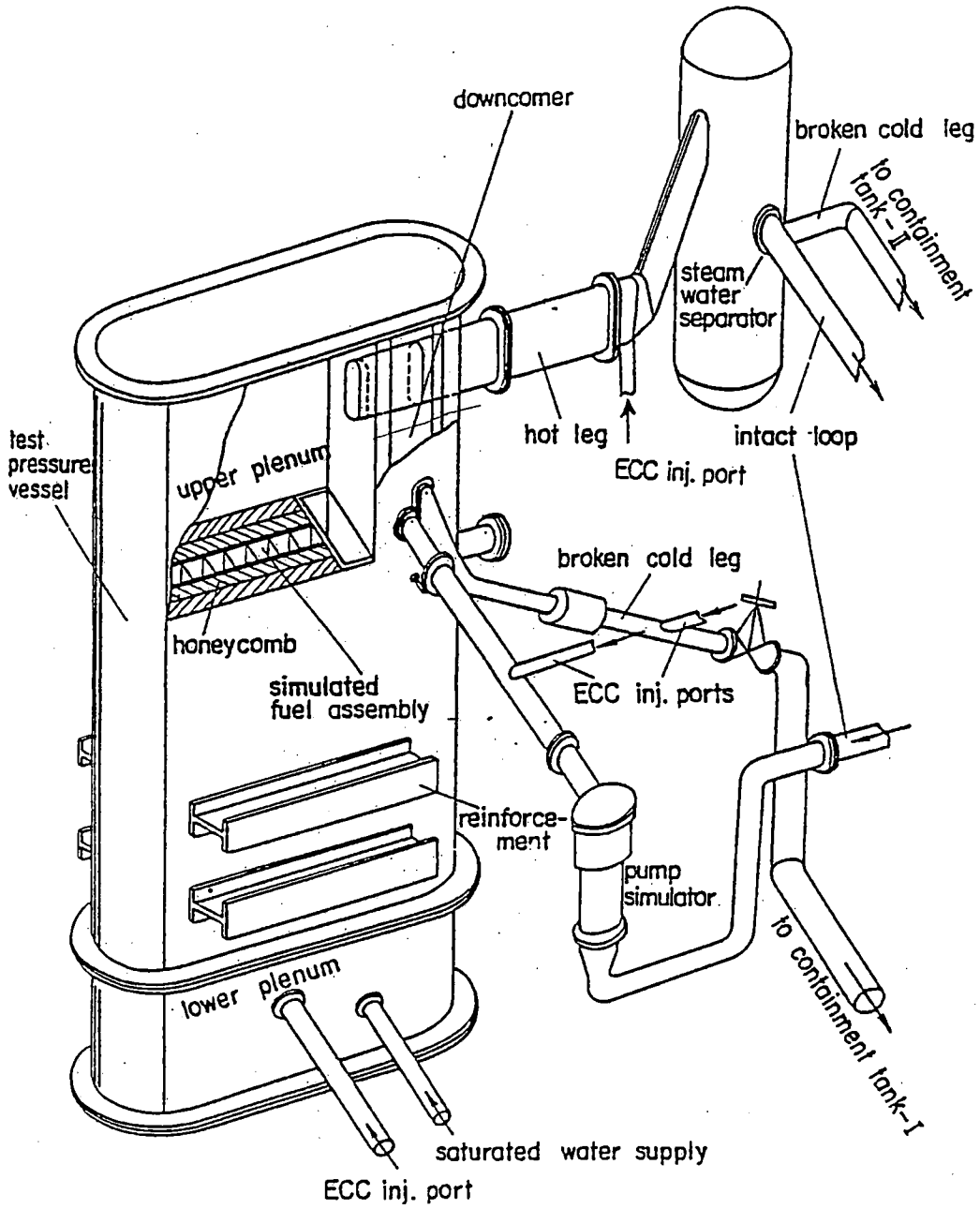

Figure 8.2-335 S-RELAP5 Nodalization of the SCTF-II

Figure 8.2-336 Temperature Comparison at 0.11 m, SCTF-II S2-11

Figure 8.2-337 Temperature Comparison at 0.52 m, SCTF-II S2-11

Figure 8.2-338 Temperature Comparison at 0.95 m, SCTF-II S2-11

Figure 8.2-339 Temperature Comparison at 1.38 m, SCTF-II S2-11

Figure 8.2-340 Temperature Comparison at 1.735 m, SCTF-II S2-11

Figure 8.2-341 Temperature Comparison at 1.905 m, SCTF-II S2-11

Figure 8.2-342 Temperature Comparison at 2.355 m, SCTF-II S2-11

Figure 8.2-343 Temperature Comparison at 2.76 m, SCTF-II S2-11

Figure 8.2-344 Temperature Comparison at 3.19 m, SCTF-II S2-11

Figure 8.2-345 Fuel Assembly Pressure Comparison, SCTF-II S2-11

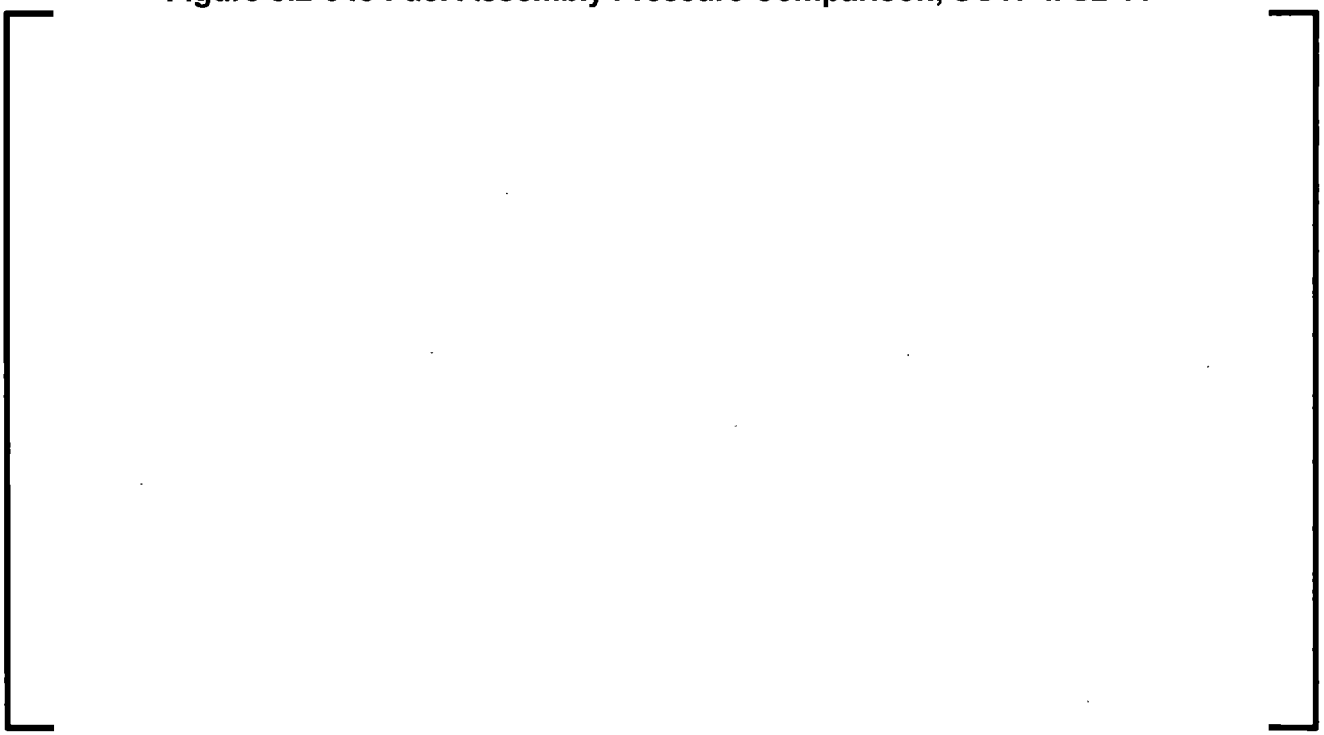

Figure 8.2-346 Core Void Fraction Comparison, SCTF-II S2-11

Figure 8.2-347 Accumulator/LPCI Injection Confirmation, SCTF-II S2-11

Figure 8.2-348 Core Differential Pressure Comparison, SCTF-II S2-11

Figure 8.2-349 Temperature Comparison at 0.11 m, SCTF-II S2-AC1

Figure 8.2-350 Temperature Comparison at 0.52 m, SCTF-II S2-AC1

Figure 8.2-351 Temperature Comparison at 0.95 m, SCTF-II S2-AC1

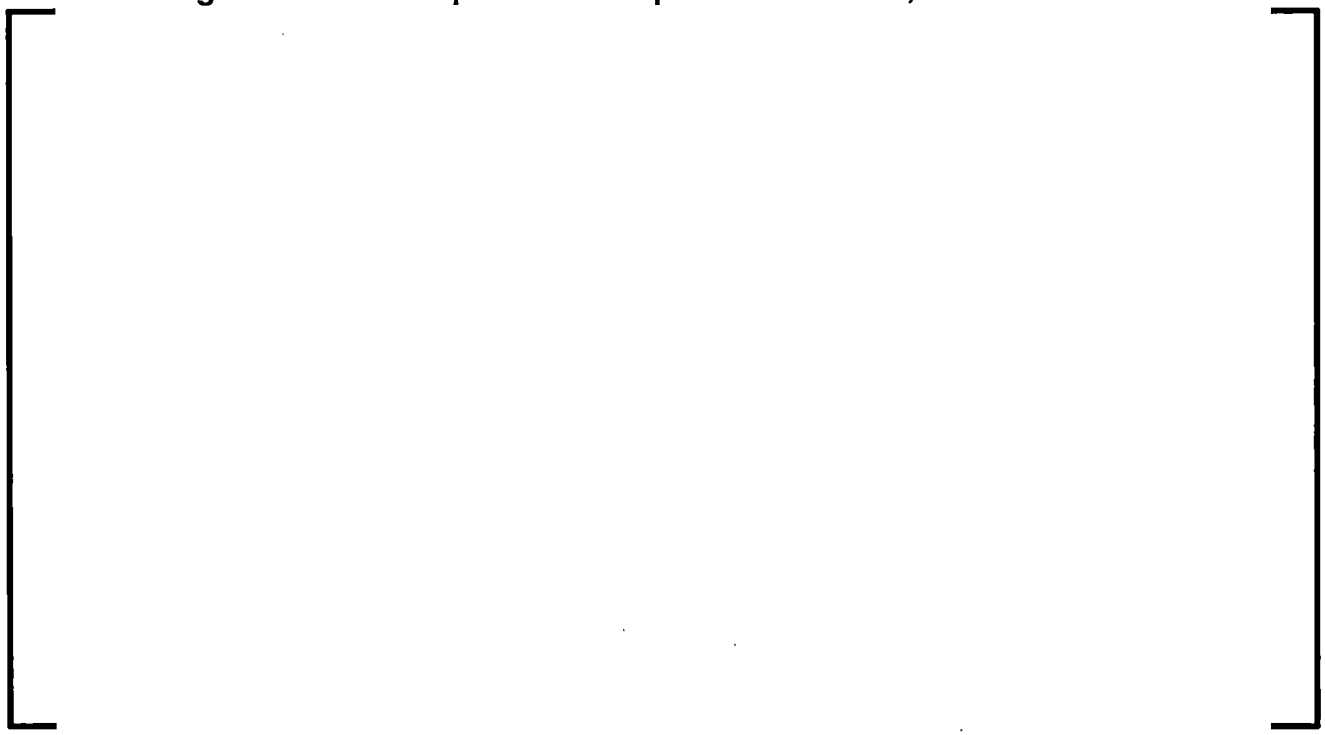

Figure 8.2-352 Temperature Comparison at 1.38 m, SCTF-II S2-AC1

Figure 8.2-353 Temperature Comparison at 1.735 m, SCTF-II S2-AC1

Figure 8.2-354 Temperature Comparison at 1.905 m, SCTF-II S2-AC1

Figure 8.2-355 Temperature Comparison at 2.355 m, SCTF-II S2-AC1

Figure 8.2-356 Temperature Comparison at 2.76 m, SCTF-II S2-AC1

Figure 8.2-357 Temperature Comparison at 3.19 m, SCTF-II S2-AC1

Figure 8.2-358 Temperature Comparison at 3.62 m, SCTF-II S2-AC1

Figure 8.2-359 Fuel Assembly Pressure Comparison, SCTF-II S2-AC1

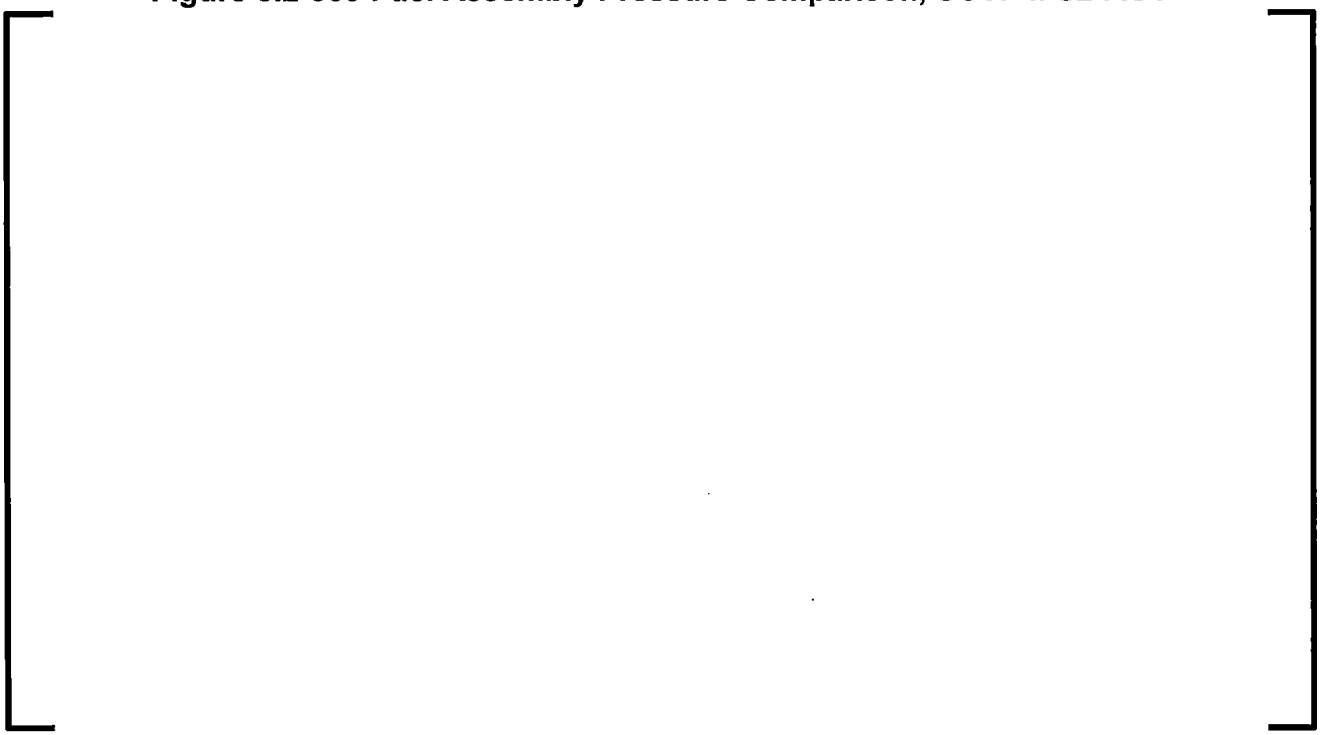

Figure 8.2-360 Core Void Fraction Comparison, SCTF-II S2-AC1

Figure 8.2-361 Accumulator Injection Confirmation, SCTF-II S2-AC1

Figure 8.2-362 Safety Injection Confirmation, SCTF-II S2-AC1

Figure 8.2-363 Core Differential Pressure Comparison, SCTF-II S2-AC1

Figure 8.2-364 Temperature Comparison at 0.11 m, SCTF-II S2-10

Figure 8.2-365 Temperature Comparison at 0.52 m, SCTF-II S2-10

Figure 8.2-366 Temperature Comparison at 0.95 m, SCTF-II S2-10

Figure 8.2-367 Temperature Comparison at 1.38 m, SCTF-II S2-10

Figure 8.2-368 Temperature Comparison at 1.735 m, SCTF-II S2-10

Figure 8.2-369 Temperature Comparison at 1.905 m, SCTF-II S2-10

Figure 8.2-370 Temperature Comparison at 2.355 m, SCTF-II S2-10

Figure 8.2-371 Temperature Comparison at 2.76 m, SCTF-II S2-10

Figure 8.2-372 Temperature Comparison at 3.19 m, SCTF-II S2-10

Figure 8.2-373 Temperature Comparison at 3.62 m, SCTF-II S2-10

Figure 8.2-374 Fuel Assembly Pressure Comparison, SCTF-II S2-10

Figure 8.2-375 Core Void Fraction Comparison, SCTF-II S2-10

Figure 8.2-376 Accumulator/LPCI Injection Confirmation, SCTF-II S2-10

Figure 8.2-377 Core Differential Pressure Comparison, SCTF-II S2-10

Figure 8.2-378 Temperature Comparison at 0.11 m, SCTF-II S2-SH1

Figure 8.2-379 Temperature Comparison at 0.52 m, SCTF-II S2-SH1

Figure 8.2-380 Temperature Comparison at 0.95 m, SCTF-II S2-SH1

Figure 8.2-381 Temperature Comparison at 1.38 m, SCTF-II S2-SH1

Figure 8.2-382 Temperature Comparison at 1.735 m, SCTF-II S2-SH1

Figure 8.2-383 Temperature Comparison at 1.905 m, SCTF-II S2-SH1

Figure 8.2-384 Temperature Comparison at 2.355 m, SCTF-II S2-SH1

Figure 8.2-385 Temperature Comparison at 2.76 m, SCTF-II S2-SH1

Figure 8.2-386 Temperature Comparison at 3.19 m, SCTF-II S2-SH1

Figure 8.2-387 Temperature Comparison at 3.62 m, SCTF-II S2-SH1

Figure 8.2-388 Fuel Assembly Pressure Comparison, SCTF-II S2-SH1

Figure 8.2-389 Core Void Fraction Comparison, SCTF-II S2-SH1

Figure 8.2-390 Accumulator Injection Confirmation, SCTF-II S2-SH1

Figure 8.2-391 Safety Injection Confirmation, SCTF-II S2-SH1

Figure 8.2-392 Core Differential Pressure Comparison, SCTF-II S2-SH1

Figure 8.2-393 Temperature Comparison at 0.11 m, SCTF-II S2-17

Figure 8.2-394 Temperature Comparison at 0.52 m, SCTF-II S2-17

Figure 8.2-395 Temperature Comparison at 0.95 m, SCTF-II S2-17

Figure 8.2-396 Temperature Comparison at 1.38 m, SCTF-II S2-17

Figure 8.2-397 Temperature Comparison at 1.735 m, SCTF-II S2-17

Figure 8.2-398 Temperature Comparison at 1.905 m, SCTF-II S2-17

Figure 8.2-399 Temperature Comparison at 2.355 m, SCTF-II S2-17

Figure 8.2-400 Temperature Comparison at 2.76 m, SCTF-II S2-17

Figure 8.2-401 Temperature Comparison at 3.19 m, SCTF-II S2-17

Figure 8.2-402 Temperature Comparison at 3.62 m, SCTF-II S2-17

Figure 8.2-403 Fuel Assembly Pressure Comparison, SCTF-II S2-17

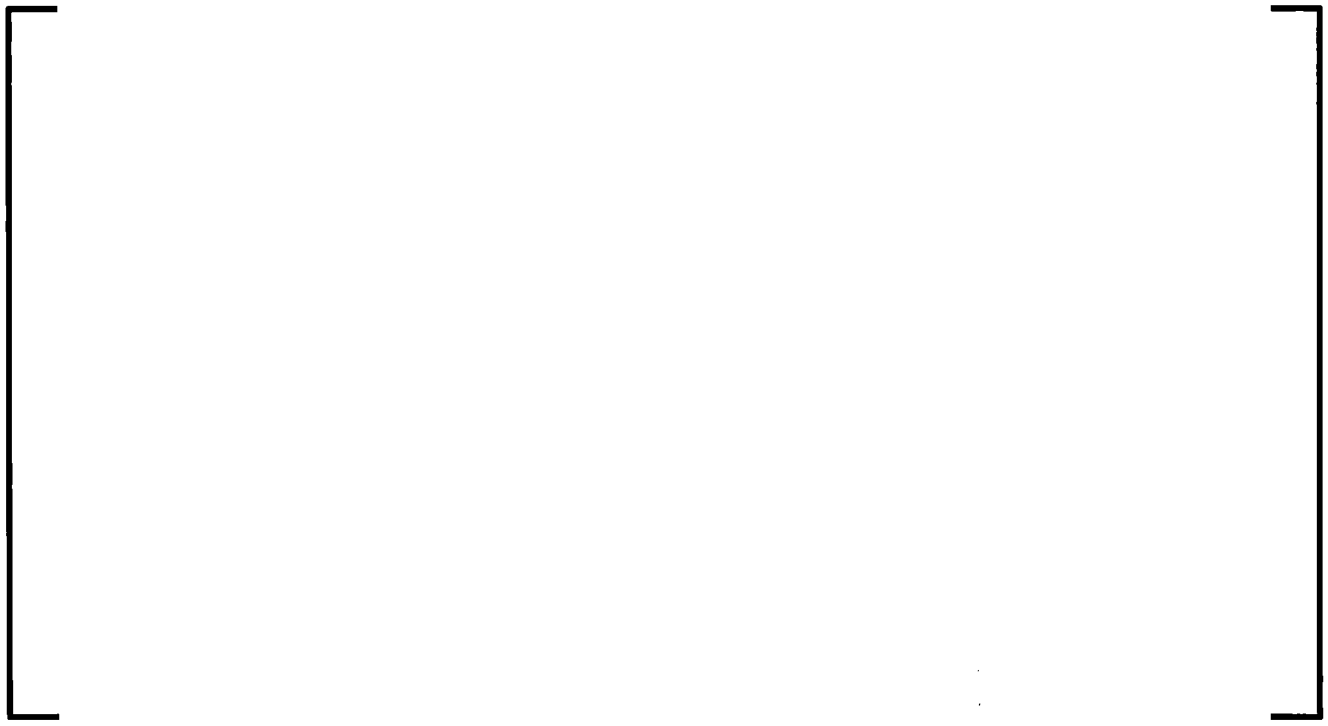

Figure 8.2-404 Core Void Fraction Comparison, SCTF-II S2-17

Figure 8.2-405 Accumulator/LPCI Injection Confirmation, SCTF-II S2-17

Figure 8.2-406 Core Differential Pressure Comparison, SCTF-II S2-17

Figure 8.2-407 Temperature Comparison at 0.11 m, SCTF-II S2-18

Figure 8.2-408 Temperature Comparison at 0.52 m, SCTF-II S2-18

Figure 8.2-409 Temperature Comparison at 0.95 m, SCTF-II S2-18

Figure 8.2-410 Temperature Comparison at 1.38 m, SCTF-II S2-18

Figure 8.2-411 Temperature Comparison at 1.735 m, SCTF-II S2-18

Figure 8.2-412 Temperature Comparison at 1.905 m, SCTF-II S2-18

Figure 8.2-413 Temperature Comparison at 2.355 m, SCTF-II S2-18

Figure 8.2-414 Temperature Comparison at 2.76 m, SCTF-II S2-18

Figure 8.2-415 Temperature Comparison at 3.19 m, SCTF-II S2-18

Figure 8.2-416 Temperature Comparison at 3.62 m, SCTF-II S2-18

Figure 8.2-417 Fuel Assembly Pressure Comparison, SCTF-II S2-18

Figure 8.2-418 Core Void Fraction Comparison, SCTF-II S2-18

Figure 8.2-419 Accumulator/LPCI Injection Confirmation, SCTF-II S2-18

Figure 8.2-420 Core Differential Pressure Comparison, SCTF-II S2-18

Figure 8.2-421 Liquid Level in S/W Separator, SCTF-II S2-11

Figure 8.2-422 Liquid Level in S/W Separator, SCTF-II S2-AC1

Figure 8.2-423 Liquid Level in S/W Separator, SCTF-II S2-10

Figure 8.2-424 Liquid Level in S/W Separator, SCTF-II S2-SH1

Figure 8.2-425 Liquid Level in S/W Separator, SCTF-II S2-17

Figure 8.2-426 Liquid Level in S/W Separator, SCTF-II S2-18

Figure 8.2-427 Differential Pressure: Upper Plenum - Downcomer, SCTF-II S2-11

Figure 8.2-428 Differential Pressure: Upper Plenum - Downcomer, SCTF-II S2-AC1

Figure 8.2-429 Differential Pressure: Upper Plenum - Downcomer, SCTF-II S2-10

Figure 8.2-430 Differential Pressure: Upper Plenum - Downcomer, SCTF-II S2-SH1

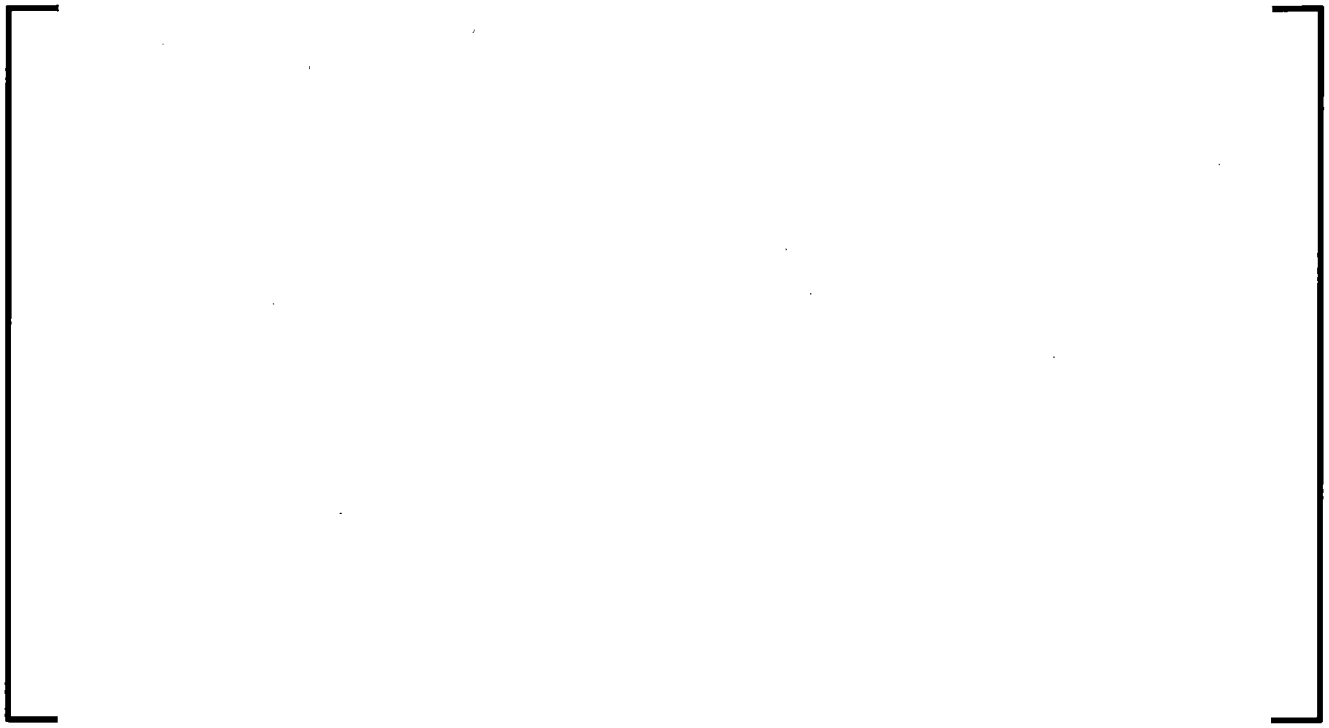

Figure 8.2-431 Differential Pressure: Upper Plenum - Downcomer, SCTF-II S2-17

Figure 8.2-432 Differential Pressure: Upper Plenum - Downcomer, SCTF-II S2-18

8.2.13 Cylindrical Core Test Facility Tests

8.2.13.1 Introduction

The Cylindrical Core Test Facility (CCTF) Core-II Test Series were undertaken to provide a major and useful data base on large-break loss-of-coolant accident (LBLOCA) reflood behavior in pressurized water reactors (PWR). Of particular interest were the simulations of reflood behavior after a LBLOCA in Westinghouse 4-loop PWRs in which emergency core coolant (ECC) is injected into the cold leg. CCTF is a full-height, 1/21 scale model of the primary coolant system of a 4-loop PWR plant. The facility was designed to reasonably simulate the flow conditions, including ECC flow behavior in the downcomer, and reactor core responses in the primary system of a PWR during the refill and reflood phases of a LOCA. The objective of this study is to assess the capability of S-RELAP5 (Reference 8.2-67) to simulate reflood transients in conjunction with AREVA's RLBLOCA EM. Therefore, the nodalization, time step, and other input parameters are set to those recommended in the RLBLOCA input development guidelines (Appendix A), and all LBLOCA uncertainty multipliers are set to their nominal values.

8.2.13.2 Summary and Conclusions

Four of the 29 tests were chosen as a diverse sample of behaviors to evaluate the performance of the model during vessel reflood. These CCTF tests were representative of a series of CCTF system gravity reflood tests with certain aspects of refill included. Calculations of these tests provide an understanding of key reflood phenomena and comparisons of predicted (calculated) and experimental (measured) results for assessment of various S-RELAP5 thermal-hydraulic models and their dynamic interactions. summarizes the key test parameters of the four tests.

As shown in Table 8.2-54, S-RELAP5, with an input model built on the current RLBLOCA modeling guidelines, generates peak cladding temperatures (PCT) that range from a conservative overprediction by 95 K, to an underprediction of the PCT by 49 K, with a large overprediction on the time of the PCT. The PCT at a higher elevation and later time, in all four cases, is consistent with the general hydrodynamic behavior calculated by S-RELAP5.

In summary, the assessment results have shown that the S-RELAP5 code calculates the important reflood phenomena occurring in the CCTF Reflood Test Runs evaluated with reasonable or better agreement to data. The assessment demonstrates the successful application of S-RELAP5 to PWR LOCA analyses, and supports the conclusion that S-RELAP5 will produce acceptable licensing simulations of reflood behavior during the postulated LOCA of a cold leg injection PWR.

8.2.13.3 Facility and Test Descriptions

The data report issued by JAERI (Reference 8.2-55), provided detailed descriptions of the CCTF Core-II system and instrumentation, including the scaling of various system components. Some key features of the test facility relevant to the assessment calculations are described in this section. CCTF was a full-height and full-axial-flow length, 1/21 scale (volume, flow area, and power) model of the primary coolant system of a 4-loop, 3400 MWt (1100 MWe) PWR. CCTF was designed to model a full-height core section, and simulate the overall thermal-hydraulic response of the primary system during the reflood phase of a 4-loop PWR cold-leg LBLOCA. Also included were some refill aspects such as the accumulator ECC injection, and the nearly adiabatic heatup of heated rods.

The reference reactors for CCTF scaling were the Trojan reactor in the United States, and certain aspects of the Ohi reactor in Japan. The facility had a pressure vessel and four primary loops with passive and active components. The pressure vessel contained a core of electrically heated rods and an annular downcomer with a gap of 61.5 mm surrounding the core. The vertical dimensions and the length of the flow paths of the system components were maintained close to those of the reference reactors. The axial flow area of each system component was scaled down in proportion to the scaling factor (1/21.44) of the core flow area. The design of upper plenum internals was based on 17 x 17-type PWR fuel assemblies.

(NOTE: The design bases for the core and the upper plenum were different.) The end box tie plate and the upper core support plate (UCSP) were installed between the core and the upper plenum. A schematic diagram of the pressure vessel is shown in Figure 8.2-433.

The primary system consisted of three intact loops and a broken loop. A schematic diagram of the top view of the primary piping is shown in Figure 8.2-434. Each intact loop contained a hot leg, an active steam generator, a loop seal section, a pump simulator, a cold leg, and an ECC (Emergency Core Cooling) injection port with associated piping. The broken loop also contained a hot leg, an active steam generator, a loop seal section, a pump simulator, and a cold leg (pump-side and vessel-side pipe sections) with an ECC injection port, though no ECC was injected into the broken loop.

The heater rod assembly consisted of 32 8 x 8-array rod bundles, arranged in a cylindrical configuration and simulating 15 x 15-type PWR fuel assemblies. Each bundle consisted of 57 electrically heated rods and 7 unheated rods. The core was subdivided into the high-, medium and low-power regions, named as A, B, and C regions, respectively. Shown in

Figure 8.2-435 are the three core power regions and the vessel cross section.

Each heated rod consisted of a nichrome heating element, magnesium oxide (MgO) and boron nitride (BN) insulators, and an Inconel-600 sheath (clad), as shown in Figure 8.2-436. The heated length, the outer diameter (O.D.) and the rod pitch were, respectively, 3.66 m (144 inch), 10.7 mm (0.422 inch) and 14.3 mm (0.563 inch), which are identical to the corresponding dimensions of actual PWR fuel rods. The heating element was a helical coil with a varying pitch to generate a 17-step chopped cosine axial power profile with a peaking factor of 1.40, as shown in Figure 8.2-437.

The unheated rods were either stainless steel pipes or solid bars of 13.8 mm (0.543 inch) O.D. All pipes were used for installation of instruments and all bars were used for carrying the assembly loads. The heater rods and the unheated rods were held in radial position by grid spacers that were located at six elevations along the axial length, as shown in Figure 8.2-437. ECCS consisted of an ACC (Accumulator) and LPCI (Low Pressure Coolant Injection). The injection points are at each cold leg and at the lower plenum. The upper plenum and downcomer injection system were available for other alternative ECCS tests.

The instrumentation was divided into two groups: the USNRC-supplied instruments, and the JAERI-supplied instruments. The USNRC-supplied instruments were the advanced instrumentation for the two-phase flow measurement. The JAERI-supplied instruments measured the temperatures, absolute pressures, differential pressures, water levels, and flow rates. Examples of instrumentation arrangements and notations are shown in Figure 8.2-438 for temperature measurements in the core and lower plenum, and in Figure 8.2-439 for differential pressure measurements in the vessel.

8.2.13.4 S-RELAP5 Model Description

The S-RELAP5 input model for CCTF Test Runs was constructed from the facility drawings, and facility and test specifications according to the standardized RLBLOCA input model prescriptions for 3- and 4-loop PWRs. In addition to the facility drawings (some of them are shown in Figure 8.2-433 to Figure 8.2-439) in the data report, AREVA NP obtained several JAERI facility drawings through Los Alamos National Laboratory (LANL). Facility and test specifications needed for the input deck were obtained from the data reports (References 8.2-55, 8.2-56, 8.2-57 and 8.2-58) and the electronic data files. The following subsection summarizes the input model including nodalization schemes, initial and boundary conditions.

8.2.13.4.1 Input Model and Nodalization

A nodalization diagram of the CCTF Facility is shown in Figure 8.2-440. The four loops were modeled as four separated loops: three intact loops and one broken loop (Loop 4). Each loop [

] The pump-side and vessel-side containments were modeled as two time-dependent volumes. The ECC injection systems were modeled as time-dependent volumes and time-dependent junctions at the three intact loops and the lower plenum.

[

] Figure 8.2-441 depicts a more detailed modeling of the reactor vessel.

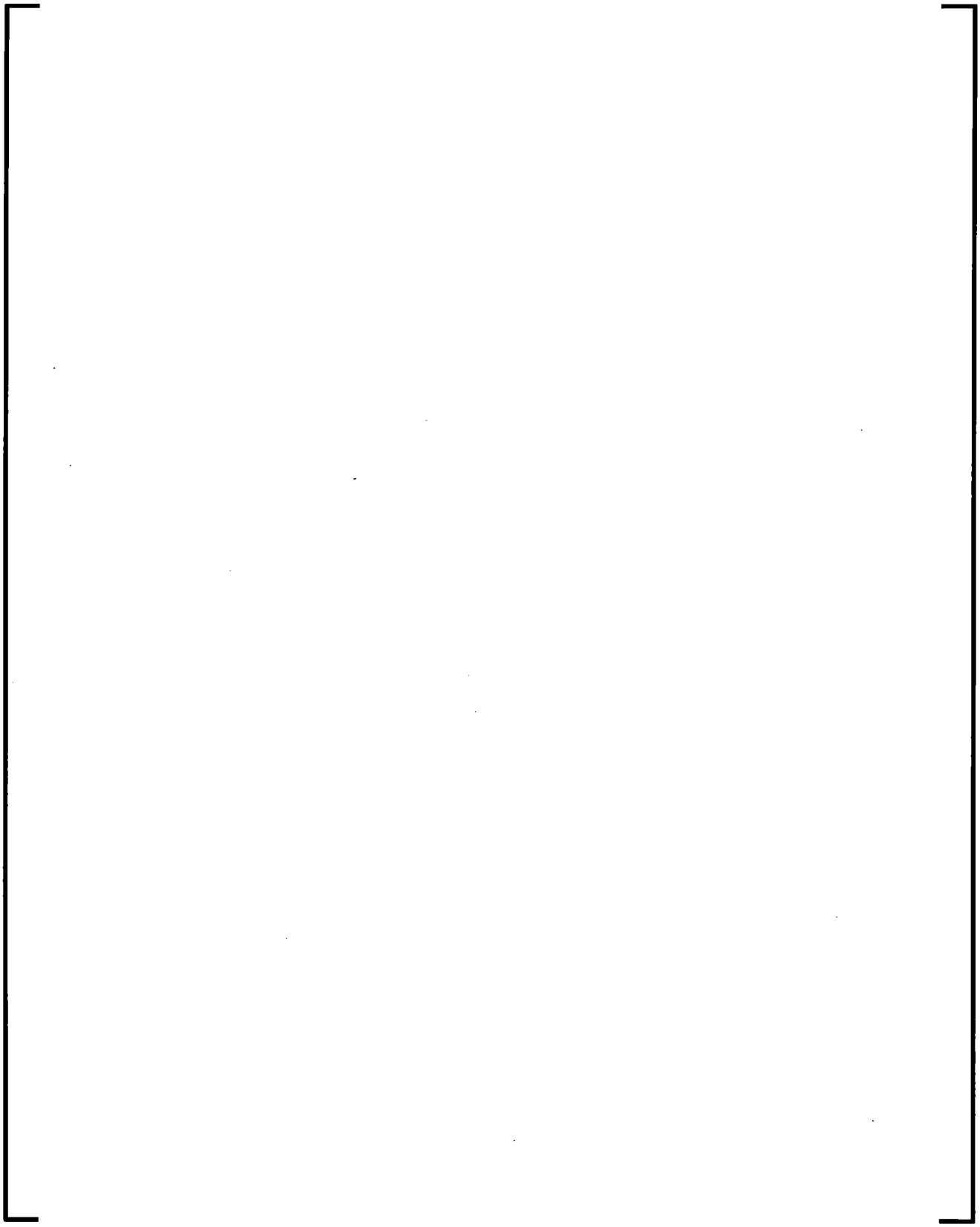

[

]

The core baffle region (see Figure 8.2-443) had a cross section area of about 0.4 m^2 and was assumed to be a sealed hollow space with no filler pieces (i.e., there were no flow paths and no thick metal structures). This assumption was made from a careful study of the data report and the facility drawings in the position of AREVA NP.

[

] The S-RELAP5 calculations of the CCTF tests started at the test initiation (time = 0.0 seconds), and ended approximately when most of the heated rods were calculated to be quenched.

[

]

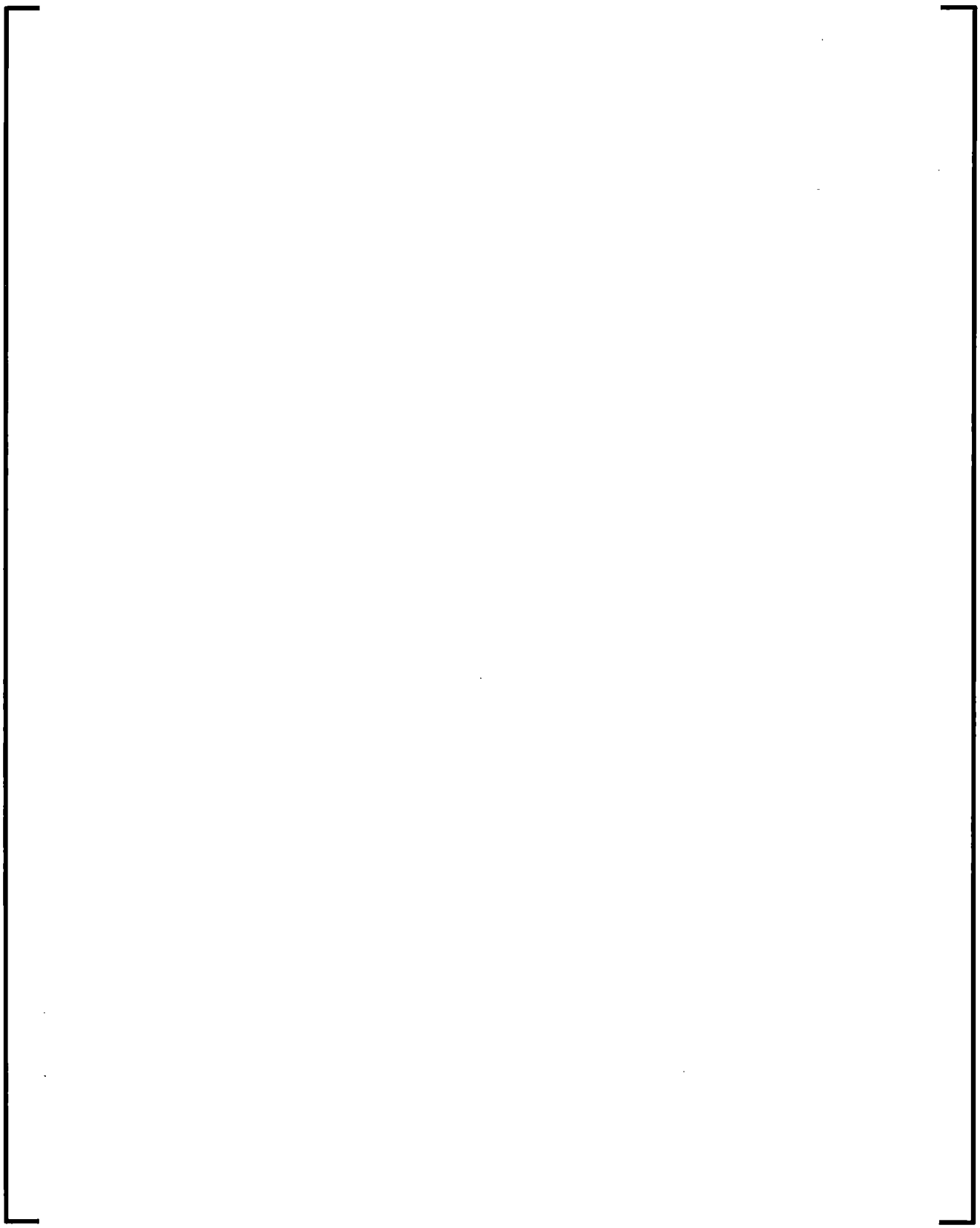

The model nodalization has been updated to comply with the requirements of the Revision 3 of the Realistic Large Break LOCA methodology. The model [

]

8.2.13.5 CCTF Test Run 54

8.2.13.5.1 Test Run 54 Description

Test Run 54 simulated the reflood phase of a cold-leg ECC injection PWR LOCA with a nominal decay power (i.e., without augmenting the 1971 ANS draft standard decay power by 20%), a system pressure of 0.2 MPa, and a LPCI flow rate of 0.011 m^3 /s.

8.2.13.5.2 Test Run 54 Input Description

The input model for test run 54 is as described in Section 8.2.13.4.1, with the only changes required to input the case specific initial and boundary conditions.

8.2.13.5.3 Test Run 54 Measured Test Conditions

In general, the test conditions for the CCTF tests were based on Appendix K design basis pre reflood assumptions, and low ECC water injection rate according to the single failure criteria. The measured test conditions for the CCTF Test Run 54 were established through the test procedure prescribed in the data report (Reference 8.2-55) and are presented in Table 8.2-55.

Note that the time shown is defined as the time after test initiation. Also, the initial water level in the lower plenum, and the injection of ECC water into the lower plenum and its timing, were designed to minimize the atypical oscillatory behavior from condensation at the ECC port in the initial stage of reflood by producing a considerable amount of steam in the core.

After the primary system was preheated to its specified temperatures, the test was initiated by turning on the power to the core heater rods with the vessel filled with steam, except for 0.86 m (2.82 ft) of saturated water in the lower plenum. Because the initial water level in the lower plenum was below the bottom of the core, the rods in the core heated up virtually adiabatically in the steam environment before reflood began.

Accumulator injection began at 81 seconds and was initially directed into the lower plenum. The core power started to decay from the maximum value of 7.87 MW at 90.5 seconds, when the reflood began (BOCREC).

At about 94 seconds, the accumulator injection was shifted to the cold leg and continued until about 107 seconds. After accumulator injection ended, low-pressure coolant injection (simulating LPCI) was injected into the intact cold legs until the end of the test. All heated rods were quenched by about 553 seconds into the transient (462 seconds after BOCREC). The sequence of events for the test is summarized in Table 8.2-56.

8.2.13.5.4 Test Run 54 Initial and Boundary Conditions

The initial and boundary conditions were taken from the data report (Reference 8.2-55). The initial conditions described in Section 8.2.13.5.3 were used to set up the initial conditions for the S-RELAP5 hydrodynamic components and heat structures.

In addition, the S-RELAP5 CCTF input model required tabulated input values for 11 time-dependent boundary conditions. These included total core power, liquid state and flow conditions for ECC injection at the lower plenum and at the three intact cold legs, and both containment tank pressures.

Figure 8.2-444 shows the total power curve used in S-RELAP5 calculations, Figure 8.2-445 and Figure 8.2-446 show the two containment pressure conditions, and Figure 8.2-447 shows the ECC mass flow rate, including the accumulator and LPCI. Note particularly that the two containments were not at a constant pressure of 0.2 MPa as specified in the data report.

A polynomial interpolation scheme was used, based on the measured temperatures, yielding an initial temperature distribution for the downcomer as shown in Table 8.2-57.

8.2.13.5.5Test Run 54 Calculated Results and Comparisons

Test Run 54 simulated the reflood phase of a cold-leg ECC injection PWR LOCA with a nominal decay power (i.e., without augmenting the American Nuclear Society (ANS) 1971 draft standard decay power by 20%), a system pressure of 0.2 MPa, and a low-pressure coolant injection (LPCI) flow rate of 0.011 m^3/s.

S-RELAP5 calculations of CCTF Test Run 54 are presented here with code-data comparisons. In the code-data comparison figures the measured quantities are generally identified by the instrumentation identifiers (see Figure 8.2-438 and Figure 8.2-439). Exceptions are those derived from the data. The calculated quantities are mostly identified by the S-RELAP5 minor edit parameters and component numbers. The results of the test run 54 are illustrated in Figure 8.2-448 through Figure 8.2-473.

Test Run 54 Broken Loop Behavior

Comparisons of the calculated mass flow rates and data in the broken-loop hot leg (BLHL) and broken-loop cold leg (BLCL) pump-side break flow are shown in Figure 8.2-448 and Figure 8.2-449, respectively. For the BLCL break flow (Figure 3.11.17), the calculation lies around the data on average, with higher values after 500 seconds. The calculated hot-leg mass flow rate shows some relatively large spikes, caused by the infrequent liquid carryover into the hot leg during the early reflood period when the ECC flow is high (simulating the accumulator ECC flow). On average, the calculated hot-leg mass flow rate is higher than the calculated pump-side break flow rate and higher than the measured hot-leg mass flow rate.

There might be large uncertainty associated with the measurement of hot-leg mass flow rate caused by the presence of a small amount of liquid under stratified flow conditions. As shown in Figure 8.2-450, the measured cold leg pump-side break flow is higher than the measured hot-leg mass flow rate by about, on average, 0.2 kg/s to 0.3 kg/s. The addition of approximately 0.2 kg/s to 0.3 kg/s of mass between the two measurement locations under quasi-steady-state conditions violates the equation of mass continuity. Therefore, at least one of the measured mass flow rates is not accurate. Because most entrained liquid is vaporized when passing through the steam generator, the mass flow at the pump-side break flow measurement location is mostly steam and was therefore presumed to be accurately measured. Thus, the discrepancy between the measured hot leg and the measured pump-side break mass flow rates indicates that there is a large uncertainty in the two-phase, hot-leg mass flow data. Further analysis of measured steam and mass flow rates shows that the larger uncertainty in hot-leg mass flow rate data is mostly caused by the liquid mass flow rate measurement.

Figure 8.2-451 compares the calculated hot-leg void fraction with data. The measured void fraction is slightly less than 1.0 and oscillates between approximately 0.998 and 0.99 (i.e., the measured liquid fraction is between approximately 0.002 and 0.01) during the pre-quench portion of the transient. Except for a short period towards the end of the transient, the calculated void fraction is between 0.98 and 1.0. The calculated lower void fraction during the early reflood period of simulated ACC ECC injection corresponds to the larger calculated hot-leg mass flow in this period. The potential uncertainty in measuring the hot-leg liquid mass flow rate suggests that the uncertainty in void fraction measurement could be large. Also, the difference in calculated and measured void fraction could be the result of a slight elevation difference across the hot leg in the test facility that is not accounted in the model, thus allowing the liquid to drain back into the upper plenum or into the steam generator lower plenum. The small liquid fraction and the large uncertainty in measurement make it difficult to draw conclusions on the comparison of measured and calculated hot-leg void fraction.

Test Run 54 Intact Loop Behavior

The transient responses for the three intact loops are very similar in both the calculated results and the measured data. Therefore, the calculated results and comparisons with the data for Loop 1 are presented as examples to illustrate the overall intact loop behavior in the reflood phase.

The calculated and measured differential pressures across the pump simulator, which simulates the loop resistance, are overlaid in Figure 8.2-452. The calculation shows continuous fluctuations of small amplitudes. On average, the calculated pressure loss is slightly higher than the data. The relatively good agreement indicates good simulation of the loop resistance and the mass flow rate upstream of the ECC injection port.

Figure 8.2-453 compares the calculated ILHL mass flow rate and the data. In general the calculation agrees reasonably well with the data throughout the transient, even though it shows a few relatively large spikes during the early reflood. During the ACC injection period, the high flow of ECC water into the core generates a large amount of steam and causes entrainment of significant amounts of liquid into the hot legs.

Figure 8.2-454 compares the calculated and measured steam mass flow rate in the ILHL. A short period of lower calculated steam mass flow rate is seen after the end of the simulated ACC injection. Other than this period of underprediction of steam flow caused by the depletion of liquid in the core and the slight overprediction at the end of the transient, the calculation and data agree reasonably well. This result indicates that the vapor generation in the core is properly calculated.

Figure 8.2-455 shows calculated and measured mass flow rates in the intact loop cold leg (ILCL). The ILCL mass flow rate was measured downstream of the ECC injection nozzle and is the combined mass flow rate from the intact loop pump simulator and the ECC injection flow. The calculated mass flow rate after the termination of the ACC injection is higher than the rate shown in the data. However, the measured ILCL mass flow rate is about 1 kg/s below the LPCI mass flow rate. This indicates that the uncertainty in the measured ILCL mass flow rate is large.

Figure 8.2-456 displays the calculated and measured void fractions in the ILHL. The measured void fraction fluctuates between 1.0 and 0.99. This means there is only a trace amount of liquid is present for the period from 100 seconds to about 500 seconds. (NOTE: The measured void fraction is about 0.99 before 100 seconds when no liquid exists in the hot leg.) With exception of the ACC injection period, and near the end of the reflood, the calculated ILHL void fraction is between 1.0 and 0.98. The small liquid fraction (measured to be below 0.05) may require high-precision instrumentation to measure it accurately. Also, a system code such as S-RELAP5 may not be able to accurately calculate the very small liquid fraction in the hot leg.

Figure 8.2-457 shows the void fraction comparison for the ILCL. In the simulated ACC injection period, the void fraction decreases to below 0.2 in the data and almost zero in the calculation. Afterwards, the calculated void fraction is lower than the data by approximately 15%. Also, the figure shows that the cold leg plugging was calculated for a longer period than measured. This effect was caused by the combined influence of the cold leg condensation and interphase friction RLBLOCA multipliers and the lower plenum accumulator injection location for CCTF. The injection location, which prevented significant bypass, allowed the lower plenum and downcomer to become almost completely filled so that the cold leg ACC injection finished filling the downcomer and cold legs between 92 s and 105 s. After the cold leg injection shifted to LPCI, at approximately 107 s, the cold leg should have drained rather quickly, but the drain was prolonged and took approximately 30 s due to the impact of the aforementioned multipliers. It is during this period, approximately 105 s to 135 s, that adverse flow spikes, such as shown in Figure 8.2-455, occur. The extended plugging did not impact the start of reflood since it was already underway. PCT is not impacted since the downcomer is not draining through the break or increasing the reflood rate.

Test Run 54 Vessel Behavior

The differential pressures in the downcomer were measured in four different azimuthal directions. The data shown in Figure 8.2-458 indicates that there is little asymmetrical (or multidimensional) behavior in ECC water downcomer penetration. The calculated differential pressures [ ] are also indistinguishable. Figure 8.2-459 shows the comparison of calculated and measured downcomer differential pressures from about the top to the bottom of the downcomer. The measured differential pressure follows more closely the containment pressures, (see Figure 8.2-445 and Figure 8.2-446) than the calculation. The non-symmetrical upward vapor velocity profiles in the downcomer are responsible for the heterogeneous delivery of ECC water observed in the Upper Plenum Test Facility (UPTF) ECC injection tests (References 8.2-34, and 8.2-36). In this CCTF test and during LOCA reflood phase, no flow of steam occurs from core to downcomer; therefore, no appreciable azimuthal dependency of downcomer differential pressure is expected.

Unfortunately, the upper plenum pressure channel data was invalid, and, as a result, the only other available measured pressure in the pressure vessel was used for comparison. The calculated and measured pressure vessel bottom pressures are shown in Figure 8.2-461. A sharp pressure rise is calculated in the simulated ACC injection period. This is followed by a period of lower calculated pressure for the remainder of the calculation.

The calculated collapsed liquid level in the upper plenum is higher than the measured values in the early part of the reflood, as shown in Figure 8.2-473. Only after quenching occurs do the data indicate higher level. Since the code predicts much later quenching than observed, the calculated level indicates adequate liquid entrainment to the upper plenum during reflood.

Figure 8.2-460 compares the calculated and measured differential pressure across the heated core length. The core differential pressures were measured in four azimuthal directions, and no significant azimuthal dependency was detected. The calculated differential pressures for the four core regions (hot assembly, high-, medium-, and low-power regions) also are very similar. Therefore, the figure shows only the calculated differential pressures for the hot assembly region and one of the measured pressures. The calculation and data are in good agreement, with the calculated pressure slightly lower on average. The lower calculated pressure indicates lower calculated liquid mass in the core and a large amount of entrainment into the hot legs. The overall good comparison of the code to the data on core differential pressures shows that the overall liquid mass inventory in the core is well predicted.

A key parameter for assessing reflood experiments is steam temperature, particularly the steam temperatures in the core region, because the heat transfer rate in high void fraction regions depends on steam temperature. A comparison of calculated and measured steam temperatures was not available because the measured channel data was invalid.

Test Run 54 Core Heater Rod Response

The primary concern in the LBLOCA reflood phase is the cladding temperature rise during the core heatup period. Of secondary importance is the temperature history and duration at high temperature, and of lesser importance is the occurrence and time of the final quench. The ultimate assessment of a best estimate system code such as S-RELAP5, is the code-to-data comparison of the rod temperature response. In the following, a number of comparison plots for heater rod surface temperatures will be shown. The calculations are identified by S-RELAP5 minor-edit parameters and elevations, and the data are identified by the thermocouple tags (see Figure 8.2-438) and elevations. The closest calculated rod surface temperature at either the node center or at the node boundary at an elevation closest to a given thermocouple elevation is used.

Figure 8.2-462 through Figure 8.2-468 show the comparisons of calculated and measured heater rod surface temperatures at three elevations for high-and medium-power core regions, respectively. In general, the calculation displays more fluctuations than the data. The calculation also shows better cooling (at the higher elevations compared with the data) in the period of high ECC water injection rate caused by high calculated liquid entrainment. The overshoot of liquid entrainment in the calculation depletes the core liquid mass inventory, as indicated by the core differential pressure in Figure 8.2-460, and causes the rod surface temperature to rise faster in the subsequent period. Overall, the calculated temperature rise is reasonably close to the data. For the medium- and high-power heater rods, the calculated surface temperature traces agree reasonably well with the data.

With the chopped-cosine axial power profile, the peak temperature rise is expected to occur in the neighborhood just above the mid-plane. Figure 8.2-462 and Figure 8.2-463 show the calculated rod surface temperatures at the elevations of 1.83 m and 2.035 m and the data with the highest temperature rise for the high-power core. The measured PCT of 1113 K (1544 °F) was recorded by the thermocouple at 1.83 m elevation in bundle number 30 (TE30Y37). The maximum surface temperature calculated at 1.83 m is 1055 K (1439 °F). The calculated PCT of 1064 K (1454 °F) occurs at the 2.235 m elevation. Thus, the calculated temperature rise is higher above the mid-plane and the PCT point is shifted to a higher elevation. The PCT time is 130 seconds from the measurement and is at 226 seconds in the calculation. The difference is attributable to (a) the elevation difference of the PCT locations and (b) to the observed top-down cooling proceeding at a greater rate than the calculation, which is set to minimize top-down quenching.

The heater rod surface temperatures were measured at several elevations in various bundles (see Figure 8.2-438). The maximum surface temperatures from all measurements in the high-power core region are plotted in Figure 8.2-469, along with the calculated peak temperatures as a function of elevation. The spread of measured temperature rises in the range of 10 K to 70 K depending on the elevation and the number of thermocouples. (Note that a single data point means that only one measurement was taken at that elevation). The calculated points are seen to be reasonably close to the data range. This shows that the code-calculated maximum temperature behavior, including PCT, slightly underpredict the experiment.

8.2.13.5.6 Test Run 54 Discussion of Results

According to the PIRT (Table 5-1), the most important reflood phenomena are: core post-CHF and reflood heat transfer, vapor generation/distribution and entrainment/de-entrainment in the core, entrainment/de-entrainment in the upper plenum and in the hot legs, steam binding in steam generator, pump Δp, hot wall effects in the downcomer and the lower plenum, non-condensable gases in cold leg/accumulator, loop flow oscillations, decay heat, and oxidation and gas conductance for fuel rods.

Except for the fuel rod oxidation and conductance and cold leg/accumulator non-condensable gases, all the important reflood phenomena were observed in the CCTF Test Run 54 and were calculated reasonably well by S-RELAP5.

As mentioned in previous sections, CCTF Test Run 54 power decay simulated ANS Standard 1.0 plus actinide decay heat. This power decay curve was treated in S-RELAP5 by tabulated input values (see Figure 8.2-474). The pump/loop Δp was simulated in the test by an orifice plate and in S-RELAP5 by a form loss factor . Figure 8.2-452 shows that the pump/loop Δp is well calculated.

The lower-plenum/downcomer hot-wall effects were included in the test by preheating the wall to specified temperatures. The vessel walls and internals plus piping walls were modeled in S-RELAP5 by heat structures with specified initial temperatures. Loop flow oscillations are mainly induced by the condensation of steam with cold ECC water. Large and atypical oscillations occur when the steam mass flow rate is too small to meet the demand for condensation. One example is the case of injecting accumulator ECC water into the cold legs before establishing a sufficiently strong steam flow from the reactor core through the hot legs and to the cold legs. The initial conditions and accumulator injection sequences were carefully set in the test to minimize the atypical oscillatory behavior. This was accomplished by switching the accumulator ECC injection locations from the lower plenum, to the three cold legs at the time the water level reached the 0.5 m level above the bottom of the heated region, so considerable steam generation had occurred in the core. With these special arrangements, some cold-leg oscillations still were observed in the test during the ACC injection period (see Figure 8.2-455). For the LPCI, the cold leg oscillations are generally of small amplitudes and of little significance because the loop steam flow is well established and the ECC mass flow is low. The measured cold-leg mass flow rate did not show any oscillation during the LPCI.

The calculated results show more and larger oscillations than the data in the ACC injection period, as seen in Figure 8.2-448, Figure 8.2-449, and Figure 8.2-455. The system-wide pressure oscillations caused by cold-leg condensation result in rapid spread of liquid to the entire core. The liquid increases the core heat transfer and produces a short period of overcooling, as indicated by the relatively flat temperature histories seen in Figure 8.2-462 through Figure 8.2-468. The high steam generation rate that accompanies the overcooling produces high pressure in the core, and thus expels liquid out of the core. The loss of core liquid inventory reduces the core coolability and raises the heater-rod temperatures. This over- and undercooling sequence prolongs the temperature rise period for the higher elevations. Oscillations of small amplitudes are seen in the calculated cold-leg mass flow rate (Figure 8.2-455) and void fraction (Figure 8.2-457).

The entrainment/de-entrainment phenomena affect the liquid distribution (or void distribution) in the core and in the hot legs, [

] The good agreement between the calculated and measured differential pressures in the core (Figure 8.2-460) indicates that the core liquid inventory is well calculated. The core heat transfer depends strongly on the liquid distribution. The acceptable comparisons of the code to the data for rod temperature histories (Figure 8.2-462 through Figure 8.2-468) and steam mass flow rate (Figure 8.2-454) are a combined result of well-calculated heat transfer rate, vapor generation rate, and liquid distribution in the core.

The calculated void fraction in the hot legs is acceptable, if it is somehow less, on average, than the measured void fraction. The inconsistency of measured loop mass flow rates (Figure 8.2-450 and Figure 8.2-456), and the special precautions required to accurately measure very small liquid fraction under horizontal stratification conditions, suggest that the void fraction data might have a large uncertainty. Furthermore, prediction of liquid fractions as small as the 0.01 measured in the hot leg probably is beyond the capability of the S-RELAP5 reflood model. Taking into account the data uncertainty and the code capability, the calculated liquid fraction in the hot leg is acceptable. Also it is important to note that no accumulation of liquid occurs in the hot leg until near the end of core reflood. The small fluctuations in the calculated void fraction indicate intermittent entrainment and de-entrainment.

The steam binding effect in the steam generator refers to the vaporizing of entrained liquid and the heatup of steam flow by the reverse heat transfer from the secondary to the primary side. In CCTF Test Run 54, there were no direct measured data such as steam flow rates and temperatures entering and leaving the steam generator to assess this effect. The liquid carryover can be estimated from the liquid level in Containment Tank II shown in Figure 8.2-470. Considering the large uncertainty in measurement data and the lack of a precise geometry description for the tank, the code calculated value agrees reasonably well with the measured data. Figure 8.2-471 and Figure 8.2-472 illustrate the secondary side pressure of the steam generators. The S-RELAP5 calculation shows a faster cooldown of the secondary side suggesting that a larger amount of heat is being transferred to the fluid in the tubes, than measured. This should increase the amount of liquid being vaporized and the steam heatup in the S-RELAP5 calculation, making it more conservative.

The calculated upper plenum level indicates that the code tends to entrain fluid into the upper plenum earlier than the data indicates, as shown in Figure 8.2-473, and then reaches a quasi-stationary level, which differs from the evolution of the experimental data illustrated in the same figure. This indicates that the code does not perform very well in determining the liquid distribution, however the amount of liquid entrained and removed through the break is reasonably well calculated, as shown in Figure 8.2-470.

The core recovery in CCTF Test Run 54, and in the reflood phase of a cold-leg ECC injection PWR, is accomplished by a bottom-up quench with some degree of top-down cooling caused by the fallback of the entrained liquid accumulated in the upper plenum. Small manometer oscillations between the downcomer and the core may occur because of the core steam binding effect. In the calculations, the vapor generation rate may vary considerably when the quench front progresses from the lower end of a control volume to the upper end, because of the dependence of heat transfer rate on void fraction. The change in vapor generation rate tends to amplify the downcomer to core oscillations. Consequently, the calculated rod surface temperature curves often are not as smooth as the data curves.

For licensing analyses of PWR LBLOCA, the primary concern is the cladding temperature rise. The calculations presented in this report show that the calculated maximum temperatures at upper core elevations are at the high end of the data ranges for the high-power bundles. Furthermore, the overall system responses, such as loop mass flow rates, loop Δp, downcomer Δp, and core Δp are well calculated.

8.2.13.6 CCTF Test Run 62

8.2.13.6.1 Test Run 62 Description

Test Run 62 simulated the reflood phase of a cold-leg ECC injection PWR LOCA with a high decay power (i.e., augmenting the 1971 ANS draft standard decay power by 20%), a system pressure of 0.2 MPa, and an LPCI flow rate of 0.011 m^3 /s.

8.2.13.6.2 Test Run 62 Input Description

The input model for test run 62 is identical to the input model for run 54 with the only changes required to input the case specific initial and boundary conditions.

8.2.13.6.3 Test Run 62 Measured Test Conditions

In general, the test conditions for the CCTF tests were based on the Appendix K design basis pre-reflood assumptions and low ECC water injection rate according to the single failure criteria. The following measured test conditions for the CCTF Test Run 62 were established through the test procedure prescribed in the data report (Reference 8.2-56), and are presented in Table 8.2-58.

Note that the time shown is defined as the time after test initiation. Also, the initial water level in the lower plenum and the injection of ECC water into the lower plenum and its timing were designed to minimize the atypical oscillatory behavior from condensation at the ECC port in the initial stage of reflood by producing a considerable amount of steam in the core.

After the primary system was preheated to its specified temperatures, the test was initiated by turning on the power to the core heater rods with the vessel filled with steam, except for 0.81 m (2.66 ft) of saturated water in the lower plenum. Because the initial water level in the lower plenum was below the bottom of the core, the rods in the core heated up virtually adiabatically in the steam environment before reflood began. Accumulator injection began at 84.5 seconds and was initially directed into the lower plenum. The core power started to decay from the maximum value of 9.37 MW at 93.5 seconds, when the reflood began (BOCREC).

When the liquid level reached 0.5 m (1.64 ft) above the bottom of the core at about 97 seconds, the accumulator injection was shifted to the cold leg and continued until about 111 seconds. After accumulator injection ended, low pressure coolant injection (simulating LPCI) was injected into the intact cold legs starting at 120 s and continuing until the end of the test. All heated rods were quenched by about 652 seconds into the transient (i.e., 558 seconds after BOCREC). The sequence of events for the test is summarized in Table 8.2-59.

8.2.13.6.4 Test Run 62 Initial and Boundary Conditions

The initial and boundary conditions were taken from the data report or the DMS data files for Test Run 62. These initial conditions were used to set up the initial conditions for the S-RELAP5 hydrodynamic components and heat structures. In addition, the S-RELAP5 CCTF input model required tabulated input values for 11 time-dependent boundary conditions. These included total core power, liquid state and flow conditions for ECC injection at the lower plenum and at the three intact cold legs, and both containment tank pressures.

All the tabulated input boundary conditions were extracted from the DMS data files. Figure 8.2-474 shows the total power curve used in S-RELAP5 calculations, Figure 8.2-475 and Figure 8.2-476 show the two containment pressure conditions, and Figure 8.2-477 shows the total ECC injection mass flow rate, which is a sum of mass flow rates injected to the lower plenum and the three intact cold legs. Note particularly that the two containments were not at a constant pressure of 0.2 MPa as specified in the data report.

A polynomial interpolation scheme was used, based on the same measured temperatures, yielding an initial temperature distribution for the downcomer as shown in Table 8.2-60.

8.2.13.6.5Test Run 62 Calculated Results and Comparisons

Test Run 62 simulated the reflood phase of a cold-leg ECC injection PWR LOCA with a high decay power (i.e., augmenting the 1971 ANS draft standard decay power by 20%), a system pressure of 0.2 MPa, and an LPCI flow rate of 0.011 m^3/s.

S-RELAP5 calculations of CCTF Test Run 62 are presented here with the code-to-data comparisons. Emphasis is placed on the heater rod surface temperatures for the additional calculations because the calculated results from all calculations for all major hydrodynamic parameters are very similar. In the figures comparing the code to the data, the measured quantities, except for those derived from the data, generally are identified by the instrumentation identifiers, (see Figure 8.2-438 and Figure 8.2-439 for examples) and the calculated quantities are identified mostly by the S-RELAP5 minor-edit parameters and component numbers. The results of Test Run 62 are illustrated in Figure 8.2-478 through Figure 8.2-503.

Test Run 62 Broken Loop Behavior

Comparisons of the calculated mass flow rates and data in the BLHL and BLCL pump-side break flow are shown in Figure 8.2-478 and Figure 8.2-479, respectively. For the BLCL pump-side break flow (Figure 8.2-479), the calculation is slightly lower (10% on average) than that measured. The calculated hot-leg mass flow rate shows some large spikes caused by the infrequent liquid carryover into the hot leg. These spikes occurred during the early reflood period when the ECC flow is high (simulating the accumulator ECC flow). On average, the calculated hot leg mass flow rate is about the same as the calculated pump-side break flow rate and, on average, is about the same as the measured flow rate (higher in the early reflood, around the data in the middle, and higher after 600 seconds).

A large uncertainty might be associated with the measurement of hot leg mass flow rate caused by the presence of a small amount of liquid under stratified flow conditions. Figure 8.2-480 shows that the measured cold-leg pump-side break flow is higher than the measured hot-leg mass flow rate. This agrees with Test Run 54 in that at least one of the measured mass flow rates is not accurate and the larger uncertainty in hot-leg mass flow rate data is caused mostly by the liquid mass flow rate measurement.

Figure 8.2-481 compares the calculated hot-leg void fraction with the data. The measured void fraction is slightly less than 1.0 and oscillates between approximately 0.998 and 0.996 during most of the transient. Except for the early reflood, the calculated void fraction is between 0.98 and 1.0. The calculated lower void fraction during the early reflood period of simulated ACC ECC injection corresponds to the larger calculated hot-leg mass flow in this period. This reinforces the conclusions in Test Run 54 that the uncertainty in void fraction measurement could be large.

Test Run 62 Intact Loop Behavior

The transient responses for the three intact loops are very similar for both the calculated results and the measured data. Therefore, the calculated results and comparisons with the data for Loop 1 are presented as examples to illustrate the overall intact-loop behavior in the reflood phase.

The calculated and measured differential pressures across the pump simulator, which simulates the loop resistance, are overlaid in Figure 8.2-482. The calculation shows continuous fluctuations of small amplitudes. On average, the calculated pressure loss is slightly higher than the data. The good agreement indicates good simulation of the loop resistance and the mass flow rate upstream of the ECC injection port. Figure 8.2-483 compares the calculated ILHL mass flow rate and the data. Higher mass flow rate with some flow spikes is calculated in the early reflood period when the ECC injection is high (simulating the accumulator ECC injection). Throughout the rest of the transient, the calculated mass flow rate is slightly higher than the data.

As in Test Run 54, entrainment into the hot legs is responsible for the overshoot of calculated hot-leg mass flow rate in the early reflood period. Figure 8.2-484 compares the calculated and measured steam mass flow rates in the ILHL. A short period of lower calculated steam mass flow rate is seen after the end of the simulated ACC injection. Other than this period of underprediction of steam flow caused by the depletion of liquid in the core, the calculation and data agree well. This result indicates the vapor generation in the core is properly calculated.

Figure 8.2-485 shows calculated and measured mass flow rates in the ILCL. The ILCL mass flow rate was measured downstream of the ECC injection nozzle, and is the combined mass flow rate from the intact-loop pump simulator and the ECC injection flow. The calculated ILCL mass flow is higher than the measured mass flow rate, as expected. However, the uncertainty in the measured ILCL mass flow rate is large, as discussed in Section 8.2.13.5.5, Intact Loop Behavior for Test Run 54.

Figure 8.2-486 shows the calculated and measured void fractions in the ILHL. The measured void fraction fluctuates between 1.0 and 0.99 (i.e., there is only a trace amount of liquid) for the period from 100 seconds to about 400 seconds. (NOTE: The measured void fraction is about 0.99 before 100 seconds when no liquid exists in the hot leg.) Except for the ACC injection period and near the end of the reflood, the calculated ILHL void fraction is between 1.0 and 0.98. The small liquid fraction (measured to be below 0.05) may require high precision instrumentation to measure it accurately. Also, a system code such as S-RELAP5 may not be able to accurately calculate the very small liquid fraction in the hot leg. Figure 8.2-487 shows the void fraction comparison for the ILCL. In the simulated ACC injection period, the void fraction decreases to about 0.2 in the data and almost zero in the calculation. Afterward, the calculation void fraction is lower than the data and fluctuates with smaller amplitudes. As occurred in Run 54 (see Section 8.2.13.5.5), the combined influence of the cold leg condensation and interphase friction RLBLOCA multipliers and the lower plenum accumulator injection location for CCTF, caused an extended plugging of the ILCL during the time period surrounding the switch to LPCI (Figure 8.2-487). As before, adverse flow spikes, such as shown in Figure 8.2-485, occur.

Test Run 62 Vessel Behavior

The differential pressures in the downcomer were measured in four different azimuthal directions. The data shown in Figure 8.2-488 indicates little asymmetrical or multi-dimensional behavior in ECC water downcomer penetration. The calculated differential pressures for [ ] also are indistinguishable. Figure 8.2-489 compares the calculated and measured downcomer differential pressures from about the top to the bottom of the downcomer. The measured differential pressure more closely follows the containment pressures (see Figure 8.2-475 and Figure 8.2-476) than does the calculation; however, there is reasonable agreement between the measured and calculated downcomer pressure, with the calculated value being slightly lower throughout the calculation. As explained in Test Run 54, no appreciable azimuthal dependence of downcomer differential pressure is expected.

The calculated collapsed liquid level in the upper plenum is higher than the measured values in the early part of the reflood, as shown in Figure 8.2-503. Only after quenching occurs do the data indicate higher level. Since the code predicts much later quenching than observed, the calculated level indicates adequate liquid entrainment to the upper plenum during reflood.

The calculated and measured upper plenum pressures are shown in Figure 8.2-491. A sharp pressure rise is calculated in the simulated ACC injection period. This is followed by a period of lower calculated pressure for the remainder of the calculation indicating that S-RELAP5 is probably calculating higher condensation in the cold leg than is actually occurring.

Figure 8.2-490 compares the calculated and measured differential pressure across the heated core length. As discussed in Test Run 54, only the calculated differential pressure for the high-power region and one of the measured pressures are shown in the figure. The calculation and data are in good agreement, with the calculated pressure slightly lower on average. The lower calculated pressure indicates lower calculated liquid mass in the core and a lower rate of steam production. The overall reasonable code-to-data comparison on core differential pressures shows that the overall liquid mass inventory in the core is well predicted. A comparison of calculated and measured steam temperatures was not available because the measured channel data was invalid.

Test Run 62 Core Heater Rod Response

The primary concern in the LBLOCA reflood phase is the cladding temperature rise during the core heatup period. Of secondary importance is the temperature history and duration at high temperature, and of even lesser importance is the occurrence and time of the final quench. The ultimate assessment of a best estimate system code such as S-RELAP5 is the code-to-data comparison of the rod temperature response. In the following, a number of comparison plots for heater rod surface temperatures will be shown. The calculations are identified by S-RELAP5 minor-edit parameters and elevations, and the data are identified by the thermocouple tags (see Figure 8.2-438) and elevations. The closest calculated rod surface temperature at either the node center or at the node boundary at an elevation closest to a given thermocouple elevation is used.

Figure 8.2-492 through Figure 8.2-498 compare the calculated and measured heater rod surface temperatures at different elevations for the high- and medium-power core regions. In general, the calculation displays more fluctuations than the data. The calculation also shows better cooling (at the higher elevations in comparison with the data) in the period of high ECC water injection rate caused by high calculated liquid entrainment. The overshoot of liquid entrainment in the calculation depletes the core liquid mass inventory, as indicated by the core differential pressure shown in Figure 8.2-490, and causes the rod surface temperature to rise faster in the subsequent period. Overall, the calculated temperature rise is higher than or close to the data. For the medium- and high-power heater rods, the calculated surface temperature histories are acceptable in comparison with the data.

With the chopped-cosine axial power profile, the peak temperature rise is expected to occur in the neighborhood just above the mid-plane. Figure 8.2-492 and Figure 8.2-493 show the calculated rod surface temperatures at 1.83 m and 2.035 m elevations, and the data with the highest temperature rise for the high-power core. The measured PCT of 1132 K (1578 °F) was recorded by the thermocouple at 1.83 m elevation in bundle number 30 (TE30Y37). The maximum surface temperature calculated at 1.83 m is 1106 K (1531 °F), while the calculated PCT is 1116 K (1548 °F) at 2.235 m elevation, showing good agreement with the data. Thus, the calculated temperature rise is higher above the mid-plane, and the PCT point is shifted to a higher elevation. The PCT time is 154 seconds from the measurement and is at 235 seconds in the calculation. The difference is attributable to the observed top-down cooling proceeding at a greater rate than the calculation.

The heater rod surface temperatures were measured at several elevations in various bundles (see Figure 8.2-438). The maximum surface temperatures from all measurements in the high-power core region are plotted along with the calculated peak temperatures as a function of elevation in Figure 8.2-499. The spread of measured temperature rises is in the range of 10 K to 70 K, depending on the elevation and the number of thermocouples. (Note that a single data point means that only one measurement was taken at that elevation). The calculated points are seen to be at the high end of the data range or above it. This shows that the code calculated maximum temperature behavior, including PCT, is in good agreement with the experimental behavior.

8.2.13.6.6 Test Run 62 Discussion of Results

According to the PIRT (Table 5-1), the most important reflood phenomena are core reflood heat transfer, void generation/distribution and entrainment/de-entrainment in the core, entrainment and de-entrainment in the upper plenum and in the hot legs, steam binding in the steam generator, pump Δp, hot wall in the downcomer and lower plenum, non-condensable gases in the cold leg/accumulator, loop flow oscillations, decay heat, and oxidation and gas conductance for fuel rods.

Except for the fuel rod oxidation and conductance, and cold leg/accumulator non-condensable gases, all the important reflood phenomena were observed in the CCTF Test Run 62 and were calculated reasonably well by S-RELAP5.

As mentioned in Section 8.2.13.6.1, CCTF Test Run 62 power decay simulated the 1971 ANS Draft Standard times 1.2 plus actinide decay heat. This power decay curve was treated in S-RELAP5 by tabulated input values (see Figure 8.2-474). The pump/loop Δp was simulated in the test by an orifice plate and in S-RELAP5 by a form loss factor. Figure 8.2-482 shows that the pump/loop Δp is well calculated.

The lower-plenum/downcomer hot-wall effects were included in the test by preheating the wall to specified temperatures. The vessel walls and internals plus piping walls were modeled in S-RELAP5 by heat structures with specified initial temperatures. Loop flow oscillations are mainly induced by the condensation of steam with cold ECC water. Large and atypical oscillations occur when the steam mass flow rate is too small to meet the demand for condensation. Also, as discussed in Test Run 54, some cold-leg oscillations still were observed in the test during the ACC injection period (see Figure 8.2-485). For the LPCI, the cold-leg oscillations generally are of small amplitudes and of little significance because the loop steam flow is well established and the ECC mass flow is low. The measured cold-leg mass flow rate did not show any oscillation during the LPCI.

The calculated results show more and larger oscillations than the data in the ACC injection period, as seen in Figure 8.2-478, Figure 8.2-479, and Figure 8.2-485. The calculated negative flow at the beginning of cold ECC injection indicates that a sufficiently strong steam flow had not yet been established when the cold-leg ECC injection started. The system-wide pressure oscillations caused by cold-leg condensation result in rapid spread of liquid to the entire core. The liquid increases the core heat transfer and produces a short period of overcooling as indicated by the relatively flat temperature histories shown in Figure 8.2-492 through Figure 8.2-498. The high steam generation rate accompanying the overcooling produces high pressure in the core, and thus expels liquid from the core. The loss of core liquid inventory reduces the core coolability and raises the heater rod temperatures. This over- and undercooling sequence prolongs the temperature rise period for the higher elevations.

As discussed in Section 8.2.13.5.6, in CCTF Test Run 62 there were also no direct measured data, such as steam flow rates and temperatures entering and leaving the steam generator to assess the steam binding effect. The liquid carryover can be estimated from the liquid level in Containment Tank II, shown in Figure 8.2-500. Considering the large uncertainty in measurement data and the lack of a precise geometry description for the tank, the code calculated value is in acceptable agreement with the measured data.

Figure 8.2-501 and Figure 8.2-502 illustrate the secondary side pressure of the steam generators. The S-RELAP5 calculation shows a faster cooldown of the secondary side, suggesting that a larger amount of heat is being transferred to the fluid in the tubes than measured. This should increase the amount of liquid being vaporized and the steam heatup in the S-RELAP5 calculation, making it more conservative. As seen in Test Run 54, the steam binding effect in the steam generator is difficult to quantify, but is being conservatively calculated by S-RELAP5.

The good agreement between the calculated and measured differential pressures in the core (Figure 8.2-490) indicates that the core liquid inventory is well calculated. The calculated void fraction in the hot legs is less than the measured void fraction. The improper calibration of void measurement (initial reading of less than 1.0 shown in Figure 8.2-481 and Figure 8.2-486), the inconsistency of measured loop mass flow rates (Figure 8.2-478 and Figure 8.2-483), and the special precautions required to accurately measure very small liquid fractions under horizontal stratification conditions, all suggested that the void fraction data might have a large uncertainty. As discussed in Test Run 54, the calculated liquid fraction in the hot leg is reasonable. It is also important to note that little liquid accumulates in the cold leg. The calculated rod surface temperature curves are often not as smooth as the data.

The calculations presented in this report show that the calculated maximum temperatures at all core elevations are above or at the high end of the data ranges for the high-power bundles. The overall hydraulic response shows reasonable calculation of the trends, but some responses, such as mass break flow rate, upper plenum pressure, and pump Δp show reasonable to good agreement with the data.

8.2.13.7 CCTF Test Run 67

8.2.13.7.1 Test Run 67 Description

Test Run 67 simulated the reflood phase of a cold-leg ECC injection PWR LOCA with a high decay power (i.e., augmenting the 1971 ANS draft standard decay power by 20%), a lowered system pressure of 0.15 MPa, and an LPCI flow rate of 0.011 m^3/s.

8.2.13.7.2 Test Run 67 Input Description

The input model for test run 67 is identical to the input model for run 54 with the only changes required to input the case specific initial and boundary conditions.

8.2.13.7.3Test Run 67 Measured Test Conditions

In general, the test conditions for CCTF tests were based on Appendix K design basis pre-reflood assumptions, and low ECC water injection rate according to the single failure criteria. The measured test conditions for the CCTF Test Run 67 were established through the test procedure prescribed in the data report (Reference 8.2-57) and are presented in Table 8.2-61.

Note that the time shown in Table 8.2-62 is defined as the time after test initiation. Also, the initial water level in the lower plenum, and the injection of ECC water into the lower plenum and its timing were designed to minimize the atypical oscillatory behavior from condensation at the ECC port in the initial stage of reflood by producing a considerable amount of steam in the core.

After the primary system was pre-heated to its specified temperatures, the test was initiated by turning on the power to the core heater rods with the vessel filled with steam, except for 0.86 m (2.82 ft) of saturated water in the lower plenum. Because the initial water level in the lower plenum was below the bottom of the core, the rods in the core heated up virtually adiabatically in the steam environment before reflood began. Accumulator injection began at 86.5 seconds and initially was directed into the lower plenum. The core power started to decay from the maximum value of 9.32 MW at 95 seconds, when the reflood began (BOCREC).

When the liquid level reached 0.5 m (1.64 ft) above the bottom of the core at about 96 seconds, the accumulator injection was shifted to the cold leg and continued until about 114 seconds. After accumulator injection ended, low-pressure coolant (simulating LPCI) was injected into the intact cold legs starting around 110 seconds until the end of the test. All heated rods were quenched by about 760 seconds into the transient (664 seconds after BOCREC). The sequence of events for the test is summarized in Table 8.2-62.

8.2.13.7.4 Test Run 67 Initial and Boundary Conditions

The initial and boundary conditions were taken from the data report or the DMS data files for Test Run 67. The initial conditions described in Section 8.2.13.7.3 were used to set up the initial conditions for the S-RELAP5 hydrodynamic components and heat structures. In addition, the S-RELAP5 CCTF input model required tabulated input values for 11 time-dependent boundary conditions. These included total core power, liquid state, and flow conditions for ECC injection at the lower plenum and at the three intact cold legs, and both containment tank pressures.

All the tabulated input boundary conditions were extracted from the electronic data files. Figure 8.2-504 shows the total power curve used in the S-RELAP5 calculations, Figure 8.2-505 and Figure 8.2-506 show the two containment pressure conditions, and Figure 8.2-507 shows the total ECC injection mass flow rate, which is a sum of mass flow rates injected to the lower plenum and the three intact cold legs. Note particularly that the two containments were not at a constant pressure of 0.15 MPa as specified in the data report.

A polynomial interpolation scheme was used, based on the same measured temperatures, yielding an initial temperature distribution for the downcomer as shown in Table 8.2-63.

8.2.13.7.5 Test Run 67 Calculated Results and Comparisons

The S-RELAP5 calculations of CCTF Test Run 67 provide comparisons between the code and the data. Emphasis is placed on the heater rod surface temperatures for the additional calculations because the calculated results from all calculations for all major hydrodynamic parameters are very similar. In the figures displaying the code-to-data comparisons, the measured quantities, except for those derived from the data, generally are identified by the instrumentation identifiers (see Figure 8.2-438 and Figure 8.2-439 for examples), and the calculated quantities are identified mostly by the S-RELAP5 minor-edit parameters and component numbers. The results of Test Run 67 are illustrated in Figure 8.2-508 through Figure 8.2-533.

Test Run 67 Broken Loop Behavior

Comparisons of the calculated mass flow rates and data in the BLHL- and BLCL-pump-side break flow are shown in Figure 8.2-508 and Figure 8.2-509, respectively. As in the previous two discussions, the calculated pump-side break flow is lower, on average by 15% than the measured flow (Figure 8.2-509). The calculated hot-leg mass flow rate shows some large spikes caused by the infrequent liquid carryover into the hot leg during the early reflood period when the ECC flow is high (simulating the accumulator ECC flow). On average, the calculated hot-leg mass flow rate is about the same as the calculated pump-side break flow rate, and slightly higher than the measured hot-leg mass flow rate.

A large uncertainty might be associated with the measurement of the hot-leg mass flow rate caused by the presence of a small amount of liquid under stratified flow conditions. As shown in Figure 8.2-510, the measured cold leg pump-side break flow is higher than the measured hot leg mass flow rate. This same difference also was observed in Test Runs 54 and 62, and leads to the conclusion that at least one of the measured mass flow rates is not accurate, and the larger uncertainty in hot leg mass flow rate data is caused mostly by the liquid mass flow rate measurement.

Figure 8.2-511 compares the calculated hot-leg void fraction with the data. Both the measured and calculated void fraction are very close during most of the transient, except for the early reflood period, where the calculated void fraction is between 0.98 and 1.0. The calculated lower void fraction during the early reflood period of simulated ACC ECC injection corresponds to the larger calculated hot-leg mass flow in this period. This reinforces the previous conclusions that the uncertainty in void fraction measurement could be large.

Test Run 67 Intact Loop Behavior

The transient responses for the three intact loops are very similar for both the calculated results and the measured data. Therefore, the calculated results and comparisons with the data for Loop 1 are presented as examples to illustrate the overall intact loop behavior in the reflood phase.

The calculated and measured differential pressures across the pump simulator, which simulates the loop resistance, are overlaid in Figure 8.2-512. The calculation shows continuous fluctuations of medium amplitudes through the first half and of smaller amplitudes through the second half. On average, the calculated pressure loss is higher than the data. The good agreement indicates good simulation of the loop resistance and the mass flow rate upstream of the ECC injection port.

Figure 8.2-513 compares the calculated intact-loop hot-leg mass flow rate and the data. A higher mass flow rate with some flow spikes is calculated in the early reflood period when the ECC injection is high (simulating the accumulator ECC injection). Afterwards, the calculated mass flow rate is slightly higher than the data.

Figure 8.2-514 compares the calculated and measured steam mass flow rate in the intact-loop hot leg. A period of lower calculated steam mass flow rate is seen after the end of the simulated ACC injection. This period of underprediction is due to the lower amount of steam flow caused by the depletion of liquid in the core. Other than this period, the calculation and data agree well; however after about 400 seconds, a slight linear decrease occurs with time in the measured data, while the calculated steam flow remains, on average, constant. This result indicates the vapor generation in the core is properly calculated early, before 400 seconds, but underpredicted later.

Figure 8.2-515 shows calculated and measured mass flow rates in the ILCL. The ILCL mass flow rate was measured downstream of the ECC injection nozzle, and is the combined mass flow rate from the intact-loop pump simulator and the ECC injection flow. As previously noted, the calculated mass flow rate after the termination of the ACC injection again, is higher than the data. The calculated ILCL mass flow also is higher than the measured mass flow rate, as expected. However, the measured ILCL mass flow rate is about 1 kg/s below the calculated LPCI mass flow rate. This was observed in the previous runs and indicates that the uncertainty in the measured ILCL mass flow rate is large.

Figure 8.2-516 displays the calculated and measured void fractions in the ILHL. The measured void fraction fluctuates between 1.0 and 0.997 (there is only a trace amount of liquid for the period from 100 seconds to about 500 seconds). (NOTE: The measured void fraction is about 0.994 before 100 seconds when no liquid exists in the hot leg.) Except for the ACC injection period and near the end of the reflood, the calculated ILHL void fraction is between 1.0 and 0.98.

Figure 8.2-517 shows the void fraction comparison for the ILCL. In the simulated ACC injection period, the void fraction decreases to about 0.2 in the data and almost zero in the calculation. Afterwards, the calculation void fraction is lower than the data. As occurred in Run 54 (see Section 8.2.13.5.5), cold leg condensation and interphase friction RLBLOCA multipliers and the lower plenum accumulator injection location for CCTF caused an extended plugging of the ILCL during the time period surrounding the switch to LPCI (Figure 8.2-517). As before, adverse flow spikes, such as shown in Figure 8.2-515, occur.

Test Run 67 Vessel Behavior

The differential pressures in the downcomer were measured in four different azimuthal directions. The data shown in Figure 8.2-518 indicates that little asymmetrical (or multi-dimensional) behavior occurs in ECC water downcomer penetration. The calculated differential pressures [ ] also are indistinguishable.

Figure 8.2-519 compares the calculated and measured downcomer differential pressures from about the top to the bottom of the downcomer. The measured differential pressure follows more closely to the containment pressures (see Figure 8.2-505 and Figure 8.2-506) than the calculation. As explained in Test Run 54, no appreciable azimuthal dependency of downcomer differential pressure is expected.

The calculated and measured upper plenum pressures are shown in Figure 8.2-521. A sharp pressure rise is calculated in the simulated ACC injection period. This is followed by lower calculated pressure for the rest of the transient.

The calculated collapsed liquid level in the upper plenum is higher than the measured values in the early part of the reflood, as shown in Figure 8.2-533. Only after quenching occurs, do the data indicate higher level. Since the code predicts much later quenching than observed, the calculated level indicates adequate liquid entrainment to the upper plenum during reflood.

Figure 8.2-520 compares the calculated and measured differential pressure across the heated core length. As discussed in Test Run 54, the figure shows only the calculated differential pressure for the high-power region, and one of the measured pressures. Except for a short period right after the switch of ECC injection from ACC to LPCI, the calculation tends to be lower than the data by about 0.005 MPa. The overall code-to-data comparison on core differential pressures shows that the overall liquid mass inventory in the core is reasonably predicted.

A comparison of calculated and measured steam temperatures was not available because the measured channel data was invalid.

Test Run 67 Core Heater Rod Response

The primary concern in the LBLOCA reflood phase is the cladding temperature rise during the core heatup period. Of secondary importance is the temperature history and duration at high temperature, and of lesser importance is the occurrence and time of the final quench. The ultimate assessment of a best estimate system code such as S-RELAP5 is the code-to-data comparison of the rod temperature response. In the following discussion, a number of comparison plots for heater rod surface temperatures will be shown. The calculations are identified by S-RELAP5 minor edit parameters and elevations, and the data are identified by the thermocouple tags (see Figure 8.2-438) and elevations. Because the core region [ ] with no special consideration for thermocouple locations, the closest calculated rod surface temperature at either the node center or at the node boundary at an elevation closest to a given thermocouple elevation is used.

Figure 8.2-522 through Figure 8.2-528 compare the calculated and measured heater rod surface temperatures at three elevations for high-and medium-power core regions, respectively. In general, the calculation displays more fluctuations than the data. The calculation also shows slightly better cooling than the data in the period of high ECC water injection rate caused by high calculated liquid entrainment. The overshoot of liquid entrainment in the calculation depletes the core liquid mass inventory, as indicated by the core differential pressure in Figure 8.2-520, and causes the rod surface temperature to rise faster and remain hot longer in the subsequent period. Overall, the calculated temperature rise is much higher than or close to the data. For both the high- and medium-power heater rods, the calculated surface temperature histories display acceptable agreement with the data and the quench times are later at the higher elevations.

With the chopped-cosine axial power profile, the peak temperature rise is expected to occur in the neighborhood just above the mid-plane. Figure 8.2-522 and Figure 8.2-523 show the calculated rod surface temperatures at 1.83 m and 2.035 m elevations, and the data with the highest temperature rise for the high power core. The measured PCT of 1143 K (1598 °F) was recorded by the thermocouple at the 1.83 m elevation. The maximum surface temperature was calculated at 1.83 m is 1180 K (1664 °F). The calculated PCT of 1238 K (1769 °F) occurs at the 2.645 m elevation. Thus, the calculated temperature rise is higher above the mid-plane and the PCT point is shifted to a higher elevation. The PCT time is 164 seconds from the measurement, and 385 seconds from the calculation. The difference is attributable to the elevation difference of the PCT locations and over- and undercooling in the early reflood period.

The heater-rod surface temperatures were measured at several elevations in various bundles (see Figure 8.2-438). The maximum surface temperatures from all measurements in the high-power core region are plotted along with the calculated peak temperatures, as a function of elevation in Figure 8.2-529. The calculated points are seen to be at the high end of the data range or above it. This shows that the code calculated maximum temperature behavior, including PCT, shows conservative acceptable agreement with the experiment.

8.2.13.7.6 Test Run 67 Discussion of Results

The most important reflood phenomena, according to the PIRT (Table 5-1), are: core reflood heat transfer, void generation/distribution and entrainment/ de entrainment in the core, entrainment/de-entrainment in the upper plenum and in the hot legs, steam binding in steam generator, pump Δp, hot wall in the downcomer and lower plenum, noncondensable gases in the cold leg/accumulator, loop flow oscillations, decay heat, and oxidation and gas conductance for fuel rods. Except for the fuel rod oxidation and conductance and cold leg/accumulator noncondensable gases, all the important reflood phenomena were observed in the CCTF Test Run 67, and generally were calculated with reasonable or acceptable agreement by S-RELAP5.

As mentioned in Section 8.2.13.7.1, CCTF Test Run 67 power decay simulated ANS Standard 1.2 plus actinide decay heat. This power decay curve was treated in S-RELAP5 by tabulated input values (see Figure 8.2-504). The pump/loop Δp was simulated in the test by an orifice plate and in S-RELAP5 by a form loss factor. Figure 8.2-512 shows that the calculated pump/loop Δp is lower than measured after accumulator injection ends for about 50 seconds, then it remains greater for the duration of the test. A comparison of the intact loop steam flow rate and total flow rate (Figure 8.2-513 and Figure 8.2-514) shows that, for this test, very little water is being carried into the hot leg after accumulator injection ends. This lack of liquid accounts for the observed discrepancy in pump Δp, HL steam flow rate, and HL total flow rate.

The lower-plenum/downcomer hot-wall effects were included in the test by preheating the wall to specified temperatures. The vessel walls and internals plus piping walls were modeled in S-RELAP5 by heat structures with specified initial temperatures. Loop flow oscillations are mainly induced by the condensation of steam with cold ECC water. Large and atypical oscillations occur when the steam mass flow rate is too small to meet the demand for condensation. As discussed in Test Run 54, some cold leg oscillations still were observed in the test during the ACC injection period (see Figure 8.2-515). For the LPCI, the cold-leg oscillations generally are of small amplitudes and of little significance because the loop steam flow is well established and the ECC mass flow is low. The measured and calculated cold-leg mass flow rate did not show any oscillation during the LPCI. The calculated results show more and larger oscillations than the data in the ACC injection period, as seen in Figure 8.2-508, Figure 8.2-509, and Figure 8.2-515. The calculated negative flow at the beginning of cold ECC injection indicates that a sufficiently strong steam flow has not yet been established when the cold-leg ECC injection starts.

The system-wide pressure oscillations caused by cold-leg condensation result in the rapid spread of liquid to the entire core. The liquid increases the core heat transfer, and produces a short period of overcooling as indicated by the relatively flat temperature histories shown in Figure 8.2-522 through Figure 8.2-528. The high steam generation rate accompanying the overcooling produces high pressure in the core and thus expels liquid from the core. The loss of core liquid inventory reduces the core coolability and raises the heater rod temperatures. This over- and undercooling sequence prolongs the temperature rise period for the higher elevations. The calculated and measured differential pressures in the core (Figure 8.2-520) indicate that the core liquid inventory is well calculated up to approximately 250 seconds, but then is underpredicted for the remainder of the test. The core heat transfer depends strongly on the liquid distribution. The acceptable code-to-data comparisons for rod temperature histories (Figure 8.2-522, Figure 8.2-523, Figure 8.2-525, Figure 8.2-526), and steam mass flow rate (Figure 8.2-514) are a result of a conservatively calculated heat transfer rate, accentuated by not having enough liquid in the upper region of the core.

The lack of direct measured data, such as steam flow rates and temperatures entering and leaving the steam generator, makes it difficult to assess the steam binding effect. As discussed in Section 8.2.13.5.6, the liquid carryover can be estimated from the liquid level in Containment Tank II shown in Figure 8.2-530. Considering the large uncertainty in measurement data and the lack of a precise geometry description for the tank, the code calculated value is in acceptable agreement with the measured data. Figure 8.2-531 and Figure 8.2-532 illustrate the secondary side pressure of the steam generators. The S-RELAP5 calculation shows a faster cooldown of the secondary side suggesting that a larger amount of heat is being transferred to the fluid in the tubes, than measured. This should increase the amount of liquid being vaporized and the steam heatup in the S-RELAP5 calculation, making it more conservative. As also discussed in Test Run 54, the steam binding effect in the steam generator is difficult to quantify, but is being conservatively calculated by S-RELAP5.

The calculated void fraction in the hot legs is less than the measured void fraction. The improper calibration of void measurement (an initial reading of less than 1.0 shown in Figure 8.2-511 and Figure 8.2-516), the inconsistency of measured loop mass flow rates (Figure 8.2-508 and Figure 8.2-513) and the special precautions required to accurately measure a very small liquid fraction under horizontal stratification conditions suggested that the void fraction data might have a large uncertainty. As discussed in Test Run 54, the calculated liquid fraction in the hot leg is reasonable. It is important to note no liquid accumulates in the cold leg until near the end of core reflood. The calculated rod surface temperature curves often are not as smooth as the data.

The calculations presented in this report show that the calculated maximum temperatures at all core elevations are above or at the high end of the data ranges for the high-power bundles. The overall hydraulic response shows reasonable calculation of the trends, but some responses, such as mass break flow rate, upper plenum pressure, and pump Δp show reasonable to good agreement with the data.

8.2.13.8 CCTF Test Run 68

8.2.13.8.1 Test Run 68 Description

Test Run 68 simulated the reflood phase of a cold-leg ECC injection PWR LOCA with a standard decay power (i.e., without augmenting the 1971 ANS draft standard decay power), nominal system pressure of 0.20 MPa, and an LPCI flow rate of 0.025 m^3/s.

8.2.13.8.2 Test Run 68 Input Description

The input model for test run 68 is identical to the input model for run 54 with the only changes required to input the case specific initial and boundary conditions.

8.2.13.8.3Test Run 68 Measured Test Conditions

In general, the test conditions for the CCTF tests were based on the Appendix K design basis pre-reflood assumptions and low ECC water injection rate according to the single failure criteria. This test is based on best estimate power coupled with a higher ECC water injection rate. The following measured test conditions for the CCTF Test Run 68 were established through the test procedure prescribed in the data report (Reference 8.2-58) and are presented in Table 8.2-64.

Note that the time shown is defined as the time after test initiation. Also, the initial water level in the lower plenum, and the injection of ECC water into the lower plenum and its timing were designed to minimize the atypical oscillatory behavior from condensation at the ECC port in the initial stage of reflood by producing a considerable amount of steam in the core.

After the primary system was preheated to its specified temperatures, the test was initiated by turning on the power to the core heater rods with the vessel filled with steam except for 0.82 m (2.69 ft) of saturated water in the lower plenum. Because the initial water level in the lower plenum was below the bottom of the core, the rods in the core heated up virtually adiabatically in the steam environment before reflood began. Accumulator injection began at 86 seconds and was initially directed into the lower plenum. The core power started to decay from the maximum value of 7.87 MW at 95.0 seconds, when the reflood began (BOCREC).

When the liquid level reached 0.5 m (1.64 ft) above the bottom of the core at about 98 seconds, the accumulator injection was shifted to the cold leg and continued until about 113 seconds. After accumulator injection ended, low-pressure coolant (simulating LPCI) was injected into the intact cold legs starting at 110 seconds and continuing until the end of the test. All heated rods were quenched by about 584 seconds into the transient (488 seconds after BOCREC). The sequence of events for the test is summarized in Table 8.2-65.

8.2.13.8.4 Test Run 68 Initial and Boundary Conditions

The initial and boundary conditions were taken from the data report or the DMS data files for Test Run 68. The initial conditions described in Section 8.2.13.8.3 were used to set up the initial conditions for the S-RELAP5 hydrodynamic components and heat structures. In addition, the S-RELAP5 CCTF input model required tabulated input values for 11 time-dependent boundary conditions. These included total core power, liquid state and flow conditions for ECC injection at the lower plenum and at the three intact cold legs, and both containment tank pressures. All the tabulated input boundary conditions were extracted from the DMS data files.

Figure 8.2-534 shows the total power curve used in S-RELAP5 calculations, Figure 8.2-535 and Figure 8.2-536 show the two containment pressure conditions, and Figure 8.2-537 shows the total ECC injection mass flow rate, which is a sum of mass flow rates injected to the lower plenum and the three intact cold legs. Note particularly that the two containments were not at a constant pressure of 0.2 MPa as specified in the data report.

A polynomial interpolation scheme was used, based on the same measured temperatures, yielding an initial temperature distribution for the downcomer as shown in Figure 8.2-540.

8.2.13.8.5 Test Run 68 Calculated Results and Comparisons

The S-RELAP5 evaluation of CCTF Test Run 68 shows the code-to-data comparisons. Emphasis is placed on the heater rod surface temperatures for the additional calculations, because the calculated results from all calculations for all major hydrodynamic parameters are very similar. In the code-versus-data comparison figures, the measured quantities, except for those derived from the data, generally are identified by the instrumentation identifiers (see Figure 8.2-438 and Figure 8.2-439 for examples), and the calculated quantities are identified mostly by the S-RELAP5 minor-edit parameters and component numbers. The results of Test Run 68 are illustrated in Figure 8.2-538 through Figure 8.2-563.

Test Run 68 Broken Loop Behavior

Comparisons of the calculated mass flow rates and data in the BLHL- and BLCL-pump-side break flow are shown in Figure 8.2-538 and Figure 8.2-539, respectively. For the pump-side break flow (Figure 8.2-539), the calculation and the data agree reasonably well, with slightly higher calculated values on average and with large spikes appearing throughout the transient. The calculated hot-leg mass flow rate shows many large spikes, caused by liquid carryover into the hot leg. Except for the spikes, on average, the calculated hot-leg mass flow rate is about the same as the calculated pump-side break flow rate and the measured hot-leg mass flow rate, which also shows spiking behavior beginning at after 400 seconds.

A large uncertainty might be associated with the measurement of hot-leg mass flow rate caused by the presence of a small amount of liquid under stratified flow conditions. Figure 8.2-540 shows that the measured cold leg pump-side break flow is higher than the measured hot-leg mass flow rate. This also was observed in the preceding three tests and indicates that at least one of the measured mass flow rates is inaccurate and the larger uncertainty in hot-leg mass flow rate data is caused mostly by the liquid mass flow rate measurement.

Figure 8.2-541 compares the calculated hot-leg void fraction with the data. The measured void fraction is slightly less than 1.0 and oscillates between approximately 0.998 and 0.996 during most of the transient. Except for the early reflood and after 700 seconds, the calculated void fraction is between 0.97 and 1.0. The calculated lower void fraction during the early reflood period of simulated ACC ECC injection corresponds to the larger calculated hot-leg mass flow in this period. This reinforces the conclusions of Test Run 54 that the uncertainty in void fraction measurement could be large.

Test Run 68 Intact Loop Behavior

The transient responses for the three intact loops are very similar in both the calculated results and the measured data. Therefore, the calculated results and comparisons with the data for Loop 1 are presented as examples to illustrate the overall intact loop behavior in the reflood phase.

The calculated and measured differential pressures across the pump simulator, which simulates the loop resistance, are overlaid in Figure 8.2-542. The calculation shows continuous fluctuations of relatively large amplitude. On average, the calculated pressure loss is slightly lower than the data. Agreement in the simulation of the loop resistance and the mass flow rate upstream of the ECC injection port is minimal.

Figure 8.2-543 compares the calculated intact-loop hot-leg mass flow rate and the data. A higher mass flow rate, on average, with flow spikes is calculated throughout the test, but the measurements show the spiking behavior only after 500 seconds.

Figure 8.2-544 compares the calculated and measured steam mass flow rate in the intact-loop hot leg. A short period of lower calculated steam mass flow rate is seen after the end of the simulated ACC injection. Other than this period of underprediction of steam flow caused by the depletion of liquid in the core, the calculation and data agree well. This result indicates the vapor generation in the core is properly calculated.

Figure 8.2-545 shows calculated and measured mass flow rates in the ILCL. The ILCL mass flow rate was measured downstream of the ECC injection nozzle and is the combined mass flow rate from the intact-loop pump simulator and the ECC injection flow. The calculated mass flow rate after the termination of the ACC injection is near the average of the data. The measured ILCL mass flow rate is about 1 kg/s above the LPCI mass flow rate (Figure 8.2-545). This indicates that the uncertainty in the measured ILCL mass flow rate is large. This behavior is the opposite of that observed in the previous three runs.

Figure 8.2-546 displays the calculated and measured void fractions in the ILHL. The measured void fraction fluctuates between 1.0 and 0.997 for the first 500 seconds. Tthere is only a trace amount of liquid, for the period from 100 seconds to about 500 seconds. (NOTE: The measured void fraction is about 0.994 before 100 seconds when no liquid exists in the hot leg.) Except for the period after 500 seconds, the calculated ILHL void fraction is between 1.0 and 0.97. The small liquid fraction (measured to be below 0.05) again may require high-precision instrumentation to measure it accurately.

Figure 8.2-547 shows the void fraction comparison for the ILCL. In the simulated ACC injection period, the measured void fraction decreases to about 0.2 and fluctuates between 0.2 and 0.3 thereafter while the calculated value remains less than 0.02 after the start of ACC cold-leg injection and only slightly increases after 550 seconds. This difference is related to either poor calibration of the instrument or, possibly, a slight elevation change in the CCTF cold leg that is not modeled.

Test Run 68 Vessel Behavior

The differential pressures in the downcomer were measured in four different azimuthal directions. The data shown in Figure 8.2-548 indicates that there is little asymmetrical (or multi-dimensional) behavior in ECC water downcomer penetration. The calculated differential pressures [ ] also are indistinguishable.

Figure 8.2-549 compares the calculated and measured downcomer differential pressures from about the top to the bottom of the downcomer. The measured differential pressure does not have the manometer oscillations observed in the preceding three tests. The calculated downcomer Δp is higher than the data for the first 350 seconds and then lower than measured through the rest of the transient, with medium to large amplitude oscillations. As explained in Test Run 54, no appreciable azimuthal dependency of downcomer differential pressure is expected.

The calculated collapsed liquid level in the upper plenum is higher than the measured values in the early part of the reflood, as shown in Figure 8.2-563. Only after quenching occurs, do the data indicate higher level. Since the code predicts much later quenching than observed, the calculated level indicates adequate liquid entrainment to the upper plenum during reflood.

Agreement between the calculated and measured upper plenum pressures is very good, on average, as shown in Figure 8.2-551. Figure 8.2-550 compares the calculated and measured differential pressure across the heated core length. As discussed in Test Run 54, only the calculated differential pressure for the high-power region and one of the measured pressures are shown in the figure. Except for a short period of higher calculated differential pressure right after the switch of ECC injection from ACC to LPCI, the calculation and data are in good agreement, with the calculated pressure oscillating about the measured pressure. The short period of higher calculated pressure indicates higher calculated liquid mass in the core and a higher rate of steam production, corresponding to the period of lower calculated temperature rise, as shown in the hot rod temperature plots. The overall good code-to-data comparison on core differential pressures shows that the overall liquid mass inventory in the core is well predicted.

A comparison of calculated and measured steam temperatures was not available because the measured channel data was invalid.

Test Run 68 Core Heater Rod Response

The primary concern in the LBLOCA reflood phase is the cladding temperature rise during the core heatup period. Of secondary importance is the temperature history and duration at high temperature, and of even lesser importance are the occurrence and time of the final quench. The ultimate assessment of a best estimate system code such as S-RELAP5 is the code-to-data comparison of the rod temperature response. A number of comparison plots for heater rod surface temperatures will be shown. The calculations are identified by S-RELAP5 minor-edit parameters and elevations, and the data are identified by the thermocouple tags (see Figure 8.2-438) and elevations. Because the core region [ ] with no special consideration for thermocouple locations, the closest calculated rod surface temperature at either the node center or at the node boundary at an elevation closest to a given thermocouple elevation is used.

Figure 8.2-552 through Figure 8.2-558 compare the calculated and measured heater rod surface temperatures at three elevations for high- and medium-power core regions. In general, the calculation displays more fluctuations than the data. The calculation also shows better cooling (compared with the data) in the period of high ECC water injection rate caused by high calculated liquid entrainment. The high rate of liquid entrainment is not sustained and the liquid falls back into the lower regions of the core, which causes the rod surface temperature to rise faster in the subsequent period. Overall, the calculated temperature rise is in very good agreement with the data. For the high- and medium-power heater rods, the calculated surface temperature histories, including the quench times, agree very well with the data.

With the chopped-cosine axial power profile, the peak temperature rise is expected to occur in the neighborhood just above the mid-plane. Figure 8.2-552 and Figure 8.2-553 show the calculated rod surface temperatures at 2.035 m and 1.83 m elevations, and the data with the highest temperature rise for the high-power core. The measured PCT of 1122 K (1560 °F) was recorded by the thermocouple at 1.83 m elevation. The maximum surface temperature calculated at 1.83 m is 1081 K (1486 °F). The calculated PCT of 1123 K (1561 °F) occurs at the 2.44 m elevation. Thus, the calculated temperature rise is higher above the mid-plane and the PCT point is shifted to a higher elevation than measured. The PCT time is 144 seconds from the measurement and is 246 seconds from the calculation.

The heater rod surface temperatures were measured at several elevations in various bundles (see Figure 8.2-438). The maximum surface temperatures from all measurements in the high-power core region are plotted, along with the calculated peak temperatures, as a function of elevation in Figure 8.2-559.

This comparison shows good agreement with the data for lower and mid-core elevations and overprediction by the calculated values for higher coer elevation, consistent with the behavior exhibited by S-RELAP5.

8.2.13.8.6 Test Run 68 Discussion of Results

The most important reflood phenomena according to the PIRT (Table 5-1) are core reflood heat transfer, void generation/distribution and entrainment/de-entrainment in the core, entrainment and de-entrainment in the upper plenum and in the hot legs, steam binding in steam generator, pump Δp, hot wall in the downcomer and lower plenum, noncondensable gases in the cold leg/accumulator, loop flow oscillations, decay heat, and oxidation and gas conductance for fuel rods. Except for the fuel rod oxidation and conductance and cold leg/accumulator noncondensable gases, all the important reflood phenomena were observed in the CCTF Test Run 68, and the agreement between S-RELAP5 calculated and measured data is reasonable to good.

As mentioned in Section 8.2.13.8.2, CCTF Test Run 68 power decay simulated the 1971 ANS Draft Standard times 1.0 plus actinide decay heat. This power decay curve was treated in S-RELAP5 by tabulated input values (see Figure 8.2-534). The pump/loop Δp was simulated in the test by an orifice plate and in S-RELAP5 by a form loss factor. Figure 8.2-542 shows that the pump/loop Δp is generally underpredicted.

The lower plenum/downcomer hot-wall effects were included in the test by preheating the wall to specified temperatures. The vessel walls and internals plus piping walls were modeled in S-RELAP5 by heat structures with specified initial temperatures. Loop flow oscillations are induced mainly by the condensation of steam with cold ECC water. Large and atypical oscillations occur when the steam mass flow rate is too small to meet the demand for condensation. Also discussed in Test Run 54, cold-leg oscillations are observed in the test during the ACC injection period (see Figure 8.2-545).

For the LPCI, the calculated cold-leg oscillations generally are of small amplitude and much lower in amplitude than the measured. The calculated results show more and larger oscillations, except for the intact cold-leg flow rate, than the data in the ACC injection period, as seen in Figure 8.2-538, Figure 8.2-539, and Figure 8.2-545. The calculated negative flow at the beginning of cold-leg ECC injection indicates that a sufficiently strong steam flow has not yet been established when the cold-leg ECC injection starts. The system-wide pressure oscillations caused by cold-leg condensation result in rapid spread of liquid to the entire core. The liquid increases the core heat transfer and produces a short period of overcooling in the upper regions, as indicated by the relatively flat temperature histories early in the reflood, as shown in Figure 8.2-552 through Figure 8.2-558. During the early period, liquid is abundant in the upper core, but vapor generation is not high enough to sustain the relatively high liquid content and some of the liquid falls back into the lower core. The loss of upper core liquid inventory reduces the upper core coolability and raises the heater rod temperatures later. This over- and undercooling sequence prolongs the temperature rise period for the higher elevations.

As discussed in Section 8.2.13.5.6, in CCTF Test Run 68 there were also no direct measured data, such as steam flow rates and temperatures entering and leaving the steam generator to assess the steam binding effect. The liquid carryover can be estimated from the liquid level in Containment Tank II shown in Figure 8.2-560. Considering the large uncertainty in measurement data and the lack of a precise geometry description for the tank, the code calculated value is in acceptable agreement with the measured data. Figure 8.2-561 and Figure 8.2-562 illustrate the secondary side pressure of the steam generators. The S-RELAP5 calculation shows a faster cooldown of the secondary side suggesting that a larger amount of heat is being transferred to the fluid in the tubes, than measured. This should increase the amount of liquid being vaporized and the steam heatup in the S-RELAP5 calculation, making it more conservative. As discussed in Test Run 54, the steam binding effect in the steam generator is difficult to quantify, but is being conservatively calculated by S-RELAP5.

The good agreement between the calculated and measured differential pressures in the core (Figure 8.2-550) indicates that the core liquid inventory is well calculated. The core heat transfer depends strongly on the liquid distribution. The reasonable to good code-versus-data comparisons for rod temperature histories (Figure 8.2-552 through Figure 8.2-558) and steam mass flow rate (Figure 8.2-544), are a combined result of well-calculated heat transfer rate, vapor generation rate, and liquid distribution in the core.

The calculated void fraction in the hot legs is less than the measured void fraction. The improper calibration of void measurement (initial reading of less than 1.0 shown in Figure 8.2-541 and Figure 8.2-546), the inconsistency of measured loop mass flow rates (Figure 8.2-538 and Figure 8.2-543), and the special precautions required to accurately measure a very small liquid fraction under horizontal stratification conditions suggested that the void fraction data might have a large uncertainty. As discussed in Test Run 54, the calculated liquid fraction in the hot leg is reasonable. It is important to note that there is no accumulation of liquid in the cold leg until near the end of core reflood. Also, the calculated rod surface temperature curves often are not as smooth as the data.

The calculations presented in this section show that the calculated maximum temperatures at all core elevations are in good agreement with the data for the high-power bundles. Furthermore, the overall system responses, such as loop mass flow rates, upper plenum pressure, loop Δp, downcomer Δp, and core Δp, are well calculated.

Table 8.2-53 CCTF Test Conditions

Test Run	Core Power	LPCI Flow (m^3 /s)	System Pressure (MPa)
54	ANS 1971 x 1.0 + Actinide * 1.1	0.011	0.20
62	ANS 1971 x 1.2 + Actinide * 1.1	0.011	0.20
67	ANS 1971 x 1.2 + Actinide * 1.1	0.011	0.15
68	ANS 1971 x 1.0 + Actinide * 1.1	0.025	0.20

Table 8.2-54 CCTF Summary of Test Results

Run	Measured PCT	Time of Measured PCT	Calculated PCT	Time of Calculated PCT
54	1113 K	130 s	1064 K	226 s
62	1132 K	154 s	1116 K	235 s
67	1143 K	164 s	1238 K	385 s
68	1122 K	144 s	1123 K	246 s

Table 8.2-55 Measured Test Conditions, Test Run 54

Power:		
	Total 7.87 MW	
	Linear 1.18 kW/m	
Radial power distribution		
A	B	C
1.37	1.20	0.76
Pressure (MPa):		
	Containment	0.2
	Steam Generator Secondary	0.76
Temperature (K):		
	Downcomer wall	468
	Vessel internals	423
	Primary piping	406
	Lower plenum liquid	394
	ECC liquid	310
	Steam generator secondary side	539
ECC injection type:	Lower plenum and cold leg injection	
Pump K-factor:	15	
ECC injection rates:		
ACC	0.104 m^3/s from 81.0 s to 94.0 s	into lower plenum
	0.088 m^3/s from 94.0 s to 107.0 s	into cold legs
LPCI	0.0116 m^3/s from 107.0 s to 979.0 s	into cold legs
Initial water level:		
	In lower plenum	0.86 m
	In steam generator secondary side	7.4 m
Power decay:		
	Constant	from 0.0 s to 90.5 s
	ANS 1.0 + Actinide x 1.1	from 90.5 s to 690.5 s
	Linear decay	from 690.5 s to 898.0 s
PCT at reflood initiation:	1074 K at TE31Y17	

Table 8.2-56 Chronology of Events for CCTF Test Run 54

Event	Time After Test Initiation (s)	Time After Reflood Initiation
Test initiation and heater rods power on	0.0	-90.5
Accumulator injection to lower plenum initiated	81.0	-9.5
Decay power initiation (BOCREC) (Reflood initiation)	90.5	0.0
Accumulator injection switched from lower plenum to cold	94.0	3.5
Accumulator injection ended and LPCI injection initiated	107.0	16.5
Maximum temperature turnaround	123.0	32.5
All heater rods quenched	552.5	462.0
Linear power decay initiated	690.5	600.0
Heater rods power off	898.0	807.5
LPCI injection ended	979.0	888.5
Test ended	1032.0	941.5

Table 8.2-57 Test Run 54 - Downcomer Initial Temperature Distribution

Test Measured Data		Model Initial Conditions	
Elevation (m)	Temperature (K)	Mid-node Elevation (m)	Temperature (K)
0.98300	398.00	0.6050	387.36
2.42300	447.00	1.6675	420.96
3.86300	448.00	2.5825	441.73
5.30300	464.00	3.4975	454.95
6.74300	440.00	4.4125	460.61
		5.2199	459.33
		6.1372	450.73
		6.9678	436.39
		7.4941	424.09

Table 8.2-58 Measured Test Conditions, Test Run 62

Power:		
	Total 9.37 MW	
	Linear 1.40 kW/m	
Radial power distribution		
A	B	C
1.92	1.67	1.07
Pressure (MPa):		
	Containment	0.2
	Steam Generator Secondary	5.3
Temperature (K):		
	Downcomer wall	467
	Vessel internals	394
	Primary piping	394
	Lower plenum liquid	394
	ECC liquid	308
	Steam generator secondary side	539
ECC injection type:	Lower plenum and cold leg injection	
Pump K-factor:	15	
ECC injection rates:		
ACC	0.105 m^3/s from 84.5 s to 97.0 s	into lower plenum
	0.091 m^3/s from 97.0 s to 111.0 s	into cold legs
LPCI	0.011 m^3/s from 120.0 s to 1005.0 s	into cold legs
Initial water level:		
	In lower plenum	0.81 m
	In steam generator secondary side	7.4 m
Power decay:		
	Constant	from 0.0 s to 93.5 s
	ANS 1.2 + Actinide x 1.1	from 93.5 s to 1005.0 s
PCT at reflood initiation:	1072 K	

Table 8.2-59 Chronology of Events for CCTF Test Run 62

Event	Time After Test Initiation (s)	Time After Reflood Initiation (s)
Test initiation and heater rods power on	0.0	-94.0
Accumulator injection to lower plenum initiated	84.5	-9.5
Decay power initiation	93.5	-0.5
BOCREC (Reflood initiation)	94.0	0.0
Accumulator injection switched from lower plenum to cold leg	97.0	3.0
LPCI injection initiated	120.0	26.0
All heater rods quenched	652.0	558.0
Heater rods power off	1005.0	911.0
LPCI injection ended	1005.0	911.0
Test ended	1035.0	941.0

Table 8.2-60 Test Run 62 - Downcomer Initial Temperature Distribution

Test Measured Data		Model Initial Conditions	
Elevation (m)	Temperature (K)	Mid-node Elevation (m)	Temperature (K)
0.98300	430.00	0.6050	423.27
2.42300	440.00	1.6675	435.21
3.86300	440.00	2.5825	442.50
5.30300	460.00	3.4975	447.03
6.74300	436.00	4.4125	448.78
		5.2199	448.03
		6.1372	444.56
		6.9678	439.02
		7.4941	434.33

Table 8.2-61 Measured Test Conditions, Test Run 67

Power:		
	Total 9.32 MW	
	Linear 1.40 kW/m	
Radial power distribution		
A	B	C
1.901	1.674	1.067
Pressure (MPa):		
	Containment	0.15
	Steam Generator Secondary	5.18
Temperature (K):		
	Downcomer wall	461
	Vessel internals	423
	Primary piping	387
	Lower plenum liquid	386
	ECC liquid	310
	Steam generator secondary side	540
ECC injection type:	Lower plenum and cold leg injection	
Pump K-factor:	15	
ECC injection rates:		
ACC	0.105 m^3/s from 86.5 s to 98.5 s	into lower plenum
	0.091 m^3/s from 98.5 s to 102.5 s	into cold legs
LPCI	0.0113 m^3/s from 110.0 s to 1010.0 s	into cold legs
Initial water level:		
	In lower plenum	0.86 m
	In steam generator secondary side	7.4 m
Power decay:		
	Constant	from 0.0 s to 95.0 s
	ANS 1.2 + Actinide x 1.1	from 95.0 s to 690.5 s
PCT at reflood initiation:	1073 K	

Table 8.2-62 Chronology of Events for CCTF Test Run 67

Event	Time After Test Initiation (s)	Time After Reflood Initiation
Test initiation and heater rods power on	0.0	-96.0
Accumulator injection to lower plenum initiated	86.5	-9.5
Decay power initiation	95.0	-1.0
BOCREC (Reflood initiation)	96.0	0.0
Accumulator injection to cold legs initiated	98.5	2.5
Accumulator injection to lower plenum ended	102.5	6.5
LPCI injection to cold legs initiated	110.0	14.0
Accumulator injection to cold legs ended	114.0	18.0
All heater rods quenched	760.0	664.0
Heater rods power off	1010.0	914.0
LPCI injection ended	1010.0	914.0
Test ended	1040.0	944.0

Table 8.2-63 Test Run 67 - Downcomer Initial Temperature Distribution

Test Measured Data		Model Initial Conditions	
Elevation (m)	Temperature (K)	Mid-node Elevation (m)	Temperature (K)
0.98300	420.00	0.6050	413.54
2.42300	430.00	1.6675	425.15
3.86300	431.00	2.5825	432.47
5.30300	451.00	3.4975	437.30
6.74300	430.00	4.4125	439.66
		5.2199	439.68
		6.1372	437.36
		6.9678	433.10
		7.4941	429.35

Table 8.2-64 Measured Test Conditions, Test Run 68

Power:		
	Total 7.87 MW	
	Linear 1.18 kW/m	
Radial power distribution		
A	B	C
1.608	1.414	0.898
Pressure (MPa):		
	Containment	0.2
	Steam Generator Secondary	5.2
Temperature (K):		
	Downcomer wall	468
	Vessel internals	395
	Primary piping	395
	Lower plenum liquid	310
	ECC liquid	540
	Steam generator secondary side	468
ECC injection type:	Lower plenum and cold leg injection	
Pump K-factor:	15	
ECC injection rates:		
ACC	0.1070 m^3/s from 86.0 s to 102.0 s	into lower plenum
	0.092 m^3/s from 98.0 s to 113.0 s	into cold legs
LPCI	0.0252 m^3/s from 110.0 s to 1010.0 s	into cold legs
Initial water level:		
	In lower plenum	0.82 m
	In steam generator secondary side	7.4 m
Power decay:		
	Constant	from 0.0 s to 95.0 s
	ANS 1.0 + Actinide x 1.1	from 95.0 s to 1010.0 s
PCT at reflood initiation:	1073 K	

Table 8.2-65 Chronology of Events for CCTF Test Run 68

Event	Time After Test Initiation (s)	Time After Reflood Initiation (s)
Test initiation and heater rods power on	0.0	-96.0
Accumulator injection to lower plenum initiated	86.0	-10.0
Decay power initiation	95.0	-1.0
BOCREC (Reflood initiation)	96.0	0.0
Accumulator injection to cold legs initiated	98.0	2.0
Accumulator injection to lower plenum ended	102.0	6.0
LPCI injection to cold legs initiated	110.0	14.0
Accumulator injection to cold legs ended	113.0	17.0
All heater rods quenched	584.0	488.0
Heater rods power off	1010.0	914.0
LPCI injection ended	1010.0	914.0
Test ended	1040.0	944.0

Table 8.2-66 Test Run 68 - Downcomer Initial Temperature Distribution

Test Measured Data		Model Initial Conditions	
Elevation	Temperature	Mid-node Elevation (m)	Temperature (K)
0.98300	439.00	0.6050	434.75
2.42300	434.00	1.6675	437.21
3.86300	434.00	2.5825	438.77
5.30300	453.00	3.4975	439.81
6.74300	434.00	4.4125	440.33
		5.2199	440.36
		6.1372	439.90
		6.9678	439.03
		7.4941	438.26

Figure 8.2-433 CCTF Core-II Pressure Vessel

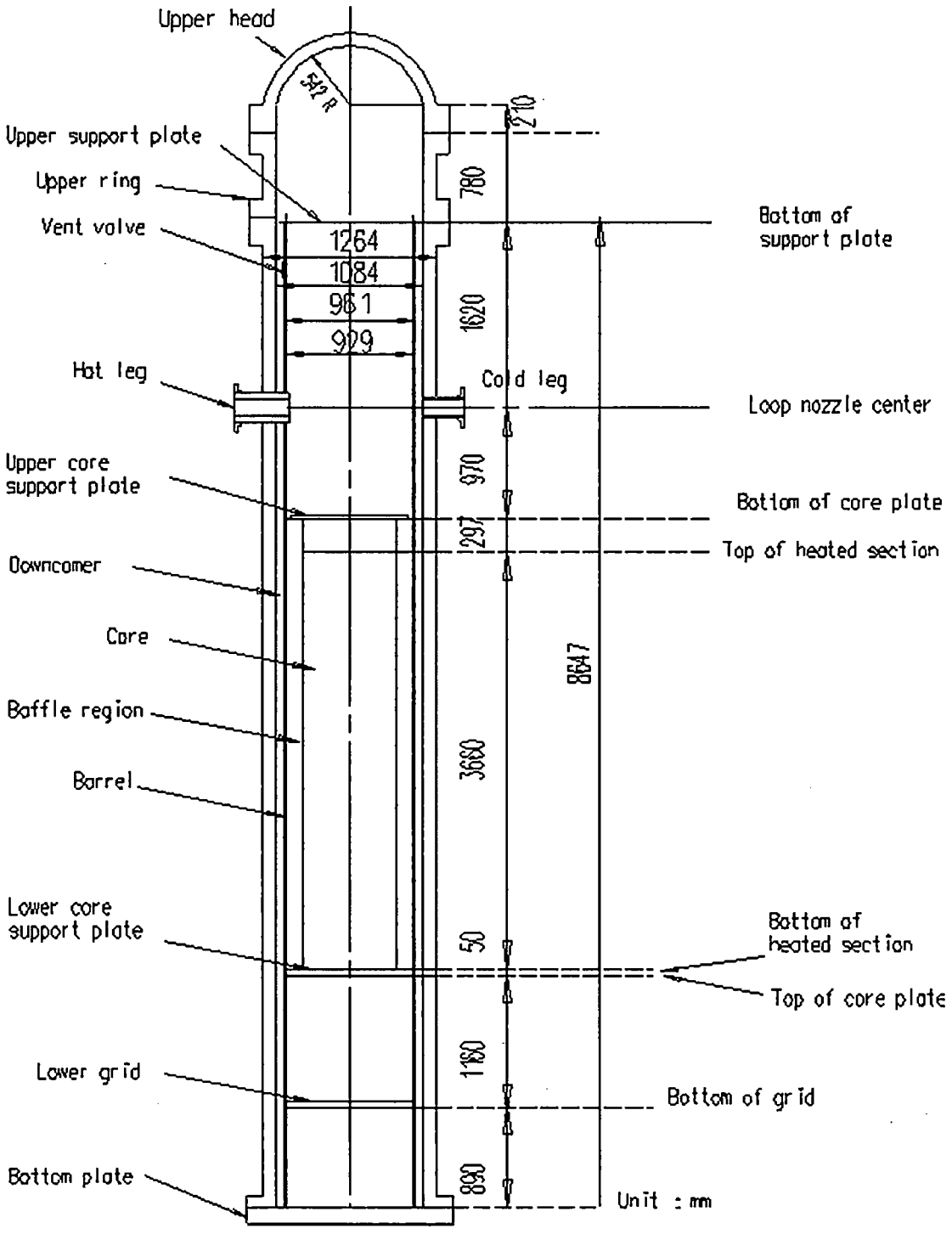

Figure 8.2-434 CCTF Top View of Primary Loop Piping

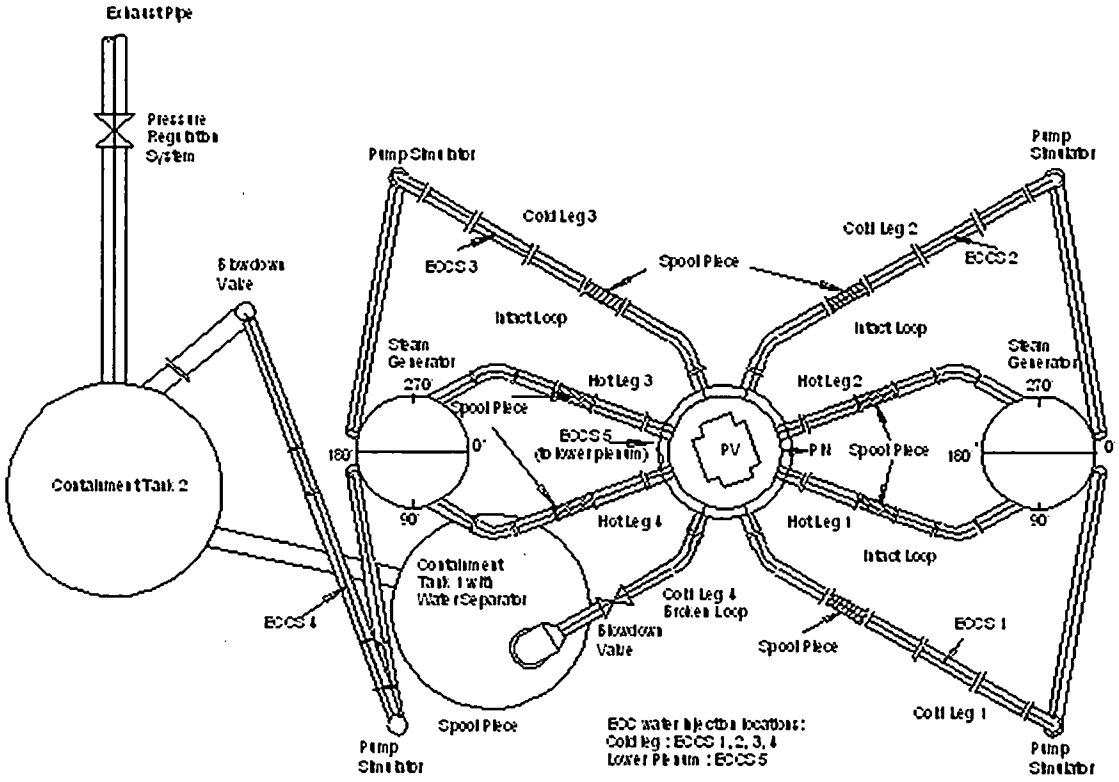

Figure 8.2-435 CCTF Core Cross Section Depicting Three Power Regions and Cross Section Dimensions

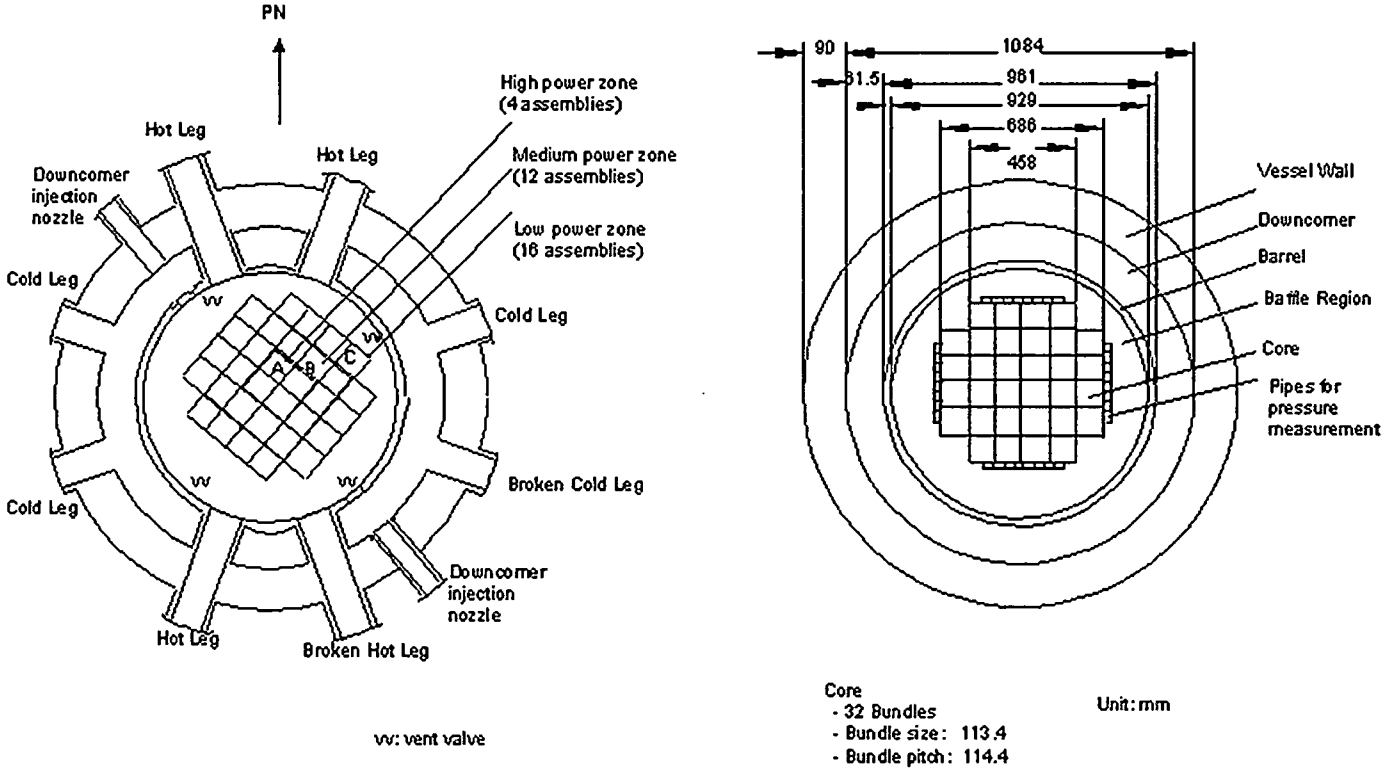

Figure 8.2-436 CCTF Core-II Heater Rod

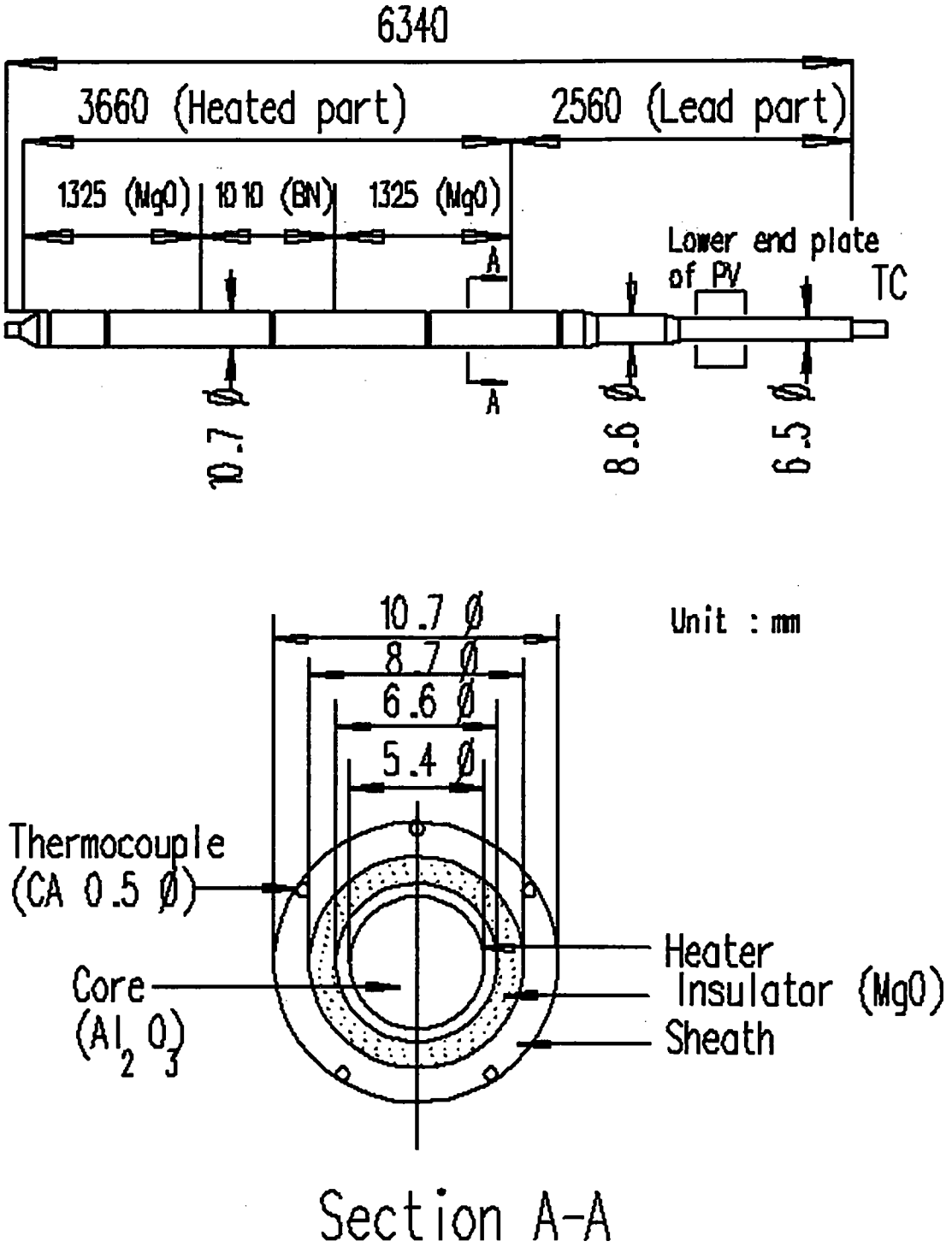

Figure 8.2-437 CCTF Core-II Axial Profile and Grid Spacer Locations

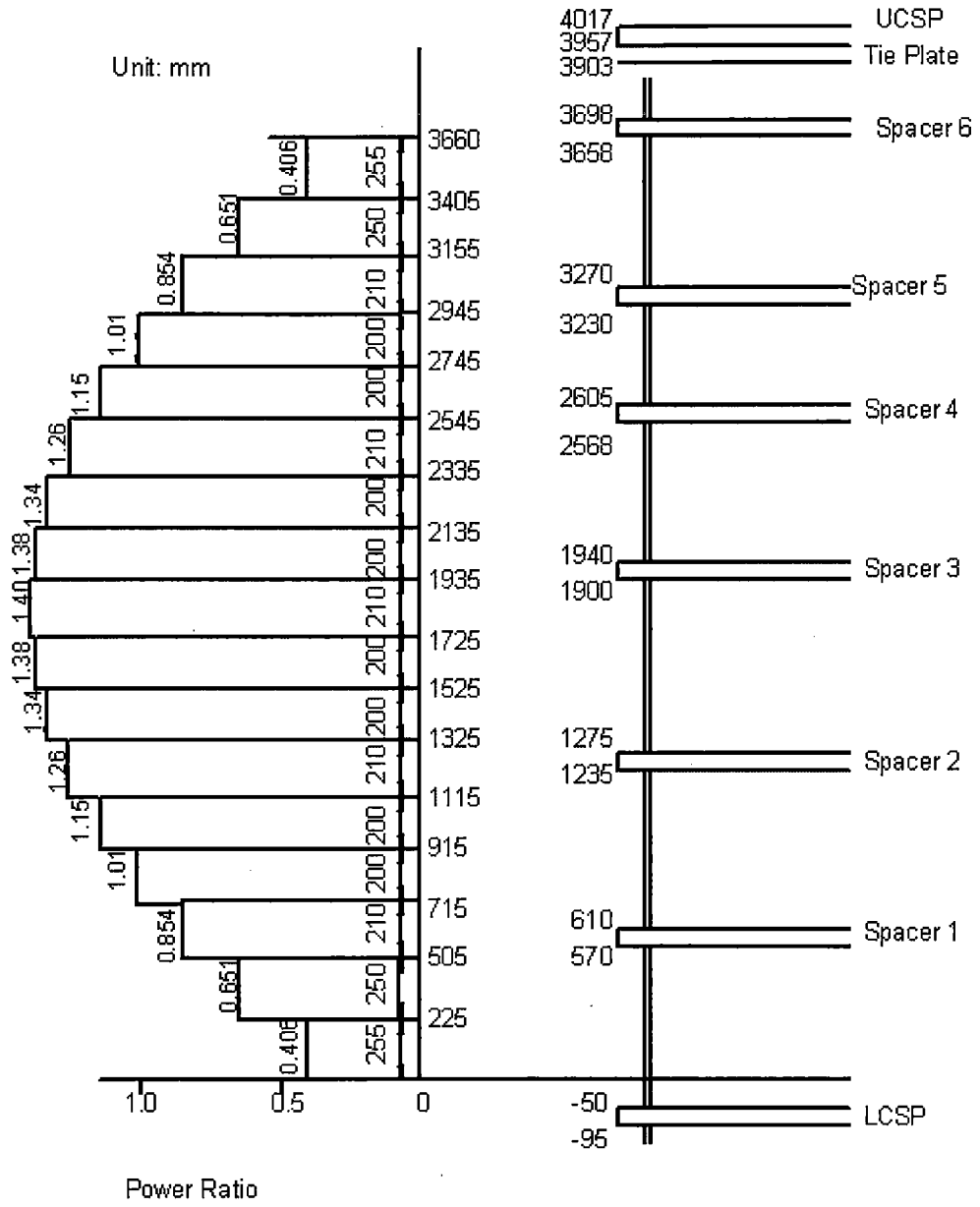

Figure 8.2-438 CCTF Temperature Measurement Instrumentation in the Core Region

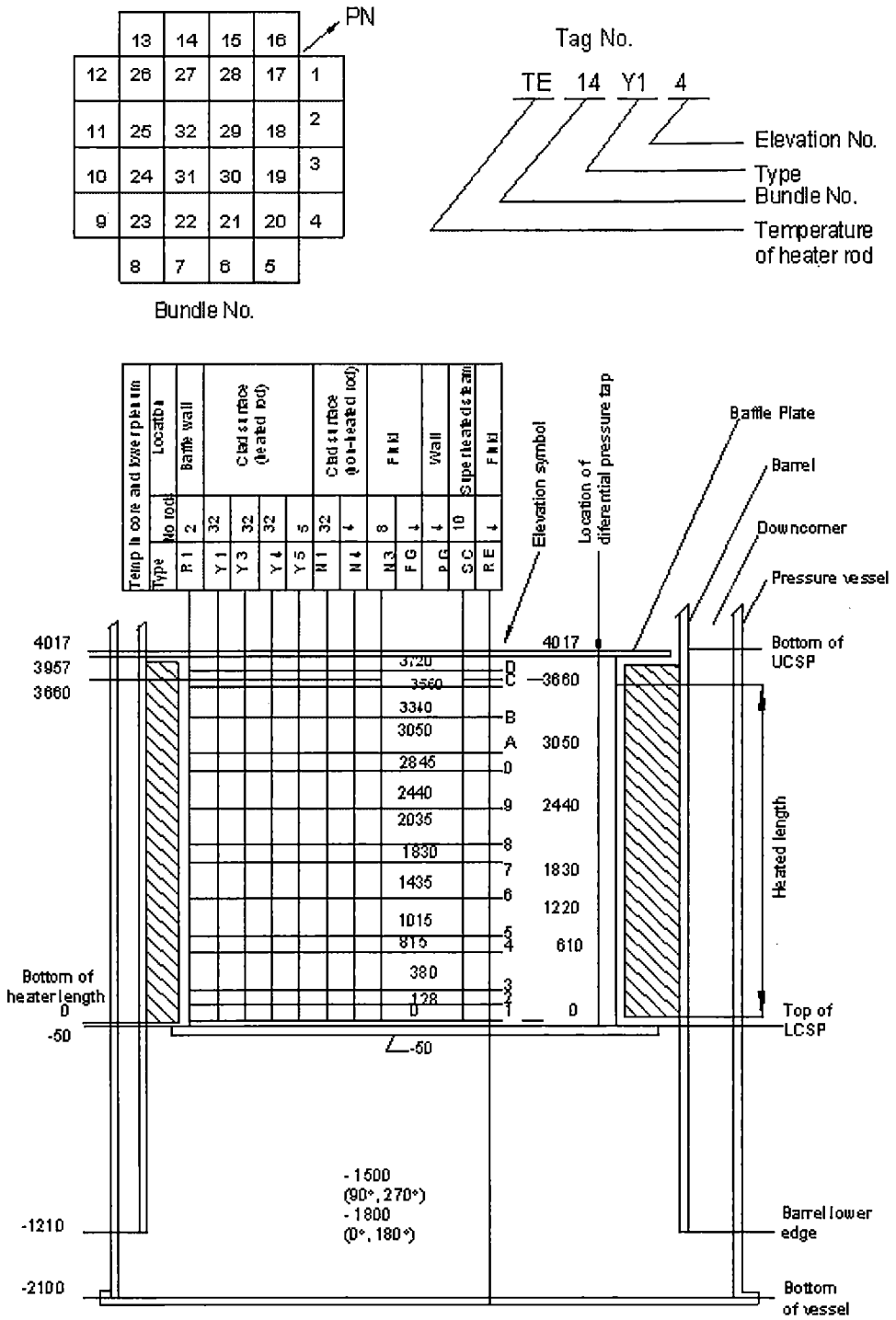

Figure 8.2-439 CCTF Differential Pressure Instrumentation in Pressure Vessel

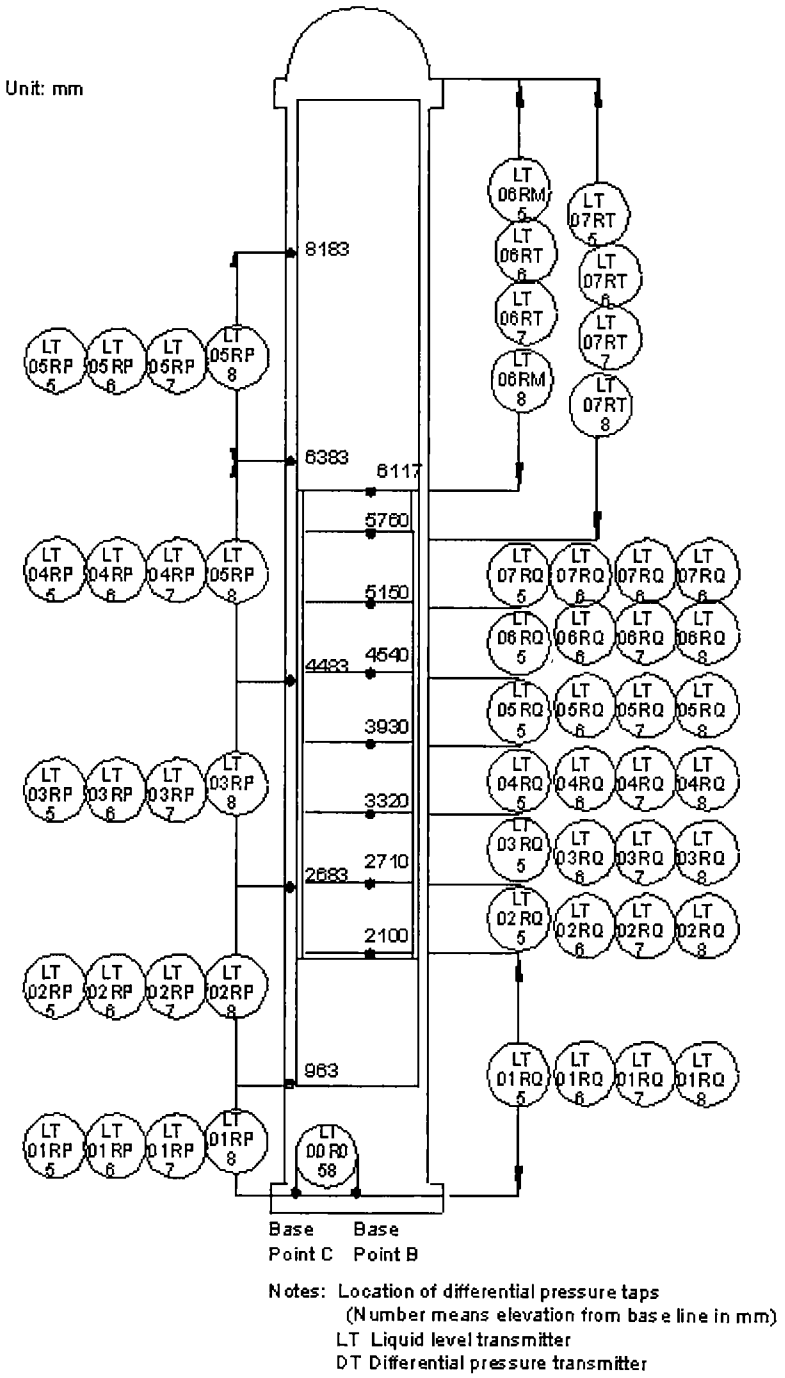

Notes: Location of differential pressure taps
(Number means elevation from base line in mm)
LT Liquid level transmitter
DT Differential pressure transmitter

Figure 8.2-440 CCTF Facility Nodalization

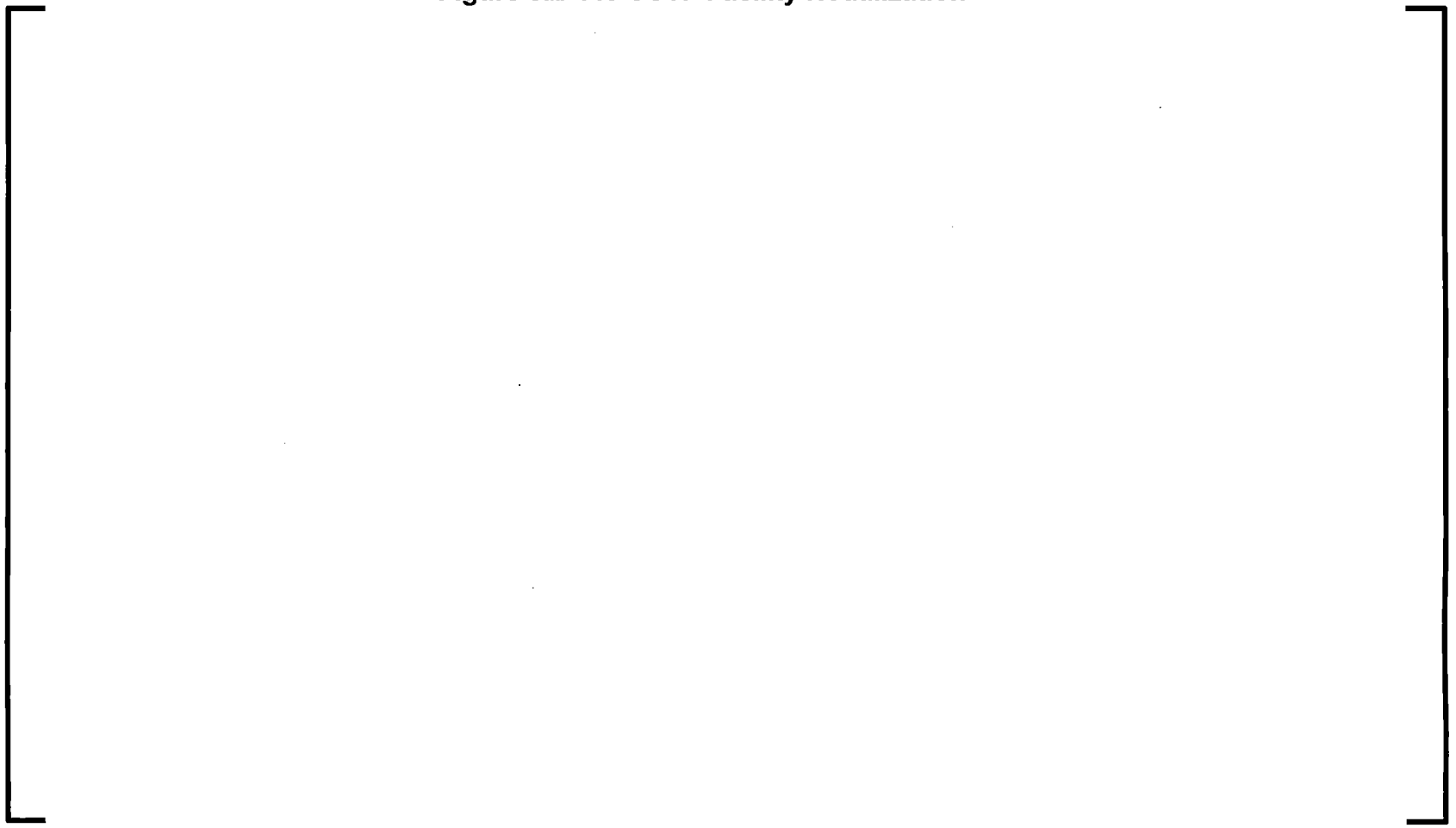

Figure 8.2-441 CCTF Vessel Nodalization

Figure 8.2-442 CCTF Downcomer Azimuthal Nodalization

Figure 8.2-443 CCTF Core Nodalization

Figure 8.2-444 Tabulated Total Core Power, Test Run 54

Figure 8.2-445 Input Pressure of Pump-side Containment, Test Run 54

Figure 8.2-446 Input Pressure of Vessel-side Containment, Test Run 54

Figure 8.2-447 Input of ECC (Lower Plenum and Cold Legs) Mass Flow Rates, Test Run 54

Figure 8.2-448 Calculated and Measured BLHL Mass Flow Rates, Test Run 54

Figure 8.2-449 Comparison of Mass Flow Rates for Pump-Side Break, Test Run 54

Figure 8.2-450 Measured Mass Flow Rates for the BLHL and BLCL, Test Run 54

Figure 8.2-451 Calculated and Measured BLHL Void Fraction, Test Run 54

Figure 8.2-452 Differential Pressure Across the Intact Loop Pump Simulator, Test Run 54

Figure 8.2-453 Calculated and Measured Intact Loop Hot Leg Mass Flow Rates, Test Run 54

Figure 8.2-454 Calculated and Measured Intact Loop Hot Leg Steam Mass Flow Rates, Test Run 54

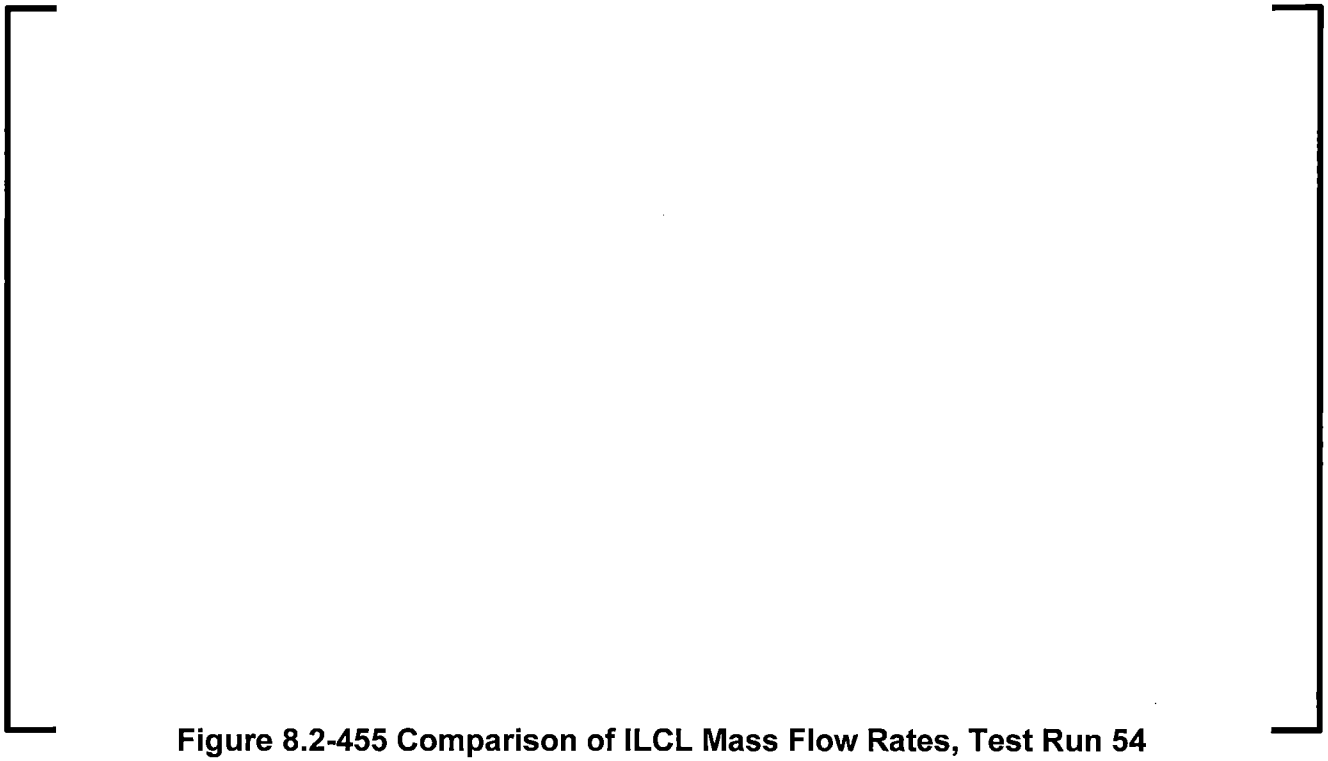

Figure 8.2-455 Comparison of ILCL Mass Flow Rates, Test Run 54

Figure 8.2-456 Calculated and Measured ILHL Void Fractions, Test Run 54

Figure 8.2-457 Calculated and Measured ILCL Void Fractions, Test Run 54

Figure 8.2-458 Measured Downcomer Differential Pressures in Four Azimuthal Directions, Test Run 54

Figure 8.2-459 Calculated and Measured Downcomer Differential Pressure, Test Run 54

Figure 8.2-460 Comparison of Core Differential Pressures, Test Run 54

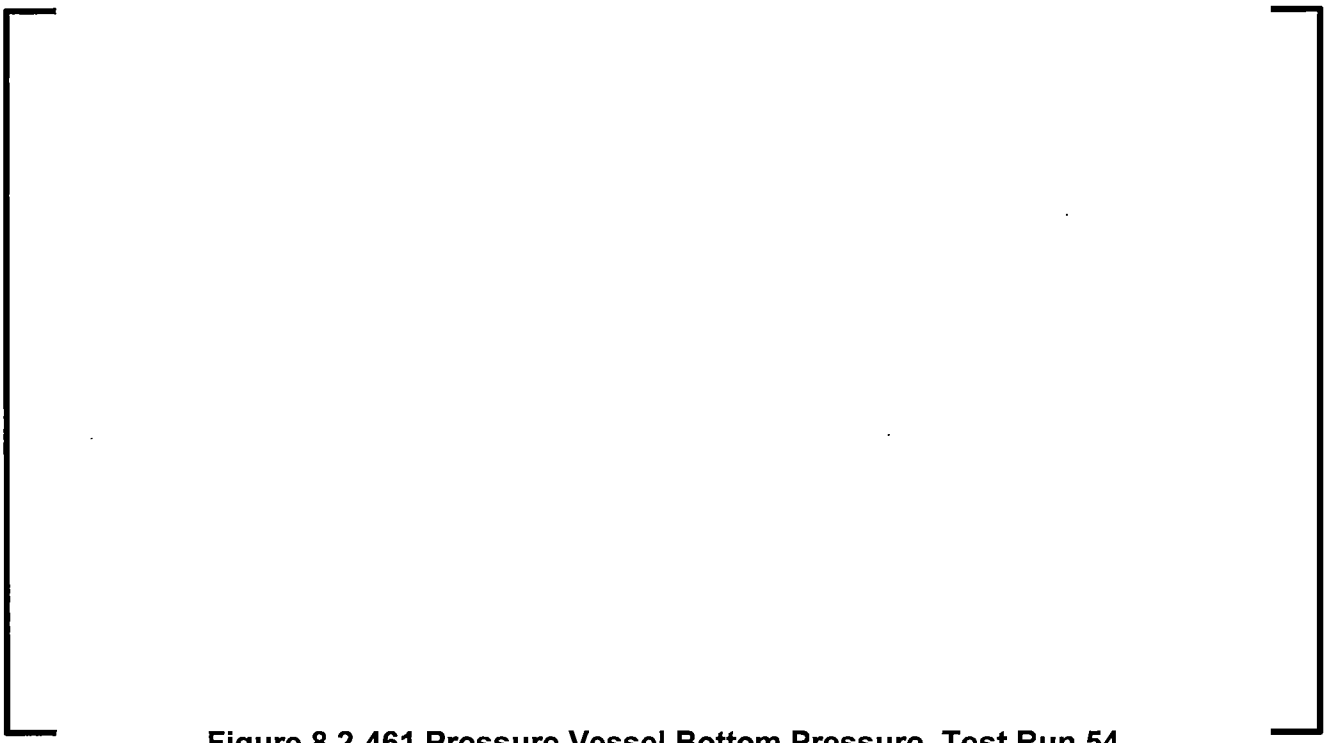

Figure 8.2-461 Pressure Vessel Bottom Pressure, Test Run 54

Figure 8.2-462 Comparison of Rod Surface Temperatures for High Power Bundles at 1.83 m Elevation, Test Run 54

Figure 8.2-463 Comparison of Rod Surface Temperatures for High Power Bundles at 2.035 m Elevation, Test Run 54

Figure 8.2-464 Comparison of Rod Surface Temperatures for Medium Power Bundles at 1.015 m Elevation, Test Run 54

Figure 8.2-465 Comparison of Rod Surface Temperatures for Medium Power Bundles at 2.44 m Elevation, Test Run 54

Figure 8.2-466 Comparison of Rod Surface Temperatures for Medium Power Bundles at 3.05 m Elevation, Test Run 54

Figure 8.2-467 Comparison of Rod Surface Temperatures for Low Power Bundles at 2.44 m Elevation, Test Run 54

Figure 8.2-468 Comparison of Rod Surface Temperatures for Low Power Bundles at 3.05 m Elevation, Test Run 54

Figure 8.2-469 Comparison of Peak Surface Temperatures vs. Elevation for High Power Bundles, Test Run 54

Figure 8.2-470 Comparison of Liquid Level in Containment Tank II, Test Run 54

Figure 8.2-471 Comparison of Intact Loop Steam Generator Secondary Side Pressure, Test Run 54

Figure 8.2-472 Comparison of Broken Loop Steam Generator Secondary Side Pressure, Test Run 54

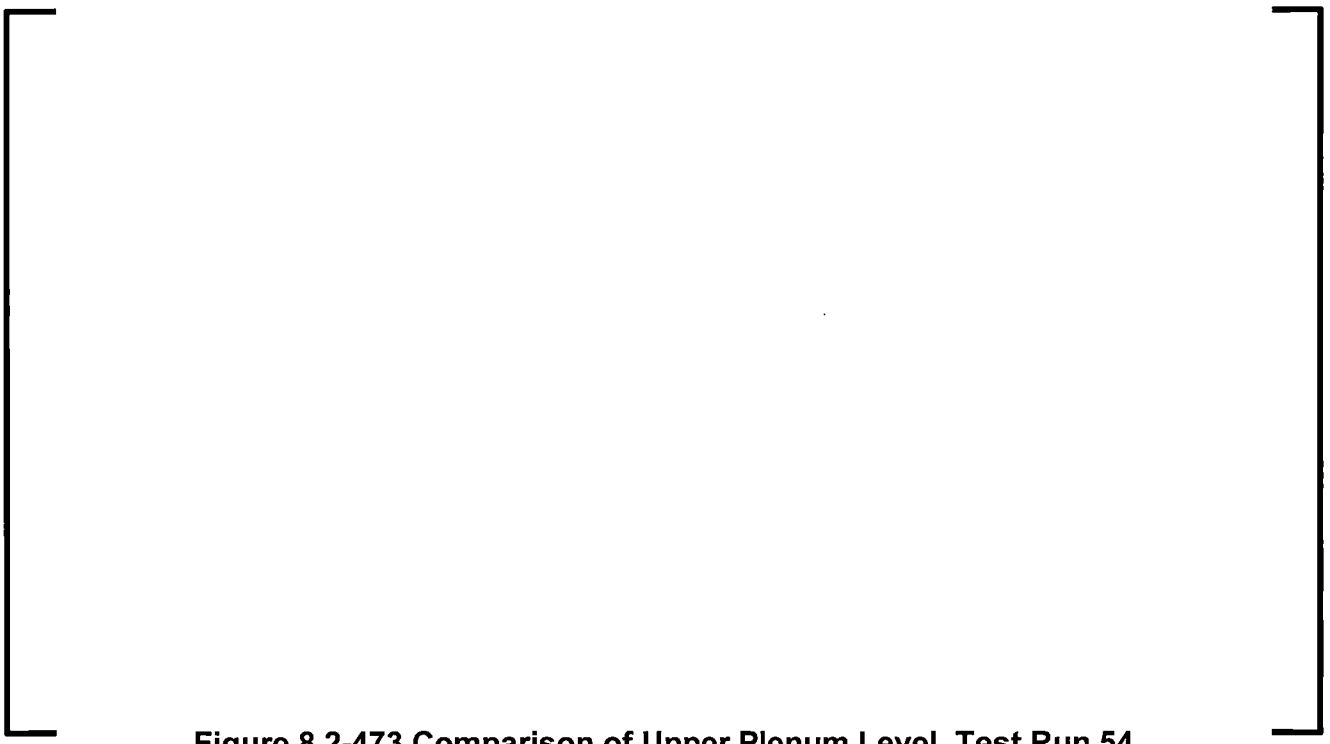

Figure 8.2-473 Comparison of Upper Plenum Level, Test Run 54

Figure 8.2-474 Tabulated Total Core Power, Test Run 62

Figure 8.2-475 Input Pressure of Pump-side Containment, Test Run 62

Figure 8.2-476 Input Pressure of Vessel-side Containment, Test Run 62

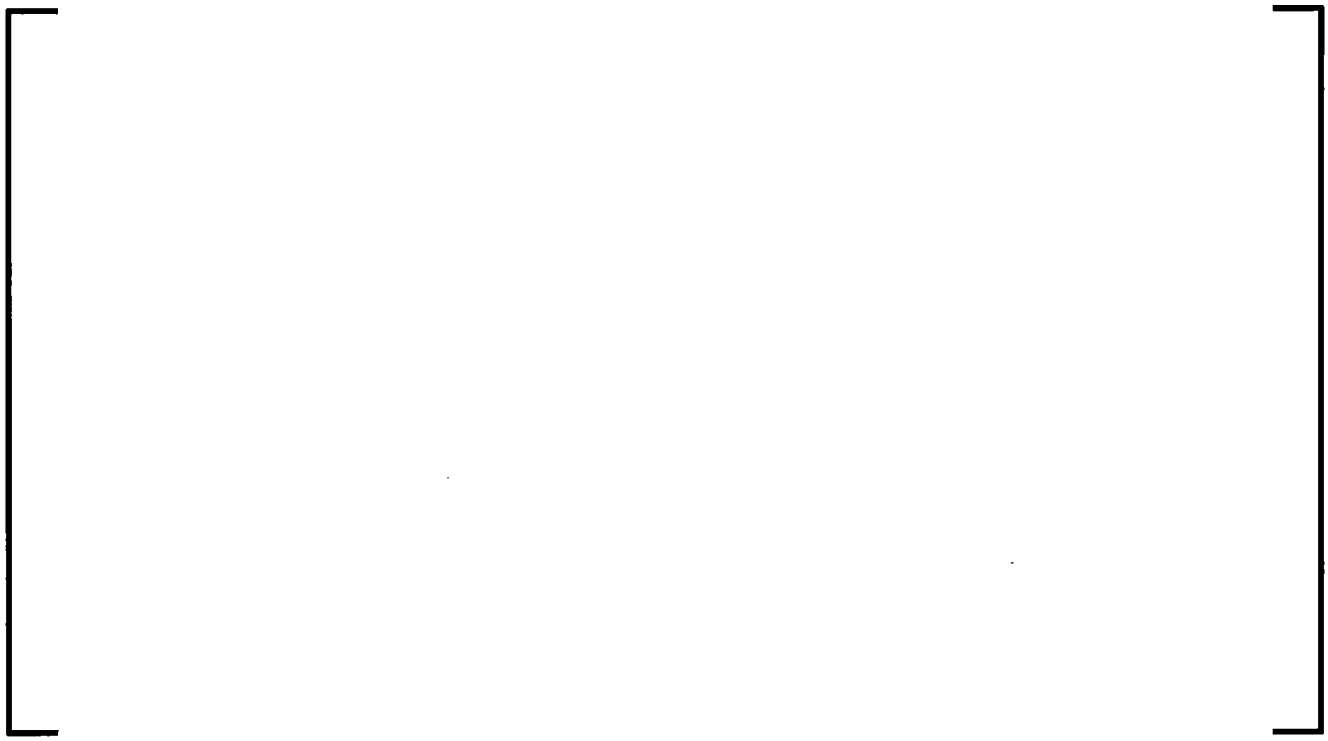

Figure 8.2-477 Input of ECC (Lower Plenum and Cold Legs) Mass Flow Rates, Test Run 62

Figure 8.2-478 Calculated and Measured BLHL Mass Flow Rates, Test Run 62

Figure 8.2-479 Comparison of Mass Flow Rates for Pump-Side Break, Test Run 62

Figure 8.2-480 Measured Mass Flow Rates for the BLHL and BLCL, Test Run 62

Figure 8.2-481 Calculated and Measured BLHL Void Fraction, Test Run 62

Figure 8.2-482 Differential Pressure Across the Intact Loop Pump Simulator, Test Run 62

Figure 8.2-483 Calculated and Measured Intact Loop Hot Leg Mass Flow Rates, Test Run 62

Figure 8.2-484 Calculated and Measured Intact Loop Hot Leg Steam Mass Flow Rates, Test Run 62

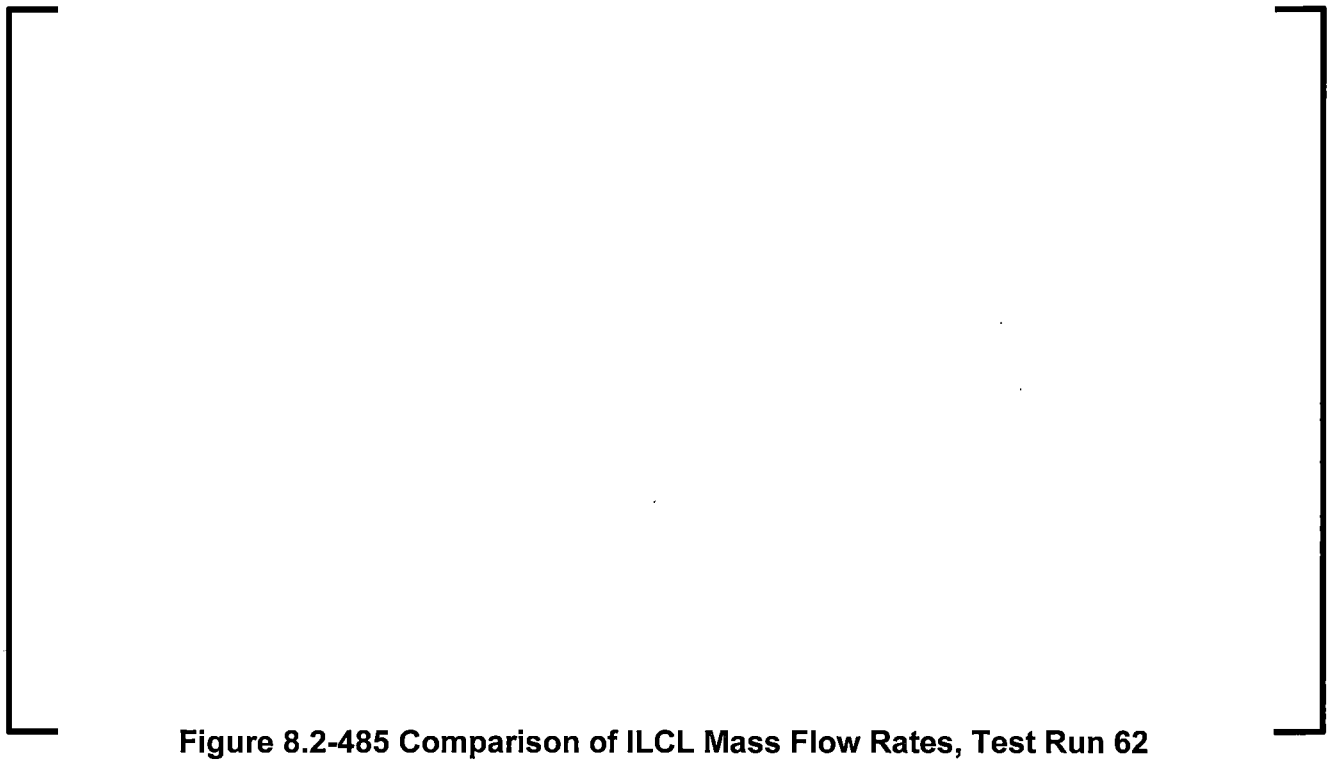

Figure 8.2-485 Comparison of ILCL Mass Flow Rates, Test Run 62

Figure 8.2-486 Calculated and Measured ILHL Void Fractions, Test Run 62

Figure 8.2-487 Calculated and Measured ILCL Void Fractions, Test Run 62

Figure 8.2-488 Measured Downcomer Differential Pressures in Four Azimuthal Directions, Test Run 62

Figure 8.2-489 Calculated and Measured Downcomer Differential Pressure, Test Run 62

Figure 8.2-490 Comparison of Core Differential Pressures, Test Run 62

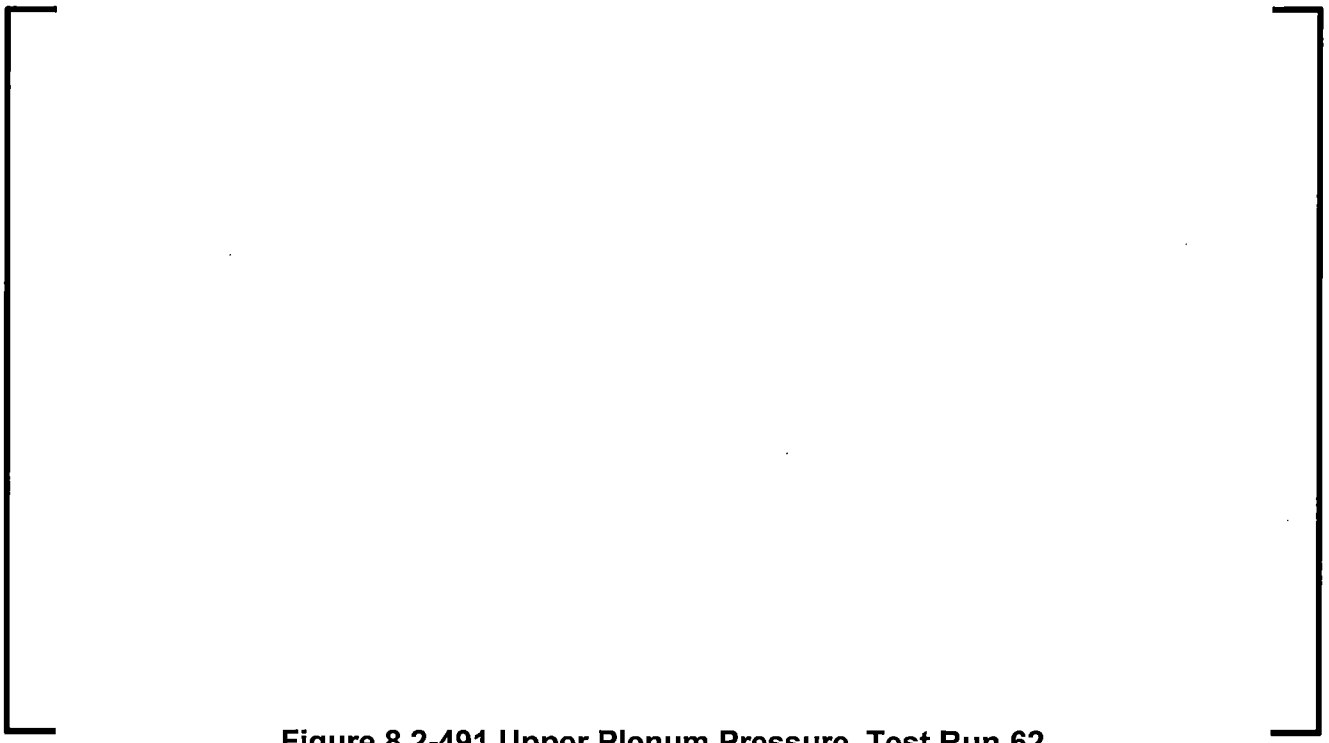

Figure 8.2-491 Upper Plenum Pressure, Test Run 62

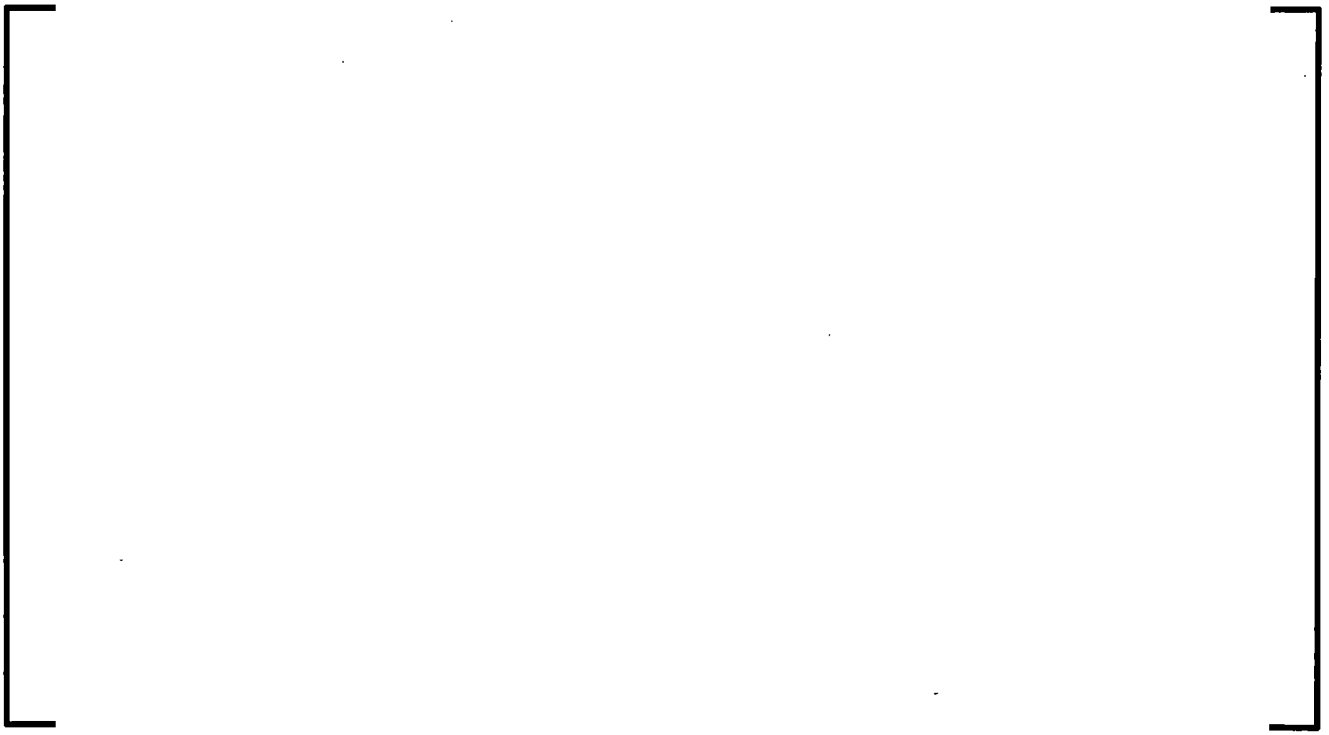

Figure 8.2-492 Comparison of Rod Surface Temperatures for High Power Bundles at 1.83 m Elevation, Test Run 62

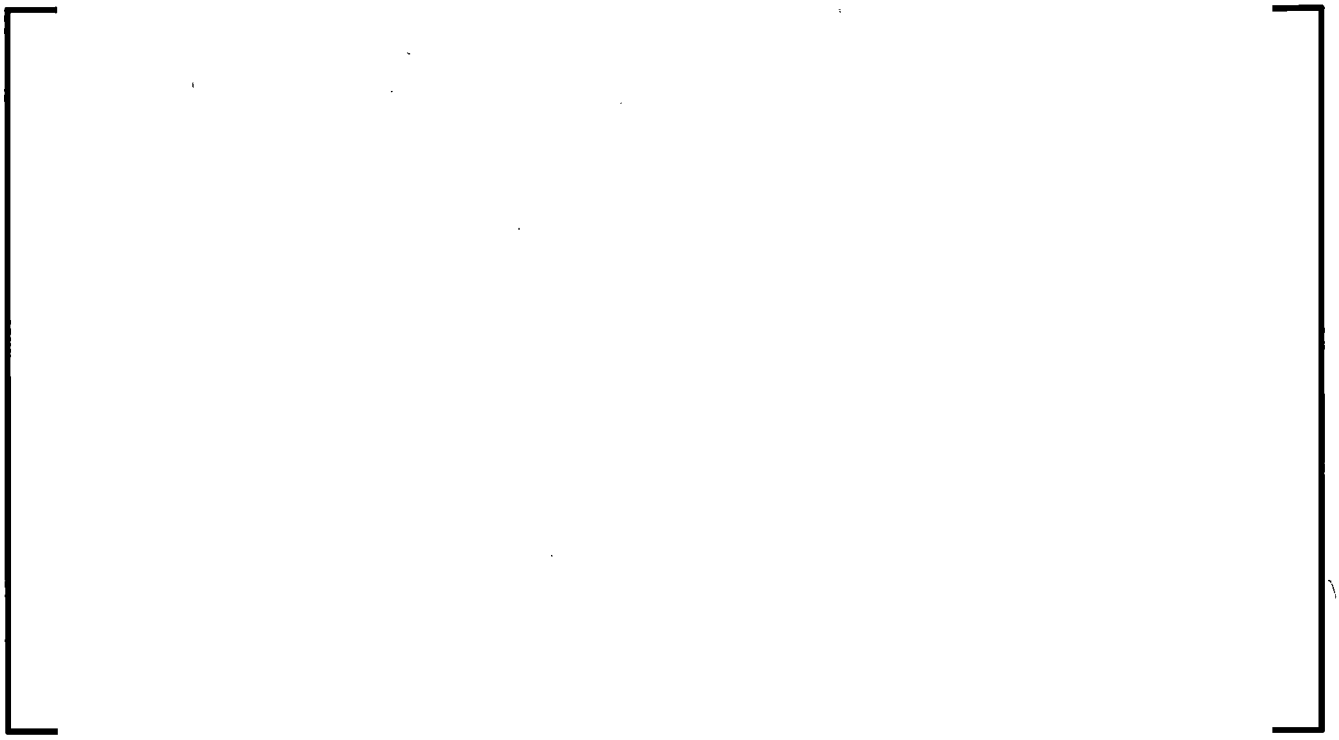

Figure 8.2-493 Comparison of Rod Surface Temperatures for High Power Bundles at 2.035 m Elevation, Test Run 62

Figure 8.2-494 Comparison of Rod Surface Temperatures for Medium Power Bundles at 1.015 m Elevation, Test Run 62

Figure 8.2-495 Comparison of Rod Surface Temperatures for Medium Power Bundles at 2.44 m Elevation, Test Run 62

Figure 8.2-496 Comparison of Rod Surface Temperatures for Medium Power Bundles at 3.05 m Elevation, Test Run 62

Figure 8.2-497 Comparison of Rod Surface Temperatures for Low Power Bundles at 2.44 m Elevation, Test Run 62

Figure 8.2-498 Comparison of Rod Surface Temperatures for Low Power Bundles at 3.05 m Elevation, Test Run 62

Figure 8.2-499 Comparison of Peak Surface Temperatures vs. Elevation for High Power Bundles, Test Run 62

Figure 8.2-500 Comparison of Liquid Level in Containment Tank II, Test Run 62

Figure 8.2-501 Comparison of Intact Loop Steam Generator Secondary Side Pressure, Test Run 62

Figure 8.2-502 Comparison of Broken Loop Steam Generator Secondary Side Pressure, Test Run 62

Figure 8.2-503 Comparison of Upper Plenum Level, Test Run 62

Figure 8.2-504 Tabulated Total Core Power, Test Run 67

Figure 8.2-505 Input Pressure of Pump-side Containment, Test Run 67

Figure 8.2-506 Input Pressure of Vessel-side Containment, Test Run 67

Figure 8.2-507 Input of ECC (Lower Plenum and Cold Legs) Mass Flow Rates, Test Run 67

Figure 8.2-508 Calculated and Measured BLHL Mass Flow Rates, Test Run 67

Figure 8.2-509 Comparison of Mass Flow Rates for Pump-Side Break, Test Run 67

Figure 8.2-510 Measured Mass Flow Rates for the BLHL and BLCL, Test Run 67

Figure 8.2-511 Calculated and Measured BLHL Void Fraction, Test Run 67

Figure 8.2-512 Differential Pressure Across the Intact Loop Pump Simulator, Test Run 67

Figure 8.2-513 Calculated and Measured Intact Loop Hot Leg Mass Flow Rates, Test Run 67

Figure 8.2-514 Calculated and Measured Intact Loop Hot Leg Steam Mass Flow Rates, Test Run 67

Figure 8.2-515 Comparison of ILCL Mass Flow Rates, Test Run 67

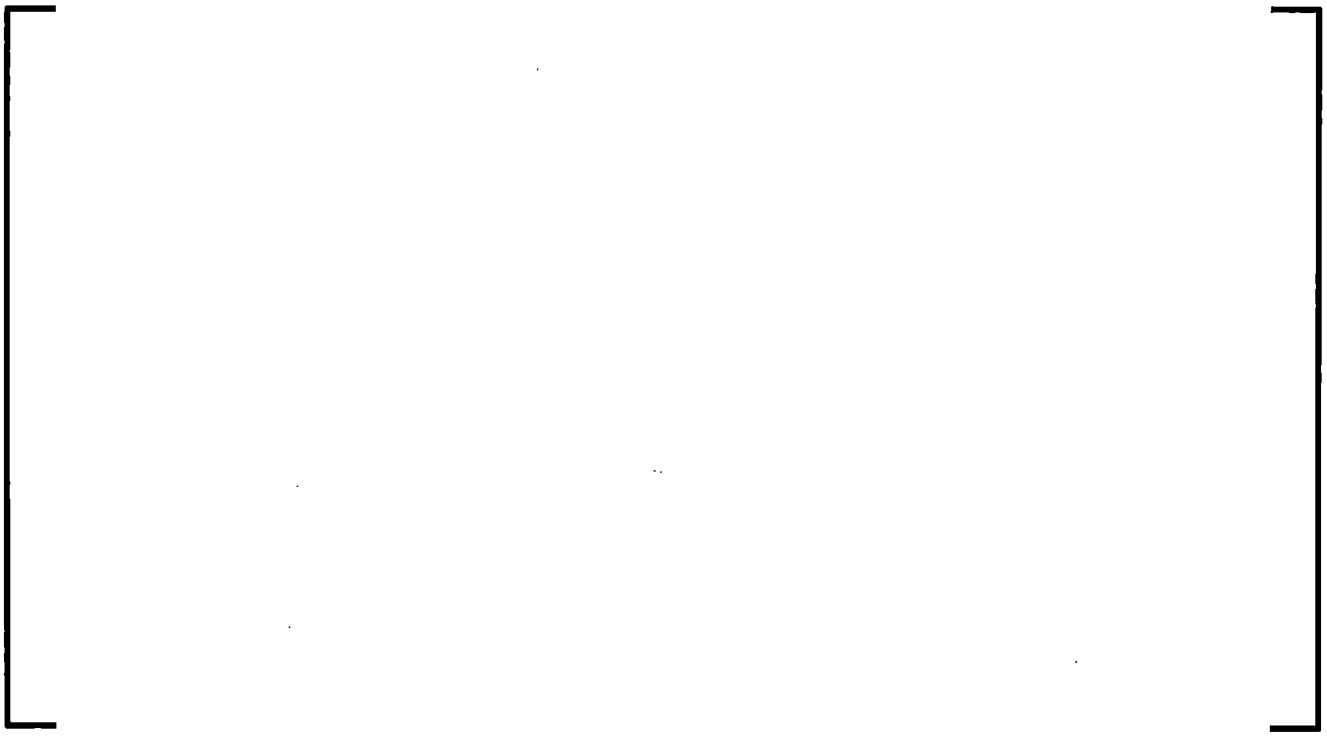

Figure 8.2-516 Calculated and Measured ILHL Void Fractions, Test Run 67

Figure 8.2-517 Calculated and Measured ILCL Void Fractions, Test Run 67

Figure 8.2-518 Measured Downcomer Differential Pressures in Four Azimuthal Directions, Test Run 67

Figure 8.2-519 Calculated and Measured Downcomer Differential Pressure, Test Run 67

Figure 8.2-520 Comparison of Core Differential Pressures, Test Run 67

Figure 8.2-521 Upper Plenum Pressure, Test Run 67

Figure 8.2-522 Comparison of Rod Surface Temperatures for High Power Bundles at 1.83 m Elevation, Test Run 67

Figure 8.2-523 Comparison of Rod Surface Temperatures for High Power Bundles at 2.035 m Elevation, Test Run 67

Figure 8.2-524 Comparison of Rod Surface Temperatures for Medium Power Bundles at 1.015 m Elevation, Test Run 67

Figure 8.2-525 Comparison of Rod Surface Temperatures for Medium Power Bundles at 2.44 m Elevation, Test Run 67

Figure 8.2-526 Comparison of Rod Surface Temperatures for Medium Power Bundles at 3.05 m Elevation, Test Run 67

Figure 8.2-527 Comparison of Rod Surface Temperatures for Low Power Bundles at 2.44 m Elevation, Test Run 67

Figure 8.2-528 Comparison of Rod Surface Temperatures for Low Power Bundles at 3.05 m Elevation, Test Run 67

Figure 8.2-529 Comparison of Peak Surface Temperatures vs. Elevation for High Power Bundles, Test Run 67

Figure 8.2-530 Comparison of Liquid Level in Containment Tank II, Test Run 67

Figure 8.2-531 Comparison of Intact Loop Steam Generator Secondary Side Pressure, Test Run 67

Figure 8.2-532 Comparison of Broken Loop Steam Generator Secondary Side Pressure, Test Run 67

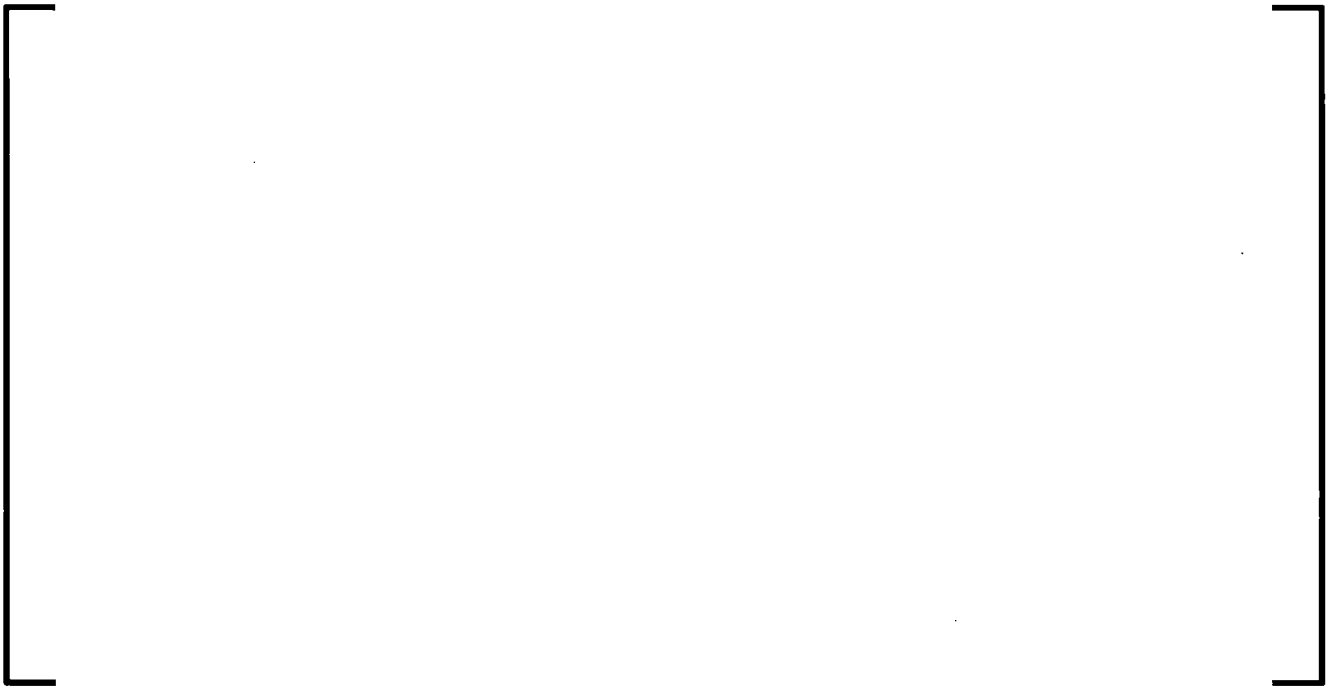

Figure 8.2-533 Comparison of Upper Plenum Level, Test Run 67

Figure 8.2-534 Tabulated Total Core Power, Test Run 68

Figure 8.2-535 Input Pressure of Pump-side Containment, Test Run 68

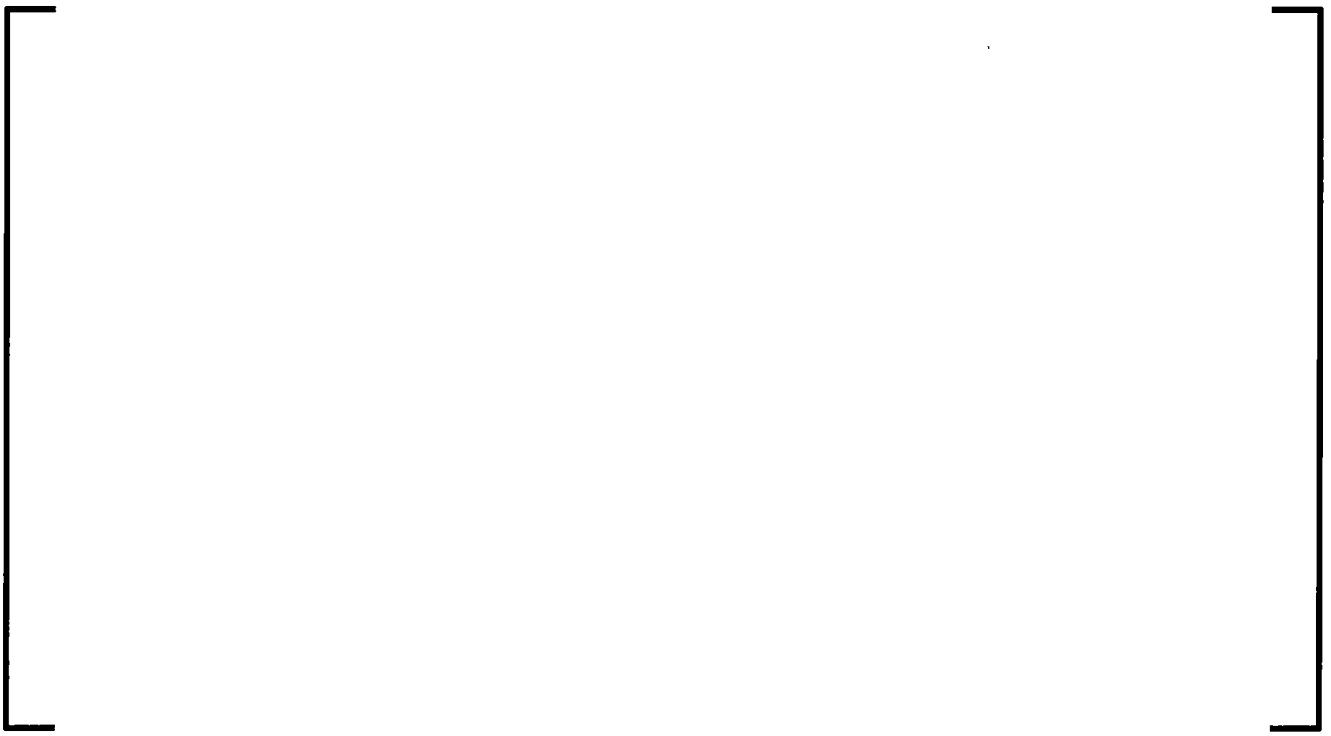

Figure 8.2-536 Input Pressure of Vessel-side Containment, Test Run 68

Figure 8.2-537 Input of ECC (Lower Plenum and Cold Legs) Mass Flow Rates, Test Run 68

Figure 8.2-538 Calculated and Measured BLHL Mass Flow Rates, Test Run 68

Figure 8.2-539 Comparison of Mass Flow Rates for Pump-Side Break, Test Run 68

Figure 8.2-540 Measured Mass Flow Rates for the BLHL and BLCL, Test Run 68

Figure 8.2-541 Calculated and Measured BLHL Void Fraction, Test Run 68

Figure 8.2-542 Differential Pressure Across the Intact Loop Pump Simulator, Test Run 68

Figure 8.2-543 Calculated and Measured Intact Loop Hot Leg Mass Flow Rates, Test Run 68

Figure 8.2-544 Calculated and Measured Intact Loop Hot Leg Steam Mass Flow Rates, Test Run 68

Figure 8.2-545 Comparison of ILCL Mass Flow Rates, Test Run 68

Figure 8.2-546 Calculated and Measured ILHL Void Fractions, Test Run 68

Figure 8.2-547 Calculated and Measured ILCL Void Fractions, Test Run 68

Figure 8.2-548 Measured Downcomer Differential Pressures in Four Azimuthal Directions, Test Run 68

Figure 8.2-549 Calculated and Measured Downcomer Differential Pressure, Test Run 68

Figure 8.2-550 Comparison of Core Differential Pressures, Test Run 68

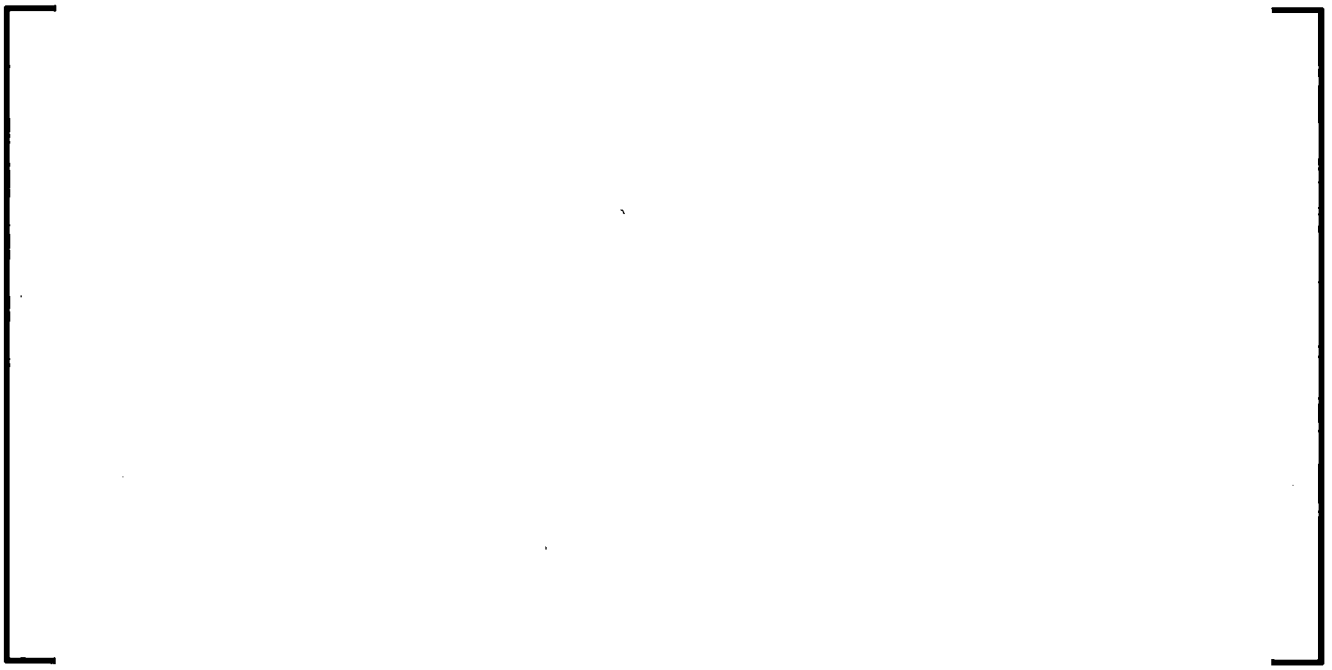

Figure 8.2-551 Upper Plenum Pressure, Test Run 68

Figure 8.2-552 Comparison of Rod Surface Temperatures for High Power Bundles at 1.83 m Elevation, Test Run 68

Figure 8.2-553 Comparison of Rod Surface Temperatures for High Power Bundles at 2.035 m Elevation, Test Run 68

Figure 8.2-554 Comparison of Rod Surface Temperatures for Medium Power Bundles at 1.015 m Elevation, Test Run 68

Figure 8.2-555 Comparison of Rod Surface Temperatures for Medium Power Bundles at 2.44 m Elevation, Test Run 68

Figure 8.2-556 Comparison of Rod Surface Temperatures for Medium Power Bundles at 3.05 m Elevation, Test Run 68

Figure 8.2-557 Comparison of Rod Surface Temperatures for Low Power Bundles at 2.44 m Elevation, Test Run 68

Figure 8.2-558 Comparison of Rod Surface Temperatures for Low Power Bundles at 3.05 m Elevation, Test Run 68

Figure 8.2-559 Comparison of Peak Surface Temperatures vs. Elevation for High Power

Figure 8.2-560 Comparison of Liquid Level in Containment Tank II, Test Run 68

Figure 8.2-561 Comparison of Intact Loop Steam Generator Secondary Side Pressure, Test Run 68

Figure 8.2-562 Comparison of Broken Loop Steam Generator Secondary Side Pressure, Test Run 68

Figure 8.2-563 Comparison of Upper Plenum Level, Test Run 68